Biomimetic Substrates for Immune Cell Activation

Derfogail Delcassian

Thesis submitted for the degree of Doctor of Philosophy (PhD)
December 2013
Department of Materials
Imperial College London

Abstract

This thesis describes the fabrication of biomimetic substrates, and their use as tools to probe cellular interactions of key immune cells. Nanoparticles of gold and zinc sulfide have been fabricated, and patterned into nanoarrays. Adaptive (T cell) and innate (NK cell) immune cell responses to nanoscale spacing of ligand-receptor pairs were measured, and the effect of presenting stimulatory ligands on substrates with varying mechanical properties has been tested for T cell responses. The advanced materials in this thesis act to create artificial immune synapses, and probe the effect of these stimuli on engagement and activation of human immune cells.

Specifically, block co-polymers were used to form polymer micelles which encapsulate metal ions and form metal or metal compound nanoparticles. Micelles encapsulating metal ions or nanoparticles were formed and deposited onto substrates using Block Co-polymer Micellar Lithography (BCML) to form nanoparticle arrays with controlled inter-particle spacing.Well controlled gold nanoparticle arrays with spacing between 25-150nm have been produced. The technique has been further developed to include fabrication of zinc sulfide particles and nanoarrays. Zinc sulfide nanoparticles showed a unique internal structure with 5nm crystalline domains set in an amorphous matrix and an optical band gap of between 3.88-4.28eV.

Nanoparticle arrays were then functionalised with biological ligands, notably antibodies that engage with the NK cell surface receptor CD16, or the T cell TCR/CD3 moiety. The cellular response to these materials was measured, and was sensitive to the nanoscale arrangement of stimulatory ligands; both cell types responded to ligands with 25nm, but not 104nm, inter-ligand spacing.

In an alternative approach, spherical PEG hydrogel particles of diameter 5-50μm were formed with controlled rigidity between 3-2000kPa. T cell response as a function of substrate rigidity was tested, and cells showed maximal response to anti-CD3 functionalised substrates with rigidities of 3-5kPa.

Declarations

Declaration of Originality

I, Derfogail Delcassian, declare that this thesis and the work reported within was composed by and originated from me. Information derived from the published and unpublished work of others, or work completed in conjunction with other parties, has been acknowledged in the text and appropriate references are given in the list of sources.

Copyright

Derfogail Delcassian
December 2013

Preface

Some of the work described in this thesis has previously been presented and published, as described below.

Papers

D. Delcassian, D. Depoil, D. Rudnicka, M. Liu, D. M Davis, M. L Dustin, I.E Dunlop, Nanoscale Ligand Spacing Influences Receptor Triggering in T cells and NK cells, Nanoletters, 2013

Presentations

Nanoscale artificial immune synapses can be used to controllably activate T and NK cells,
D. Delcassian, D. Depoil, D. Rudnicka, M. Liu, D. M Davis, M. L Dustin, I.E Dunlop, BSI 2013, *Poster Presentation*

CD4+ T cell Response to Geometry and Rheometry,
D. Delcassian and I. E. Dunlop, Nanomedicine Centre for Mechanobiology, NYU, November 2012, *Oral Presentation*

Biomimetic Nanopatterns for Immune Cell Signalling,
D. Delcassian, D. Depoil, A, Liapis, M. Dustin and I. E. Dunlop, Nanomedicine Centre for Mechanobiology, NYU, November 2011, *Poster Presentation*

Biomimetic Nanopatterns and Cell Signalling Investigations,
D. Delcassian and I. E. Dunlop, Cellular Systems Summer School, Max Plank Institute Heidelberg, August 2011, *Oral Presentation*

Investigating T cell signaling using biomimetic nanopatterns; a comparison between native TCR and CAR,
D. Delcassian and I. E. Dunlop, Nanomedicine Centre for Mechanobiology, NYU, November 2010, *Poster Presentation*

Acknowledgments

I am grateful for financial support provided by the EPSRC and the NIH throughout my research.

I'd like to thank my principal supervisor, Dr. Iain Dunlop, for giving me the opportunity to undertake this PhD. Thanks especially for your constant enthusiasm, the chance to travel and the privilege of being your first group member. The Dunlop group has also been a delight to watch develop, and I'm grateful for the support and friendship I have received from our newest members, and for the opportunity to supervise fantastic Masters students. My secondary supervisor, Professor Molly Stevens, and her research group have provided me with a great deal of inspiration and encouragement, and I'd particularly like to thank the nano-subgroup for helpful discussions.

Much of the work described in this thesis was completed as part of an NIH funded multinational collaboration, namely the "Nanomedicine Center for Mechanobiology, Directing the Immune Response" programme. Several of the research topics investigated in this thesis were performed in the context of this collaboration, specifically those in relation to T cell investigations (Chapters 7 and 8). Additionally, the programme involved exchanges at collaborator laboratories. I would especially like to thank the members of my host laboratories for making me feel welcome and assisting with my project; Prof. Mike Dustin, Dr. David Depoil, Dr. Anastasia Liapis, Dr. Silvia Curado and others at NYU, Prof. Mike Milone and Dr. Roddy O'Connor at U. Penn, and Prof. Joachim Spatz and team at MPI Stuttgart.

The expertise and assistance of several people has been crucial to the work completed in this thesis. Individual contributions to specific aspects of the work are described at the beginning of each relevent chapter, however in brief I would like to thank the following people for their assistance;
Karla-Luise Herpolt, Lucia Podhorska, Dr. Angela Goode and Giovanni Luongo for TEM imaging and EDX analysis. PANanlytical for SAXS experiments and analysis performed commercially, and Dr. Iain E. Dunlop, Lucia Podhorska and Dr. Aurel Radelscu of FRMII, Juelich Centre for Neutron Science for SANS experiments and analysis. MSc students Jun Hon Pang (microcontact printing), Michael Agyei (ZnS fabrication) and Octave Etard (hydrogel beads) for their help in developing some of the methodology described in this thesis. Sajjad Jaffer for his help with the hydrogel bead sizing aspect of this work, and bulk rheometry measurements. I am grateful to Prof. Dan Davis and Dr. Dominika Rudnicka for their partnership in the NK cell aspect of this work; specifically Dr. Dominika Rudnicka for NK cell seperation, culture and cellular imaging. Prof. Mengling Liu, Department of Biostatistics, New York University provided the Spearman's Rank Correlation and Wilcoxon rank sum statistical tests in Chapter 7, and finally I'd like to thank Dr. David Depoil for his assistance with TIRF microsopy in relation to the T cell aspect of this work.

A great number of friends have made my time at Imperial, and in London, a joy. In particular, I wish to thank the team in Imperial 2.12 and London friends for countless good times, members of the Canoe Club(s) for hilarious weekends and great friends for wild adventures abroad and at home. Finally, to my family for their endless love and support; to Mum, Dad and Sabina, without whom this thesis would not have been possible.

Contents

List of Figures

List of Tables

Nomenclature

µCP	Microcontact printing
ADCC	Antibody Dependant Cellular Cytotoxicity
AOT	Aerosol-OT
APCs	Antigen Presenting Cells
BCML	Block Copolymer Micellar Lithography
cmc	Critical micelle concentration
DLS	Dynamic light scattering
EBL	Electron beam lithography
EDX	Energy dispersive X-Ray analysis
FIB	Focused ion beam
His-tag	Six Histidine residues incorporated at the end of a genetically engineered protein sequence
HRTEM	High Resolution Transmission Electron Microscopy
IS	Immune Synapse
ITAM	Immunotyrosine Activatory Motif
ITIMs	Immunotyrosine Inhibitory Motif
MSCs	Mesenchymal stem cells
NTA	Nitrilotriacetic acid
P2VP	Poly-2-vinylpyridine
PA	Poly (acrylamide)
PBS	Phosphate Buffered Saline
PDMS	Poly (dimethylsiloxane)
PEG	Poly ethylene glycol

PLL	Poly (L-lysine)
PLL-g-PEG	Poly (L-lysine) -graft- poly (ethylene glycol)
pMHC	Major Histocompatability Complex
PS-b-P2VP	Poly (styrene-block-2-vinylpyridine)
QDs	Quantum dots
SAM	Self Assembled Monolayers
SANS	Small Angle Neturon Scattering
SAXS	Small Angle X-Ray Scattering
TCR	T Cell Receptor Complex
TIRF	Total Internal Reflection Microscopy
WHO	World Heath Organisation

Chapter 1

Motivation and Outline

The 2011 World Health Organisation (WHO) report identified the ten leading causes of human death worldwide; of these, five can be directly related to failures in host immune responses, together causing 9.6 million deaths per year.[1] Respiratory infections, diarrheal diseases and HIV/AIDS can be attributed to the inability of the host immune system to combat external pathogens and infection.[2, 3, 4, 5, 6] Conversely, the inappropriate response of the immune system to its own cells is a factor in autoimmune diseases such as diabetes mellitus, where an overzealous and uncontrolled immune response can result in destruction of insulin producing cell islets,[7, 8, 9, 10, 11, 12] and cancer, where the failure of the immune system to recognise and destroy malignant cells is implicated in cancer metastasis.[13, 14, 15, 16, 17, 18, 19, 20]

In order to design suitable therapies for these diseases, an in-depth understanding of the immune system and the way in which it mediates its function is necessary. A host's immune system is part of their intrinsic defence mechanism; in situations where the immune system fails to respond appropriately to threats, the health of an individual is seriously compromised.

The immune system possesses a complex network of interconnected cells and cellular activation pathways, and operates through a range of processes including cellular cytotoxicity, generation of cytokines and cell-cell signal transmission.[21, 22, 23, 24, 25] Many of the immune cell functions are initiated through cell-cell contacts, however the nature of the signaling processes driving immune cell activation remain elusive.

This thesis describes the fabrication of biomimetic substrates and their use to probe key cellular interactions within the immune system. We fabricate artificial antigen presenting cells (APCs) and control the presentation of stimulatory ligands. By creating environments with controlled stimuli, we can monitor the formation of artificial immune synapses between cells and these materials, and elucidate key signaling requirements to given stimuli. Here, biomimetic materials are created with control of inter-ligand spacing, or substrate rigidity. Cellular responses to these surfaces are probed using both NK and T cells, thus exploring both the innate and adaptive immune systems.

The outline of the thesis is as follows; Chapter 2 discusses the design of biomaterials that can controllably present specific stimuli to cells. Cell substrate fabrication methodologies are discussed, focusing on methods that control the nanoscale spatial distribution of ligand molecules, and on the fabrication of substrates with controlled mechanical properties. Additionally, a detailed explanation of the adaptive and innate immune cells explored in this thesis is provided; cellular receptors, signaling mechanisms, and the current understanding of the sensitivity of these cells to mechanical and geometrical ligand presentation is discussed.

The experimental techniques used in the thesis are described thoroughly in Chapter 3. Both physical characterisation methods, for the investigation of substrate properties, and biological characterisation techniques utilised in measuring cellular activation levels and responses to prepared materials are reviewed.

Chapter 4 describes the optimisation of micellar lithography in this lab, using a poly (styrene-*block*-2-vinylpyridine) polymer. Gold nanoarrays with controlled inter-particle spacing, particle size and local order are produced, and the control of each of these parameters is described. Biofunctionalisation of these nanoparticles with thiolated peptides is demonstrated. Finally, micro-contact printing is used to produce more advanced micro-nanopattern geometries, and novel surface patterning of nanopattern geometries is described.

In Chapter 5 the fabrication of an alternative nanoparticle, again using the micellar lithography technique, is examined. The section discusses the fabrication of zinc-based compound nanoparticles, notably ZnS quantum dot particles, inside polymer templates. This chapter provides an extension to the currently available gold nanoparticle fabrication technology, and promises the development of more advanced nanopattern interfaces for selective biofunctionalisation with histidine tagged or phosphate tagged ligands.

NK cellular responses to functionalised gold nanopatterned arrays are considered in Chapter 6. The NK cell surface receptor CD16 is probed with anti-CD16 and Rituximab bound to gold nanoarrays fabricated using the methodology optimised in Chapter 4. Ligands are presented with nanometer precision, and the response to cellular engagement on substrates with inter-ligand spacing of between 25- 104nm is investigated. Cellular response is measured by cell spread area, and outcomes compared as a function of spacing and between the different CD16 engagement mechanisms.

Chapter 7 complements this work by evaluating responses of T cells to CD3 engagement. UCHT1 $F(ab')_2$ is bound to the nanoarrays prepared in Chapter 4 to create an artificial antigen presenting surface. T cell responses to these substrates at early time points are measured using TIRF microscopy, and both phosphotyrosine signaling and adhesion are used as markers to compare cellular response to CD3 engagement at fixed anchoring points.

Together, Chapters 6 and 7 offer the first investigations into nanoscale ligand sensitivity of planar stimulatory ligand engagement in NK cells and T cells, respectively.

Although the previous chapters focus on the response of cells to planar substrates, Chapter 8 investigates the response of cells to rigidity controlled culture substrates. Spherical hydrogel particles are fabricated with controlled mechanical properties. This extends current research developed on PDMS planar substrates to more physiological systems, mimicking the natural APC-T cell interaction. These substrates are then used to present T cell stimulating antibodies to transfected Jurkat cells. Activation of the cells is compared across different rigidity values, and a range of antibody and co-stimulatory ligands is tested.

In summary, this thesis explores the effect of two specific stimuli (stimulatory ligand nanospacing, and the mechanical properties of substrates functionalised with stimulatory ligands) on immune cell activation to generate fundamental insights into signalling in T and NK cells.

Chapter 2

Introduction

2.1 Biomimetic Environments

2.1.1 Overview

In vivo, cells inhabit niche environments that vary dramatically from one cell type to the next, with over 200 distinct cell types and environments in the human body. These include cells that are adapted to exist in fluid environments (cells of the blood and lymph), those that live in a close packed dense solid state, and those that border fluid/solid or fluid/air barriers.[26, 27] The cells in each of these environments are subjected to distinct stimuli; these stimuli, or "cellular cues," can be loosely classified as physical (including the topographical, geometrical and mechanical nature of the cell-substrate interface) or chemical (including engagement of cell surface receptors and response to soluble factors).

In order to understand the effect of specific stimuli on cellular behaviour, it is important to be able to create environments where these stimuli are controlled. Broadly, biomimetic environments are artificially created or modified systems that mimic certain principles of *in vivo* systems with which cells can engage. They can be used to controllably present specific stimuli to cells, and so cellular responses to materials with controlled features can be investigated.

Once the stimuli orchestrating a cellular response are well understood, it is possible to manipulate cellular behaviour by fabricating artificial environments in which cells receive specific cues designed to direct their development and ultimate fate. Biomimetic environments therefore have applications ranging from developing the fundamental understanding of specific cellular processes, to more advanced multi-cellular applications, including aiding implantable construct design and directed cellular behaviour in tissue engineering or adoptive cell transfer applications.

This chapter describes the key principles underpinning biomimetic design, and highlights examples of successful fabrication of biomimetic materials, specifically focusing on the cell-material interface.

2.1.2 Chemical and Physical Stimuli

In vivo, cells engage with their immediate environment, this includes cells in close proximity to themselves, the Extracellular Matrix (ECM) (a complex network of insoluble proteins and glycoproteins), and the chemical stimuli found in the fluid surrounding them.[28, 29] Here, we define chemical stimuli as substances that can engage with cell surface receptors to invoke a cellular response; these can be small molecules, chemokines, cytokines, salts, larger biological molecules such as antibodies or repeating amino acid residues.[30, 31]

The chemical environment in which a cell is placed determines cellular processes and cell fate. The most simplistic example of this is the provision of nutrients in certain ratios, which effects the ability of cells to grow and replicate.[32, 33] Specific media compositions are known to direct cell phenotypic differentiation by providing selected soluble chemical stimuli. Utilising knowledge of the effect of specific soluble chemical stimuli on cellular behaviour has led to the design of new biotherapeutics. Recent developments in drug delivery systems have coated particles with specific markers that enable the particles to be masked from certain cells in the body, whilst being specifically targeted to other cell or tissue types.[34] Furthermore, development of mono, bi-specific and tri-specific antibody therapies has led to drugs which can simultaneously bind a target cell surface receptor and an immunogenic cell target receptor, facilitating close interaction between the cell types, and therefore enhancing the response of the immune system to a specific target.[35, 36, 37, 38, 39]

Importantly, chemical stimuli can be provided in soluble, and so "texture-less" form, or can also provide some physical stimulation simultaneously. For example, molecules anchored to a physical support can resist mechanical force applied by a cell. Equally, ligand motifs can be self-assembled into larger protein structures that provide spatially-controlled stimulation to cells, such as RGD sequences within helical fibronectin fibres.[40] With knowledge of the key soluble factors required to induce specific cell function, biomaterials in which these factors are tethered to solid supports can be used to develop more advanced materials capable of stimulating cells via both chemical and physical cues.

Physical cues largely act at the cell-material interface; either through the presence of cells in contact with each other, or through interaction with the Extracellular Matrix (ECM) that provides both a structural and signaling scaffold for cells.[41] Alongside offering a basic physical support or construct in which cells can reside, the ECM largely provides the landscape, or topography, with which cells engage, and is organised on the macro, micro and nanoscale.[42] In addition to topography, this physical environment also provides mechanical stimulation to the cells and offers some control over the spatial distribution of stimulatory ligands within the physical matrix.

Cellular sensing of the physical environment is thought to occur through a variety of receptors, both mechanosensitive receptors on the cell surface for determining rigidity of the material with which cells are engaging, and receptors that co-ordinate responses to geometrically patterned ligands. The interplay of the chemical and physical stimuli in terms of ligand presentation is still not fully understood. Providing geometrically controlled chemical stimulation on varied physical supports has shown that there is a complex balance between dominating factors.[43] Next generation biomaterials will attempt to decouple physical and chemical stimuli in order to develop systems that can probe each factor independently. The next sections discuss investigations into the control of, and cellular response to, these parameters in fabricated biomimetic environments, with particular focus on physical stimuli.

2.1.3 Cellular response to topographical ligand presentation

Cellular response to biomaterials has demonstrated that a range of cells are able to sense and respond to nanotopography, including the presentation and height of depressed and elevated features such as wells, pits[44, 45] and nanopillars.[46, 47, 48] Cells appear affected by interfacial forces, organised by nanotopography, and orientate themselves around features on presented substrates. [49, 50, 51, 52, 53]

Human fibroblasts have been shown to be particularly sensitive to nanotopography; they responded to 27 nm high nanoislands that were spaced discretely, however whilst cells initially showed adhesion and cytoskeleton formation after 4 days, this was unstable after 30 days in culture.[46] Fibroblasts are also sensitive to collagen fibril density and so local topography, with changes in density affecting both cell morphology and cell size.[54, 55] Studies have suggested that although several cell types are found to adhere and grow along asymmetrical topography, ordered surface arrays reduce cell adhesion compared with planar surfaces or more irregular structures.[44, 56, 57, 58, 59] In a recent review article, Good *et al.* have shown the importance of spatially orientated scaffold proteins and their interactions as a key factor in internal cell organisation.[60]

2.1.4 Cellular response to mechanically controlled substrates

Cells exist in niche environments with distinct mechanical properties, Young's Modulus values in the body range from those of soft tissues (0.1-1kPa) to calcified tissues such as mineralised compact bone (18-30GPa).[61, 62] Recent work has identified that cells are responsive to the mechanical properties of the environment around them, and that changing the mechanical properties of a cellular substrate can causes significant changes in cellular response, and even direct stem cell differentiation. A potent example of this is the work completed by Engler *et al.* which showed Mesenchymal stem cells (MSCs) differentiate selectively into neurogenic, myogenic, or osteogenic cells when cultured on substrates whose rigidity reflected the typical values for brain, muscle or bone respectively.[63, 64, 65]

Since these early studies, the effect of substrate rigidity has been investigated in a range of cell types, however has primarily focused on stem cells with a view to tissue engineering and regenerative medicine applications, currently there are very limited studies on engineered environments for immune cells, however many other cell types have been investigated. Substrate stiffness can be used to control cell spreading in muscle cells,[66, 67, 68, 69, 70, 71] and differentiation in neurones,[72, 73] hematapoietic stem cells[62] and osteocytes.[74] Interestingly, cells can also respond durotactically to materials, sensing and moving along rigidity gradients towards a preferred substrate stiffness.[75, 76]

There is also much interest in whether the cell is physically sensing force through the chemical ligand attachment mechanisms, or the underlying substrate rigidity, as these parameters are linked.[43, 77] An intriguing experiment using magnetically controlled poly (acrylamide) gels showed that cells were dynamically responsive to acute changes in substrate physical properties caused by rigidity on the same substrate, [78] perhaps suggesting that it is the underlying rigidity directing cellular interactions.

2.1.5 Cellular response to ligand geometry

It is well known that many types of cell processes are dependent on specific configurations and spacing of certain biomolecules, including antibody-antigen recognition,[79, 80, 81, 82] enzyme substrate recognition[83, 84, 85] and ligand-receptor interactions.[86, 87, 88] Whilst the conformation of the specific site is important, it is thought that spacing and organisation of ligands (including the overall geometry, inter-ligand distance and clustering of stimulatory ligands) are also important.

The majority of human cells are sized on the microscale, between 10-40µm in diameter.[89] Cells engage with their environment through a variety of receptors, and are able to understand cues about their natural environment presented to them by other cells of similar scale. It is unsurprising then, that cells can respond to proteins patterned into geometries of the same size scale as the cell itself. There has been much interest in the selective response of stem cells to such patterned proteins, where more circular patterns tend to direct Mesenchymal stem cells to adipose fates, and anisotropic ligand geometries towards neurogenic lineages, thought to be mediated by mechanotransduction in adhesion receptors.[89, 90]

Although cells are sized on the microscale, the individual cellular receptors which engage with these ligands are of nanoscale dimensions, so it is also important to investigate cell signaling requirements at these length-scales. The techniques used to pattern biological molecules on the nanoscale are discussed in detail in Section 2.3, but broadly involve creating nanoscale features on a 2-Dimensional substrate that are functionalised with biological ligands, shown schematically in Figure 2.1.1.

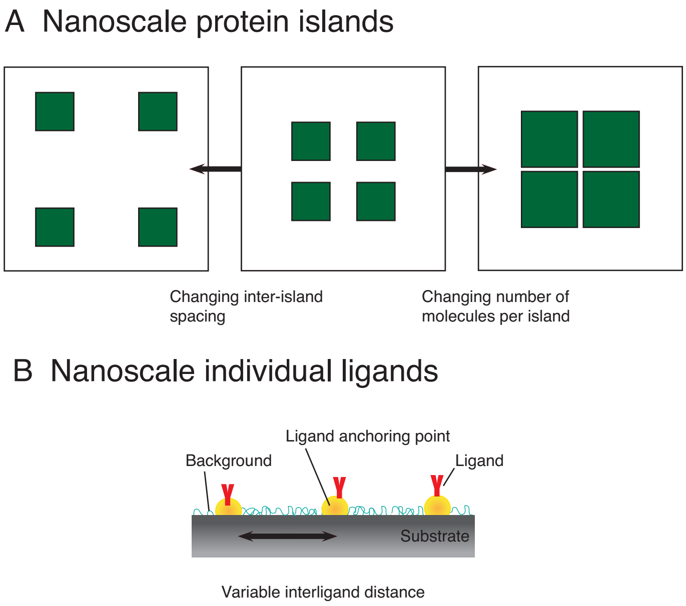

Figure 2.1.1: Nanoscale Protein Presentation. (A) Micro- or nanoscale protein islands can be produced that allow the geometric presentation of stimulatory ligands. Protein islands can be altered to produce the same shape and ligand density at different protein island spacings, or different ligand amounts at the same overall ligand density. (B) Proteins and ligands can be patterned with nanoscale inter-ligand spacing by anchoring proteins to underlying nanofeatures.

Nanoscale protein islands, such as those shown in 2.1.1(A), allow factors such as ligand density and ligand island proximity to be investigated separately; cellular responses appear sensitive to many factors, including the total number of ligands, the ligand density on each protein island, and the spacing between individual protein islands.[91, 92, 90] This implies that cells are sensing and responding to the precise nanoscale positioning of cellular ligands. In order to investigate the effect of nanoscale ligand positioning on cellular activation, surfaces which present controlled ligand orientation need to be employed. Figure 2.1.1(B) illustrates precise ligand positioning, where ligand anchoring points can be fabricated on substrates at controlled inter-anchor distances between 10-1000nm, therefore allowing biomolecules to be presented at this inter-ligand spacing. The fabrication of this type of surface is discussed in more detail in Section 2.3, here, we focus on cellular responses to such interfaces, which are currently limited in the literature to studies in cellular fibroblast adhesion and some simple activation investigations.

One of the many processes a cell can undergo on encountering a surface is attachment. Cellular adhesion to synthetic surfaces is sensitive to ligand density and chemistry, pattern geometry and substrate rigidity.[93, 94] With the extracellular size of an integrin receptor ranging from 9-12nm examined by crystallography[95, 96] it becomes clear that cells are sensing and attaching to ligands on a nanometre scale. Recent investigations into the effect of controlling RGD (a typical cellular adhesion ligand for the adhesion receptor integrin) spacing have determined that there is both a minimal inter-ligand spacing and minimum cluster number that need to be reached before a cell will form mature and stable attachments, termed focal adhesions. In fact, Maheshwari *et al.* used a star PEG patterning method to show that a minimum of 5 clustered RGD peptides were needed to form mature focal adhesions, and that random distribution of peptides did not achieve this, whilst Huang and Ding state that a minimum number of 6 ligands are required.[97, 93]

A current hypothesis used to explain these findings suggests that cell spreading may be dependent on critical densities of submicron integrin clusters to begin recruitment of focal adhesions,[98, 99, 100, 101] and that nanometer lateral spacing between single integrin ligands could regulate cell spreading and adhesion.[102, 103, 104, 105] Current estimates suggest an ordered inter-ligand distance of below 70nm is required for MC3T3 osteoblasts and fibroblasts to engage sucessfully with adhesion ligands.[106, 51, 107, 108, 109] Meyer *et al.* also investigated the possibility of a dual receptor system being necessary for cellular adhesion using an integrin dimer,[110] however most current research focuses on the presentation of single integrin ligands and individual interactions with a receptor, with the possibility of these individual receptor-ligand pairs clustering to induce signals. Cells have also been shown to move along chemo-attractant RGD gradients, where variable spacing of ligands induces cellular migration, and other more complex studies are being performed with adhesion ligands in both 2D and 3D.[42]

In addition to adhesion, activation and stimulation have also been studied. Ranzinger *et al.* used controlled presentation of Tumour Necrosis Factor (TNF) (attached to gold nanoparticles fabricated by block copolymer micellar nanolithography arrays) to demonstrate controlled apoptosis and activation of the TNFR1 receptor and its chimeras. They found that TNFR1 showed an on-off relationship with variations in spacing. Presenting TNF at inter-ligand spacings between 58-200nm induced comparable signaling leading to cell apoptosis, however inter-ligand spacing of 260nm showed intermediate effects and ligands spaced greater than 290nm apart did not induce an apoptotic response. This suggests TNFR1 activation is regulated by compartments in the cell membrane, possibly determined by cholesterol rich domains, that are approximately 200nm apart.[111]

To date, there is very limited research on the effect of nano-spacing ligands on cellular signaling and activation beyond those studies performed on integrins and cellular adhesion molecules. If other cells respond to substrates in a similar ligand spatial dependent matter, it may be possible to control signaling in cells through the use of these surfaces, ensuring that activation is directed down a desired pathway. Coupled with the evidence showing the response of cells to other physical cues, such as mechanical properties and topography, it is likely that a combined approach with control of stiffness, topography, ligand density and inter-ligand spacing is needed to more fully understand dominant factors in receptor signaling, and is largely unrepresented in the field of immunology.

2.2 Mechanically Controlled Environments

2.2.1 Overview

Biomimetic interfaces with controlled mechanical properties are essential for elucidating the effect certain physical stimuli have on cellular actions. With an enormously vast range of tissue types in the body, spanning from soft tissues to firmer mineralised structures similar to bone and calcified tissue,[67, 112, 113, 114] it is unsurprising that a large number of cells have been shown to interact with substrates with mechanical sensitivity, discussed extensively above. Creating a mechanical environment that can imitate a cell niche is paramount to being able to accurately mimic the range of cellular interactions that occur *in vivo*, and is also crucial in investigating cellular responses to rigidity. This section briefly describes hydrogels as an important class of materials used to create artificial cell-surface interfaces with mechanical properties, and their functionalisation with biological molecules.

2.2.2 Hydrogel Fabrication and Functionalisation

Hydrogels are biocompatible hydrophilic networks constructed from either natural or synthetic materials, or combinations of both, that are saturated with water.[115] They are often made of photocrosslinkable polymers, where monomers are chosen due to their unique properties, and can therefore undergo responses to selected stimuli such as pH and temperature.[116, 117, 118, 119, 120, 121, 122, 123] Typical materials used to make hydrogel networks include natural materials such as chitosan and hyaluronic acid, and synthetic materials such as poly (amidoamides), poly (ethylene glycol), and poly (N-isopropylacrylamide), all of which are can crosslinked by the inclusion of appropriate end groups if necessary, such as the inclusion of diacrylates to poly (ethylene glycol) monomers.[124, 115] Whilst natural materials can possess desirable bioactive properties and are often biodegradable,[125, 126, 127, 128, 124, 118, 129, 130] there can be differences in batch to batch variability, so mechanical properties are more difficult to control than in synthetic systems.[131, 128, 132]

In order to produce a hydrogel network, individual monomers must be crosslinked. Crosslinking can occur through a variety of methods; either chemically through the conjugation of two molecules, or physically through charged interactions, such as ionic and hydrogen bonding, comprehensively reviewed by Kharhar *et al.*[128] The choice of crosslinking method is important considering the end application of the hydrogel. Several catalysts and chemicals used in crosslinking methods are toxic to cells, such as copper catalysts used in azide and alkyne click crosslinking reactions,[133] and so cytocompatible methods should be used where possible for bioapplications. Photoinitiation is often used, as the amounts of radical initiatior required are low, and this method also allows for spatial control over the hydrogel produced.[134, 135]

The 3D network, once formed, allows migration of nutrients and waste materials when placed in cell culture environments, and additional desirable features can be selectively incorporated.[135, 128, 72, 136, 132] Protein-based gels often already present a range of physiological cues that are difficult to distinguish from one another,[115, 137, 138, 61] however synthetic polymer matrices can be selectively functionalised with bioactive moieties to deliver selected properties to the hydrogel materials.[130, 139] Additionally, degradable linkers can be added to the hydrogel matrix in order to add additional versatility to the material.[128, 140, 141] Bioconjugation schemes usually employ a free NH_2 or SH group found on most peptide and protein sequences to chemically link free hydrogel polymer matrix end groups, such as methacrylates, directly to protein sequences.

2.2.3 Geometric Control of Hydrogel Systems

Cells rarely interact with planar substrates *in vivo*, in fact, most cellular niches possess unique conformations with distinct 3-Dimensional (3D) architecture. In order to more accurately reflect the *in vivo* cell environment, control of the 3D structure of hydrogels on the micro- and nanoscale is imperative.[142, 143, 144, 120, 145, 146] Some of the simplest methods of fabricating hydrogels with geometric control include the synthesis of a uniform planar hydrogel, where selective geometric regions of activatory proteins can be patterned through the use of micro-contact printing.[147, 148, 149] This technique allows selective protein immobilisation in 2-Dimensional shapes (2D), and could be advanced with nanoscale molds.

An advancement of this methodology involves the selective crosslinking of areas of hydrogel using electron beam or photolithographic methods. Here, planar hydrogel polymer environments can be prepared, but micro- or nanoscale geometries can be selectively formed by electron beam or photolithography derived cross-linking.[127, 150] These materials have been employed as stimulus-sensitive sensors, where individual hydrogels swell in response to stimuli, providing a mechanical read-out for chemical changes in a system that could be read by piezoelectric methods.[151, 78] Recently, the process of dip-coating has produced 100nm thick albumin microgels,[152] if this method was used in conjunction with selective crosslinking, it could become possible to produce thin film hydrogel materials with shaped protein interaction areas.

Small spherical hydrogel particles are of particular interest due to their ability to be used in detection systems such as flow cytometry, and potential for drug delivery applications where they can be suspended in the blood stream.[115] Additional uses for these particles include encapsulation of cells within polymer matrices,[132, 153, 154, 155, 156] and sensing or analyte detection which utilise the polymers sensitivity to pH, temperature, or intrinsic cavities to capture fluorescent probes.[157] The fabrication of spherical hydrogel particles has largely focused on emulsion methods, where a hydrogel matrix is stabilised in surfactant before UV crosslinking.[120, 158] High throughput techniques, such as microfluidic chips, have been modified to enable the manufacture of microscale spherical hydrogel particles,[159, 160, 161] although other low cost methods of producing particles of this scale are also being developed, such as precipitation polymerisation and aerosol assisted microsphere fabrication.[151, 162]

Although spherical hydrogel particles have a variety of applications, presenting a large surface area and ability to be incorporated into fluid systems, other geometries are also being probed for tissue engineering approaches. Cylindrical gels have been produced by template pore synthesis, and gels have been functionalised with a variety of ligands.[163, 144] More recently, hydrogel materials have been spun into fibers, offering promise in the development of more advanced 3D scaffolds.[164] The ability to control the geometry and mechanical properties of these materials independently will enable a rapid evolution in biomaterials.

2.3 Nanopatterning Proteins and Biological Molecules

2.3.1 Overview

Many key biological structures are on the nanoscale, and so creation of nanoscale materials where properties can be examined using materials with features on the same size-scale as the cellular receptor in question are paramount to being able to fully characterise biological responses. Crucial to cell studies is the ability to ensure the independence of factors such as nanotopography and chemical cues.[165, 166] This section discusses various techniques for biological surface patterning on the nanoscale, focusing on current methodologies, limitations and applications.

Previously, advances in technology patterning substrates on a submicron scale have been particularly useful for microelectronics[167, 168] and have only recently been applied to biotechnology, where they have applications in bio-sensing, biomaterials, and tissue engineering.[169] The ability to precisely position peptides, proteins and biological signaling agents on a planar surface is imperative for these applications. Currently, there are a variety of techniques that can be used to pattern biologically relevant molecules on surfaces, working on both a "top down" and "bottom up" approach, and the types of methodology can roughly be categorised into methods using scanning probe microscopy tools, electron beam lithography, stamping or printing methods (broadly categorised as "Soft Lithography") and finally self-assembly based methods.

2.3.2 Scanning Probe Microscopy Techniques

Scanning probe microscopy tools have been used successfully to create features with a smallest size range of 10-250nm depending on the precise technique. These methods use a modified atomic force microscopy (AFM) or scanning probe microscopy (SPM) cantilevered tip to deliver molecules to a surface in a spatially orientated manner, either via a liquid "ink" that can be written onto a surface in dip-pen nanolithography,[170] by scratching patterns onto a pre-assembled surface via nanografting,[171, 172] or through the more recent conductive methods, which apply a potential through the tip to modify the way in which the biomolecules interact with the tip or surface.[170, 173]

Dip-pen nanolithography allows soluble molecules to be delivered directly to a substrate surface, where they can be "written" in both 1-Dimensional (1D) patterns such as lines and dots and more complex 2D shapes; the writing requires pre-programming as the route of the tip on the surface must be pre-designed. Direct dipping of the molecule of interest and then "drawing" on the surface is one method of attachment, alternatively, indirect attachment can occur by immobilising a biological linker molecule on a surface that is subsequently reacted with a biomolecule.[173, 174, 175] The linkages can be electrostatic in nature[176] or covalently conjugated primarily through the affinity of alkanethiols and gold[173] or through amine chemistry.[177]

Although the exact method of transfer from tip to surface remains unclear, it is thought to be due to a water meniscus that forms between the tip and surface under atmospheric conditions[178] which can then allow feature size to be controlled by aspects such as humidity and chemical modification of tips.[174, 179]

A previous limitation with dip-pen nanolithography was the requirement to dip the tip into a suitable solution, which would need to be re-coated with the relevant solution when it ran dry; however advances in nanolithography have introduced the idea of using a cantilevered nanopipette rather than a tip to deliver substances to a surface.[180, 181] Whilst this method has obvious advantages in delivering a continuous stream of liquid, it could also allow the combination of several methodologies, such as selectively delivering certain molecules from a mixture by first running the solution through a HPLC which could be tethered to the nanopipette.[91]

The tip used in nanolithography can also be modified for use electrically; the application of a voltage through the tip can allow electrochemical deposition, where the movement of biomolecules from the tip to the surface is facilitated by an electric signal. Other variations of this method involve chemically modifying the surface through electrical oxidation, selective formation of disulfide bonds, and using the charge delivered to the tip to allow the water meniscus to act as an electrochemical cell.[182] An obvious limitation of the method is the requirement of a conductive substrate and biomolecules that interact favourably with electric current, plus a high voltage is also required.

Other methods using a cantilevered tip are nanoshaving and nanografting, where resist material is removed by a tip which can then be replaced with the selected biomolecule.[183] Combinations of molecules need to be selected carefully, as the replacement biomolecule needs to bind quickly and strongly to the surface before migration of the surrounding molecules. This method can be combined with indirect nanolithography to allow for indirect immobilisation of biomolecules on the surface,[184] and its use has allowed highly orientated biomolecules to be patterned on surfaces with 10nm resolution.[185, 186]

Scanning probe methods allow for different shapes and patterns of biomolecule attachment to be produced with fine control, however the major current limitation with this method is the size and shape of an AFM tip and also the speed and area that can be written at any one time, which is currently limited to around 100x100 μm^2 reducing the usefulness of this technique for producing cell culture substrates.[166]

2.3.3 Soft Lithography

Printing, stamping and molding show great promise as methods allowing large scale patterning (of the order of centimetres) with nanoscale ordering. The basic principle is that a “stamp” with inked protrusions is placed on the surface to be patterned, and deforms slightly to make intimate contact with a surface that facilitates diffusion of the biomolecules from stamp to substrate.[187] This procedure can usually be carried out under ambient conditions, and has the benefit that one stamp can be re-inked many times with different molecules, to produce the same pattern with different molecules.

Poly (dimethylsiloxane) (PDMS) stamps coated with polymers, silanes and alkane thiols are the standard tool,[188] where the use of biomolecules with a high molecular weight is preferable in order to prevent lateral diffusion that could lead to low resolution.[189] Stamps are usually fabricated from a master Si wafer which has been patterned by photolithography or electron beam lithography.[190] A variation of this technique is nanoimprint lithography, where features in a substrate are made by stamping a thin film of polymer above its glass transition temperature, causing a polymer imprint, which can then be modified to produce protein adherent patterns.[191]

The limitations of these techniques are the difficulty of performing multicomponant patterning, due to the challenges with aligning the stamps,[178] and the stamp resolution. The soft material of the stamp and non-uniform pressures involved in printing can cause diffusion of the patterns and reduce pattern fidelity,[192] however recent investigations into other stamping forms, such as using poly (olefin) plastomer stamps for micro-contact printing in the 100nm range[193] and using AFM V shaped test gratings as original masters for PDMS stamps,[187, 194] are seeking to overcome these limitations.

2.3.4 Electron-beam and Photo-resist Lithography

Electron beam lithography predominantly uses a highly focused electron beam to ablate resist layers on surfaces in specific patterns. The areas removed can then be replaced with biomolecules in specific patterns. This method can be used to remove masking polymer, thereby creating feature patterns, or also to remove material from a substrate surface, resulting in varied topography created by mask ablation.[195] Aside from electron beam lithography, both photolithographic methods using photosensitive resist polymers that can be cross linked or ablated, and mask removal by pulsed laser ablation are becoming more popular.[196, 197, 169]

Photoresist methods usually use a polymer mask, that when exposed to UV-light becomes either cross-linked (so less soluble) or more soluble in specific solvents, depending on the interactions with short wavelength energies. These masks can be exposed to UV-light in different areas, and so subsequent removal of the polymer, either in areas that have been unexposed to UV-light and are not crosslinked, or those that have been chemically modified to make them more soluble in certain solvents, leaves a exposed pattern that can be functionalised.[188]

Electron-beam lithography can be used to selectively oxidise molecules or change the surface charge of a substrate, allowing selective patterning of biomolecules in a similar way to conductive AFM methods. Lithography can also be combined with other techniques to create more complex features.[198] The limitations of this technique, such as the ultrahigh vacuum required, the difficulty of nanoscale alignment and the potential concerns over secondary electron processes make mulitcomponent synthesis impractical and time consuming,[199] however advances in the resolution of the electron beam have allowed 15nm features spaced 100nm apart to be produced, and some groups have used these to immobilise single molecules of ferritin.[198]

Interestingly, Hong *et al.* have recently used the high resolution of EBL to selectively crosslink a PEG silane monolayer to amine terminated PEG's, which allowed the formation of hydrogels on a surface that were subsequently attached to biomolecules,[199] offering the potential to produce geometrically constrained areas of varying mechanical properties on a very small scale. Lately, focused ion beam (FIB) lithography has also been used to selectively pattern proteins, in this case pits in gallium arsenide were formed that allowed selective immobilisation of human serum albumin.[200]

2.3.5 Self Assembly

Self-assembly techniques rely on the formation of nanoscale ordered morphologies that can be arranged (or self-arrange) into structures, often periodic in nature. Examples of these methodologies include colloidal masking,[201, 202] block copolymer micelle nanolithography[203, 204, 205] and self-assembled DNA lattices.[206]

Colloidal masking involves the use of a periodic array of self-assembled polymer structures that bind as a mask to surfaces. Once a passivating agent is applied between the mask and the mask is subsequently removed, biomolecules bind where it was absent, causing them to reflect the original pattern of the mask.[201]

DNA templates can also be used to produce nanoarrays[206] in the form of self-assembled lattices of nanoribbons or nanogrids with high resolution, by introducing DNA tiles with sticky ends that associate with each other. Alternating tiles can be produced, which allow selective binding of different molecules.[207]

Block copolymer micelle lithography (BCML) involves the self-aggregation of co-polymers into micellar structures due to solvent incompatibility.[204, 203, 205] These micelles can be directly functionalised or cross-linked to provide nanoscale biological reactants [208, 209] or loaded with metal salts and deposited onto substrates to provide a robust methodology of fabricating nanopatterned particle arrays for functionalization with biological ligands.[210, 211, 212]

These self-assembly methods can also be expanded by introducing templated self-assembly, which controls surface characteristics of micrometre sized areas that can then be patterned on the nanoscale, limiting pattern defects.[188] Templating is largely performed by molecules, in which self-assembled structures are combined with other techniques, such as photolithography, to produce topographical structures on which self-assembly can occur. There has also been research into self-assembly around particles, where charged particles can be used to direct the self-assembly of layer-by-layer morphologies, using polyelectrolytes (charged polymers)[188] to form repeating layers of alternating polymers.

The self-assembly techniques are particularly promising, allowing large areas to be patterned quickly, and with pattern spacing controlled by varying components of the solutions. Limitations are currently based on the fact that the pattern is often repetitive, and the feature shape is predetermined by the molecules involved. It is only recently that nanopatterning of multicomponent systems has become available using some of the other methods described earlier in combination with self-assembly,[213] to date this is one of the only techniques that allows the control of nanoscale regions of protein attachments over large surface areas of the order of centimetres. A robust self-assembly-based method can be found in block co-polymer micellar lithography.

2.3.6 Block Co-Polymer Micellar Lithography (BCML)

Block copolymer micelle nanolithography (BCML) is a self-assembly method allowing the fabrication of nano-features on a large substrate area. Using di-block co-polymer micelles is an effective way of synthesising metallic nanoarrays on a surface with a range of spacing and order and so it is particularly suitable for cellular investigations.[102, 214, 104, 215] The cellular nanopatterning investigations performed in this thesis use functionalised gold nanoarray substrates fabricated by BCML, and an extensive review of controlled fabrication of gold nanopatterns via this method is covered more extensively in Chapter 4.

The technique comprises exposing a di-block copolymer at a concentration above the critical micelle concentration (cmc) (which is the minimum amount of polymer required in solution before self-assembled aggregation can occur,[216, 217, 218, 219]) in solution to a hydrophobic solvent, which causes spontaneous formation of self-assembled structures such as reverse micelles, shown schematically in Figure 2.3.1. The polymer arranges itself so that the more polar polymer is at the micelle core, with the less polar polymer forming a shell. The micelle can subsequently be loaded with metallic precursor which migrates to the core.

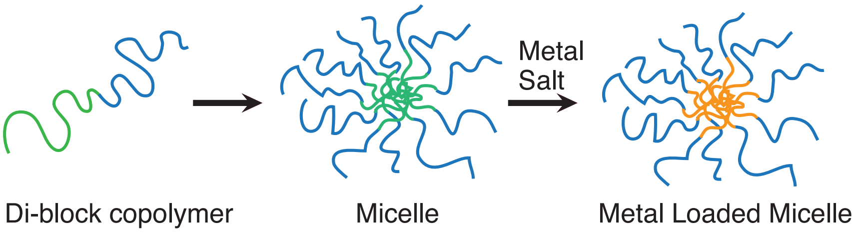

Figure 2.3.1: Schematic of polymer self assembly into micelles

The micelles can be dip-coated onto a range of substrates, the polymer removed and the metal salt simultaneously reduced to its metallic form using plasma treatment, where the metal-metal spacing reflects the micelle diameter. Metallic nanoarrays can subsequently be used for biomolecule attachment, where the nanoarray provides a template of specific order and spacing for biomolecule presentation.[211] Di-block copolymer micelle nanolithography has a range of applications, which predominantly focus on the use of metallic nanoarrays with metals such as zinc[220] gold[221, 222] and compounds such as cadmium sulphate,[223] for catalysis,[224] nanowire synthesis[222] and biological ligand attachment.[211, 102, 51]

The gold nanoarrays, once formed, can provide anchors for attachment of biomolecules. This can be simply achieved by thiol chemistry. A thiol-metal bond can be as strong as 100kJ/mol, however more reasonably in the 45kJ/mol region.[225] Thiols also have a high affinity for gold, and will displace other materials from the surface readily.[226] The selectivity and strength of this interaction means that biomolecules can be covalently bound to linker molecules containing a thiol group at one end, which will then bind to the gold.

2.3.7 Advanced Micellar Nanolithography

Whilst the formation of nanoarrays typically involves a hard substrate that is resistant to polymer removal and plasma treatment, recent research has developed the production of nanoarrays on soft substrates, such as hydrogels.[94, 227]. Ding *et al.* have shown that gold nanospheres can be functionalised with thiol linked macromolecules, which can then be polymerised to give PRG hydrogels that are separated from the original substrate by swelling or peeling.

This method allows presentation of the nanopattern on a soft polymeric support, which can then later be functionalised through the same method and provides methods to investigate the nanoscale control of ligand presentation with mechanical substrate control. Additional crosslinking of the hydrogel substrate has increased the hydrogel stability in culture media,[100, 98, 228, 227, 94] and this technology allows the fabrication of nanoarrays on a variety of substrate shapes and structures, including tubular, spherical and flat forms as well as geometrical constraints[229] so is a promising development of micellar nanolithography.

2.4 Cellular Signalling in the Immune System

2.4.1 Overview

The human immune system is largely comprised of two types of immune cells, those classified as innate, which respond to pathogen and infection via predefined mechanisms, and adaptive immune cells, whose differentiation and effector functions are modified based on prior experience and learned response to a specific stimuli.[230, 231, 232, 233] This thesis describes the effect of fabricated biomimetic materials on immune cell activation, and focuses on Natural Killer (NK) cells as an example of an innate immune cell, and T cells as adaptive immune cells.

The range of immune cell therapies currently undergoing clinical trials for a variety of serious diseases highlights the importance of developing a greater understanding of immune cell function *in vivo*. [234, 235, 236, 237, 38, 238, 239, 240, 37, 241, 242] Recently, adoptive immunotherapy, in which immune cells are manipulated *ex vivo* and then delivered to the body, has provided a new method of combating disease in people with compromised immune systems. This holds promise for the development of individual specific disease therapies, however this work is in its early stages and investigations into the best methods to develop and deliver these therapies, and indeed which cell subtypes are preferred, is still ongoing. Whether it would be beneficial to have long-term immunity against a specific antigen or whether a shorter highly effective response, eradicating pathogens totally, would be preferred is still undetermined.[242, 243, 235, 38, 16]

Of great importance to immunology, and to the development of successful therapies, is a better understanding of the fundamental principles underlying immune cell communication and activation. It is vital that the signaling mechanisms allowing control of function in immune cells are determined; once understood, these mechanisms can be manipulated for a range of applications. This chapter explains the roles that both NK and T cells play in the immune system, as well as providing a general overview of antigen recognition, signaling mechanisms and controlled activation of immune cells towards desired function in these cell types.

2.4.2 Role of NK cells in the immune system

The Natural Killer (NK) cell is an innate immune cell that primarily uses cell surface receptors to recognise infection or stressed autologous cells *in vivo*, termed target cells. Virally infected cells, and cells that are damaged or partially transformed by cancers, express specific markers on their surfaces that are recognised by NK cells. The surface bound NK cell receptors largely fall into three categories; Killer Lectin Like Receptors (KLR), Killer Immunoglobulin Like Receptors (KIR) and Natural Cytotoxic Receptors (NCR).[244, 245]

Upon appropriate engagement of these receptors, NK cells mediate the death of these cells through cytotoxic and cytolytic methods, shown schematically in Figure 2.4.1.

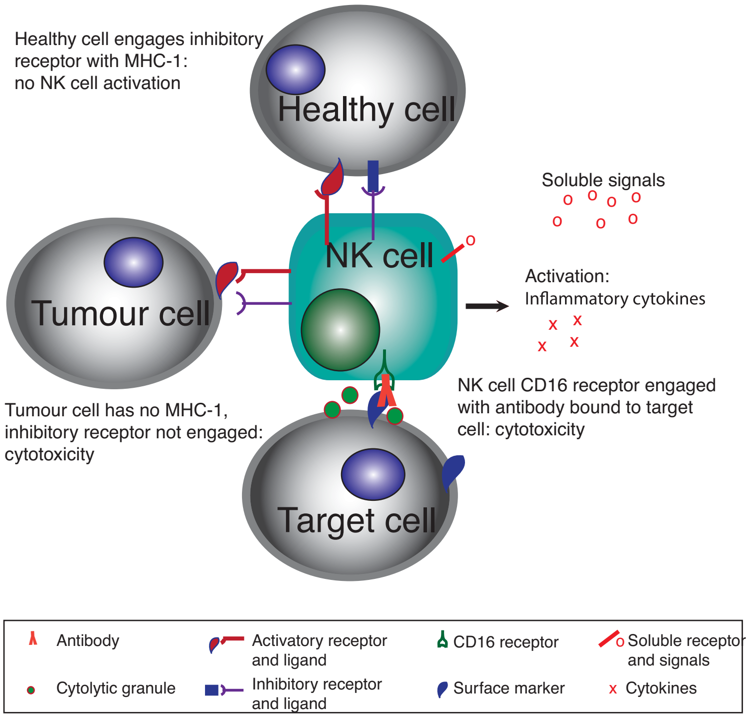

Figure 2.4.1: NK cell activation pathways. NK Cells can show tolerance to healthy cells through the balance of activatory and inhibitory receptors, without inhibitory receptor engagement, NK cells display cytotoxic and cytolytic effects. NK cells can also respond to the direct engagement of surface ligands through soluble factors, target cell surface markers, or target cell antibody tagged surface markers.

NK cells can also stimulate other immune cells through the release of cytokines and chemokines, directing both innate and adaptive function in the target cell locality.[244] Additionally, these cells act directly on target cells through the expression of death receptor ligands on the NK cell surface[246] or through the targeted secretion of lytic granules at the NK cell-target cell interface.[247, 248, 249, 250] The secretion of lytic granules is a major mechanism of inducing cell death in nearby target cells. This mechanism involves the redistribution of the intrinsic actin network and microtubule organisation centre (MTOC) around the NK cell interface. Lytic granules containing perforin and granzymes then locate to the synapse, and are exocytosed into a cleft between the NK and target cell, where they cause death of the target cell.[232, 250] The exact nature of the activatory signals inducing this pathway is complex, and discussed in the next section.

2.4.3 NK cell signaling

Although the NK cell surface possesses a variety of activatory and inhibitory receptors, NK cells usually require engagement of multiple complementary receptors to induce full function.[245] The signals from NK cell activatory receptors are thought to be integrated to propagate downstream signaling, whilst the inhibitory receptors down-regulate activation. [251, 252]

NK cell surface receptors broadly signal via phosphorylation of the internal signaling components associated with cell surface receptors.[252, 253] When appropriate ligands are encountered on a target cell, activatory receptors engage with these ligands and their signaling domains become phosphorylated. Many cell surface receptors, such as CD16, NKp46 and NKp30 are coupled to Immunotyrosine Activatory Motifs (ITAMs). These polypeptides are phosphorylated by protein tyrosine kinases, which recruit tandem tyrosine kinases to activate SyK family adaptor proteins, leading to downstream signaling.[253] Some activatory receptors, such as NKG2D, use an alternative intrinsic signaling domain (DAP10), which also becomes phosphorylated on engagement and can lead to activatory pathways.[252] The NK cell requires the integration of these phosphorylation events, and other downstream signaling events, to induce activation, and uses signaling events occurring at distinct receptor types to moderate the cytotoxicity of the cell. [254, 255, 25]

The NK cell also possesses inhibitory receptors, which ensure that NK cells act only on infectious agents, or infected autologous cells. An example is the inhibitory receptor class KIR, which engages with Major Histocompatability Complex-1 (MHC-1) that is expressed on the surface of most cells found in the human body. When NK cell surface activatory receptors engage with surface ligands on the target cell, they stimulate an activatory pathway as described. If the target cell also possesses MHC-1, this binds to the KIR receptor with an inhibitory effect. The KIR signals through a competitive Immunotyrosine Inhibition Motif (ITIM),[256, 257] which is analogous to the Immunotyrosine Activation Motifs (ITAMs). The NK cell integrates the signals from both activatory and inhibitory pathways, and uses this mechanism to ensure the NK cell does not destroy autologous cells that express MHC-1. If cells do not have MHC-1, or autologous cells have down-regulated MHC-1 expression, then the NK cell destroys the cell. This process is called the "missing self hypothesis" and is thought to be important in cancer immunosurveillance, where cancer cells, and several other infected cell types, down-regulate MHC-1 expression in an attempt to escape detection.

Normally, human CD8+ T cells inspect other cells of the body by engaging their TCR with MHC-1 on presented cells. MHC-1, in combination with small peptide fragments from inside the cell presented in the MHC-1 cleft to the TCR, therefore gives the CD8+ T cell an indication as to the internal status of the cell it is engaging with, explained in detail below. If the peptides being presented in conjunction with MHC-1 are not normal (ie. indicating a pathogenic infection or mutation due to cancer) the CD8+ T cell will activate and destroy the cell. Some cancers therefore down regulate the amount of MHC-1 present on the cell surface, in order that CD8+ T cells are less likely to recognize that the cell is stressed or mutated, and so they escape the CD8+ T cell immune surveillance mechanism. The NK "missing self hypothesis" is an alternative surveillance mechanism to compensate for this. Whilst down regulation of MHC-1 does indeed help infected or damaged cells escape detection by CD8+ T cells, as discussed this down-regulation reduces the NK cell inhibitory response, enhancing the NK killing response. In this way, whilst MHC-1 down-regulation is an advantageous escape mechanism for infected and stressed cells from CD8+ T cell immunosurveillance, the down-regulation of MHC-1 induces a cytotoxic effect in NK cells, and allows the NK cells to monitor cell status in a complementary way to the CD8+ T cells. [258, 259, 260, 261]

These complementary and antagonistic pathways are carefully regulated so that the NK cell responds appropriately; they provide a "dynamic equilibrium" through which the NK cell can act. The integration of several signals is imperative to NK cell function in most cases,[257, 23] however there is a unique pathway through which NK cell activation can be controlled by a single surface receptor class; the NK cell surface receptor CD16 can act independently.[253]

NK CD16 surface receptors engage with the Fc portion of antibodies bound to surface receptors expressed on target cells, rather than cell surface receptors directly.[262, 263, 264, 36, 253] Using this mechanism, the NK cell can induce Antibody Dependent Cellular Cytotoxicity (ADCC),[247, 265, 266, 267, 245] where cytolytic granules are released towards the target cell as described earlier, resulting in the destruction of the target cell. This pathway is mediated by the production of specific antibodies by B lymphocytes of the adaptive immune system, and here, engagement of CD16 alone can induce activation and cytolytic effect in NK cells. This receptor and mechanism of action are discussed in greater detail in Chapter 6, where the effect of nanoarrays with stimulatory CD16 ligands on NK cells is investigated.

2.4.4 Role of T cells in the immune system

T cells are a subset of lymphocytes primarily involved in adaptive immune responses to pathogens in humans. The role of the T cell is largely to recognise external pathogens that have infected other cells, and induce appropriate immune responses. They originate from the hematopoietic stem cell line, which develops into a lymphoid progenitor cell and can differentiate into a thymocyte in the thymus, before further differentiating into one of several T cell types; regulatory T cells which express CD4 or CD25 on their surface, helper T cells (T_H) which express CD4, cytotoxic T cells (T_C) expressing CD8 and NK/T cells expressing a combination of CD56 and CD3.[268, 269] T cells primarily offer an antigen recognition role coupled to effector/helper function in the immune system however elucidation of the signaling methods through which they identify and respond to pathogens is not yet entirely clear.[235, 16, 243, 242] Several subtypes of T cells are involved in the adaptive immune system, such as regulatory T cells (T_{REG}) cytotoxic T cells (T_C) and helper T cells (T_H) and each has a specific function in the immune response. This review will focus on T_C and T_H cells, both of which recognise antigen presented to the cell in combination with Major Histocompatability Complex (MHC), and are shown schematically in Figure 2.4.2.

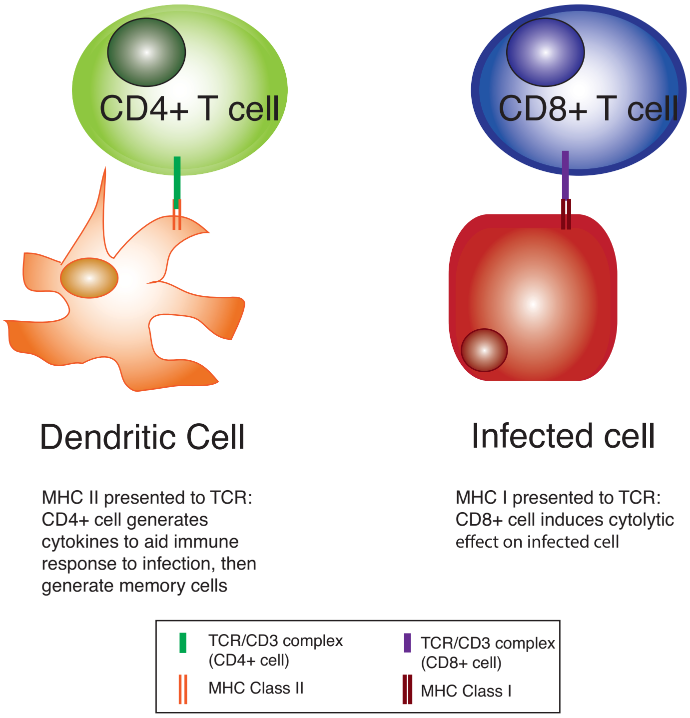

Figure 2.4.2: Schematic of T cell activation. CD4+ cells engage predominantly with other cells of the immune system, and once activated, show T helper function. CD8+ cells engage with other autologous cells, and have T cytotoxic function when activated.

T_C cells express the co-receptor CD8+ on their surface, and recognise antigen presented in complex with MHC class I, conversely T_H cells recognise antigen presented with MHC class II. The two different types of MHC are found on different types of cell tissue in the body, meaning that T_C cells recognise antigen presented on any type of body cell, and T_H cells largely recognise antigen presented by other cells of the immune system.[17] T_C cells are largely involved in the control of intracellular pathogens, and once activated, can promote apoptotic death of target cells through granule and receptor mediated mechanisms using Fas receptors and lytic enzymes.[270] CD4+ T helper cells, T_H cells, once activated can differentiate into several subsets. Whilst they have no direct cytotoxic activity they mediate the immune response through the secretion of cytokines, and the subset of cells present depends on the microenvironment and signals received; T_{H1} cells activate bactericidal activity in macrophages and induce B cells to produce opposing antibodies through interferon-γ secretion, whilst T_{H2} cells secrete interleukin-4 allowing B cells to produce neutralising antibodies. There are other subsets that are emerging as important in the immune response, such as T_{H17} cells, however the exact role of these subsets has yet to be determined.[17]

After activation, immune function is realised through differentiation into appropriate subsets and clonal expansion. It has been shown that from initial response to maximal response CD8+ cells can expand 500,000 times *in vivo*, these clones are destroyed after pathogen elimination, except for a small subset that remain as memory cells.[17]

2.4.5 T cell signaling

The T Cell Receptor (TCR) complex is recognised as the main receptor for activation of T cells towards immune function. Despite intensive research into the TCR complex since the 1990's, there is much that remains unknown about the minimum signal required to induce stimulation. The "2 signal hypothesis" suggests that aside from the initial TCR engagement signal (signal 1) a secondary signal is needed to induce differentiation into subsets of both CD8+ and CD4+ cells and so activate full immune function. This secondary signal is usually provided by a co-stimulatory molecule such as CD28 (signal 2), and induces the recruitment of other stimulatory proteins.[271] On both CD4+ and CD8+ cells it is believed these co-stimulatory receptors bind to the non- polymorphic regions of MHC class I and II molecules and function synergistically with the TCR during antigen recognition to increase sensitivity of TCR responsiveness.[272, 273, 274, 17]

It is widely accepted that engagement of the TCRs by agonist MHCs initiates several signaling pathways inside the cell, however the exact mechanism of signal transduction remains unclear, as there are several possible outcomes. Initial signaling can result in several distinct signaling pathways being induced, with key events including phosphorylation of the ITAM's, recruitment of Lck and Zap-70 and the formation of protein complexes around the TCR. These complexes cause receptor clustering and integrin adhesion to occur, followed by cytoskeletal reorganisation leading to the formation of a mature Immune Synapse (IS) with distinct spatial organisation, discussed in more detail in Section 2.4.7.[275, 276, 277]

2.4.6 Mechanical Sensitivity of Immune Cells

Several cell types have been shown to respond to alterations in the mechanical properties of their environments,[71, 278, 70, 66, 279] however it is only recently that these investigations have been extended to immune cells. O'Connor *et al.* varied the rigidity of planar poly (dimethylsiloxane) (PDMS) substrates functionalised with stimulatory anti-CD3 ligands, and showed that maximal proliferation in CD4+ and CD8+ T cells was induced on surfaces with a rigidity of <100kPa compared to 2MPa,[280] however other studies on poly (acrylamide) (PA) surfaces indicate maximal T cell responses were observed on substrates with rigidity of 200kPa compared to softer substrates at 10kPa.[281] Separately, B cells showed preferential activation on PA gels at around 20kPa (compared to softer 2kPa substrates)[282] and hematopoetic cells (immune cell stem cell precursors) demonstrated increased cell spreading on much stiffer PA substrates of around 200kPa compared to less rigid matrices.[62] In order to compare these results more fully, the response of each cell type to substrates fabricated from the same material across the same range of rigidities needs to be explored.

Currently, there are no mechanistic explanations for these results, and so the exact nature of the mechanosensitivity of these immune cells remains unclear. Despite this, there are several distinct systems within the immune cell capable of sensing force, and so mechanosensitivity in the main receptor complexes of several immune cell types is unsurprising.[275, 233]

Receptor-ligand interactions can be broadly categorised into slip, catch or ideal bonds depending on their response to force.[283, 284, 285, 286] Slip bonds have a K_{off} value that increases with force, and typical examples are antibody-antigen recognition. Conversely, catch bonds have a K_{off} that decreases with force, and have been demonstrated in leukocyte adhesion systems using selectins, [285] whilst ideal bonds have no response to force applied through the bond.

In several receptor types, such as selectins, there is a transition between catch and slip bond systems at specific force values, implying that the cell can sense force over a dynamic range and that force can regulate conformational changes in these systems.[285, 233, 275] The hypothesis that TCR/CD3 conformation changes are induced by cytoskeletal pulling forces which are required for signaling has been postulated by Ma *et al.*[287] Intact actin cytoskeletal function is required for optimal T cell signaling, and changes in the actin cytoskeleton are known to compromise signaling in T cells, supporting this hypothesis.[288, 289, 290] Additionally, there is evidence to suggest that only surface bound, and not soluble, agonist is capable of triggering T cell activation, but that this surface bound triggering requires additional cytoskeletal ligands.[233, 291, 292]

The sensitivity of immune cell signaling to force has also been demonstrated in other systems. Biochemical studies using PIP2 describe TCR clustering which is delayed and impaired on more rigid surfaces, possibly through an inability to down-regulate ERM proteins. Additionally, this rigidity effect is spatially controlled with specific isoforms of PIP2.[293]

One hypothesis suggests that the binding energy of each extracellular protein-protein interaction can drive signaling directly. Binding occurring at optimal forces may force exclusions of large or un-ligated extracellular domains, which can induce spatial segregation of unnecessary proteins. This spatial segregation could help to organise the immune synapse into an activatory conformation, through which signaling is enhanced. [294] The importance of spatial organisation in immune cell signaling is discussed next.

2.4.7 Spatial Organisation in Immune Cells

The region of contact between an immune cell and antigen presenting cell (APC) is termed the immune synapse (IS). The IS is defined as the interface between immune and other cells types, where molecules are arranged in an organised manner.[25] The organisation of specific proteins at this interface is an important part of immune cell signaling;[295, 296, 277, 297, 298] alterations to the natural configuration of these proteins on artificial cell substrates can be used to direct and control activation levels in a number of cell phenotypes.[299, 21, 295, 296]

Several APCs self-organise their agonist surface receptors into clusters; MHC-1 clusters, with a minimal inter-cluster distance of <10nm, have been observed in virally infected cells.[81, 300, 301, 96]Additionally, B cells targeted with anti-NK stimulating drugs have been shown to redistribute CD20 surface markers into membrane lipid rafts on one side of the cell.[302, 303, 304, 305] Although some target cell types possess ordered domains of ligands, the majority of the spatial organisation at immune synapses appears to be driven by the immune cells.

Broadly, the immune synapse contains Super Molecular Activatory Clusters (SMAC), which are divided into central c-, peripheral p- and distal d- rings. Each of these SMACs contains domains of distinct receptors and signaling molecules specific for certain cell types.[25, 306] Many cell types have shown microstructured protein domains on the cell surface.[276, 307, 308, 309, 310]

In NK cells protein microdomain organisation is thought to play a key role in cellular activation.[311] Rafts of both inhibitory and activatory receptors have been observed on cell surfaces,[312, 253, 22, 313, 314, 315] and the confinement of these receptors to specific protein domains is thought to control tolerance in NK cells.[316] Additionally, the proximity of inhibitory and activatory receptor microclusters to each other is thought to direct cellular activation, where exclusion of inhibitory microclusters from domains of activatory clusters could allow signaling to propagate.[297, 317, 318, 312] Several proteins are only successfully phosphorylated when they exist in domains, as oppose to as individual receptors, and so it may be that these domains amplify signals and signal transduction.[312, 319, 320, 321, 322]

T cells show similar protein domains; signaling in the T cell is thought to involve TCR/CD3 microclusters that form in the p-SMAC and are transported to the c-SMAC, and these microclusters are required for efficient activation.[323, 289] Other receptor and signaling proteins such as Lat, Zap-70 and SLP-76 have also been shown to exist in microdomains,[324, 325, 326, 327, 328, 271, 329, 330, 331] indicating that the micro and nanoscale structure of these molecules on cell surfaces is important to cellular activation. Additionally, the role of actin in this spatial arrangement appears to be crucial; without actin, several receptors are unable to form microclusters and protein rearrangement crucial for signaling cannot occur.[316, 318, 317, 332, 333, 261]

The organisation of these protein microdomains has been shown to be different for several cell subclasses, and is summarised in Figure 2.4.3.[239] Mature T cells typically demonstrate a bulls-eye pattern, with a TCR/CD3 enriched protein microcluster in the c-SMAC surrounded by ring of adhesion receptor LFA-1, whilst T_{REG} show a multifocal pattern of distinct TCR/CD3 domains within the LFA-1 rich environment.[334] NK cells demonstrate either an activatory (SMAC) or inhibitory (SMIC) pattern, surrounded by adhesion receptors.[254, 25]

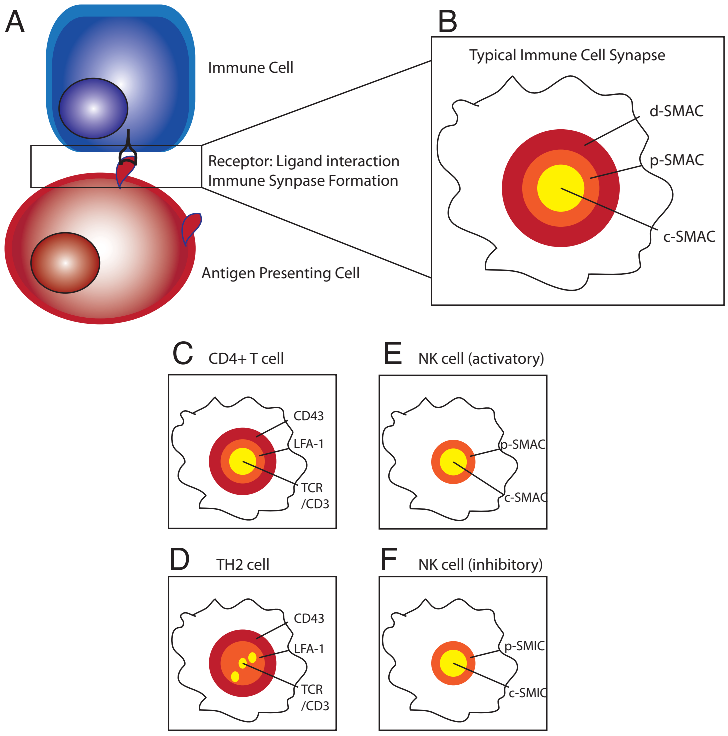

Figure 2.4.3: Typical stable synapse structures. (A) Immune cells contact target cells at a region known as the immune cell synapse (B) The synapse is normally organised into central, peripheral and distal Super Molecular Activatory Clusters (SMACs) (C) Mature T cell synapses usually display a c-SMAC enriched with TCR/CD3 and co-stimulatory molecules, p-SMAC with adhesion molecules such as LFA-1 and p-SMAC with other molecules such as CD43 and CD44, in T_{REG} cells (D) the pattern is multifocal. (E) NK cells express a similar pattern, where engaged stimulatory receptors are found in the c-SMAC and adhesion molecules in the p-SMAC. Here inhibitory receptors are excluded from the synapse. Additionally, in inhibitory receptors (F) a c-SMIC forms with inhibitory molecules in the centre surrounded by adhesion molecules.

Clearly, receptor-receptor proximity, and even proximity of several different receptor types, appears to be very important to cellular signaling. Some investigations have focused on whether this requirement may be due to engagement valency or crosslinking of key receptors; both CD4+ and CD8+ cells are not stimulated by monovalent TCR binding in either soluble or surface bound forms, however dimeric or greater engagement is necessary for activation,[287, 289] suggesting that crosslinking, or receptor proximity, plays a crucial a role in cellular signaling.

Separately, protein micropatterns have been used to direct cellular activation in T cells, indicating that the micropatterned structure of stimulatory ligands is capable of controlling cellular activation levels. Artificial cell substrates with micropatterned regions of anti-CD3 in focal or annular forms were used to activate T cells, much higher IL-2 and IFN-γ secretion occured on patterns with focal anti-CD3 protein organisation.[299] Additionally, the inclusion of co-stimulatory agents such as anti-CD28 in distinct ligand organisation patterns can also affect cellular activation; positioning anti-CD3 and anti-CD28 in separate distinct focal points resulted in much higher IL-2 production than a singular focal point.[21] Fluid bilayers have also been used to probe the sensitivity of T cell activation to the ligand mobility; constraining the TCR microcluster mobility can cause altered signaling and activation levels in T cells, [295, 335, 296] where signaling is maximised if TCR microclusters are contstrained to the p-SMAC.

The spatial structure of the immune synapse interface is an important part of immune cell signaling;[297, 311, 296, 277] alterations to the natural configuration of these proteins on artificial cell substrates can be used to direct and control activation levels in a number of cell phenotypes, although the mechanisms driving these differences have not yet been identified.[299, 21, 295, 296] Much work has been conducted to elucidate the general pathways of signaling and activation in NK and T cells, however there is as yet not a clear understanding of the minimum requirements for cellular activation and differentiation in terms of the spatial organisation of stimulatory ligands. More work is needed to determine both the minimum signaling requirements and how to deliver these signaling requirements *ex vivo* before clinical applications, such as immunotherapy, can reach their full potential.

2.5 Summary and Objectives

Biomaterials research has arguably contributed greatly to the advancement of tissue engineering as a whole, however this multidisciplinary field has largely focused on fabricating materials for applications in regenerative medicine, which often concentrate on stem cell differentiation. Immunology is largely unrepresented in this field, despite the variety of conditions prevalent in modern-day society attributed to immune system disorders.[1] In order to design materials capable of driving immunotherapy in clinic, it is imperative that the biomaterial field begins to address this unmet clinical need. Both a greater fundamental understanding about the signaling processes involved in key immune cell interactions, and the design of materials capable of delivering the signals required to induce immunotherapeutic effects, are required.

This thesis seeks to design biomaterials capable of probing key cellular signaling pathways in immune cells, with the hope of gaining insight into immune cell signaling requirements. The objectives of this thesis are broadly as follows; to fabricate biomaterials capable of binding biological ligands with controlled inter-ligand spacing or ligand-substrate rigidity, and to test the effect of varying these specific stimuli on immune cell activation in T and NK cells.

Specifically, this thesis aims to fabricate arrays of gold nanoparticles with controlled inter-particle spacing capable of binding biological molecules, and to extend the current nanopatterning technology to enable the fabrication of new nanomaterials with advanced functionality; able to bind biological materials with alternative geometries and alternative binding mechanisms.

Additionally, the fabrication of new materials with control of substrate mechanical properties capable of presenting stimulatory ligands, is also desired. These materials should also be able to mimic the natural conformation of immune cell engagement with Antigen Presenting Cells in order to extend the currently available technology.

Finally, this thesis seeks to test the activatory response of immune cells to these fabricated materials; both the effect of varying the inter-ligand spacing of stimulatory ligands over crucial lengthscales, and the response to mechanically controlled substrates functionalised with stimulatory ligands, will be investigated.

Chapter 3

Characterisation Techniques

Several methods were used to characterise both the materials described in this thesis and the cellular responses to these substrates. This section discusses the principal techniques common to several chapters employed in this thesis.

3.1 Scanning Electron Microscopy (SEM)

Scanning Electron Microscopy (SEM) is an imaging technique used to characterise samples from the micro- to nanometre scale.[336, 337, 338, 339, 340] An intense beam of high energy electrons are focused onto a surface using electromagnetic lenses, and the characteristics of the reaction products from electron interference with the substrate are measured, shown schematically in Figure 3.1.1.

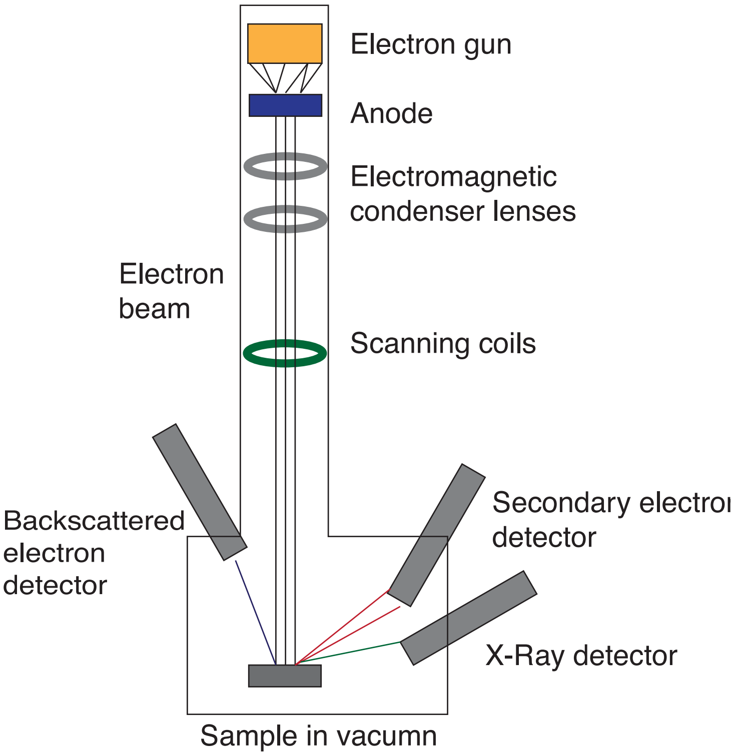

Figure 3.1.1: Scanning Electron Microscopy.

The electrons are produced by an electron gun, which is either thermionic or field emission class. Thermionic guns apply thermal energy to metals with extremely high melting points to induce ionisation and generate an electron stream. Alternatively, field emission guns generate an electron stream through a strong electrical field, which separates the electrons from the source atoms. The resulting stream of electrons is directed towards the sample using electromagnetic condenser lenses, which direct and focus a narrow beam of electrons onto the sample, and is scanned over a narrow area of the sample. Scanning coils, which create a fluctuating magnetic field to bend the electron beam in different directions, control the movement of the beam over different areas of the surface. The intense beam of electrons can cause damage to the sample, and so samples are usually mounted on conductive material, or coated with a thin layer of conductive material, in order to earth the incident electrons that are not used in detection. [341, 342]

The reaction products from the interaction of the incident electron beam with the sample can then be examined; secondary electrons, back scattered electrons and X-rays can all be collated to give information on surface topography and composition. Secondary electrons are the result of inelastic scattering in substrate surface atoms, caused by the electron beam, whilst back scattered electrons are the result of elastic scattering of incident electrons with atoms in the substrate. Detectors usually attract the resultant electrons, and these electrons hit the detector surface before being computed into images. Usually, the brightness of an image is related to the number of electrons reaching the detector per unit area over a comparative timeframe. X-rays can also be produced; inelastic scattering of incident electrons with surface atoms can result in the emission of X-Rays, which possess a characteristic energy value depending on the element from which they originate. These can be analysed to give elemental composition of the sample using energy-dispersive X-Ray spectroscopy with an additional detector.[342, 167, 168]

All analysis is carried out in vacumn, as gaseous particles could interfere and scatter the incident electron beam. Here, samples were analysed with a Field Emission Gun SEM using a working distance of 4mm and voltage 5-10kV unless otherwise stated. Samples were either mounted on conductive silicon wafer or coated with a thin layer of carbon (2-5 minutes, 45mA, QVF instrument, Film Thickness Monitor estimated 5-15nm) or chromium (1 minute, 45mA, EMITECH K550 instrument, estimated 15nm).

3.2 Transmission Electron Microscopy (TEM)

Transmission Electron Microscopy (TEM)[343, 344] is an imaging technique used to characterise materials by passing an electron beam through a thin sample section ~100nm thick. The beam of electrons is generated in an electron gun (again either thermionic or field emission) and the electrons are accelerated towards the sample, where they interact with the material to produce either diffraction patterns dependent on the lattice spacing of planes of atoms, allowing the crystal structure of the material to be investigated,[344, 345] or images. Images may be contrast based, where the comparison between sample regions that absorb electrons (dark) and sample regions that do not (bright) can be recorded based on the number of electrons reaching the detector as bright field images. Alternatively, diffraction contrast, where regions that scatter electrons appear bright, can be used instead. Additionally, energy-dispersive X-ray spectroscopy (EDX) analysis can be performed as described for SEM techniques.

3.3 UV-Visible and Fluorescence Spectroscopy

UV-Visible Spectroscopy is a technique that excites certain molecules to higher energy levels using electromagnetic waves in the UV-Vis region. The photons, once absorbed, promote electrons in the molecule to higher unoccupied electronic energy levels; the electrons must subsequently lose this “extra energy”. If the excited electron is in a ground vibrational state, it can lose this energy directly by emitting a photon. However, if it is in an excited electronic state and higher vibrational state it must first return to a lower vibrational energy level by internal conversion (such as loss of energy by heat through bond vibration) before emitting a photon to return to the ground electronic energy level. The photon emission can be termed fluorescence if it is in the UV-Vis range, and is usually the result of an emission from one excitation state to a lower energy level, shown schematically in Figure 3.3.1.

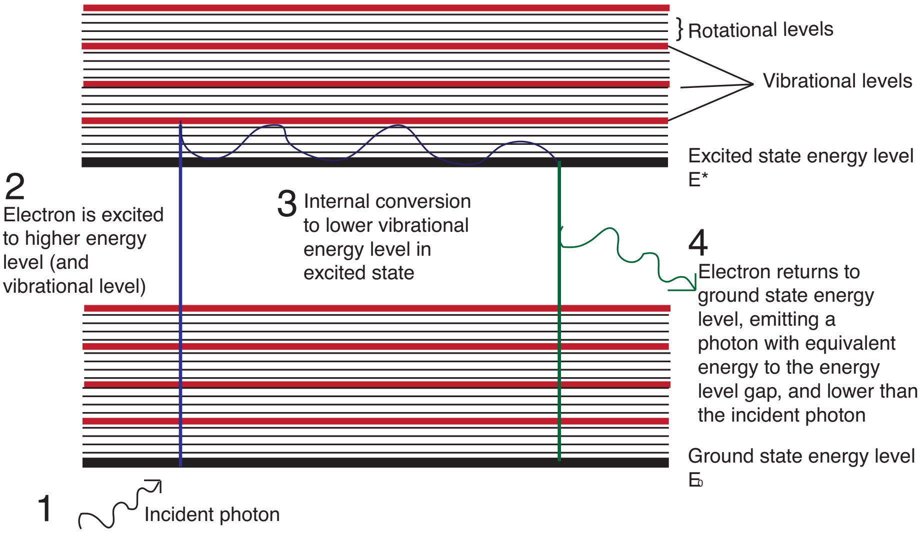

Figure 3.3.1: Principles of UV-Visible excitation and emission. Electrons exist in distinct electronic energy states with vibrational and rotational energy sub-levels. Excitation with a photon of incident light can promote electrons to high electronic energy levels. The electron can cause photon emission when it returns to its ground state.

The photon emission can be visualised using specific filters and detectors, which measure the change in an absorption and emission spectra by monitoring wavelengths absorbed or emitted by a sample after irradiation with a controlled light source. Measuring the electromagnetic wavelengths that induce these changes in excitation level can be used to determine the optical band gap between energy levels. The absorbed and emitted photons correspond to discrete transitions between energy levels, and so provide information about the electronic structure of the material. In this thesis, UV-Visible and Fluorescence spectroscopy has been used to analyse the optical band gaps of materials, discussed in more detail in Chapter 5, and the general principles of fluorescence applied in biologically material characterisation are described below.

3.4 Optical Microscopy

Several types of microscopy were used to monitor and measure cellular responses to biomimetic materials in this thesis, including confocal and Total Internal Reflection Fluorescence, discussed below.

3.4.1 Confocal Microscopy

Confocal microscopy allows very thin sections of a sample to be illuminated through modification of standard optical microscopy.[346, 347] A typical schematic of confocal microscopy is shown in Figure 3.4.1.

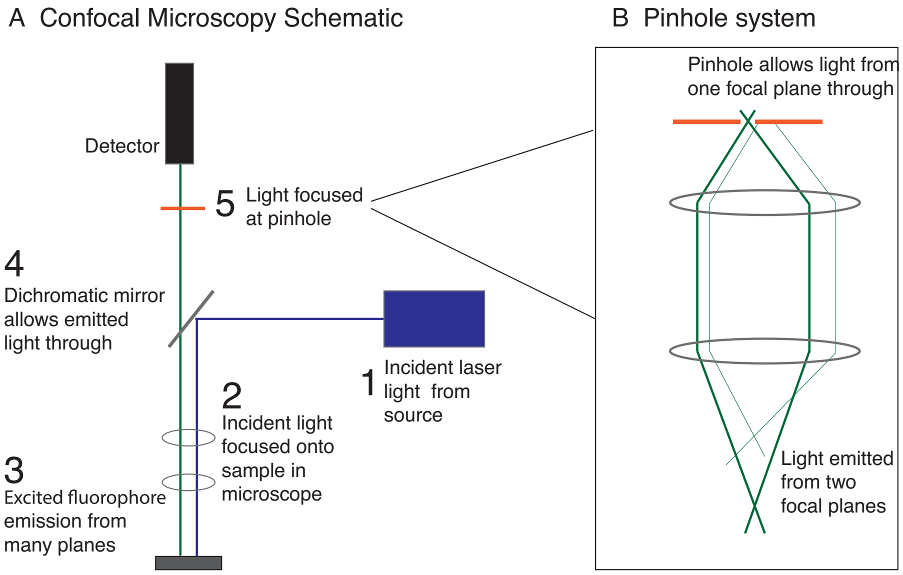

Figure 3.4.1: Schematic of confocal microscopy. Incident light is directed towards and focused on the sample, which emits light when selected fluorophores are excited. The emitted light then passes through a dichromatic mirror and through a pinhole (which allows light from only one focal plane to pass through) before being detected.

The confocal microscope uses the principles of traditional fluorescence microscopy with additional focusing tools. In the microscope, incident light of a certain wavelength is emitted and bent by a dichromatic mirror, then focused onto a sample. The light emitted by excited fluorophores in this sample passes back along the illumination pathway until reaching the dichromatic mirror, which it passes through (it is of a shorter wavelength than the incident light and so travels through the mirror) to the detector. In a confocal microscope, a pinhole is added in front of the detector in order to eliminate out-of-plane light, and only allows light from the conjugate planes to pass to the detector. This allows the Abbe resolution to be narrowed to approximately 200nm depending on the exact wavelength of light used and the objective settings, and therefore the focal plane is very narrow; in conjunction with scanning vertically through a sample, this allows slice-by-slice analysis of a sample where individual images can be stacked to give an overall image with enhanced clarity.

3.4.2 TIRF Microscopy

Total Internal Reflection Fluorescence (TIRF) uses a laser beam to illuminate and totally internally reflect the light at the interface between a glass coverslip and cell surface, shown schematically in Figure 3.4.2, and is a powerful technique for imaging at cellular-interface boundaries.[348, 331]

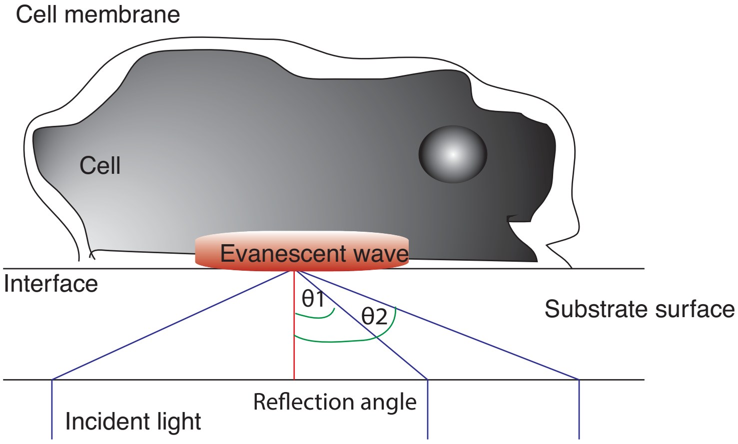

Figure 3.4.2: Schematic of total internal reflection microscopy (TIRF). At a cellular-substrate interface TIRF of incident laser light can occur due to differences in the refractive indicies of the materials at the interface. This causes an evanescent wave to penetrate into the cell, exciting fluorophores located close to the cell-surface interface.

TIRF microscopy uses the total internal reflection of incident light at the interface between two materials with different refractive indices to create an incident evanescent wave that travels only a few 100nm into the sample. At the point of total internal reflection, some of the incident light converts to an electromagnetic field and passes through the interface, creating an evanescent wave with the same frequency as the incident light. The fluorophores are excited by the interaction with the electromagnetic field, which penetrates up to 200nm into the sample. The penetration depth of the field is dependent on the angle of incidence of the incident light, which can be controlled through the use of objectives. The penetration depth is also sensitive to differences in the refractive indicies of the materials at the interface. The evanescent wave decays exponentially away from the point of origin; due to this small penetration depth, only fluorophores in close proximity to the glass interface are excited. Emitted light therefore provides information about the features of the cell at the cell-glass interface.

3.5 Flow Cytometry

Flow cytometry allows the analysis of small particles via their interaction with electromagnetic radiation. A stream of liquid containing particles or cells is flowed through a chamber, where they are illuminated by laser light of a specific wavelength.[349, 350] The cells will then either scatter this light, allowing analysis of the granularity, size and nuclear shape of the cell, or may absorb it if tagged with a fluorescent marker sensitive to that wavelength. The absorption and emission of selected frequencies of light (described above) allows detectors placed close to the flow of cells to characterise the materials based on their scattering or absorption and re-emission of incident light. Flow cytometry is particularly useful for examining cell populations, where cell surface receptors can be tagged with fluorescent biomarkers. This allows the proportion of cells within a population expressing a certain marker to be identified.

Standard flow cytometry experiments typically use cells exposed to negative and positive stimuli as controls to “gate” the population. The positive controls are usually cells that have been exposed to a known stimulus, and are fluorescently tagged with an antibody against a surface or intracellular marker for response caused by this stimulus. This may be a marker for cell lineage, however this thesis specifically describes cellular activation markers. Negative controls are required to ensure that the antibody can be used selectively to monitor expression of the marker as a gauge of activation. Firstly, unstimulated cells treated with the same antibody are required to ensure that this marker is only present on activated cells, or to determine the basal level of this marker in unactivated cells. Secondly, an antibody of the same isotype but which is specific for a different, non expressed marker is usually used to ensure that the binding of the positive antibody is specific to its cellular marker, and is not binding through non-specific protein interactions.

These controls are then examined by passing them through the chamber and setting the sensitivity of the detectors to suitable incident wavelengths. The sensitivity of each of the detectors is altered through the voltage gain, in order to provide a cellular profile range suitable for analysing both positive and negative controls. Once the detector sensitivity has been modified in this way, the negative and positive cellular controls are examined. The aim is to display the population response to incident light in such a way that clear differences in the response to incident light between the positive and negative controls are detected. The profile of a typical negative cell, and the profile of a typical positive cell, can then be marked (or gated) across several wavelengths. Further samples can then be quantitatively examined, allowing rapid determination of the profile of cellular populations in terms of the identified markers, and allowing direct comparison to positive and negative controls.

Several markers can be examined at the same time, allowing a more in depth study of the cellular population if antibodies or markers with different fluorophores are used. Due to the overlap of several fluorophore’s spectral profiles, careful consideration has to be given to compensation in experiments with more than one fluorescent molecule being used to mark the cell at the same time. The flow cytometry experiments in this thesis were performed on a Fortessa, and used a single fluorescent marker. Gates were drawn based on cellular profiles at 8 hour time-points; unstimulated cells were used as negative controls, and cells stimulated for 8 hours with anti-CD3 on tissue culture plastic as standard positive controls. Further details on the experimental procedure and selection of population gates is given in the relevant chapter (Chapter 8).

Chapter 4

Biomimetic Gold Nanopatterns

4.1 Introduction

In order to determine whether the nanoscale spacing and clustering of biological ligands has an effect on cellular signaling, it is important to be able to fabricate robust surfaces that can be used to answer these questions. Earlier, block co-polymer micellar lithography (BCML) was highlighted as a well described methodology for the fabrication of nanoparticle arrays, which uses the selective solubility of the hydrophilic polymer region of a di-block co-polymer in organic solvents to form self-aggregating structures. In this project, the diblock copolymer poly (styrene-*block*-2-vinylpyridine) (PS-b-P2VP) was used as a precursor to form micelles in solution.[209, 204, 203, 221, 351, 220] PS-b-P2VP contains a polar pyridine unit repeated in the poly-2-vinylpyridine (P2VP) segment; when solubilised in organic materials, the P2VP blocks aggregate in the centre of the micelle to form a core. The less polar polystyrene units then surround the P2VP as a diffuse shell, which reduces energetically unfavourable interactions between the immiscible non-polar solvent and the more polar P2VP. Recent investigations from other groups have shown that these micelles, once formed, can then be functionalised directly using crosslinking methods [209, 352, 353, 354] and that tri-block copolymer micelles can also be formed,[355] however such investigations are beyond the scope of this project, which uses micellar lithography solely as a tool to produce nanoparticle arrays.

Figure 4.1.1 shows a schematic of block copolymer micellar lithography; the micellar core-shell structure forms a nanoreactor that allows selective dissolution of metal salts into the core.[356] For gold nanoparticle formation, $HAuCl_4$is normally the metal salt used. The ions dissociate so that the nitrogen of the pyridine unit is now positively charged and the Au complex adjacent creates a stable favourable ionic interaction. [205, 351, 222] Micellar stability is further enhanced through this process; aggregation is reduced as the micelles repel each other. Furthermore, each micelle is likely to contain fewer individual polymer chains due to the repulsion between charged pyridine units, leading to smaller micelles. Finally, the neutralisation of the pyridine, acting as a Brønsted base, by the $HAuCl_4$also increases the incompatibility of the solvent/polymer core interaction. [205, 222]

Micelle deposition onto substrates can then be achieved by dip-coating[203] or spin-coating[357] which allow the formation of a large monolayer area of close packed micelles.[358, 359] The formation of a closely packed film is affected by long range Van der Waals interactions, solvent characteristics and dipping velocity.[360, 361] The balance between the attractive micellar forces, such as capillary forces, and the

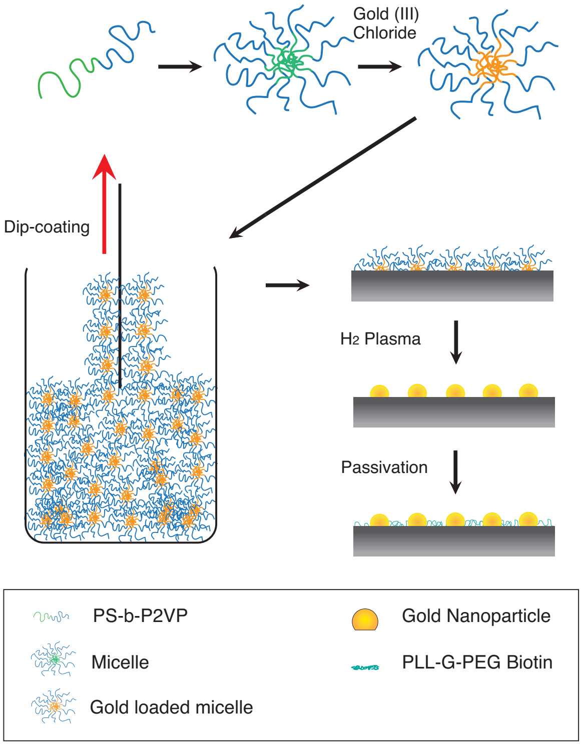

Figure 4.1.1: Schematic of micelle and nanoparticle formation. Micelles are formed when PS-b-P2VP is dissolved in para-xylene and loaded with $HAuCl_4$. These micelles can then be dip-coated onto substrates and nanoarrays formed by plasma treatment, before being passivated between particles with protein resistant materials and later functionalised. The protein resistant material PLL-g-PEG can also provide additional functionality through the incorporation of biotin binding groups in the passivation layer, provided commercially.

repulsive micellar forces such as electrostatic interactions between positively charged pyridine units[221] also help determine the inter-micelle spacing. Additionally, the physical parameters of the dipping process itself, such as the surface energy of the substrate[362] and the solvent evaporation rate (variable dependent on day-to-day temperature and humidity values) also play a role. The original equation relating film thickness to withdrawal speed was proposed by Landau and Levich in 1942,[360] an updated version is shown in equation 4.1.1 taken from Yimsiri *et al.*[363]

$$h_0 = 0.944((nu_0)^{2/3})/(\sigma^{1/6}(\rho g)^{1/2}) = 0.944(Ca)^{1/6}((nu_0)/\rho g))^{1/2}, \tag{4.1.1}$$

where h_0 is the film thickness, u_0 the withdrawal speed, n the solution viscosity, p the solution density, σ the solution surface tension and Ca capillary number (nu_0/σ). Film thickness is closely related to lateral micellar spacing, as a thicker liquid film causes closer micelle packing, and so smaller inter-micelle spacing.

After micelle formation, nanoparticle fabrication can then be achieved through a variety of methods; the metal complex can either be directly reduced in solution and micelles deposited to produce micelle constrained nanoparticles,[362] or reduced after deposition of ordered hexagonal close packed micelles on a substrate, as shown in Figure 4.1.1. Direct reduction of the Au^{3+} complex is achieved with reducing agents such as hydrazine[364] added to the loaded micellar solution which chemically reduce the Au (III) to Au

(0). A significant drawback of this method is the production of precipitate by-products such as hydrazinium chloride, however this method allows deposition of polymer-coated nanoparticles onto substrates. Alternatively, post deposition plasma treatment can be used to simultaneously remove the polymer micelle shell and form the gold nanoparticle. This is thought to be due to a combination of direct reduction from the plasma and polymer degradation products created during the plasma process, such as CO and electrons, which chemically reduce the gold.[203, 204, 362] The plasma process can be varied through pressure (both starting and operating), chemical atmosphere, power and time. It is important that the appropriate plasma method is chosen for the substrate in question. If oxygen was used in conjunction with silicon n+ doped wafer an insulating interlayer between the silicon and the nanoarray could be produced,[365] and although CF_4 could instead be ultilised to reduce the gold, this could cause erosion of the substrate.

The formation of polymer nanoparticles by these methods has been shown to be equivalent, indicating that reduction and crystallisation of the gold during polymer removal is faster than full degradation of the polymer.[362] Other methods of degrading the polymer and reducing the gold include laser ablation. This method breaks strong intra-chain covalent bonds through either thermal or photochemical methods, and has also been shown to often cause the polynucleation of nanoparticles due to a balance of the macroscopic temperature of the polymer and the energy density per laser pulse.[364] Thermal ablation is another common method of polymer removal, where electronically excited states formed through a mechanism involving chemically reactive oxygen species undergo internal conversion to other states, causing bond breakage.[364, 366] Plasma reduction of the Au^{3+} complex is favoured, as it eliminates the extra step of reduction in solution and the associated unwanted byproducts.

The synthesised gold nanoparticles usually range between 3-20nm in diameter,[362] and have been studied by High Resolution Transmission Electron Microscopy (HRTEM) which indicates a twinned crystal structure.[367, 368] For cellular investigations requiring nanopatterned arrays, gold is the metal of choice due to both its ease of fabrication and non-toxicity to cells.[226] Gold is also a reasonably inert metal, which is not prone to oxidation at low temperatures and is easy to handle in ambient conditions, as well as having been extensively studied and characterised.[369, 367] Once gold nanoparticles are synthesised, the binding of thiols on gold is a useful tool for attaching biological molecules to nanoparticles, and studies have shown that Self Assembled Monolayers (SAM) of thiolates on gold are stable to cell culture media and non-toxic to cells. [226]

The current resolution of BCML allows micelles and nanoparticles with spacing ranging from around 20-290nm to be formed,[94, 370] implying that the density of micelles (and so nanoparticles) can range over a factor of 10 (from 100-1100 micelles / μm^2). Although a robust technology for the formation of uniformly spaced gold nanoparticle arrays, currently, as the inter-particle spacing increases, the global particle density on the substrate decreases and so these aspects are coupled. [51, 109] Recent attempts to advance this technology have focused on creating micropatterned regions of nanoparticles,[356] predominantly using BCML in conjunction with Electron Beam Lithography (EBL) and Focused Ion Beam (FIB) methods.[371, 372] These methods allow pattern resolution in the µm range, however patterning of large areas by these methods is currently both costly and time consuming.

The development of Block Co-polymer Micelle Lithography (BCML) has been well documented, describing the identification of critical micelle concentration, loading parameters, and substrate extraction rate as key factors in array control.[203, 204, 364, 205, 351] The fabrication of nanoarrays by this method, and their subsequent functionalization with biological molecules through thiol interactions, present a platform technology that can be developed to present spatially controlled biomolecules for cellular studies. This chapter describes the fabrication of these arrays using the parameters already described in the literature, focusing on particle spacing, size and functionalisation. The final section of this chapter details the synthesis of novel nanoparticle arrays in which the simultaneous application of several nanopatterning techniques allows the fabrication of complex arrays, which seek to generate nanopattern surfaces where global particle density is decoupled from local nanoparticle spacing.

4.2 Contribution Statement

The work reported in this chapter was supported by the following people;
TEM imaging was performed by Karla-Luise Herpolt on samples made by Derfogail Delcassian.
Uni-directionally micro-contact printing of micelles was developed together with Jun Pang, working under the supervision and guidance of Derfogail Delcassian. Aspects of this work were reported in the MSc thesis "Scalable Fabrication of Micronanopatterned Cell Culture Substrate, Jun Hon Pang".

4.3 Materials and Methods

4.3.1 Preparation of micellar solutions

0.1 – 7mg/ml Poly(styrene-*block*-2-vinyl pyridine) (Polymer Source), of varying molecular weight and styrene to 2-vinyl pyridine ratio, was dissolved in para-xylene (99.0%, VWR) and stirred for at least 12 hours. Individual polymers are classified by the number of repeat units of each block, represented by subscript $PS_{(x)}$-b-$P2VP_{(y)}$, detailed in Table 4.3.1. $HAuCl_4$ (Sigma Aldrich) was then added at 0.1 – 2 molar ratio to the total amount of 2-vinyl pyridine units and left to stir for another 24 hours to generate micelles with gold-loaded cores. Gold-micellar solutions were then left untouched or treated with 1-30× excess hydrazine (1M in Tetrahydrafuran (THF) (Sigma Aldrich)) Additional solutions were made by mixing unloaded micellar solutions with loaded micellar solutions of the same molecular weight polymer and leaving to stir for 5 minutes before immediate use. Glassware and apparatus used in these procedures had been soaked in DECON-90 (Decon laboratories Ltd) for a minimum of 2 hours, before being rinsed in ultrapure deionised water (18ΩM.)

$PS_{(x)}$	$P2VP_{(y)}$	Polydispersity	Loading Conditions
110000	52000	1.10	5mg/ml in p-xylene
52000	31500	1.05	5mg/ml in p-xylene
32000	12500	1.12	5mg/ml in p-xylene
16000	3500	1.05	5mg/ml in p-xylene

Table 4.3.1: Table of PS-b-P2VP polymer characteristics, Mn, polydispersity, and loading concentration. Mn represented by number of repeat units of each polymer, $PS_{(x)}$-b-$P2VP_{(y)}$.

4.3.2 Formation of monolayers on substrate

Glass and silicon substrates were cleaned by immersion in a fresh 1:3 v/v mixture of hydrogen peroxide 30% aqueous solution (VWR) and concentrated sulfuric acid (95%, VWR) for at least 2 hours, before rinsing in ultrapure water (18.2 MΩ). Substrates were coated with a monolayer of gold-loaded micelles by dip-coating using a home-built setup with a retraction speed of between 0.12 – 0.63 mm/s. The glass slide was either left to dry in air, or excess para-xylene from the base 2mm of the slide was blown dry with N_2 and stored for further experiments.

4.3.3 Formation of the nanoarray

Gold nanosphere arrays were generated from these micelle-coated substrates by exposure to plasma treatment. A Reactive Ion Etcher (RIE) (Sentech, Etch Lab 200) using physical sputtering and chemical degradation with 20 Pa oxygen, for 40 minutes at bias RF voltages ranging from 200-500 V, an oxygen plasma (GaLa Instrumente PlasmaPrep5) or a hydrogen/argon plasma (10% hydrogen, 0.4 mbar, 350 W) in a plasma etcher (PVA TePla, Kirchheim, Germany) were used with a variety of conditions for array formation optimisation.

The different plasma treatments produced small differences in the quality of the nanoarrays; RIE physical sputtering occasionally induced nanoparticle ablation at high bias RF voltages, whilst oxygen plasma treatment occasionally induced polynucleation of the gold nanoparticle inside the micellar template. As such, hydrogen/argon plasma, which produced uniform arrays of well-spaced single nanoparticles, was used for the majority of the studies unless otherwise stated, and was chosen as the default plasma technique for nanopattern fabrication.

Analysis of the fabricated nanoarrays was performed using FIJI. SEM images of nanopattern surfaces were used to quantify particle diameter and inter-particle spacing. Particle diameter was measured by thresholding SEM images to minimum contrast, before converting images to binary format, then calculating the area of nanoparticles in the surface plane. This geometric area value was converted to diameter using the formula

$$area = \pi r^2, \tag{4.3.1}$$

where r is radius, and diameter is 2r.

Inter-particle spacing was calculated by drawing a line of best fit between 5-10 particles, and calculating the average inter-particle spacing for particles on that line by dividing the line length by the number of inter-particle gaps. A minimum of 10 separate best fit lines in several orientations were drawn for each surface type to ensure the average spacing of 50-100 particles was measured.

Error bars represent the standard error in the mean, calculated as follows:

$$S.e.m = \frac{(SD(n))}{(\sqrt[2]{n})}, \tag{4.3.2}$$

where SD represents the standard deviation of n measurements, divided by the square root of n measurements. Statistical analysis was performed in Origin and used non-parametric Mann-Whitney tests to compare across conditions.

4.3.4 Transmission Electron Microscopy (TEM)

Transmission Electron Microscopy (TEM) images were taken with an FX 2000 TEM. Samples were dropped onto holey carbon grids (Taab).

4.3.5 Scanning Electron Microscopy (SEM)

SEM Scanning Electron Microscopy (SEM) images were taken with a LEO Gemini 1525 Field Emission Gun (FEG) SEM at 5-10kV acceleration voltage. Samples coated on silicon were imaged directly, and glass slides after sputter-coating with a thin layer of carbon.

4.3.6 Functionalisation of nanoarrays

Glass substrates bearing gold nanoparticle arrays were incubated with 1mg/ml PLL-g-PEG (SuSoS) or PLL-g-PEG (50% Biotin graft) (SuSoS) for 1-2 hours, before being rinsed with ultrapure water and incubated with 0.1-0.5mg/ml FITC-EQDLISEEDL-PEG$_{(6)}$-NH-CH_2CH_2-SH or Fluorescein-β-Ala-DAKAC (courtesy of Dr. Hubert Kalbacher; provided by the University of Heidelberg) in Phosphate Buffered Saline (PBS) for 1-2 hours before being thoroughly rinsed in ultrapure water and stored for further use. Fluorescence was imaged with an Olympus 1X51 microscope with DP70 camera.

4.3.7 Fabrication of micro-contact printed (µCP) arrays

µCP masters were fabricated from a CD-R cut into 8cm by 8cm pieces, concentrated nitric acid (VWR) was used to dissolve the acrylic layer, the remaining aluminium membrane was then separated from the polycarbonate master which was rinsed and stored for future use. PDMS stamps were fabricated using Sylgard-184 (Dow Corning, 10:1 elastomer to curing agent ratio) mixed and degassed in vacuum before curing on top of the polycarbonate master for 2 hours at 60°C. Stamps were then dip-coated as previously described, and left to dry for 15 minutes. After drying stamps were inverted onto silicon chips and pressed for 3 minutes with a weight of 13g.

4.4 Results and Discussion

4.4.1 Controlling micelle size and spacing

In order to create features of a comparable spacing to cellular receptor clusters and signaling components deemed key to immune cell activation, nanopatterns with inter-particle spacing of between 10-150nm are desired. [108, 214, 103, 104, 105, 373, 374, 375] To create nanoparticles with spacing of this order a range of micelle sizes were explored. By varying the length of the individual polymers in the block copolymer different sized micelles are formed, meaning the micelle diameter, and subsequently the inter-micelle spacing, can be controlled within a certain range. Figure 4.4.1 illustrates the micelle sizes fabricated for use in this project using a range of polymer molecular weights.

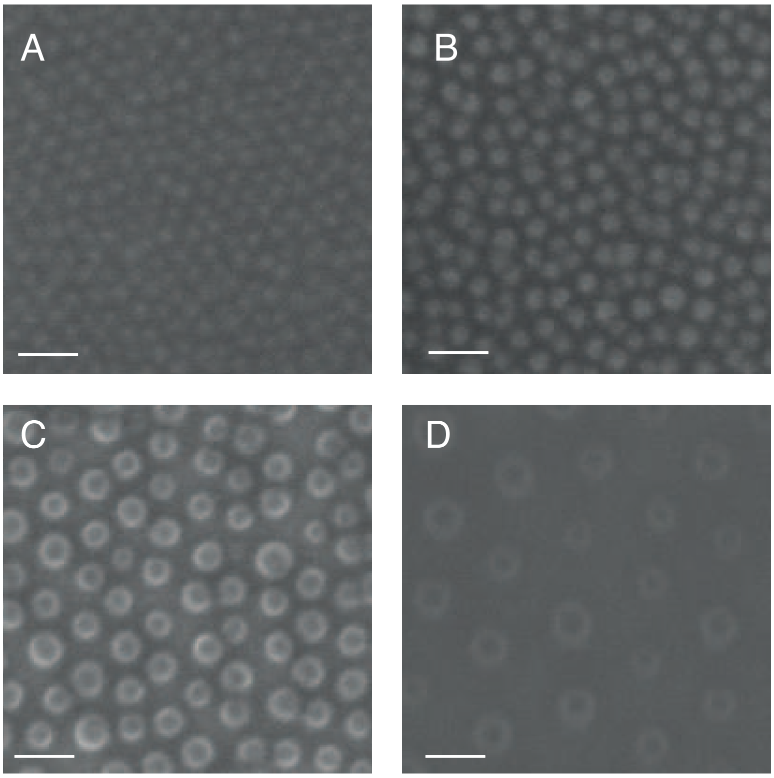

Figure 4.4.1: Effect of polymer template on micelle size. SEM images of PS-b-P2VP gold loaded micelles. Scale bar 100nm.(A) $PS_{(16000)}$-b-$P2VP_{(3500)}$ (B) $PS_{(32000)}$-b-$P2VP_{(12500)}$ (C) $PS_{(52000)}$-b-$P2VP_{(32000)}$ (D) $PS_{(110000)}$-b-$P2VP_{(52000)}$

The spacing between micelles on a substrate is flexible within a range predetermined by the micelle size. This fine spacing can be controlled by substrate extraction rates, amongst many other factors. Micelles with longer corona polymer chains are often considered more compressible, due to the reduced precision of micellar placement and the deformation or compression that can occur from surrounding micelles due to flexibility in the corona.[204] Micelles of $PS_{(110000)}$-b-$P2VP_{(52000)}$ repeat units, containing the longest individual polymer chains used in micellar synthesis in this thesis, were therefore used to confirm that extraction rate can be used to determine fine micellar spacing.

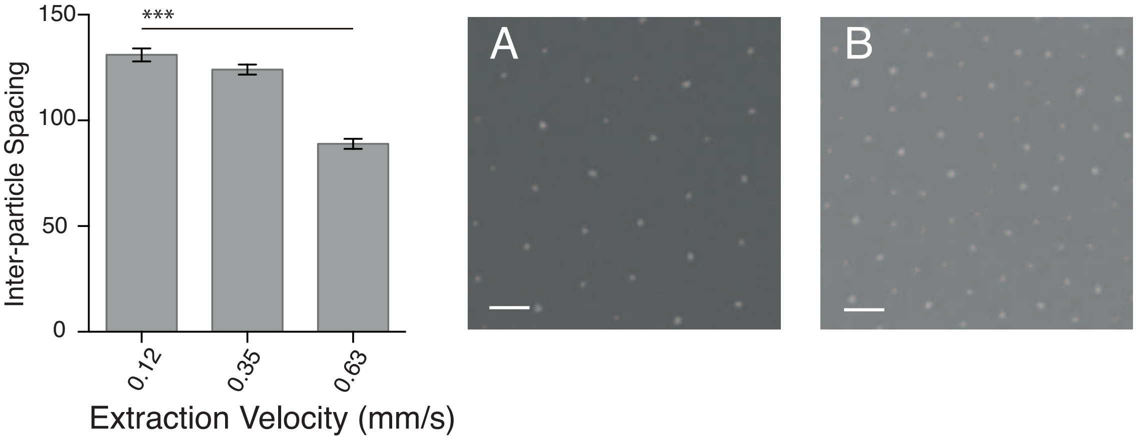

Figure 4.4.2: Gold nanoparticle inter-particle spacing as a function of extraction velocity. Bar chart shows mean spacing value calculated across extraction voltages, spacing calculated as described in the Materials and Methods section, statistical tests performed with a Mann-Whitney non-parametric test, ***p<0.001, error bar is the standard error mean in each case. SEM images were used to measure the inter-particle spacing of PS$_{(110000)}$-b-P2VP$_{(52000)}$ (A) SEM of sample dip-coated at 0.35mm/s and (B) 0.63mm/s with scale bar 100nm.

Extraction rates were controlled by the voltage applied to the DC motor driving the dip-coater extraction speed, and rates were varied from 0.12 – 0.63 mm/s. The effect of extraction rate, shown in Figure 4.4.2, was determined by measuring the inter-particle spacing of gold nanoparticle arrays as descibed in the Materials and Methods section. As expected, the extraction velocity is closely linked to the micellar spacing; with increasing velocity, the micellar spacing decreases, as described in the literature.[360] Earlier, we showed the film thickness equation described by Yimsiri *et al*.[363] which can be simplified to

$$h_0 \propto (n u_0)^{2/3}, \tag{4.4.1}$$

where h_0 is the film thickness, u_0 the withdrawal speed and n the solution viscosity. From this, we would expect the film thickness to increase as the velocity of extraction increases. The increase in film thickness is closely related to the lateral inter-micelle spacing, as the film thickness increases, the inter-micelle spacing decreases. Whilst our data does show that increasing velocity leads to a decrease in inter-particle spacing as expected from the equation, the exact nature of the relationship is not straightforward. There are a large number of other components in the equation, including viscosity and density, that may vary due to differences in sample preparation or ambient conditions. In practice, this means that this equation, whilst offering some indication as to which parameters can affect the fine-tune spacing, does not provide a robust method to pre-determine spacing values based on extraction velocity. Instead, a trial-and-error approach needs to be employed to optimise inter-particle spacing for different polymer templates.

Other factors that have been identified as key to micellar formation include the Critical Micelle Concentration (cmc) which is the point at which unimeric polymer units start to associate with each other.[205, 216, 217, 219, 218] This value is unique for each polymer, and is sensitive to solvent,[376] ionisation of the micellar core [204] and internal polymer ratio; where a longer core-forming block lowers the cmc if the number of monomers in the shell is maintained.[376, 377] For PS-b-P2VP, the cmc has been estimated to lie between 0.01 and 0.1g/ml, however the phase diagram of PS-b-P2VP is complex.[378] For this project, it is important to ensure that the solution phase is dominated by spherical micelles rather than unimeric polymer units or large aggregate phases. Figure 4.4.3 shows SEM images of substrates dip-coated at a range of micellar concentrations, and demonstrates that PS-b-P2VP is able to form various aggregate structure types across the concentration range of 0.1-5mg/ml (4.4.3).[204]

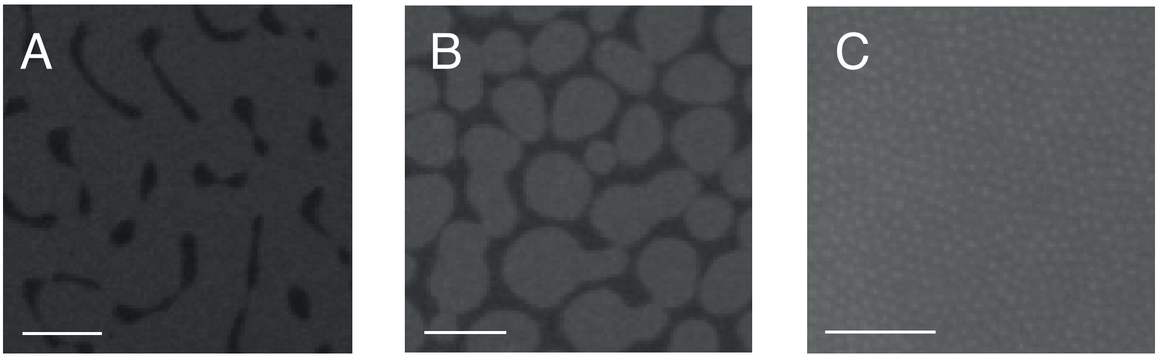

Figure 4.4.3: SEM micrographs of substrates dip-coated with micellar solution at varying concentrations. $PS_{(16000)}$-b-$P2VP_{(3500)}$ was solubilised at various concentrations in para-xylene and substrates dip-coated onto silicon wafers, before being examined by SEM. (A) 1mg/ml (B)2.5mg/ml (C) 5mg/ml. Scale bar (A,B 2µm, C 200nm)

Polymer loading concentrations were optimised for each polymer to produce micelles in solution, and details are given in Table 4.3.1 of the Materials and Methods section, describing the conditions used in this project. An exploration of the range of possible PS-b-P2VP phase formations has previously been carried out using the more appropriate technique of Small Angle Neutron (SANS) and Small Angle X-ray Scattering (SAXS). [378] Here, we used concentrations of 5mg/ml to produce a spherical micelle phase.

4.4.2 Formation of gold nanoparticles

Once the micelles have been deposited on the surface in a monolayer, the polymer can be removed leaving the noble metal (if the salt has been previously reduced). Alternatively, the metal salt can be reduced to its zero valence form whilst simultaneously removing the polymer matrix and maintaining the order of the nanoarray using plasma treatment, as described in the Introduction. Fabrication of arrays by plasma reduction is favourable due to fewer preparation steps. The degradation of the polymer micelle under oxygen plasma conditions was compared at different time-points by contact angle, using the hydrophobicity of the surface after plasma exposure as a measure of polymer removal (Figure 4.4.4). Contact angle measurements indicated that there is a rapid increase in the hydrophillicity of the substrate immediately after plasma treatment, likely due to the direct effect of the oxygen atmosphere making the polymer more hydrophillic before polymer degradation. Additionally, polymers of greater molecular weight require longer plasma exposure times to fully degrade the polymer micelle shell and form nanoparticle arrays.

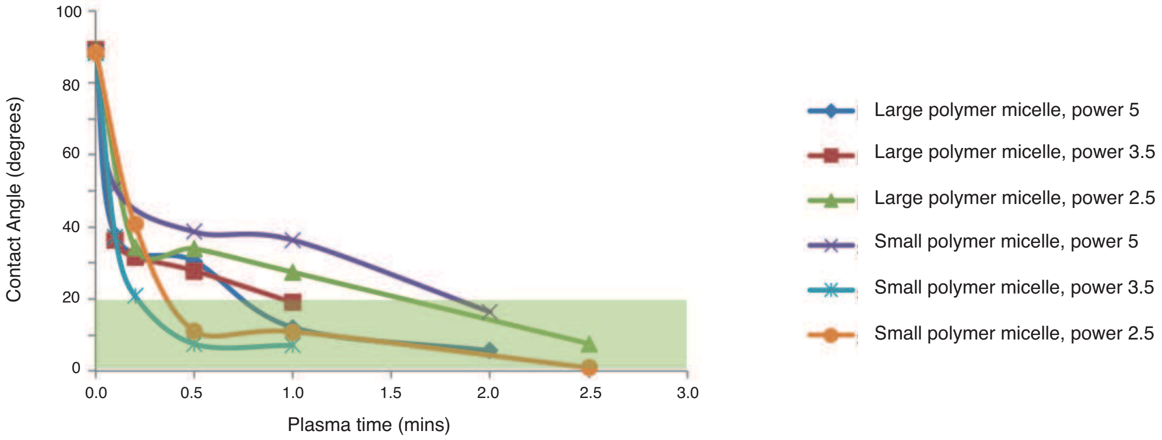

Figure 4.4.4: The effect of plasma treatment on micelle substrate hydrophillicity by contact angle measurements. $PS_{(110000)}$-b-$P2VP_{(52000)}$ (large) and $PS_{(16000)}$-b-$P2VP_{(3500)}$(small) micelles were dip-coated onto silicon substrates. Samples were exposed to oxygen plasma at 0.4mBar operating pressure in a GaLa Instrumente PlasmaPrep5 machine, at standard operating power 2.5, 3.5 or 5W and samples measured at timepoints between 0.0-2.5 minutes as shown in the graph. Contact angle of the substrates were measured as a function of plasma exposure power and time for both small and large micelles. Contact angles of below 20 degrees were classified as “bare” silicon where full polymer degradation had occurred (represented by the shaded area).

Nanoparticle arrays were formed using reducing plasma conditions, and particles produced across a range of spacings seen in Figure 4.4.5.

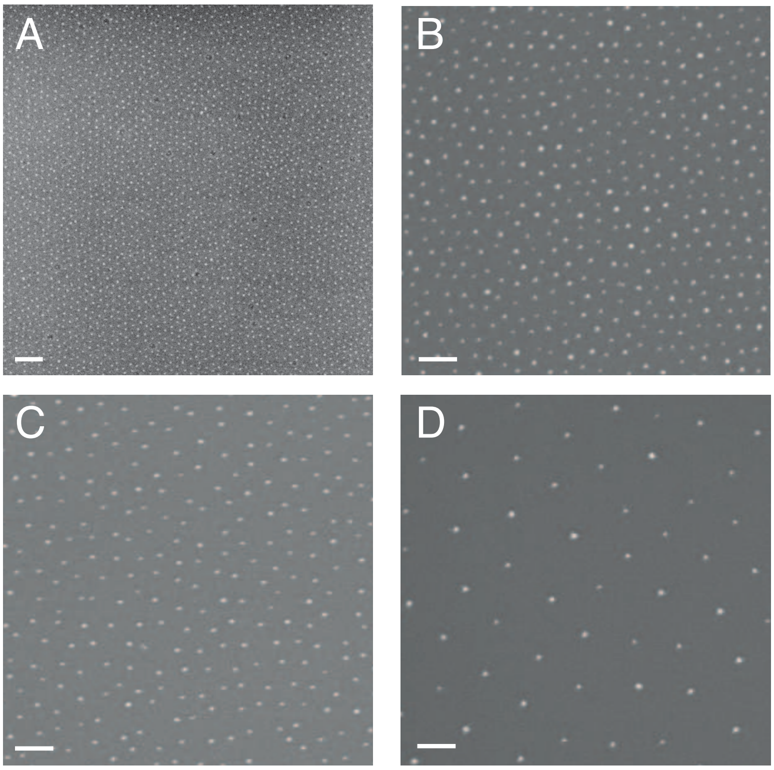

Figure 4.4.5: SEM micrographs of nanoparticle arrays spaced between 10 and 150nm. PS-b-P2VP of varying molecular weights was solubilised at 5mg/ml in para-xylene, loaded with gold, and nanoarrays formed through exposure to a hydrogen plasma and examined by SEM. (A) $PS_{(16000)}$-b-$P2VP_{(3500)}$ (B) $PS_{(32000)}$-b-$P2VP_{(12500)}$ (C) $PS_{(52000)}$-b-$P2VP_{(32000)}$ (D) $PS_{(110000)}$-b-$P2VP_{(52000)}$. Scale bar 100nm in all cases.

An alternative approach to nanoparticle formation, using chemical reducing agents, was also investigated. Gold loaded micelles were exposed to hydrazine at varying concentrations and gold nanoparticles formed inside the micelle were examined by SEM and TEM (Appendix A). The formation of well controlled gold nanoarrays requires interplay between many factors. Constraining the gold-pyridine complex in a quasi-hexagonal order, allowing the polymer-shell to be fully removed and ideally creating a single gold nucleation point, or allowing multiple nucleation with many particles eventually coalescing to form a single nanoparticle, are all required. The other methods investigated (reduction in oxygen rich environments and the pre-reduction of gold by hydrazine) were found to produce some polynucleation, resulting in multiple small gold particles per lattice point (Appendix A). Plasma treatment in reducing conditions was therefore selected as the favoured mechanism to fabricate well defined nanoparticle arrays (Figure 4.4.5) on substrates with quasi-hexagonal order.

Nanoparticle size was independently controlled through ionic loading (the ratio of gold ions compared to the number of pyridine units). Gold loading was altered within a single polymer template to produce nanoparticles of different diameters, shown in 4.4.6.

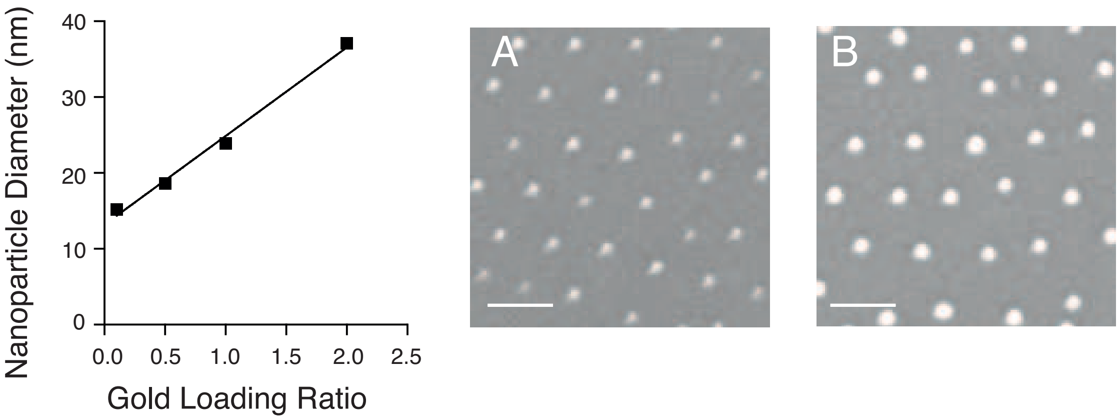

Figure 4.4.6: Gold loading and particle size. PS$_{(52000)}$-b-P2VP$_{(34000)}$ micelles were loaded with varying gold concentrations, dip coated, exposed to plasma treatment and examined by SEM. Nanoparticle size was calculated for a minimum of 500 particles per condition. Sample SEM images show (A) 0.1 loading ratio (B) 1.0 loading ratio. Scale bar 100nm.

As expected, particle diameter is directly related to loading ratio. As the concentration of gold per micelle core is increased, the relative size of the nanoparticle produced on the substrate post plasma treatment is also increased. This linear relationship means that it is possible to tightly control the nanoparticle dimension for each polymer, and produce a range of nanoparticle sizes at specific spacings. In this case, particle size analysis was performed by calculating the particle diameter from the geometric area shown on the SEM image as described in the Materials and Methods section. This assumes that the geometric area displayed is uniformly circular, and also relies on appropriate thresholding of the SEM images in order to provide contrast for particle area analysis. The threshold value therefore could affect the calculated particle size, as over-thresholding could result in an SEM image displaying a particle of reduced contrast area, and therefore a smaller geometric contrast area resulting in a reduced diameter value. The diameter values shown here do not give a true indication of the 3D structure of the particle, as they are a representative diameter calculated from the SEM region of contrast which we assume reflects the nanoparticle 2D area presented on the substrate plane. However, they do allow indicative comparisons to be made between gold loading conditions within polymer templates. More accurate information about the geometry of the particle formed could be determined using cross-sectional TEM. These results indicate that gold loading can directly affect the size of the nanoparticle produced, as the polymers controlling the micelle size (and therefore centre-to-centre micelle spacing) have different poly-2-vinylpyridine core lengths, gold loadings can be altered through the different polymer templates to produce nanoarrays with uniform gold nanoparticle size, and different spacing.

For cellular signaling investigations, being able to control the precise position and size of these nanoparticles across a 10-150nm lengthscale allows utilisation of these arrays for functionalization with small biological moieties and versatility in cellular investigations; the next section discusses proof-of-principle in functionalising these nanoarrays with biologically relevant materials.

4.4.3 Functionalisation of gold nanoparticle arrays

The functionalization of gold surfaces has typically been performed through thiol-gold coupling. In order for this to be a selective process, where ligand binding only occurs on the gold nanoparticle, the exposed substrate between nanoparticles needs to be rendered protein resistant. In this case, a graft co-polymer PLL-g-PEG was chosen to cover the surface between the gold dots and attach non-covalently to the substrate. PLL-g-PEG is protein resistant and presents a charged PLL backbone which is strongly attracted to the substrate surface.[379, 380, 381, 382, 383] Other studies, using AFM, have shown that when hydrated the graft co-polymer becomes swollen and forms a layer approximately 10nm thick.[383, 379] In this system, nanoparticle arrays were functionalised with a protein resistant PLL-g-PEG layer in between nanoparticles before biofunctionalisation.

Initial biofunctionalisation studies performed here focused on using peptides functionalised with thiol groups. Thiol groups were chosen for biomolecule binding for several reasons; they offer quick, strong binding, allow some control over ligand orientation and offer high stability.[30, 384] As the primary objective for these surfaces is as a cellular-material interface, stability of the ligand attachment mechanism is imperative to withstand cellular contractile forces[385] and prevent internalisation of ligands by cells.[386, 210, 211, 373] Two short peptide sequences with fluorescent tags and flexible PEG linkers (with thiol conjugation units at one end) were used to demonstrate preferential binding to the gold nanopatterned region and the successful passivation of the background between the particles (Figure 4.4.7).

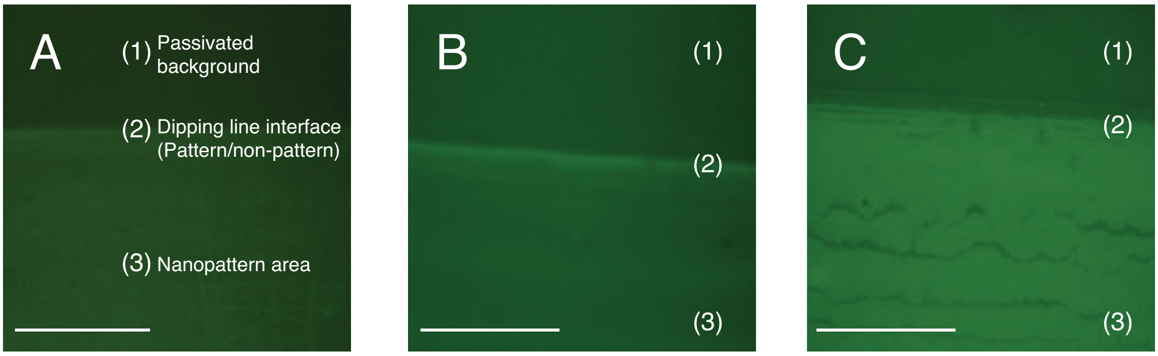

Figure 4.4.7: Nanoparticle arrays on glass were passivated with PLL-g-PEG graft co-polymer and functionalised with thiolated peptides (A) FITC-EQDLISEEDL-$PEG_{(6)}$-NH-CH_2CH_2-SH and (B,C) Fluorescein-β-Ala-DAKAC. Different nanoarrays were used to demonstrate intensity changes in functionalization; (A, B) $PS_{(110000)}$-b-$P2VP_{(52000)}$(mean nanoparticle spacing 104nm +/- 5nm) (C) $PS_{(16000)}$-b-$P2VP_{(3500)}$ (mean nanoparticle spacing 25nm +/- 2nm). Scale bar 200µm for all images. Areas of the slide are marked as follows; (1) Glass without nanopatterns, (2) the interface between nanopatterned and non-nanopatterned areas, (3) the nanopattern area. PLL-g-PEG was used as a passivation agent in all cases, and slides show selective fluorescence in the nanoparticle region indicating successful passivation and selective functionalisation of the gold nanoparticles.

The appearance of these slides indicates successful passivation and functionalization of the nanoarray; there is a clear distinction between the non-nanopatterned area (marked (1) in Figure 4.4.7) which shows minimal fluorescence, representing successful passivation of the background with PLL-g-PEG, and the nanopatterned area (marked (3) on figure). The interface between the patterned and non-patterned area on the nanopattern slide (marked (2)) often shows a region of non uniform and heavy gold deposition due to the fabrication process, which can extend up to 1mm from the dipping boundary into the nanopatterned area of the slide. This dipping boundary is therefore often visualised after functionalisation with appropriate fluorescent molecules as a bright line (as seen in Figure 4.4.7B), representing the heavy gold deposition at this interface, or as in Figure 4.4.7C, some deposition sub-structure can be seen at the interface between the nanopatterned and non-nanopatterned region due to the extraction procedure used to coat the slide with nanoparticles. In all cases, this interfacial region is not used for subsequent cellular experiments, which instead focus on the uniform area of nanopattern arrays across the rest of the slide.

The fluorescence shown in the nanopatterned area (Figure 4.4.7A,B,C marked (3)) indicates that the biomolecules are binding to the gold nanopatterns preferentially, rather than the passivated background between the nanoparticles and on the top half of the surface. Although the fluorescent data shown here suggest that binding of fluorescent biomolecules into the passivated background area is limited, indicated by the lack of fluorescence in the non-patterned and passivated area (marked (1)), it is possible that a few biomolecules bind into the passivation layer but that these are beyond the limit of detection of the microscope. Cellular studies performed as part of Chapters 6 and 7 measured cellular response to glass coated with PLL-g-PEG passivation agent, PLL-g-PEG and antibody, and positive antibody controls (data not shown) to confirm that surfaces treated with PLL-g-PEG and subsequently functionalised with antibody did not induce cellular responses above those of background, and so surfaces were considered protein resistant, implying that cellular response to biomolecules is mediated through the specific attachment to the gold nanoparticle.

Additionally, the preferential nature of the attachment mechanism can be confirmed by comparing surfaces with small and large nanopattern deposition. We could expect to see a difference in fluorescence due to particle density changes on nanoarrays with different inter-particle spacing. Assuming that each nanoparticle is singly functionalised, the change in fluorescence seen in Figure 4.4.7 (B-C) is attributed to the change in particle density as we move from one spacing to another. Here, spacing of approximately 25nm (C) represents a particle density of 1600/μm^2 whilst (B) is approximately 100/μm^2; the increase in fluorescence intensity on smaller nanoarrays indicates that it is the nanoparticle itself being functionalised with the thiolated peptides, and we have therefore created functionalised biomimetic arrays with a passivated and biomolecule resistant background, with controllable spacing between 10-150nm.

4.4.4 Fabrication of advanced nanoparticle arrays

The fabrication of uniformly patterned gold nanoarrays has been achieved using diblock copolymer lithography and deposition through substrate dip-coating, however a limitation of this technique is that the parameters of local inter-particle spacing and global particle density on these surfaces are coupled; through altering one the other is also varied. This section describes attempts to fabricate nanoparticle arrays in which these parameters operate orthogonally, where local inter-particle spacing can be maintained, but global particle density varied over the cellular lengthscale.

A simple approach involves the overlap of several nanopatterns on a planar substrate. By sequentially dip coating and plasma treating micelle solutions, multiple overlapped arrays can be produced on one substrate. By using a different types of micelle, a range of particle sizes on one substrate can also be produced; a typical SEM image is shown in Figure 4.4.8. This method ensures that the smallest inter-particle spacing remains largely constant, but that the density of particles can be vastly varied. However, a disadvantage to these binary arrays lies in the reproducibility of the overlapping nanopatterns, which is not well controlled and therefore remains largely statistical. An improvement to this technique would be to use several materials in different, layered arrays; this could allow the spacing and density of one material (functionalised with its own ligand) to be maintained whilst altering the spacing and density of a second material functionalised with an alternate ligand.

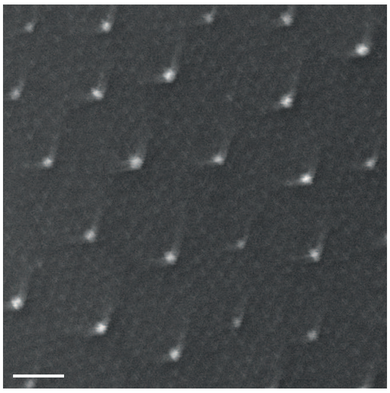

Figure 4.4.8: SEM micrographs of advanced functionalised nanoparticle arrays formed using combinatorial block copolymer micellar lithography. Binary arrays of small and large spaced nanoparticles. Scale bar 100nm.

Alternate approaches were also investigated, including combining loaded and unloaded micelles to produce micellar arrays with uniform micellar coverage but statistically varied particle density, but were difficult to optimise due to gold lability. As the gold ions are rapidly redistributed amongst the micelles, uniform particle arrays are instead formed, where particle size is proportional to the ratio of empty to loaded micelles. (Appendix B)

A second technique focuses on the combination of micellar lithography with micro-contact printing. The combination of BCML with other advanced nanopatterning techniques (predominantly EBL, FIB and other photolithography methods) has already demonstrated power in producing surfaces with separately controlled spacing and density parameters.[371, 372] The limitations in fabrication of large areas ($1cm^2$) make these methods costly and time consuming for production of substrates suitable for cellular studies. An alternative approach to micro-nanopatterning allows the combination of micro-contact printing (μCP) with BCML, by inking stamp protrusions with micellar solutions.[387] The smallest pattern currently available using BCML μCP is approximately 1μm wide. Additionally, pattern edges are often blighted by particle agglomeration making them unsuitable for studies where particle size needs to be tightly controlled.[388] Early efforts to fabricate μCP patterns using micellar lithography found that μCP of micellar solutions was sensitive to stamp coating procedure, applied force, trough depth, drying and contact time.[387, 389, 390] These parameters were investigated (acknowledgement: MSc student J. Pang under supervision of D. Delcassian, data not shown) in order to fabricate nanoparticle surfaces with controlled spacing and modified particle density through combinatorial μCP BCML (Figure 4.4.9(A)). SEM analysis shows dark striped regions which are indicative of successful micelle transfer, and the resolution of these micropattern features is greater than that currently reported in the literature (at 600nm stripe width). An advancement of this technology is in the fabrication of bidirectional lines, shown in Figure 4.4.9(B). Here an SEM image of latticed micellar stripes can be seen, where the polymer micelles are different sizes in different orientations. This technology allows the presentation of latticed stripes, where each stripe is approximately 600nm wide, and contains close packed micelles of predetermined size and loading capable of producing nanopatterned gold arrays.

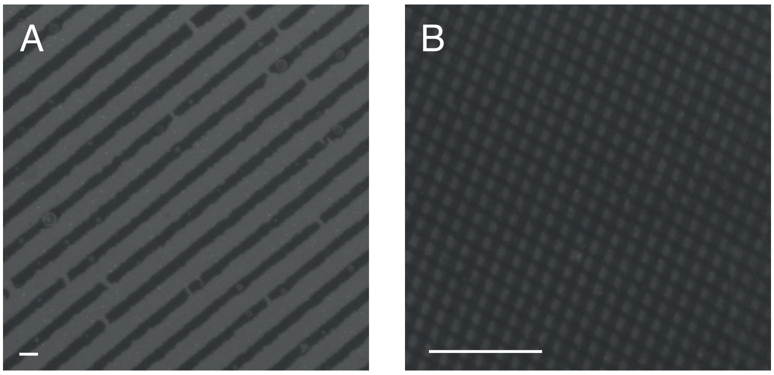

Figure 4.4.9: SEM micrographs of advanced functionalised nanoparticle arrays formed using combinatorial block copolymer micellar lithography and micro-contact printing (A) Unidirectional printed lines. Scale bar 1μm (B) Latticed micronanopatterned lines of differently sized micelles. Scale bar 10μm.

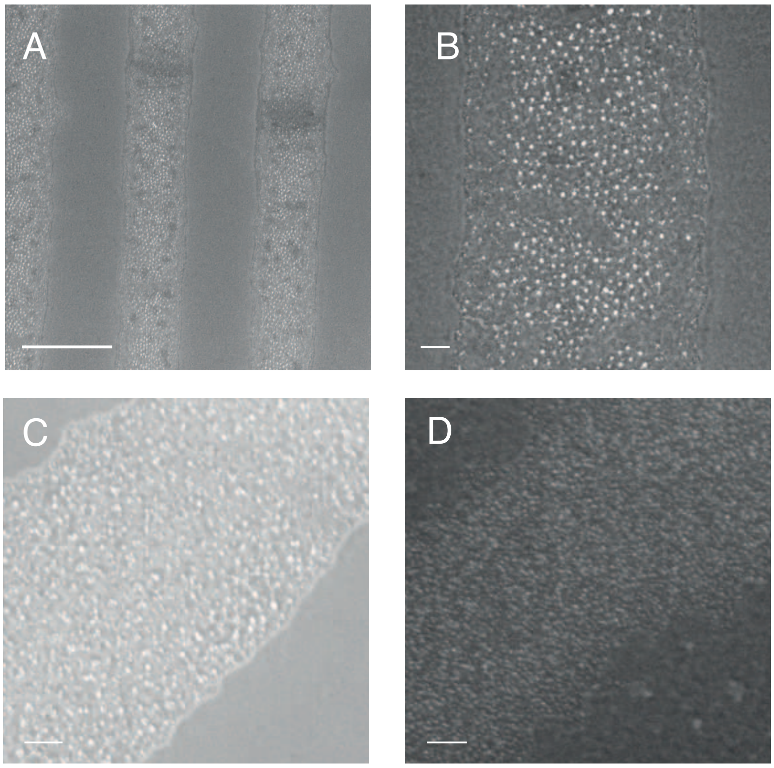

Figure 4.4.10: PDMS stamps were dip-coated with micellar solutions (A, B) $PS_{(52000)}$-b-$P2VP_{(34000)}$ (C) $PS_{(34000)}$-b-$P2VP_{(12500)}$ (D) $PS_{(16000)}$-b-$P2VP_{(3500)}$ Lines of approximately 600nm width were printed. Scale bar (A) 1μm (B-D) 100nm.

Figure 4.4.10 shows SEM images of the nanopatterns formed post plasma treatment through the microcontact printing technique. The nanoparticle spacing is largely controlled by the polymer template, and shows that the overall geometry (600nm stripes) can be maintained whilst varying the individual nanoparticle size and spacing . Further work on this system to extend the technology to other geometries using alternate

PDMS stamps, and a more thorough investigation into the range of nanoparticle sizes and spacings that could be fabricated in unidirectional and bidirectional geometries will extend the currently available technology to develop nanopatterned interfaces than can answer more complex biological questions.

4.5 Conclusions

We have shown the controlled fabrication of gold nanoparticle arrays on planar substrates with precise nanoparticle size and a range of spacings between 10-150nm through block copolymer micellar lithography and reducing plasma treatment. Nanoparticle formation can be controlled by polymer template size and dip-coating extraction rate to produce particles with precise inter-particle spacing. Additionally, nanoparticle size can be tightly controlled by gold ionic loading, which increases the versatility of these substrates for uses beyond cellular interactions, beginning to make them attractive for applications in a variety of other fields where tightly controlled nanoparticle size is imperative to device function.[369, 391, 392, 393, 394].

Once formed, these highly ordered nanopatterned substrates have been treated with a protein resistant layer in between the particles, and particles functionalised with thiol linked small biological molecules. The methods explored in this chapter present a platform technology that can be adapted to study cellular response to nanoscale ligand environments.

Using the principles explored in the early sections of this chapter, we have also fabricated more complex novel nanoparticle arrays that advance the current technology from beyond planar nanoparticle arrays with uniform spacing to include other geometries. Deposition of multiple micellar layers has produced surfaces where uniform nanoparticle spacing remains constant, but nanoparticle density can be varied, and separately micellar μCP has been used to produce single linear stripes of nanoparticle arrays and criss-crossed striped nanoparticle arrays. The nanoparticle arrays produced by micellar μCP shown in this chapter are the first to show regular linear geometries with sub-micrometer (600nm) resolution, and to our knowledge, also present the first evidence of a combinatorial micellar μCP method able to produce latticed arrays of linear nanopattern geometries, where the nanopattern array can be controlled orthogonally in the different directions by selection of appropriate pre-cursor solutions.

4.6 Future Work

Immediate future work can be categorised into the further development of these nanopatterned arrays and the use of the already fabricated materials. Initially, it will be important to test these nanoparticle interfaces as biomimetic materials with which cells can engage. This will involve the development of the functionalization technique in order to be able to conjugate more complex biologically relevant ligands, such as whole and partial-antibodies, followed by the investigation of these materials as artificial immune synapses determining the minimal stimulation required for cellular activation.

With additional μCP masters, fabricated by e-beam lithography (EBL) or photolithograpy, the μCP method could be further developed to allow fabrication of surfaces with independently controlled geometry and nanoscale architecture. This would be particularly interesting for investigating combinatorial cellular effects, such as the spacing of adhesion ligands (known to have a nanometre scale threshold for successful attachment[214, 105, 103]), with cellular adhesion and differentiation on geometric patterns.

For example, it would be interesting to see if the differential differentiation of stem cells on geometric nanopatterns was conserved when adhesion is destabilised through nanopatterned position of adhesive RGD ligands.[395, 396, 397]

More simplistically, the latticed nanopatterned materials could be used to investigate and direct cellular activation and motility; one could provide an activatory background, and "fence" that area with nanopatterned lines functionalised with inhibitory receptors. This would be particularly interesting for studying cellular responses in NK cells, which are known to integrate inhibitory and activatory signals for activation (Chapter 6). By controlling the spacing of the inhibitory receptors through the μCP it may be possible to force orientated cellular mobility on these surfaces, or alternatively to provide gradiented surfaces allowing controlled cellular migration and activation in selected regions of these types of surface.

Advanced functionalization methods could be achieved by allowing co-deposition of an alternative material in the micelle core through any of these advanced fabrication methods. With fabrication of an alternative nanoparticle, and orthogonal functionalization chemistry, it could be possible to create surfaces with a mixture of gold nanoparticles and alternate materials, that could then be used to create mixed particle surfaces (enabling the density/spacing studies discussed above). Separately, lines of differing materials in differing directions will allow investigations into cellular co-stimulation to be performed, and aid the decoupling of local ligand spacing and global ligand density parameters. The nanopattern methodologies described in this chapter allow the fabrication of materials with controlled inter-particle spacing, particle size, and surface geometry (either linear stripes or uniform planar arrays of nanoparticle material as shown here). As such, they are a useful resource for the fabrication of biomimetic interfaces that can be used to answer fundamental questions about cellular interactions; Chapters 6 and 7 describe cellular experiments on biomimetic interfaces fabricated using these methods in more detail.

Chapter 5

Templated Zinc Particle Fabrication

Block Co-polymer Micellar Lithography: a tool for compound metal particle formation

5.1 Introduction

The versatility of the Block Co-polymer Micelle Lithography (BCML) method allows fabrication of a range of metal and metal oxide particles in ordered nanoarrays.[203, 204, 362] Optimisation of the technique using gold precursors was discussed extensively in Chapter 4: Biomimetic Gold Nanopatterns, this chapter describes the extension of the micellar lithography technique to the fabrication of zinc-based nanoparticles. Zinc-based materials offer two key advantages, firstly, they can be used to fabricate nanoparticles with different surface chemistry to gold. As such, the nanoparticles can then be used to provide alternative biomolecule attachment mechanisms which are complementary to the gold nanoparticle formation and thiol linkage already discussed. Additionally, when sized at the nanoscale they often provide distinctive optical properties.

Genetically engineered proteins are commonly expressed with six histidine residues (His-tag) at one end of the protein sequence in order to facilitate purification.[398, 399, 400] These histidine residues are capable of chelating metal ions through the nitrogen electron lone pair and this principle can be employed in protein immobilisation strategies.[401, 402, 403, 211] Commonly, nickel (II) ions are use to chelate proteins and small linkers simultaneously in an octahedral complex. A typical example is shown in Figure 5.1.1, which indicates the chelation of two histidine units and a nitrilotriaceticacid (NTA) group through an Ni^{2+} ion. The NTA group can be coupled to a small linker molecule allowing linkers to be attached to other molecules or particles; in this case an alkane terminated with a thiol group is shown, which would allow functionalisation of gold nanoparticles. [404]

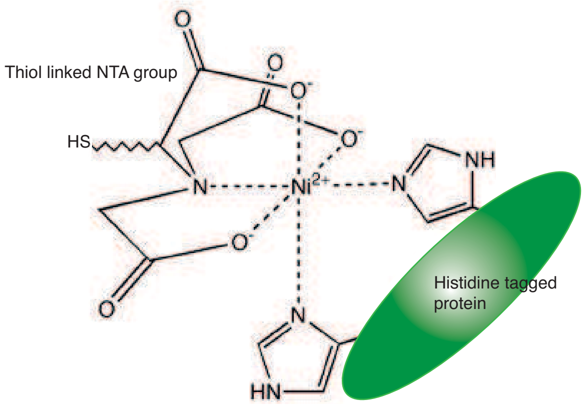

Figure 5.1.1: Schematic showing NTA thiol linker bound to gold nanoparticle, chelated nickel ion, and a Histidine tagged protein binding through the remaining octahedral sites.

An alternative strategy is to directly conjugate the His-tag moiety to a suitable nanoparticle, removing the requirement for an additional linker molecule. Using this method, His-tag proteins have been conjugated to nanoparticles in suspension[405, 402, 406] though conjugation to nanoparticle arrays has yet to be shown. There are limitations in the methods currently used to biofunctionalise nanoparticle arrays for cellular studies. Namely, they often rely on either the direct binding of thiolated peptides, which is only suitable for receptors where small molecule ligands have been identified, or the immobilisation of proteins through chelated His-tags and other non covalent strategies. If nanoarrays of zinc-based particles could be formed, and these could be selectively biofunctionalised with ligands or proteins, this would provide a significant advantage in biomolecule functionalisation strategies.

Zinc sulfide nanoparticles could allow the selective functionalisation described; ZnS has been shown to bind to His-tag proteins, and is used as a capping agent to stabilise other quantum dots due to its relative non toxicity to cells.[407, 408, 341, 409, 410, 411, 412, 413, 414, 415, 416, 417, 418, 419, 420] The binding of histidine tagged proteins to the ZnS material is likely mediated by the nucleophillic attack of the lone nitrogen pair on a histidine moiety to the zinc on the ZnS surface forming a covalent bond, as described in His-tag binding to (CdSe)ZnS systems [421, 422, 405].

Additionally, ZnS is a compound group II-VI material, and so when constrained on the nanoscale can act as a quantum dot (QDs) with unique spectroscopic properties due to the three dimensional spatial confinement of its electrons.[423, 424, 425] The fabrication of well ordered and controlled nanoscale quantum dot arrays could also have future applications in a wide range of fields, including optoelectronics[426, 427] and bio-sensing.[428, 429, 430, 431]

Compound nanoparticles are typically synthesised from precursors at high temperatures, which are cooled and exposed to capping agents allowing co-precipitation of the elements in a nanocrystal. Although this method allows a range of commercially viable elements to be combined, it often requires high temperatures, toxic reagents and multiple processing and purification steps.[432] In contrast, micellar lithography is a one pot synthesis method, often performed at room temperature and pressure, where metal ions can be chelated at the core of a polymer template in reverse micelle formation.[215] Synthesis of controlled sized single elemental nanoparticles such as cobalt, gold and silver[433, 387] have been widely reported, however compound nanoparticle synthesis has been limited to oxides[220] and some basic bi-elemental nanoparticle synthesis. BCML has produced metal nanoclusters that were surface bound and subsequently exposed to compound elements to produce QDs where only the central nanocluster has been produced in a micelle core,[434] AOT micellar templates have been used for synthesis of multiple CdS particles inside compound micelles[435, 223] and complex micro emulsion cage assemblies have been used to synthesise numerous ZnS particles inside selective solvent regions.[436]

This chapter discusses the fabrication of zinc-based nanoparticles in polymer template cores, where fabrication of a single particle per micelle template is desired. Poly(styrene-*block*-polyvinylpyridine) templates were used to encapsulated Zn^{2+} ions, which were exposed to H_2S gas generated in situ, to form a single complex nanocomposite crystal ZnS particle inside micelle cores.

5.2 Contribution statement

The work reported in this chapter was supported by the following people;
TEM imaging was performed by Lucia Podhorska, Dr. Angela Goode and Giovanni Luongo on samples made by Derfogail Delcassian.
EDX analysis was performed by Lucia Podhorska and Dr. Angela Goode on samples made by Derfogail Delcassian.
SAXS experiments and analysis were performed commercially by PANalytical on samples made by Derfogail Delcassian.
SANS experiments and analysis were performed by Dr. Iain E. Dunlop and Lucia Podhorska on samples made by Derfogail Delcassian. We also acknowledge the beamline scientist Dr. Aurel Radelscu of FRMII, Juelich Centre for Neutron Science, Garching, Germany.
This project was aided by an MSc student Michael Agyei under the supervision of Derfogail Delcassian, and aspects of this work were reported in the MSc thesis “Forming Quantum Dot Nanoparticle Array for Biofunctionalization, Michael Agyei”.

5.3 Materials and Methods

5.3.1 Fabrication of Zn^{2+} loaded micelles

Poly(styrene-*block*-2-vinyl pyridine) (Polymer Source, Montreal, Canada), of varying molecular weight and styrene to 2-vinyl pyridine ratio depending on the nanopattern spacing required, was dissolved in p-xylene (99.0%, VWR, Radnor, P.S., U.S.A.)) and stirred for at least 12 hours. Zinc Acetate (Sigma Aldrich) was predissolved in propan-1-ol (VWR) at a concentration of 0.073mg/µL and added to the polymer solution at a ratio of zinc to pyridine units of 0.5-0.1, then left to stir for another 24 hours to generate micelles with zinc-loaded cores.

5.3.2 Fabrication of ZnS encapsulated particles

Loaded micellar solutions prepared as described above were decanted into a central flask in a three- flask tandem (shown schematically in Figure5.3.1) with a controlled atmosphere. The set up for carrying out sulfidation reactions using small quantities of locally-generated H_2S is based on the design reported in the

MSc thesis "Photoelectrochemistry of CdS Multilayers, B Van Hattem" kindly provided by Prof. Jason Riley of Imperial College London. The first flask contained 60mg of sodium sulfide (Sigma Aldrich), the second flask 2-5ml of loaded micellar solution, and the third flask contained a solution of 2g inc nitrate (Sigma Aldrich) in 30ml deionised water (18.2 MΩ). The flasks were de-oxygenated with nitrogen gas for 10 minutes whilst stirring. 2M Nitric acid was then added to the first flask, generating H_2S gas, which permeated the second flask via the N_2 carrier gas, and this was left to stir for 40 minutes. Excess H_2S was bubbled through the third flask and quenched by the $ZnNO_3$ solution.

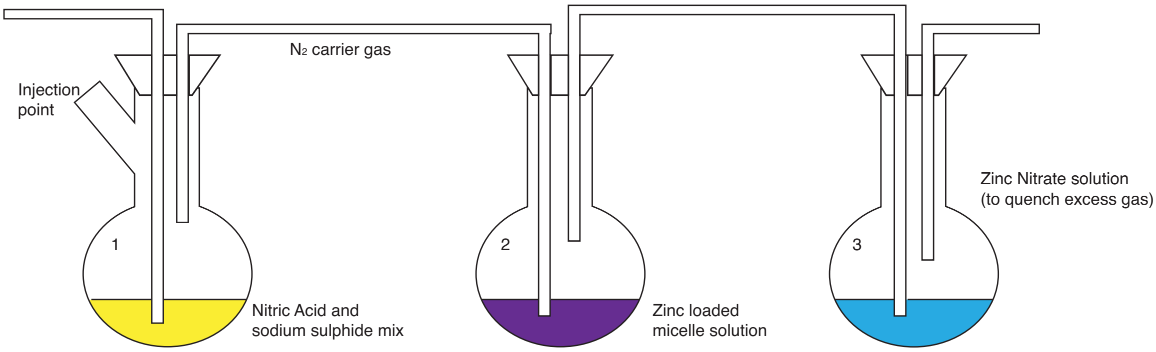

Figure 5.3.1: Schematic showing three flask set up. 1- contains 2M nitric acid an sodium sulfide, generating hydrogen sulfide gas in situ. 2- contains the micellar solution, hydrogen sulfide is bubbled through flask two with the aid of the nitrogen carrier gas, excess gas is quenched in flask three.

5.3.3 TEM analysis

Droplets of solution were deposited on carbon coated TEM grids (holey carbon grids, Taab) and examined by TEM, both an FX2000, Jeol 2010 and Titan 80/300 TEM/STEM depending on the resolution required.

5.3.4 Optical Investigations

UV Visible Absorption Spectroscopy Measurements were performed with a PerkinElmer Lambda 25 UV-Vis, using a quartz cell with 10mm pathlength. Fluorescence Spectroscopy Measurements were performed with a Fluorolog Horiba Jobin Yvon and recorded using fluorescence V3.5 software, using a quartz cell with 10mm pathlength.

5.3.5 Substrate deposition

Silicon substrates were cleaned by immersion in a 1:3 v/v mixture of hydrogen peroxide 30% solution (VWR) and concentrated sulfuric acid (95%, VWR) for at least 2 hours, before rinsing in ultrapure water (18.2 MΩ). Substrates were coated with a monolayer of either zinc loaded, or zinc sulfide containing micelles by dip-coating using a home-built setup with a retraction speed of 0.36 mm/s. Zinc nanosphere arrays were generated from these micelle-coated substrates by exposure to a hydrogen/argon plasma (10% hydrogen, 0.4 mbar, 350 W) in a plasma etcher model name (PVA TePla, Kirchheim, Germany), and similarly, zinc oxide arrays were generated by exposure to an oxygen plasma PlasmaPrep 5 (100% oxygen, 0.4mbar).

5.3.6 SEM and nanoparticle analysis

Sample nanoarrays from each batch were characterised by SEM (Leo Gemini at an EHT 5-10kV).

5.3.7 Small Angle X-Ray Scattering (SAXS)

SAXS experiments were performed in 1mm quartz capillaries and measured with Pan Analytical Empyrean, 45KV, 40mA. Samples were prepared as above and analysed using PanAnalytical Easy SAXS 2.0.

5.3.8 Small Angle Neutron Scattering (SANS)

SANS experiments were performed on KWSII at FRM-II, Juelich Centre for Neutron Science, Garching, Germany. Samples were prepared as above, using either PS(protonated)-b-P2VP(protonated), or PS(deuterated)-b-P2VP(protonated) polymer (Polymer Source) and protonated or deuterated *p*-xylene (Sigma Aldrich) to give contrast for SAXS imaging, and analysed using a Gaussian approximation of spherical particles.

5.4 Results and Discussion

5.4.1 Zinc Loaded Micelles

Loading poly(styrene-*block*-polyvinylpyridine) (PS-b-P2VP) micelles with zinc salts allows the fabrication of several types of nanoparticle through the block copolymer micellar lithography (BCML) technique.[205] The schematic in Figure 5.4.1 illustrates the two approaches discussed in this chapter; direct exposure of surfaces coated with ordered zinc loaded micelles to reducing or oxidising conditions, or the reaction of zinc ion cores with H_2S to form compound ZnS nanoparticles encapsulated within micellar templates.

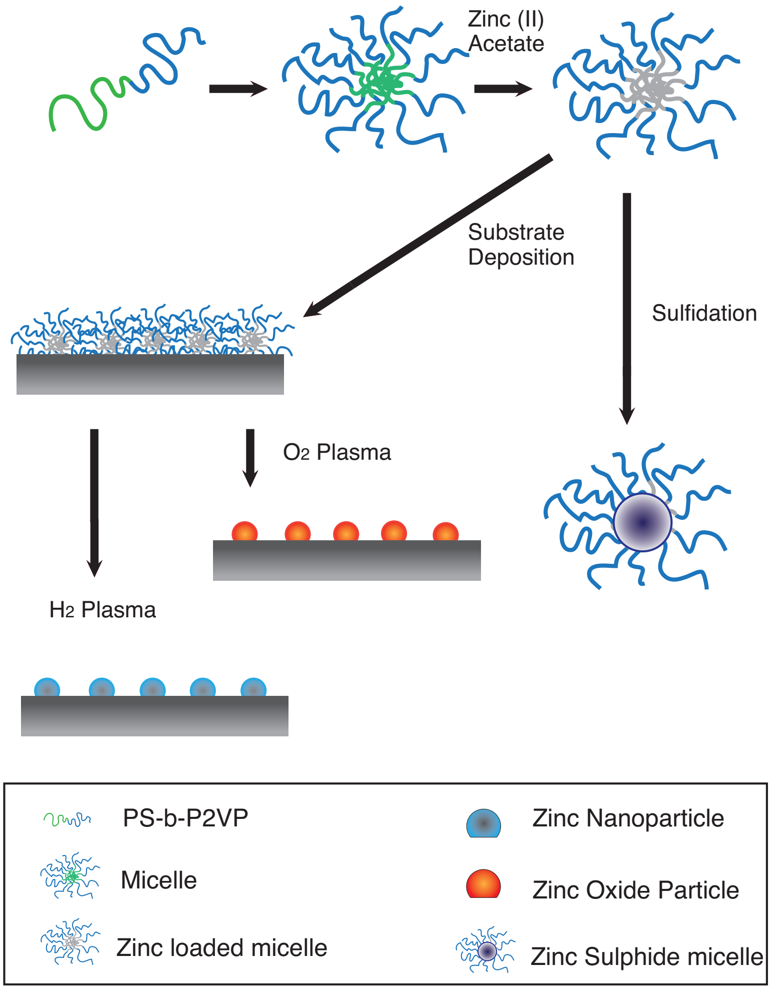

Figure 5.4.1: Schematic of polymer templated zinc micelle formation. Zinc loaded micelles can be used to produce a range of nanoparticles including noble zinc, zinc oxide, and zinc sulfide.

Micelles were loaded with zinc ions using a zinc acetate salt that was pre-dissolved in minimal amounts of propanol. Zinc acetate was chosen over other common zinc salts (such as zinc chloride, or zinc nitrate) due to its solubility in organic material, enabling it to be dissociated in organic solvents, and therefore giving the zinc ions the ability migrate to the micelle core. Additionally, the use of a zinc salt with an organic negative ion ensures precipitation of coordinated ions in solution or on the nanoparticle array surfaces is not induced, as the organic acetate group can be degraded similarly to the polymer micelle during plasma treatment. The exact loading conditions are described in the Materials and Methods section, and the rest of this chapter describes fabrication of zinc based materials from this zinc-loaded precursor micelle.

5.4.2 Zinc Sulfide Particle Formation

PS-b-P2VP polymer micelle templates were used as nanoreactors for zinc sulfide nanoparticle formation. ZnS was synthesised by exposing zinc loaded micelles to H_2S gas (Figure 5.4.2) facilitating the formation of a group II-VI compound particle.

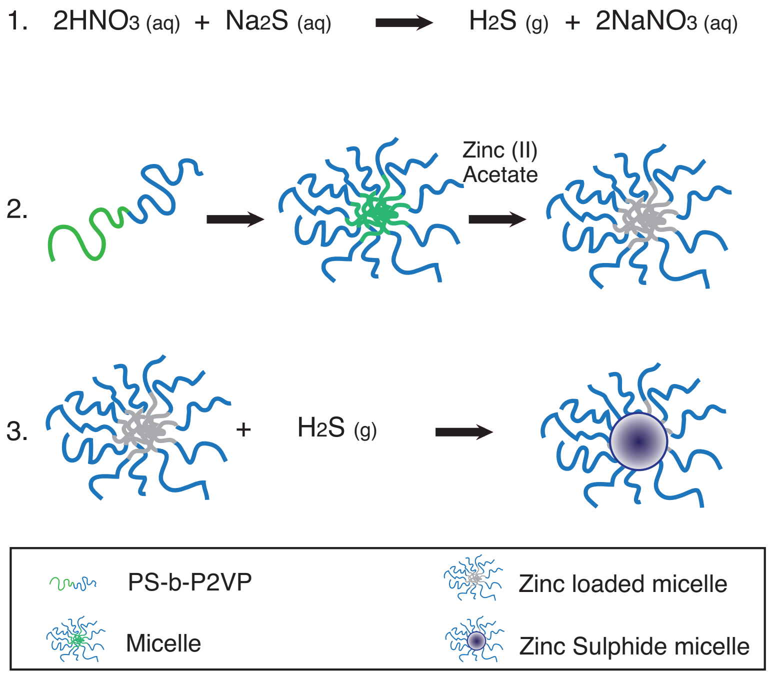

Figure 5.4.2: Zinc sulfide particle formation; H_2S is generated in situ and chemically combined with zinc loaded micelles to fabricate ZnS particles inside the micelles.

Analysis of the solution by TEM indicated that particles had been formed, (Figure 5.4.3) and that these were well distributed throughout the suspension. A more detailed investigation of the particles indicated that particle diameter was 18.8nm +- 0.14nm, however each particle possessed a complex structure.

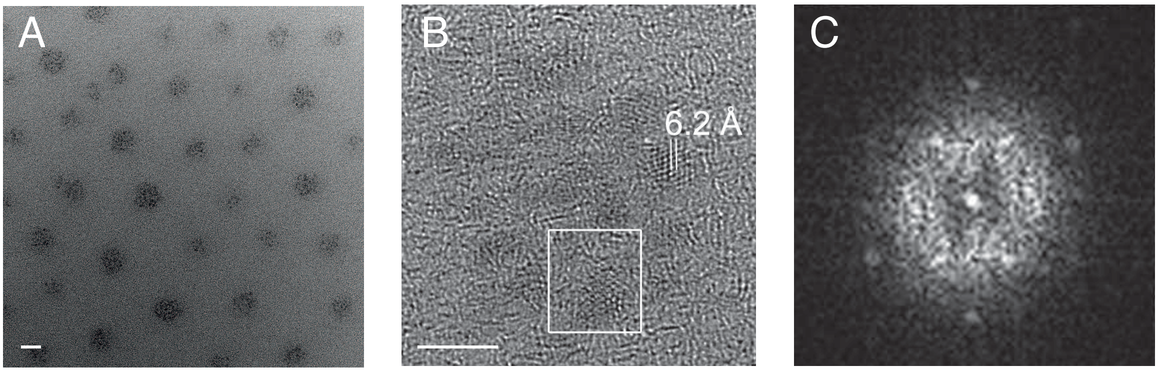

Figure 5.4.3: Nanoparticles produced by sulfidation were examined by TEM. Figure A) samples made by Derfogail Delcassian, imaged by Lucia Podhorska and Dr. Angela Goode, scale bar 20nm. B,C) samples prepared by Derfogail Delcassian, TEM imaging and FT image by Dr. Angela Goode, scale bar 10nm. Boxed region displays inset FT.

Individual particles, approximately 18.8nm in diameter, were each composed of several smaller nanoparticles measuring approximately 5nm across. The complex particles shown in Figure 5.4.3(B) are ellipse in shape, and composed of smaller crystalline units with distinct lattice fringes. Figure 5.4.3(C) indicates a typical Fourier Transform of the nanoparticle region of the image; the well-defined lattice points indicate a crystalline material whilst the broad diffraction ring suggests amorphous material is also present in these particles. To determine the elemental composition, EDX Analysis (Figure 5.4.4) was performed on particles and equivalently sized background areas using a narrow beam in TITAN STEM mode.

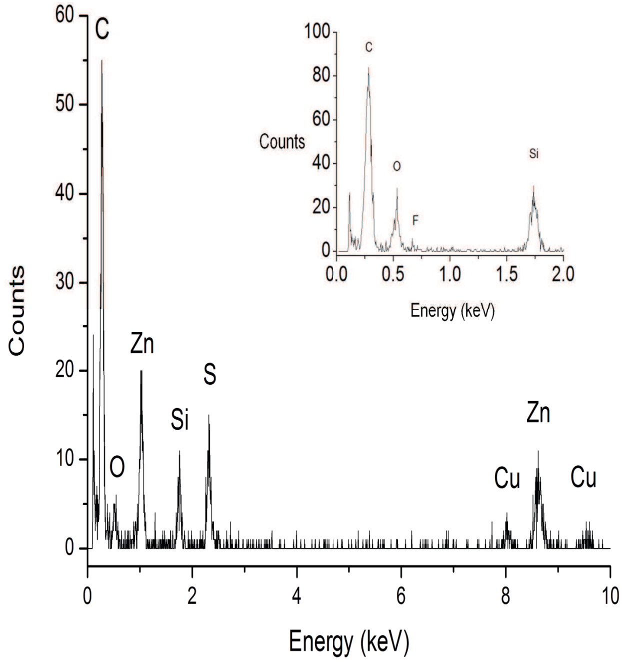

Figure 5.4.4: EDX analysis. Counts and eV values are shown for a single particle (main image) and background area (inset). EDX analysis performed on samples made by Derfogail Delcassian by Dr. Angela Goode and Lucia Podhorska.

Comparative evaluation of background areas and the nanoparticle itself indicate the presence of elemental zinc and sulfur in the particle; these elements are present at a 1:1 ratio, which is expected for ZnS material. This confirms that trace oxygen has been eliminated from the reaction set-up, and that zinc oxide nanoparticles, which could be formed from oxygen contaminants combining with chelated zinc, have not been formed. The presence of trace elements such as oxygen, silicon and copper are attributed to contaminants in the TEM grid. The lattice fringe spacing in the crystallites confirms the particles are made of ZnS material. The small crystalline domains exhibit dominant lattice fringes of 0.32nm, in good agreement with the literature values of 0.31nm, confirming the presence of ZnS in (111) orientation and Sphalerite zinc sulfide crystal structure.[437, 438, 439] Interestingly, a lattice fringe of 0.62nm is also seen, which could suggest the (001) plane of Wurtzite ZnS is also present in this compound nanocrystal.[419] In order to confirm the exact crystal structure and ratio of nanodomains of each of these phases, Synchotron X-Ray diffraction could be employed.

The compound nature of the nanoparticle, with ZnS material in both crystalline and amorphous phases, implies a complicated nucleation takes place at the micelle core. Figure 5.4.3(A) demonstrates that the nanoparticles are well separated from each other, additionally, they have a relatively narrow size distribution with an average diameter of 18.8nm. This indicates that the particle growth is constrained in some way, most likely at the micelle core due to pyridine-zinc chelation. Small Angle Neutron Scattering (SANS) analysis was used to determine the radius of the polymer micelle core, measured at 10nm, and the ZnS nanoparticle radius was analysed using Small Angle X-Ray Scattering (SAXS) at 14nm. (Appendix C) Although the SANS results indicate a core structure size that correlates well with the particle size seen here, there is some discrepancy in nanoparticle size as measured by TEM or SAXS. This may be due to sample preparation, batch to batch variability, or could be due to post synthesis particle "ripening" and growth described in other systems. [440, 441, 442, 443, 444]

There is good correlation between the average particle size as measured by TEM (Figure 5.4.3) and the SANS core diameter measured at 10nm; we expect the particle size to be closely associated with the core diameter due to the complexation of the Zn^{2+} ion with the poly-2-vinylpyridine units in the micelle core. Polymers with different PS-b-P2VP lengths were therefore used to investigate the relationship between polymer template size and ZnS nanoparticle size (Figure 5.4.5, 5.4.6).

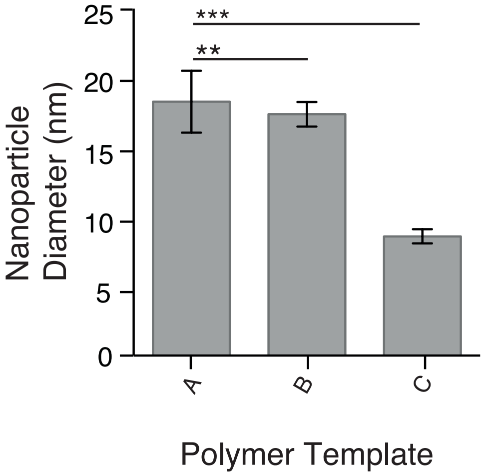

Figure 5.4.5: The effect of polymer templates on average zinc sulfide nanoparticle size, measured by TEM. All samples were prepared by Derfogail Delcassian, particles produced were imaged by Derfogail Delcassian and Giovanni Luongo (A, B) or Lucia Podhorska and Dr. Angela Goode (C) by TEM. Size analysis of particles was performed by Derfogail Delcassian in all cases. Polymer repeat units are $PS_{(x)}$-b-$P2VP_{(y)}$(A) x=52000, y= 31500 (B) x=32000, y= 12500 (C) x=16000, y= 3500. Where (A, B) are average values measured from a single manufacture, and error bars show a standard error in the mean, (C) is the average of the mean of two separate manufactures. Statistics: *** $p< 0.001$, **$p<0.01$, * $p<0.05$

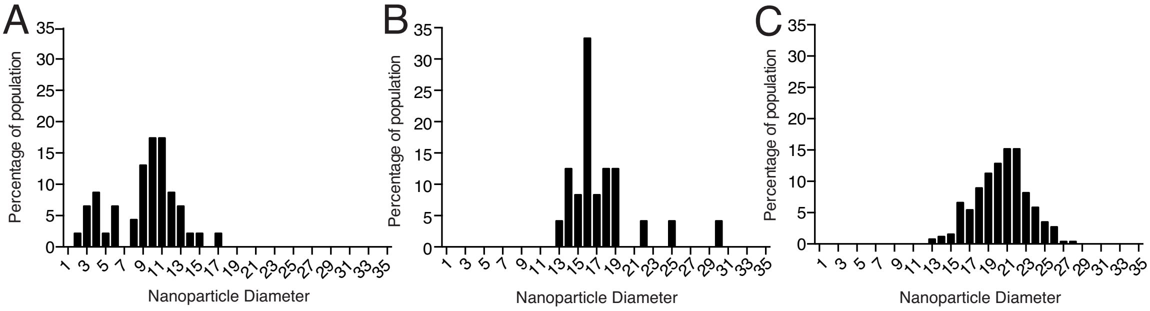

Figure 5.4.6: The effect of polymer template on nanoparticle size distribution. Graphs show histograms of nanoparticle diameter distribution within one sample at each molecular weight, polymer repeat units are $PS_{(x)}$-b-$P2VP_{(y)}$ (A) x= 16000, y= 3500 (B) x= 32000, y= 12500 (C) x= 52000, y= 31500. All samples were prepared by Derfogail Delcassian, particles produced were imaged by Derfogail Delcassian and Giovanni Luongo (A,B) or Lucia Podhorska and Dr. Angela Goode (C) by TEM. Size analysis of particles was performed by Derfogail Delcassian in all cases.

Figure 5.4.5 shows that different micelle templates can be used as nanoreactors to produce significantly different ZnS particle sizes, with a longer poly-2-vinyl pyridine block the ZnS particle is larger. This supports the assumption that particle nucleation and growth is constrained to the micelle core. Although the sizes of nanoparticles synthesised inside $PS_{(52000)}$-b-$P2VP_{(31500)}$ and $PS_{(32000)}$-b-$P2VP_{(12500)}$ polymer templates appear similar, the size distribution (Figure 5.4.6) of each population is different, and the average particle size is significantly different. Each micellar template can therefore produce a narrow range of particle sizes, for which the average particle diameter is distinct. The range in particle sizes may be attributed to small local variations in the micellar structure.

Separately, the ratio of zinc ions to 2-vinylpyridine units was also varied within one polymer template (Figure 5.4.7) to investigate the effect of ionic loading on nanoparticle size.

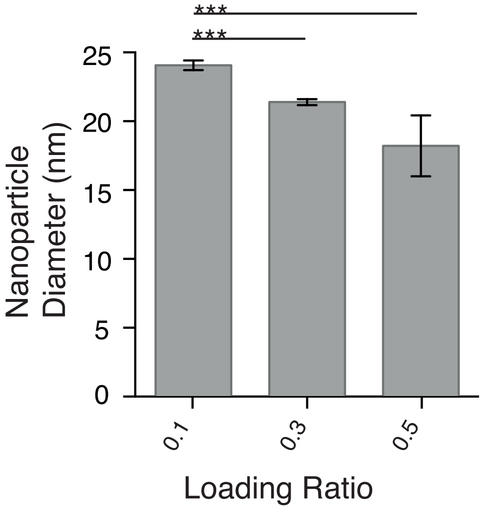

Figure 5.4.7: $PS_{(52000)}$-b-$P2VP_{(31500)}$polymer was used to template zinc ion chelation, where zinc ion loadings were varied from 0.1 to 0.5 zinc moles per 2-vinylpyridine unit. All micelles were then exposed to the same ZnS fabrication methodology, samples were prepared by Derfogail Delcassian and Lucia Podhorska, particles produced were imaged by Lucia Podhorska and Dr. Angela Goode by TEM. Size analysis of particles produced was performed by Derfogail Delcassian. Where (A, B) are average values measured from a single manufacture, and error bars show the standard error in the mean, (C) is the average of the mean of two separate manufactures, with a comparative sem. Statistics: *** $p< 0.001$, **$p<0.01$, * $p<0.05$

Figure 5.4.7 illustrates the effect of ionic loading ratio on nanoparticle size. There appears to be an inverse relationship between particle size and ionic loading; as the ratio of zinc ions to pyridine units decreases, the particle size increases. This is counter intuitive; we could expect that adding more zinc ions to the polymer core would result in a larger particle size. An explanation for this can be found in changes that occur within the micelle on addition of zinc ions. As block copolymer micelles complex ions, there is a change in the charge density of the polymeric template. This change in charge density can affect the micellar solubility and therefore size of the micelle in organic solvents.[205, 222] As the overall micelle size changes, so too does the core size, resulting in a differently sized nanoreactors for the formation of ZnS particles at various ionic loadings.

To test this, $PS_{(52000)}$-b-$P2VP_{(31500)}$ polymer micelle sizes were examined as a function of zinc ion loading (Figure 5.4.8) by Dynamic Light Scattering (DLS). Figure 5.4.8 confirms that as ionic loading is increased, the hydrodynamic diameter of the micelle formed decreases, and therefore we could expect the micellar core size to also be smaller. There is a complex interplay between ionic loading, micellar size, and nanoparticle formation. It is likely that addition of zinc ions at different ratios causes the micelles to alter their structure, and therefore the size of the core of the micelle is also changed, giving rise to alterations in nanoparticle size with ionic loading. An additional complication is in the nature of the particle being formed; different ionic loadings, which cause altered core structures, may also interact with the H_2S gas to produce different particle compositions and sizes.

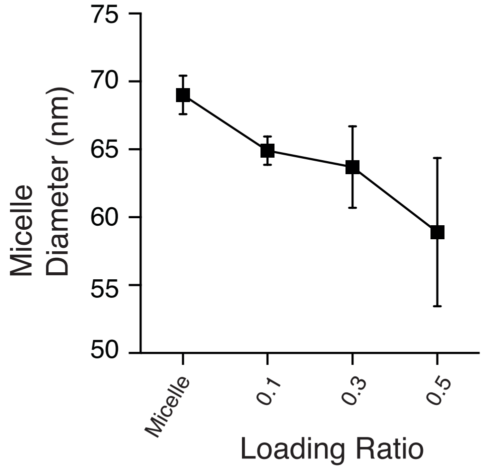

Figure 5.4.8: Dynamic Light Scattering (DLS) was used to measure the diameter of micelles in solution after loading with different zinc ion ratios.

The effect of varying the polymer template on the substructure of the nanoparticle formed was investigated by TEM (Figure 5.4.9). The smaller micellar templates also produced well-dispersed nanoparticles (Figure 5.4.9(A)), which measured under 10nm in diameter. These small particles appear to be made of closely packed crystalline domains (Figure 5.4.9(B)) which are sized at approximately 5nm (Figure 5.4.9(C)). The formation of multiple small 5nm crystallites inside a composite nanoparticle here, compared to those produced within larger polymer templates, hints at a common mechanism of formation.

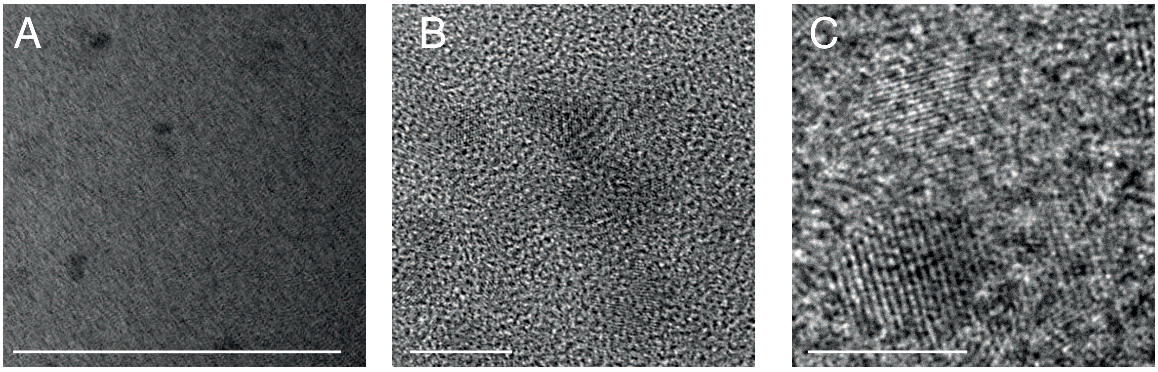

Figure 5.4.9: TEM of nanoparticle substructure from ZnS produced inside polymer templates ($PS_{(16000)}$-b-$P2VP_{(3500)}$). All samples were prepared by Derfogail Delcassian, particles produced were imaged by Derfogail Delcassian and Giovanni Luongo by TEM. Analysis of particles produced was performed by Derfogail Delcassian. Scale bars 50nm, 10nm, 5nm.

The fabrication of ZnS through these polymer template methods seems to produce unique nanoparticles where zinc sulfide exists in small crystalline domains surrounded by an amorphous matrix. Although no composite particles of this sort have been described in the literature, there is some evidence for mixed nanoparticle phases being co-created in other synthesis methods; separate nanoparticles of between 2-3nm were formed in each crystallite phase in CdS synthesis [445] and in ZnS generated in thiolate cages. [345] Here, it is likely that the encapsulation of the zinc provides a unique nanoreactor allowing the nucleation of distinct phases. It would be interesting to define the nature of the nanocomposite at different ionic loadings, to determine if it is the local ionic concentration of zinc that drives formation of different phases, which is normally controlled by temperature.

5.4.3 Optical Properties of Formed Particles

The optical properties of the ZnS particles were examined by UV-Vis absorption and Fluorescence emission (Figure 5.4.10). As the organic solvent and polymer itself display some absorbance in the UV range, background traces were subtracted.

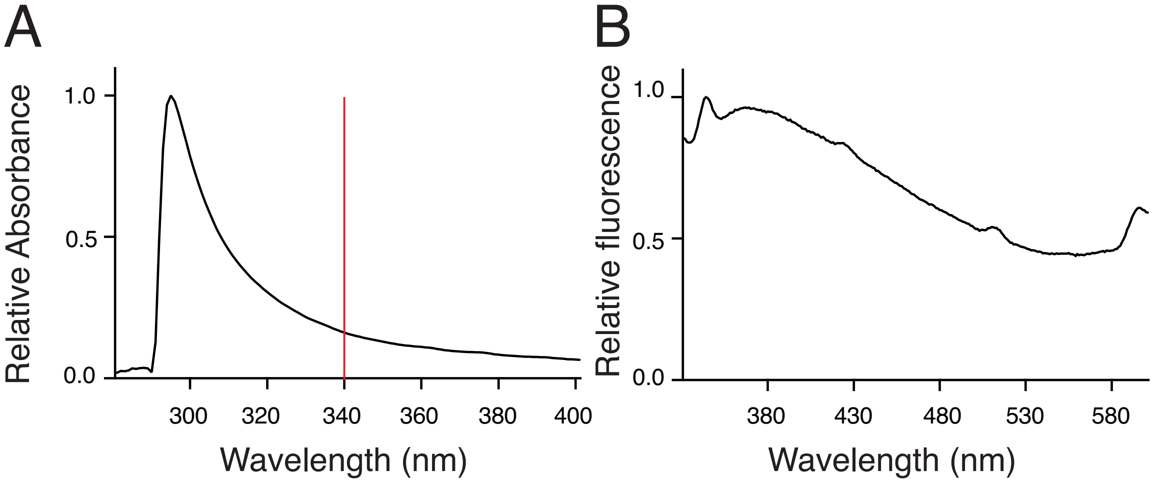

Figure 5.4.10: Optical properties of ZnS particles formed inside $PS_{(52000)}$-b-$P2VP_{(32100)}$ polymer micelles were examined by (A) UV-Vis absorption and (B) fluorescence excitation at 311nm. The onset of bulk absorption by ZnS material (of optical band gap 3.65eV) is shown by the red line in (A).

Figure 5.4.10(A) shows typical UV Visible absorption traces for these particles; the spectra are blue-shifted, where the maximal absorption is at a shorter wavelength than the standard 340nm peak of bulk ZnS material. This indicates that the ZnS material is constrained on the nanoscale, as the typical UV-Vis trace has moved to a shorter wavelength (and so higher energy) region of the spectra. The UV-Vis of nanoparticles produced within different micellar templates are similar (data not shown), and broadly consist of an onset absorption edge at 290nm, and absorption has largely fallen to background levels by 320nm. Using these values we can calculate the optical band gap (Equation 5.4.1) of these nanoparticles.

$$E = hc/\lambda, \tag{5.4.1}$$

where E= Energy of the transition, h= Planck's constant, c= the speed of light and λ= the wavelength of the absorption edges.

Using typical values for these nanoparticles, we calculate the optical band gap of these particles lies between 4.28eV (onset absorption of 290nm) and 3.88eV (absorption edge 320nm), above the expected bulk value of 3.65eV.[446, 447, 448, 449]

The photoluminescence spectra in Figure 5.4.10(B) represent both the different types of material in the nanocomposite crystallite and the range of intrinsic bad gap energies present in the ZnS nanoparticle. Excitation produces multiple emission peaks in the traces shown, which could reasonably be assigned as follows; the luminescence peak at 520nm is likely due to recombination of electrons in the amorphous material with holes in the surface of the ZnS crystalline species, or defect recombination, previous work has assigned this to elemental sulfur contaminants in ZnS nanobelts,[450, 451, 452] whilst the peak at 450nm could be due to recombination of electrons in the conduction band with holes on the surface,[453] and a band at around 360nm has previously been assigned to UV excitonic emission in ZnS nanowires.[454, 455, 456, 419]

Additionally, it may be that the exact nature of the spectra is dependent on the number and nature of the nanocrystallite domains within the particle. TEM has indicated ZnS particles produced inside different templates each contain small crystallite domains of around 5nm. It is possible that the optical properties are driven by these crystallites, explaining the similarity of the UV-Vis traces independent of polymer template and overall nanoparticle size. Interesting further work lies in the characterisation of the crystallisation of composite nanoparticles inside micellar templates, and an investigation into the full optics of these particles. The optical data shown here help to support the conclusion that we have formed ZnS particles with nanoscale dimensions.

5.4.4 Nanoarrays of zinc-based materials

One of the prime motivations for studying the formation of ZnS particles inside of micellar templates is to facilitate the fabrication of nanoarray materials that are complementary to gold. Earlier, we discussed the functionalization of gold nanoparticles with thiolated molecules (Chapter 4: Biomimetic gold nanopatterns). Here, the long-term aim is to functionalise zinc sulfide particles with histidine tagged proteins, and zinc oxide could also be selectively functionalised with phosphate ligands. If these functionalization methods are orthogonal, it may be possible to present mixed nanoparticle array surfaces with distinct functionalization. A prerequisite to these studies is the fabrication of zinc-based nanoarrays.

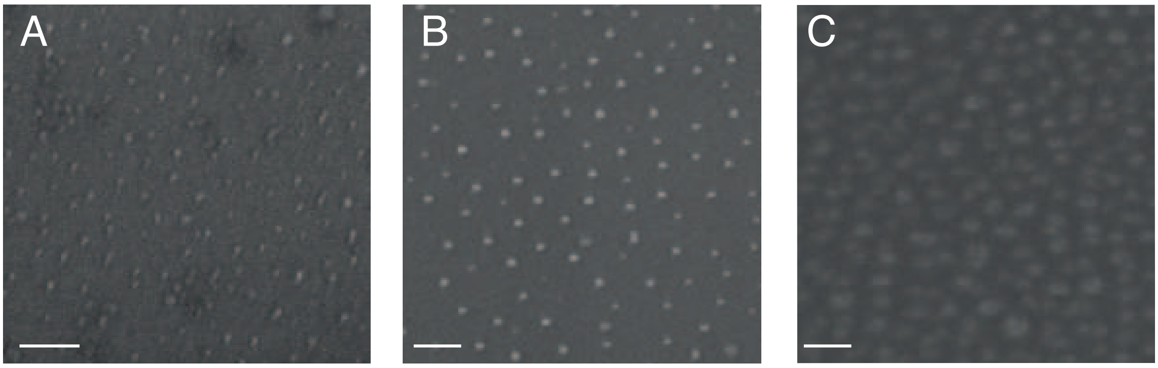

Figure 5.4.11: SEM images of nanoparticles produced by plasma treatment on silicon surfaces. Plasma treatment is expected to have produced (A) zinc particles, (B) zinc oxide particles and (C) zinc sulfide particles encapsulated within polymer templates. Scale bar 100nm in all cases.

Zinc loaded micelles can be deposited on substrates in an analogous way to the gold micellar deposition method, discussed extensively in Chapter 4. Plasma conditions determine the type of particle produced; environments favouring chemical reduction will most likely produce zinc nanoparticles whilst oxidising conditions will produce zinc oxide particles. Additionally, ZnS compound particles can be exposed to reducing plasma conditions in order to remove the polymer shells and leave nanoparticle arrays. The exact nature and surface chemistry of the exposed particle post-plasma treatment has not been verified, it is possible some degradation of the particle occurs under these conditions, and also possible that on re-exposure to air, the zinc particles may partially or completely oxidise.

Advanced substrates, which are patterned with various materials, can be prepared through more complex micellar lithography (Figure 5.4.12).

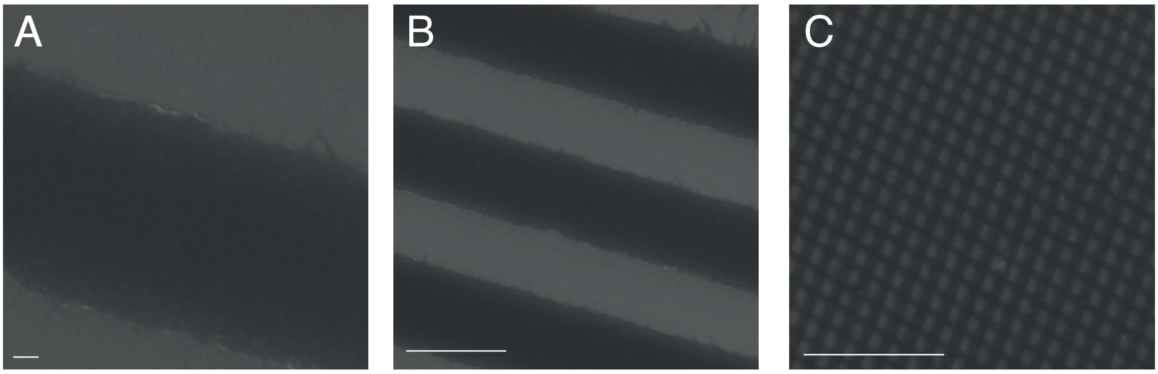

Figure 5.4.12: SEM images of advanced nanopatterning with zinc acetate loaded micelles. Microcontact printing was used to deposit stripes of zinc acetate loaded micelles approximately 600nm wide. (A, B) zinc acetate micellar stripes- dark areas indicate succesful micelle transfer. (C) Latticed gold micelles, with micelles of two dimensions being printed in opposite directions, shown in Chapter 4. Scale bar 100nm, 1μm, 10μm

Figure 5.4.12 shows surfaces with nanoscale stripes of ZnAc loaded micelles, fabricated by micro-contact printing. These simple unidirectional lines of zinc loaded micelles could be latticed with other zinc materials in an analogous way to the earlier described gold micelle micro-contact printing technique (Figure 5.4.12(C)). A further advancement of this technology would involve the latticing of different materials, where stripes of gold particles could be printed in one direction, and zinc-based particles in the other direction. The surfaces presented here offer additional versatility in nanopatterned interfaces for cellular studies.

5.5 Conclusions

We have chelated zinc salts to polymer micelle cores to produce a zinc loaded precursor micelle capable of producing zinc, zinc oxide, and zinc sulfide nanoparticles. The zinc sulfide particles generated inside micellar cores are the first single, non agglomerated particles to be produced and their size can be controlled by selection of an appropriate polymer template. Confirmation of the production of nanoscale ZnS material comes from lattice fringe spacings identified in TEM, and EDX analysis of the elemental ratio of the particle components. The optical properties and calculated band gap further confirm that the particles generated are ZnS, which is confined on the nanoscale and so can be termed a quantum dot. Additionally, these particles possess a unique composition, with nanoscale domains of crystalline ZnS material embedded in an amorphous ZnS matrix.

We have also produced planar nanoparticle arrays with distinct synthesis conditions designed to fabricate zinc, zinc oxide or zinc sulfide nanoparticles with good order and controllable inter-particle spacing using the block copolymer micellar lithography technique. Finally, we have demonstrated that advanced micellar lithography is capable of producing bi-functional well-ordered nanoarrays, which can be extended to mixed zinc and gold interfaces with micropatterned features.

5.6 Future Work

The interesting properties of the zinc sulfide particles produced offers potential for extensive future work. The formation of multiple domains of distinct crystalline phases should be investigated; the experiment could be repeated at different temperatures to determine if distinct nanoparticles containing the separate phases can be produced under their preferred conditions. Additionally, the nucleation of these phases should be investigated in terms of both kinetics and the loading ratio or local concentration of zinc ions.

Although the optical properties indicate that these particles are confined on the nanoscale, further work could characterise the optical properties on exposed nanoparticles without polymer capping agent. By depositing the particles on a surface, and removing the polymer through plasma treatment as shown, the surface bound QDs could be investigated in more detail. Furthermore, the fabrication of nanoscale ordered arrays of single quantum dots could have many applications, including in the optoelectronic industry, and even for use as a tool to aid super-resolution microscope calibration.

For cellular studies, it will be important to prove that these nanoparticles are capable of binding biomolecules, either phosphate tagged (such as DNA sequences) or histidine tagged (such as recombinant proteins) as described in similar systems.[405, 229, 399, 211, 398, 406] Additionally, the stability of the ZnS particle for the duration of cellular studies would need to be verified; currently ZnS is used commercially to stabilise other materials, such as core-shell quantum dots used for cellular studies, and so we would expect it to be relatively stable for these applications. [405] However, some particle growth has been observed in other fabrication systems and so it will be important to verify the ZnS stability over time. [440, 441, 442, 443, 444]

Orthogonal functionalization using these selective binding mechanisms could also be investigated. Finally, it will also be important to test the biocompatibility of these nanoscale materials before they can be used as robust tools for *ex vivo* activation investigations.

Chapter 6

NK cell stimulation with ligand nanoarrays

Nanoscale ligand geometries in the innate immune system: NK cell response to CD16 engagement with anti-CD16 and Rituximab

6.1 Introduction

The control of viral infection and tumour growth restriction is mediated, in part, by NK cells.[457, 244, 232, 458, 459] These innate immune cells express a wide variety of cell surface receptors[245] and cause cytotoxic effects on target cells, including cellular degranulation and cytokine secretion,[460, 461, 462, 463] discussed extensively in Chapter 2.

Although NK cells are traditionally classified as innate immune cells,[230, 231, 232] they do present one cell surface receptor that occupies a unique position at the interface of adaptive and innate immunology. The NK cell surface receptor CD16, also known as the low affinity IgG FcγRIIIA receptor, engages with the Fc portion of antibodies bound to target cells.[262, 264, 253] Here, the NK cell acts as an effector for B lymphocytes of the adaptive immune system, that have targeted these cells for destruction. The target and NK cell are brought into close contact by this engagement, inducing a signaling pathway in the NK cell termed “Antibody Dependant Cellular Cytotoxicity” (ADCC)[36, 253, 264, 262, 245, 247, 266] which results in destruction of the engaged target cell through secretion of enzymes, shown schematically in Figure 6.1.1.

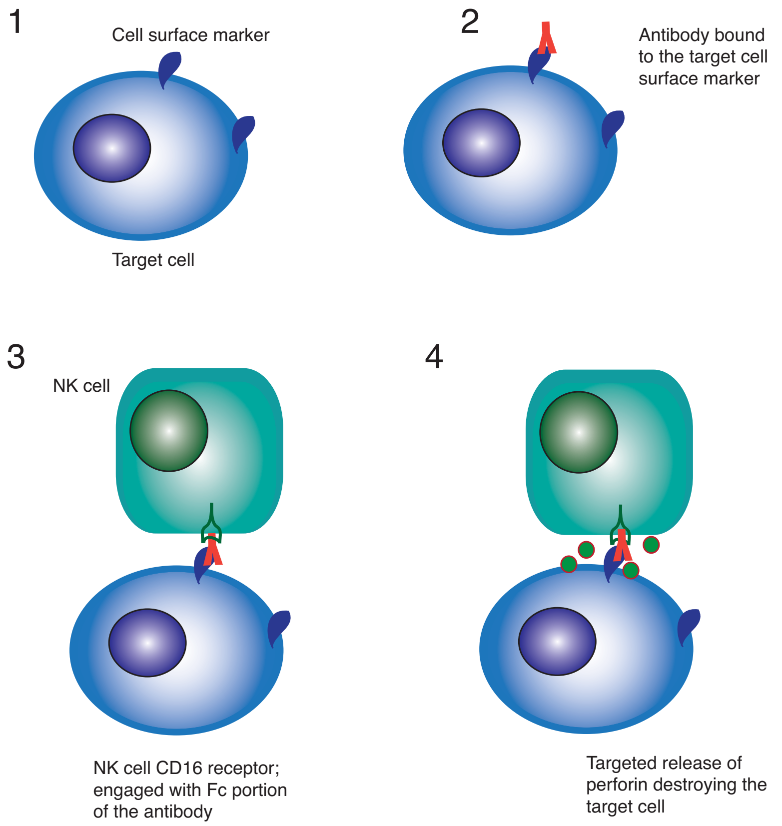

Figure 6.1.1: Schematic of NK cells encountering a labeled target cell, and ADCC being induced by engagement of the NK cell surface CD16 receptor.

The unique role of this pathway has led to development of a range of designer antibodies for cancer immunotherapy applications.[464, 37, 465, 466, 39, 458] Antibodies against specific cell surface receptors or disease markers can be used to induce NK derived ADCC on target cell types. A potent example of this is found in Rituximab, a chimeric monoclonal antibody which binds to the CD20 surface marker on B cells, and is used to induce ADCC in B cell lymphocyte lymphomas.[465, 464, 305, 264, 36] Rituximab is a type I anti-CD20 mAb, known to redistribute target cell surface CD20 into clusters, thought to be due to coalescence of membrane lipid rafts.[305, 302]

Recent work has identified that Rituximab also “caps” one surface of B cells, leading to the recruitment of ICAM-1 and moesin at the NK-target synapse,[35] and that this polarisation augments the therapeutic effect. In other cells types the ERM proteins moesin, exrin and radixin are known to have an important role in cell surface lateral receptor mobility[467, 468, 469, 470], and interestingly it has been shown that movement of lipid rafts and lipid raft conjugation have a role in controlling NK responses.[471, 314] NK cells Immune Synapses (IS) possess CD16 microclusters,[472, 265] however CD16 microcluster mobilisation is thought to be dependent on the small adaptor protein Crk.[472] Taken together, these studies suggest that one effect of Rituximab may be to drive the clusters of CD20 on target cells close together, perhaps through the action of moesin (which has been shown to assist movement of cell surface receptors in other cell types and is known to redistribute to the target synapse on Rituximab tagged target cells[35, 467, 468, 469]) or through other, as yet undefined, mechanisms.

The microscale organisation of proteins at the immune cell- target cell interface into distinct substructures has been shown in several immune cell types, including NK cells,[311, 25, 254, 312, 261, 316, 297] T cells [473, 21, 334, 290, 323, 288, 276] and B cells[470, 307]. Altering the microscale organisation of receptors and proteins at the Immune Synapse (IS) can be used to direct different levels of immune cell activation in both NK cells[474] and other immune cells,[21, 299] discussed extensively in Chapter 2.

The evidence supporting the congregation of Rituximab molecules on areas of target cells, and the known importance of the microscale organisation of the immune synapse on cellular activation levels leads to an important question. Is the therapeutic effect of Rituximab mediated by the proximity of Rituximab molecules (and therefore CD16 receptor molecules) to each other on the target cell surface? In order to test this, we fabricate biomimetic nanopatterns by Block Co-polymer Micellar Lithography (BCML- described in detail in Chapter 4 [362, 205, 204, 203]) functionalised with CD16 ligands, that can engage with NK cells to form an artificial immune synapse.

This chapter describes the functionalization of gold nanoparticles with inter-particle spacing between 25-104nm with Rituximab or anti-CD16 antibodies and the cellular responses to these surfaces, to present the first studies investigating innate immune responses to nanopattern ligand engagement.

6.2 Contribution statement

The work reported in this chapter was supported by the following people;
NK cell separation, culture and incubation were performed by Dr. Dominika Rudnicka. Cell fixation, staining and imaging was performed by both Derfogail Delcassian and Dr. Dominika Rudnicka.

6.3 Materials and Methods

6.3.1 Fabrication of nanopattern arrays

As described in detail in Chapter 4: Biomimetic Gold Nanopatterns. Briefly, poly(styrene-*block*-2-vinyl pyridine) (Polymer Source, Montreal, Canada), of varying molecular weight and styrene to 2-vinyl pyridine ratio depending on the nanopattern spacing required, was dissolved in p-xylene (99.0%, VWR, Radnor, P.S., U.S.A.)) and stirred for at least 12 hours. Gold (III) chloride trihydrate (Sigma Aldrich, St Louis, M.O., U.S.A.) was then added at 0.1 – 0.5 molar ratio to the total amount of 2-vinyl pyridine units and left to stir for another 24 hours to generate micelles with gold-loaded cores. Glass substrates were cleaned by immersion in a 1:3 v/v mixture of hydrogen peroxide 30% solution (VWR) and concentrated sulfuric acid (95%, VWR) for at least 2 hours, before rinsing in ultrapure water (18.2 MΩ). Substrates were coated with a monolayer of gold-loaded micelles by dip-coating using a home-built setup with a retraction speed of 0.36 mm/s. Gold nanosphere arrays were generated from these micelle-coated substrates by exposure to a hydrogen/argon plasma (10% hydrogen, 0.4 mbar, 350 W) in a plasma etcher model name (PVA TePla, Kirchheim, Germany). Sample nanoarrays from each batch were characterised by SEM (Leo Gemini at an EHT 5-10kV), after sputter-coating with a thin layer of carbon. Mean and standard deviation spacings were calculated by measuring a representative number of nearest neighbors.

6.3.2 Functionalisation of nanopatterned array.

Nanopatterns were cleaned immediately before use by exposure to UV-ozone (10 minutes, Procleaner Plus, Bioforce Nanoscience, Ames, I.A., U.S.A.), and an 8-well flexible chamber insert (PDMS, Sarstedt, Nuembrecht, Germany) was immediately affixed. To passivate the glass background against non-specific protein adsorption, wells were incubated with either poly(L-lysine) – graft – poly(ethylene glycol) (PLL-g-PEG) (PLL(Mw = 20kDa) grafted with an average of 3.5 chains of PEG(Mw = 2 kDa) chains, SuSOS, Zurich, Switzerland) or PLL-g-PEG-biotin (same with 51% of PEG chains biotinylated at free end, SuSOS, Zurich, Switzerland) at 1 mg/ml in PBS for 1.5 hours. Surfaces were rinsed with PBS and incubated with relevant biological ligands, with further PBS-rinsing after each step. NK-stimulating nanoarrays were produced by first functionalising PLL-g-PEG passivated gold nanoarrays with biotin-thiol (2 mM in ethanol, 2 hours incubation, HS-C11-NH-C(O)-Biotin, ProChimia, Sopot, Poland) followed by tetravalent streptavidin (Life Technologies, 0.1 mg/ml in PBS, 2 hours incubation) or bi-valent streptavidin (gift of Mark Howarth, University of Oxford, 0.1mg/ml in PBS, 2 hours incubation). NK cell-stimulating antibodies Rituximab (Rituxan, Roche, Basel, Switzerland)) and 3G8 (BD Biosciences, Franklin Lakes, N.J., U.S.A.) were biotinylated using EZ-link NHS-PEG$_{(4)}$Biotin (Thermo Scientific, Waltham, M.A., U.S.A.) kit, and purified using a centrifugal filter with 50 kDa cutoff (Millipore, Billerica, M.A., U.S.A.) and incubated with streptavidin-functionalized nanoarrays (Rituximab, 10 µg/ml, PBS, 1-2 hours, 3G8, 5 µg/ml, PBS, 1-2hours). To generate a cell-adhesive poly (L-lysine) (PLL) background, the PLL-g-PEG was then displaced by incubation with a PLL solution (Mw = 150 – 300 kDa, Sigma Aldrich, 0.1% in PBS, 30 minutes). PLL controls were prepared by incubating glass slides as described; glass slides were incubated with passivation agent PLL-g-PEG for 1.5 hours as described, before the surface was treated with the PLL solution to displace PLL-g-PEG. For verification, 488-3G8 (Invitrogen, 1/100 in PBS) was attached as above, and functionalised surfaces examined by an Olympus 1X51 microscope with DP70 camera.

6.3.3 Protein Structures

Protein crystal structures were obtained from the European Protein Data Bank and projected using PyMOL. (Specific protein structures used: Streptavidin (1mk_5) Rituximab (1IGT) 3G8 (1IGY)).

6.3.4 Cellular experiments

NK cells were isolated by negative selection from leukocyte cones purchased from the UK National Blood Service or fresh blood using NK cell isolation kit (Miltenyi Biotec, Bergisch Gladbach, Germany). All fresh blood donors were healthy and provided informed consent for their blood to be used in accordance with the Declaration of Helsinki (ethics approved by The National Research Ethics Service, ref 05/Q0401/108). Purified NK cells were resuspended in Dulbecco's Modified Eagle's Medium supplemented with 10% human serum (Sigma Aldrich), 30% nutrient mixture F12, 2mM L-glutamine, 1x non-essential amino acids, 1mM sodium pyruvate, 50µM 2-mercaptoethanol, 50 U/mL penicillin, 50 µg/mL streptomycin (all Life Technologies), and 150 U/ml human recombinant IL-2 (Roche). Cells were allowed to rest for at least 5 days at 37 °C and 5% CO_2 before being used for experiments. Cells were incubated in biofunctionalised nanoarray wells for 6 minutes, immediately fixed with 4% PFA and permeabilized with 0.05% Saponin/PBS (Sigma Aldrich). Cells were stained with 2 U/ml phalloidin-AlexaFluor 488 (Life Technologies), and imaged using a confocal microscope (Leica SP5 RS) with a 63× water immersion lens (NA 1.2). Images were processed using FIJI with cell spread area measured in the surface plane. Spread areas were normalized per donor to non-patterned PLL surfaces and compared across multiple donors. Donors who showed no differential response to non-patterned 3G8-PLL versus plain PLL surfaces were discarded. Statistical testing used pair-wise comparisons between conditions, conducted using Mann-Whitney nonparametric tests in Origin (OriginLabs, Northampton, M.A., U.S.A.).

6.4 Results and Discussion

6.4.1 Functionalisation of nanoparticle arrays

As described previously in Chapter 4, gold nanopattern arrays with well controlled particle spacing were fabricated using Block Co-polymer Micellar Lithography. Spacings of the order of 10-100nm were fabricated, and typical surfaces are shown in Figure 6.4.1.

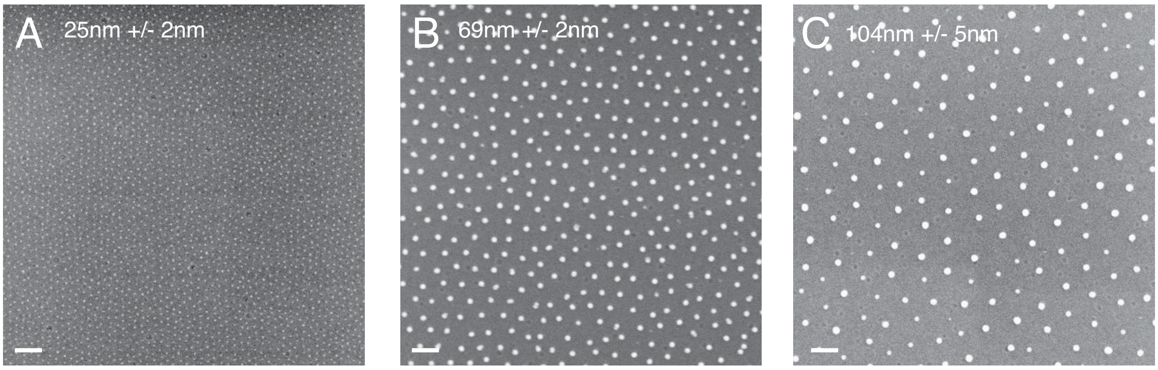

Figure 6.4.1: Gold nanopattern arrays. BCML was used to fabricate gold nanopattern arrays. SEM images and inter-particle spacing analysis is shown, with mean values and standard deviation. Panel (A) shown previously in Chapter 4. Scale bar 100nm.

In order to test the effect of stimulation of the NK cell surface FcγRIIIA receptor, functionalization of nanopatterns with both anti-CD16 and rituximab was desired. These antibodies are known to engage with the CD16 receptor in different ways; the anti-CD16 through its variable region, and the rituximab through its Fc portion. Selection of an anti-CD16 antibody which will only bind to the NK CD16 receptor through its variable regions, rather than its Fc portion, is possible by choosing an appropriate isotype. In this case, anti-CD16 with a mouse IgG$_{2a}$ was used which only binds to the human NK cell surface receptor through the bivalent epitope binding regions, shown schematically in Figure 6.4.2.

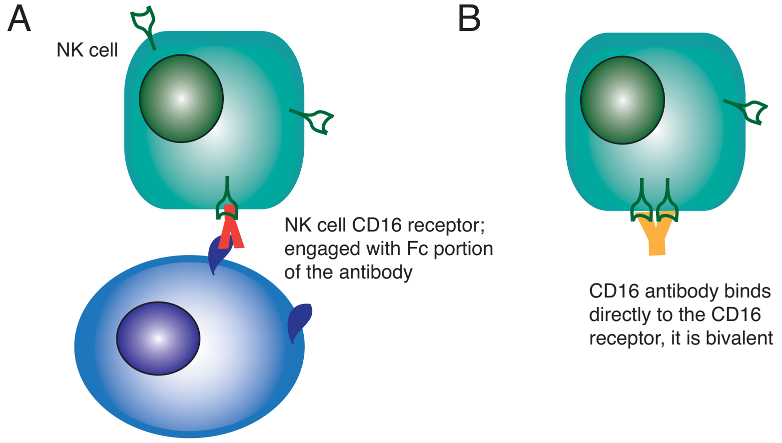

Figure 6.4.2: Schematic of NK cell surface receptor CD16 binding. (A) Target cell with Rituximab bound to the outside, and Rituximab engaging with the CD16 receptor through its Fc portion. (B) Anti-CD16 binding directly to the CD16 receptor through its variable regions. There are two variable regions per antibody, it can therefore bind to two closely spaced CD16 receptors on the NK cell surface.

Due to the different mechanisms, it was important to find a functionalization methodology that allowed both antibodies to be bound to the gold nanopattern similarly, yet also gave the antibodies flexibility to engage with the NK cell surface receptor on the substrate. Figure 6.4.3 shows a schematic of the binding process, where a small alkane thiolated biotin linker is bound to the gold nanoparticle, followed by the streptavidin and finally the biotinylated protein. As the biotinylation position on the protein is random, mediated by a short biotin linker bound to surface -NH2 groups, a range of orientations are possible, and therefore both methods of CD16 engagement are possible. The strong bonds based on the near-covalent chemisorption of thiol and disulfide groups to gold, and on biotin-streptavidin bonding, promise a stronger attachment than is given by the alternative NTA-histidine system.[211] CD16, unlike many other NK receptors, does not require a co-stimulatory agent in order to activate NK cells,[475, 311, 247] however adhesion between two cells is normally augmented by additional integrin binding.[466, 265] For these experiments, the protein resistant layer added during nanoparticle functionalization was displaced with poly(L-lysine) (PLL) to provide a non-stimulatory adhesive background layer.[476]

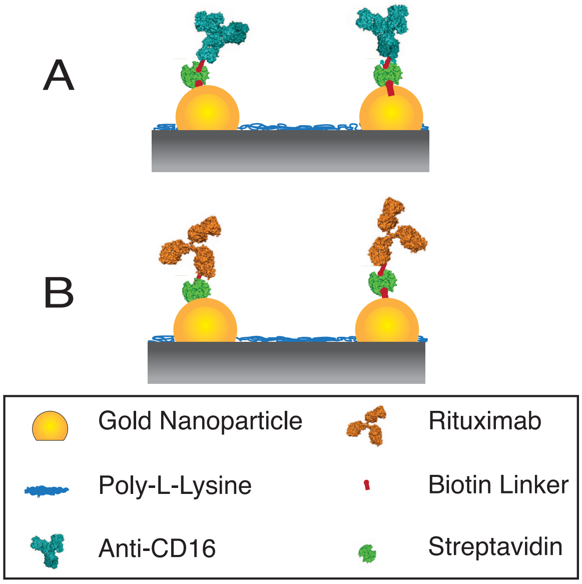

Figure 6.4.3: Schematic NK cell engaging surfaces. Gold nanopatterns are functionalised with (A) anti-CD16 or (B) Rituximab antibodies.

The functionalisation of the nanopatterns was tested using fluorescent anti-CD16 antibodies, (Figure 6.4.4) which showed surfaces with uniform coverage and bright fluorescent bands in regions of heavy gold deposition, indicating preferential binding to the gold particles. Note that whilst cellular studies are carried out on nanopatterned areas with uniform nanoparticle deposition, these regions of excess gold deposition are useful for visualising the preferential nature of the functionalisation.

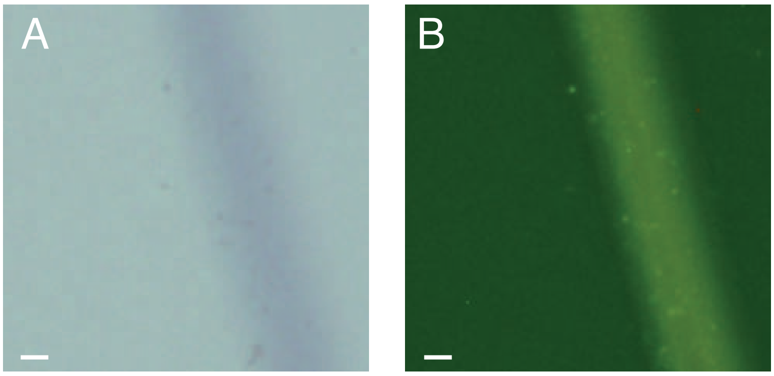

Figure 6.4.4: Fluorescent anti-CD16 binding. Binding of biotinylated proteins was performed using a fluorescently labeled anti-CD16 antibody. Binding is enhanced in the heavy gold deposition area. (A) Bright-field and (B) fluorescent channels show visible stripes of heavy gold deposition and enhanced binding, indicating preferential binding to the gold nanopattern regions. Scale bar 100µm.

The functionalized nanoparticle arrays were then used to probe cellular responses to nanoscale CD16 receptor engagement.

6.4.2 Cellular response to Fc engagement

As changes in the actin cytoskeleton are a marker of NK cell activation,[254] we measured actin specific cell spread area as an indication of cellular response to these surfaces. Actin rearrangement is one of the prerequisites of lytic synapse formation, and is required for lytic granule release.[254, 25, 477, 291, 474, 311] A comparison between planar surfaces functionalised with Rituximab or anti-CD16 indicated that although there was no significant change in the number of cells per unit area, (data not shown) the change in cell spread area was equivalent in both cases, (Figure 6.4.5) and significantly different to that on PLL adhesive surfaces alone. The significant increase in cell spread area when cells encounter activatory surfaces of Rituximab or anti-CD16 (cell spread area increase of 21.3% and 20.7% respectively) indicates that cells have redistributed their actin network to increase engagement with the surfaces and are beginning to form synaptic structures, a precursor to NK cell killing activity, and so cell spread area provides information about the early stage activation levels of the NK cells.

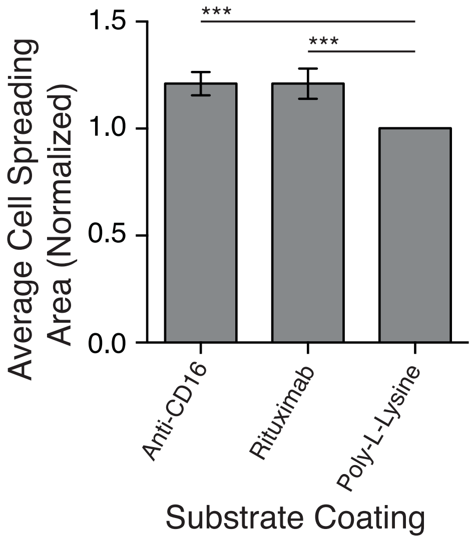

Figure 6.4.5: Cell spread area, normalised to response on PLL surfaces, of cells exposed to CD16 ligands on planar substrates. PLL surfaces were prepared by passivating glass with PLL-g-PEG and displacing this with PLL, as described in the Materials and Methods section. Bars represent average cell spread area on each condition for 5 donors. Error bars are standard error in the mean of donor average values. PLL responses normalised to one for each donor to compare responses across donors. Approximately 350 cells analysed per condition across donors. Statistical testing *** $p < 0.001$

Functionalised nanopatterns spaced 25, 69 or 104nm apart were then tested, and cell spread area calculated for anti-CD16 (Figure 6.4.6) and Rituximab (Figure 6.4.7) functionalised interfaces.

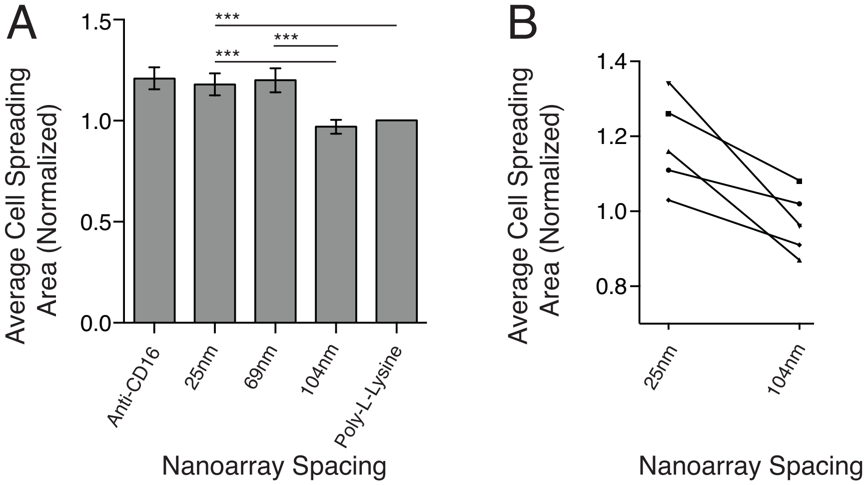

Figure 6.4.6: Cell spread area, normalised to response on PLL surfaces, of cells exposed to anti-CD16 3G8 nanoarray surfaces. Left panel indicates averaged cell spread area on each condition for 5 donors, right panel shows individual donor response to small and large spacing, where a total of approximately 300 cells were analysed per condition. Error bars are standard error in the mean of donor average values. PLL responses normalised to one for each donor to compare responses across donors. Statistical testing *** $p < 0.001$

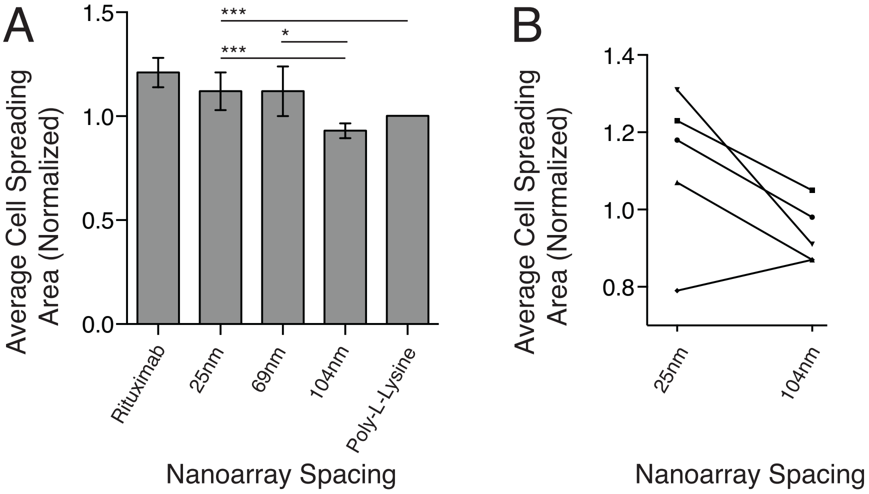

Figure 6.4.7: Cell spread area, normalised to response on PLL surfaces, of cells exposed to Rituximab nanoarray surfaces. Left panel indicates averaged cell spread area on each condition for 5 donors, right panel shows individual donor response to small and large spacing, where a total of approximately 300 cells were analysed per condition. Error bars are standard error in the mean of donor average values. PLL responses normalised to one for each donor to compare responses across donors. Statistical testing *** $p < 0.001$, ** $p < 0.01$, * $p < 0.05$

Figure 6.4.6 shows cell spreading responses to anti-CD16 3G8 nanoarrays, as the nanopattern spacing increases from 25nm to 104nm, there is a significant decrease in the average cell spread area (Figure 6.4.6(A)) and this is true for all donors tested (Figure 6.4.6(B)) Intriguingly, there is also a sharp threshold in cell spread area between 69nm and 104nm, where cellular response to the nanopatterns falls to background levels as anti-CD16 antibodies are spaced 104nm apart. The response of Rituximab was also tested (Figure 6.4.7) and shows very similar results. As the inter-particle spacing of functionalised array increases, the cellular response to the surface decreases, again falling to not significantly greater than background by 104nm. Interestingly there is no significant difference between engaging the CD16 receptor with Rituximab or anti-CD16 antibody, indicating that the cell is undergoing similar actin skeleton rearrangement in both cases.

These results show that as the spacing of anti-CD16 ligands is increased from 25 to 104nm, the cell spread area is dramatically reduced, and falls to not significantly greater than cell spread area on an adhesive background. This indicates that when ligands are positioned 104nm apart, the cell fails to engage with the substrates in an activatory manner. This is the first time NK cells have been shown to be sensitive to nanoscale ligand arrangement, and we propose several hypotheses for this phenomenon discussed in turn below. These are; required concatenation of CD16 microclusters for additive signaling or inhibitory receptor exclusion, a minimal receptor engagement number per cell or per cluster, or mechanosensitivity to applied force through the CD16-receptor bond.

The existence of protein microclusters on immune cell surfaces has been verified by microscopy; inhibitory receptor KIR2DL1 exists in nanodomains approximately 110nm across as sized by PALM microscopy, [315] and several different receptor and signaling protein microclusters have been identified in T cells between 35-300nm in size.[334, 289, 328, 478, 290] CD16 protein microclusters have also been visualised on NK cell surfaces,[265, 472] and with the development of super-resolution techniques will soon be sized more accurately. Here, we assume that CD16 clusters are of the same scale as inhibitory receptors sized at 110nm, and term them nanodomains.

A possible explanation for our results lies in the requirement for nanodomain concatenation, which has been proposed as a signaling mechanism in T cells. Separate islands of Lat and CD3ζ have been observed to come together into microclusters on activation in T cells.[328] Similarly, assuming here each nanoparticle is capable of anchoring receptors in distinct CD16 nanodomains, we postulate that it is the concatenation of these nanodomains that is crucial to signaling. Surfaces with nanoparticles spaced 104nm apart would be capable of anchoring CD16 nanodomains with minimal overlap, and therefore concatenation of protein islands and integration of signals from several distinct receptor nanodomains would be minimal. In contrast, surfaces with 25nm or 69nm spacing would allow nanodomains to overlap significantly. These closely spaced surfaces may aid with protein nanodomain congregation and signaling, and supports the observation that moesin, a protein mobiliser, is recruited at the NK-cell interface in Rituximab use.[35]

A justification for this hypothesis considers the role of competitive phosphorylation and dephosphorylation pathways known to be present in NK cell inhibition pathways. It is thought that some activatory receptors are controlled by inhibitory pathways, such as the activatory NKG2D receptors and inhibitory KIR pathway.[257] CD16 receptors associate with CD3ζ tails, and so are coupled to Immunotyrosine Activatory Motifs (ITAM) which undergo phosphorylation on active engagement,[479, 263] leading to downstream signaling pathways that eventually result in cellular activation. Some inhibitory receptors possess Immunotyrosine Inhibitory Motifs (ITIMs) which can be tyrosine phosphorylated on ligand binding; these then activate protein tyrosine phosphotases which dephosphorylate key activatory pathways. It would be plausible to suggest that the phosphorylation of the ITAM, a key signaling component of the CD16 receptor, is a competitive process inhibited by the dephosphorylation carried out by other proteins, which seek to dephosphorylate the ITAM before additional activation events take place. An extension of the hypothesis suggested earlier, that CD16 nanodomain aggregation is required for NK cell stimulation, comes from the distance-based inhibition model.[480] Simulation and microscopy studies have suggested that inhibitory receptors act locally, and have a limited radius of influence on adjacent activatory receptors of approximately 3-10 molecules.[319, 320, 321, 480] Our data is consistent with this model, where the binding of CD16 to closely spaced nanoarrays allows concatenation of nanodomains, and could exclude inhibitory receptors. The exclusion of these receptors means they can only act on the ITAMs at the periphery of the recently concatenated CD16 protein islands, and so signaling in the protein island core occurs unimpeded. Conversely, the larger spaced nanoarrays may not allow for exclusion of inhibitory receptors in close proximity to the CD16-ligand engagement, and so the desphosphorylation dominates at these receptors and signaling is minimal.

A seperate hypothesis relates to a minimum number of signaling events being required to induce activation; where the number of receptors engaged per cell surface acts as the driving force as to whether a cell is to become activated or not. For this system, this hypothesis is unlikely to be valid, as the number of ligands presented on even the most widely spaced nanoarrays is much greater than minimum stimulation requirements that have been identified in other immune cell types.[294, 481, 325] However, as minimum ligand engagement requirements have yet to be determined for NK cells specifically, this hypothesis is discussed below.

CD16 receptors associate with CD3ζ tails, and so are coupled to ITAM motifs; there may be a basic requirement for integration of a minimum number of signals before downstream activation occurs. In T cells, a minimum of two ITAMs require phosphorylation before activation begins,[482, 300] and an intrinsic threshold whereby a certain number of receptors need to become engaged and phosphorylated in order to overcome dephosphorylation pathways occurring simultaneously may also exist. Although this model fits well with the basic concept of greater cellular response at lower nanoarray spacings, it is difficult to reconcile with the observed results when the effect of valency is taken into account. Table 6.4.1 shows a summary of the number of particles per unit area, and expected number of ligands per particle assuming only one protein is present per nanoparticle.

Nanoparticle Spacing	Particles per μm^2	Ligands per μm^2 (anti-CD16)	Ligands per μm^2(Rituximab)
25nm	1600	3200	1600
69nm	210	420	210
104nm	115	230	115

Table 6.4.1: Nanoparticle arrays per unit area. Assuming each nanoparticle is functionalised with a single antibody, and that anti-CD16 presents bivalently and Rituximab monovalently, values quoted are the number of possible CD16 engaging ligands presented by each method per unit area.

Given the monovalent nature of the engagement of Rituximab with CD16, and bivalent nature of anti-CD16 engagement (capable of binding two closely spaced CD16 receptors) it is clear that if each nanoparticle is singly functionalised with an antibody, the 69nm Rituximab surface and 104nm anti-CD16 surface would both present approximately 200 receptor engaging ligands per μm^2. If activation relied simply on ligand density, we could expect these conditions to produce equivalent spreading responses, however it is clear that with both anti-CD16 and Rituximab the threshold for cellular response lies between 69 and 104nm.

This suggests that it is the inter-ligand spacing, rather than the ligand density, which controls the activatory threshold, as the cells respond similarly to surfaces which present the same inter-ligand spacing but different ligand densities. Additionally, in other systems, some immune cells have been shown to be stimulated by very low ligand densities of only 1-4 agonist ligands per μm^2,[294, 481, 325] an order of magnitude lower than those being used in this system. Until such stimulatory ligand densities have been determined for NK cells, we can only speculate on whether a minimal number of ligand interactions, and so ligand density, are crucial factors for NK cell activation.

In order to evaluate whether ligand density does play a more crucial role than suggested here, future work should attempt to de-couple local ligand density from local inter-ligand spacing. Cellular studies on functionalised surfaces using disordered nanoparticle arrays with conserved density, or more advanced nanopattern systems such as those proposed in Chapter 5, using zinc and gold nanoparticle mixed arrays to maintain inter-particle spacing but vary density, could be employed to determine if local ligand density plays a crucial role in determining the cellular activation threshold.

An alternative explanation involves the requirement for multiple ligand anchoring points per distinct CD16 nanodomain, rather than per cell. Again, assuming the size of CD16 nanodomains to be 110nm, surfaces with 25nm spaced nanoparticles would allow multiple ligand anchoring points per nanodomain. With 69nm it is possible several distinct CD16 molecules could be engaged simultaneously, however 104nm surfaces would likely only provide one receptor engagement interaction per nanodomain.

Finally, there is also the possibility that the response to nanoarray spacing is due to mechanosensitivity in the CD16 receptor, where smaller spacing corresponds to a greater number of ligand anchoring points per cell or per individual signaling focus, and so reduced force per CD16-receptor pair.[106] There may therefore be an optimal force acting through the CD16-ligand pair engagement at which signaling occurs. Currently, there is no evidence to suggest that the CD16 receptor possesses any mechanical moieties, or that the NK cell is mechanosensitive, however Rituximab has been shown to induce changes in the mechanical properties of target cells,[483] and mechanosenitivity has been shown in other immune cell types.[281, 280, 293]

The hypotheses described here are based on the assumption that each nanoparticle is functionalised with one ligand (with Rituximab) or two ligands (with anti-CD16) per nanoparticle. Whilst we would expect the small size of the nanoparticle and steric hindrance between ligands to ensure that the binding of more ligands per nanoparticle is unfavourable, there is limited evidence shown here that each nanoparticle is functionalised with at least a single ligand, and that each ligand is bound in an active confirmation. If each nanoparticle is not functionalised with an antibody in an accessible conformation as proposed, and instead the nanoarray is only partially functionalised, then the conclusions drawn regarding the spatial threshold for activation may be underestimated. If only a small percentage of the nanoarray is successfully functionalised, the actual inter-ligand spacing values at which cells no longer respond to the surface in an activatory manner may be much larger than those proposed.

Other systems have used SEM to show that gold nanoarrays functionalised with Histidine tagged proteins present surfaces where at least 75% of the nanoparticles are functionalised with an antibody in an active confirmation capable of binding a selective monoclonal antibody (functionalised with an additional gold nanoparticle)[211] and so it is plausible that a large proportion of the nanoparticles in our system are functionalised with bound antibodies in an active confirmation.

Further evidence to support the assumption that the majority of the nanoparticles are singly functionalised with an antibody in an active confirmation lies in the comparison between the two CD16 engagement mechanisms. If immobilisation does diminish the activity of the antibody, it seems unlikely that once immobilised both the Fc engaging Rituximab system and the bivalent anti-CD16 variable region system would present ligands to the CD16 receptor with exactly the same diminished activity due to the difference in their engagement mechanisms. Despite the difference between the two ligand systems in valency, CD16 receptor affinity and engagement mechanism, both systems show a strong activity dependent threshold at between 69nm and 104nm gold nanoarray inter-particle spacing, suggesting that it may indeed be the inter-ligand spacing that is key to driving the activatory response. In order to provide additional support to these studies, it will be important to validate the number and conformation of the antibodies bound to the nanoarrays.

Here, we show that NK signaling is sensitive to the nanoscale arrangement of ligands, and that this requires spacing between ligand anchoring points in the region of 25-69nm, below 104nm. The exact mechanism driving signaling through sensitivity to nanoscale arrangement is not yet clear; required concatenation through additive signaling and inhibitory receptor exclusion, minimal engagement of receptors per individual signaling focus and mechanosensitivity have been postulated. Additionally, advanced microscopy studies should help to answer questions about the size of CD16 receptor nanodomains and develop further insights the clear difference in early stage NK response to nanopattern surfaces. With greater super-resolution capabilities, it will soon be possible to determine which of these hypotheses presents the most feasible nanosensitivity mechanism, and the ideas suggested here are also discussed in more detail in Chapters 7 and 8 in relation to T cells.

6.4.3 Advanced Functionalisation

The surfaces prepared earlier utilised the binding of streptavidin to biotinylated proteins to present a robust protein attachment mechanism to the nanoparticle. A limitation is in the tetravalent nature of the streptavidin-biotin link, which could enable up to three biotinylated proteins to be bound per streptavidin, dependent on steric factors and kinetics. An advancement of this technology is in the use of an engineered streptavidin with only two functional biotin binding sites. Bivalent streptavidin was provided by Mark Howarth *et al.* and used to prepare surfaces with minimal biotin binding sites. These surfaces were functionalised with fluorescent biotinylated anti-CD16. (Figure 6.4.8)

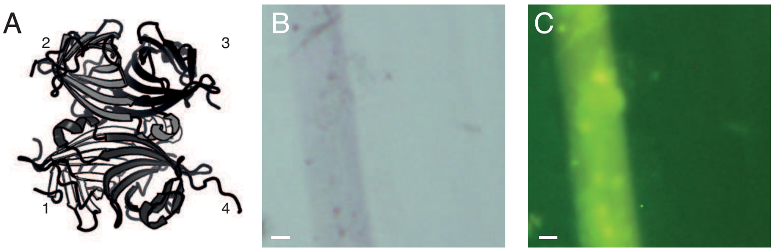

Figure 6.4.8: Bivalent streptavidin binding. (A) Individual chain protein structure of streptavidin showing 4 chains and 4 available binding sites. (B) Bright-field and (C) fluorescent images of nanopattern surfaces functionalised with fluorescent anti-CD16 through bivalent streptavidin binding. Dark purple lines in bright field (B) are indicitive of heavy gold deposition, and correlate to enhanced fluorescence.

Figure 6.4.8(A) shows the four sub-chains constituting the streptavidin; bivalent streptavidin can present either cis- or trans- functionality[484, 485, 486] where adjacent (cis) or opposite (trans) biotin binding sites remain active, and the other two sites are unfunctional. Selective binding of biotinylated anti-CD16 proteins to surfaces functionalised with bivalent streptavidin, (Figure 6.4.8(B) and 6.4.8(C)) is clearly identified by the strong fluorescence formed on uniform gold nanopattern surfaces and areas with heavy gold deposition.

The ability to functionalise gold nanoparticles with bivalent streptavidin, and therefore an expected 1:1 ratio of streptavidin to biotinylated protein, or tetravalent streptavidin gives a greater versatility in conjugation strategies and could be used to further advance specific functionalization on the nanoscale.

Without confirmation of the exact number of streptavidin molecules bound per nanoparticle, detailed analysis of the cellular response to bivalently functionalised nanoarrays is not robust. If the number of streptavidin proteins per particle is verified this would be an interesting experiment and could help provide further evidence to oust the valency hypothesis discussed earlier. Additionally, this technology could have other uses in advanced nanopatterning, as the presentation of monovalent proteins has a range of applications.[487, 488, 489, 402, 490, 491, 492]

6.5 Conclusions

We have demonstrated the fabrication of controlled nanoarrays and selective functionalization of those arrays with a range of biological conjugation methods. Both anti-CD16 and Rituximab have been bound to gold nanoparticles using streptavidin linkage. These surfaces have subsequently been used to investigate cellular responses to nanoscale ligand environments. NK cell response, assayed by cell spread area, to the formation of artificial immune synapses with anti-CD16 engaging ligands on the nanoscale has shown that activation of innate NK cells is dependent on ligand spacing of sub-104nm. Specifically, surfaces with CD16 ligand anchoring points spaced 25nm or 69nm induced a similar cell response to planar activatory stimuli regardless of ligand engagement mechanism. This response also seemed to demonstrate an on-off threshold, where response to stimuli above background levels was not detectable when ligands were spaced 104nm apart.

Several hypotheses have been presented to explain these results, focusing on the required concatenation of protein islands, the minimal number of receptor engagement points and the potential mechanosensitivity of CD16 engagement. Regardless of the underlying mechanisms, our results clearly demonstrate that spatial factors on 10 – 100 nm length-scales not only correlate with signaling, but can actually control it.

Understanding of the nanoscale structure of the NK cell response could lead to better therapeutics[465, 464, 493, 39, 458] where it may become possible to augment cell function *ex vivo*, or develop drugs that move from drugs that ligate single receptors or dimers towards larger nanoscale therapeutics. Such therapeutics will mimic and manipulate synaptic spatial structures, for example driving nanocluster concatenation.

6.6 Future Work

This work has focused on the very early stages of cellular response to these nanopatterns; it will be interesting to determine if the response to nanoscale ligand arrangement is consistent at later time-points, and also reflects the level of full activation the NK cell undergoes. Immediate experiments could focus on determining the relative expression of cell surface activation markers, such as CD69 and LAMP-1 at specific time-points across a range of nanopatterns. Additionally, IFNγ cytokine secretion could be monitored as a measure of late stage activation.

As clinical response to Rituximab is known to be mediated by the Fc affinity level, it would be interesting to investigate the effect of other antibodies binding to CD16 through their Fc portion at these spacing regimes.[464, 494, 495, 496, 497] Our results seem to indicate that the spatial response to ligand engagement is independent of engagement mechanism or valency, however this should be verified with further substrates.

The threshold seen here at between 69 and 104nm spacing raises two directions for future work; firstly, the spacing region between these two values should be explored in smaller increments, in order to determine if there is an on-off threshold, or a gradual decrease down to minimal signaling. Secondly, it would be important to determine if the effect seen here is kinetic, and whether with greater engagement time the 104nm surface may catch up to the 25nm and 69nm responses, which appear to be maximal. These results would help to identify whether the differential response is due to signaling integration or is truly limited by spatial organisation of ligands.

Whilst several other cell types have identified nanoscale ligand engagement requirements, particularly those requiring actin mediated adhesion,[102, 103, 105, 214, 51, 106, 107, 108, 93, 370, 109, 212] these are the first studies on innate immune cells. A further development of this work would be to characterise the response to nanoscale ligand engagement in other types of innate immune cell and adaptive immune cells, to determine if there is a universal immune receptor signaling dependence on nanoscale receptor engagement.

Chapter 7

T cell stimulation with ligand nanoarrays

Nanoscale ligand geometries in the adaptive immune system: T cell response to CD3 engagement

7.1 Introduction

T cells are a key component of the adaptive immune system, with a major role in host defence against pathogenic infection. Although the T cell presents many receptors on its surface and forms a variety of cell-cell contacts,[297, 498] it is the T Cell Receptor (TCR) complex that is the most central in activating T cells towards immune function. The exact nature of the stimuli required to fully activate the T cell through TCR engagement remains unclear; most research has focused on a "two signal hypothesis" although full effector function in some cells is thought to be reliant on three signals delivered sequentially.[273] In most cases, engagement of the TCR/CD3 with agonist Major Histocompatability Complex (pMHC) on Antigen Presenting Cells (APCs) is usually the first activatory signal received.

Currently, there is a wealth of evidence to suggest that the nature of pMHC presentation to TCR is critical in determining T cell activation levels. Agonist valency,[499, 374] the nature of the agonist substrate,[280, 287] and the spatial organisation of stimulatory ligands[375] have been identified as key features in T cell activation, discussed extensively in Chapter 2.

Several key receptors and signaling proteins have been shown to be organised into micro- and nanoscale protein domains on the T cell surface.[277, 328, 290, 334, 500, 289] The movement of TCR surface clusters across a T cell surface to form a central Super Molecular Activatory Cluster (c- SMAC) on activation is known to propagate and aid sustained signaling in T cells.[289, 290, 288, 331, 328, 323]

There is much interest in whether the range of intrinsic micro-scale organisation present on T cell surfaces during activation is a requirement for, or product of, activation. The fabrication of biomimetic substrates, where ligand presentation is spatially controlled on the micrometre scale, have attempted to address this.

Both fluid supported bilayers,[295, 296, 21] and more restrictive micro-patterned proteins patches[299] have shown that control of protein positioning with different micro-scale structures results in modified T cell activation states,[501, 299, 21, 502, 239] and can direct TCR microcluster motion.[296, 295]

The TCR/CD3 receptor complex is 10-20nm in size,[503] and exists in nanodomains of several TCR/CD3 receptors which together measure between 35-70nm in size.[328] On activation, these nanodomains are thought to aggregate with nanodomains of other signaling proteins to form microclusters (containing several nanodomains), which occurs before formation of larger synaptic structures such as c-SMAC formation.[323, 328] There is therefore a sequence in which isolated TCR/CD3 units associate to form nanodomains on quiescent cells, then to form larger microclusters on activation, and transition from individual nanoscale units to larger structures.

Currently, there have been no investigations of the effect of receptor engaging anchoring points across the lengthscale 10-100nm, despite the range of key activatory structures of these dimensions. This chapter seeks to utilise nanoparticle substrates of the order of 10-100nm to pattern TCR/CD3 engaging ligands, and determine the outcome of nanoscale ligand spacing on T cell stimulation.

The fabrication of well controlled nanoparticle arrays by Block Co-polymer Micellar Lithography (BCML) [204, 351] (discussed in detail in Chapters 4 and 5) allows the fabrication of small features (~10nm) over substrate areas on the order of cm^2 [351, 404] capable of binding biological ligands for the study of nanoscale ligand effects on cellular activation.[215, 370, 93, 108, 105, 103, 102, 106, 51, 210, 212] Specifically, this chapter describes nanoarrays formed by BCML [362] functionalised with anti-CD3ε antibody fragments, and investigates the T cell response to these artificial immune synapses across the nanoscale spacing regime.

7.2 Contribution statement

The work reported in this chapter was supported by the following people;
T Cell isolation and culture was performed by various members of the laboratory of Prof. Michael L. Dustin, Skirball Institute of Biomolecular Medicine, New York University.
T Cell TIRF experiments were aided by Dr. David Depoil. Cellular experiments and analysis were performed by Derfogail Delcassian.
Spearman's Rank Correlation and Wilcoxon rank sum statistical tests were performed by Prof. Mengling Liu, Department of Biostatistics, New York University.

7.3 Materials and Methods

7.3.1 Fabrication of nanopattern arrays

Gold nanoparticle arrays of various spacings were prepared as described in Chapter 4 using BCML. Briefly, poly(styrene-*block*-2-vinyl pyridine) (Polymer Source, Montreal, Canada), of varying molecular weight and styrene to 2-vinyl pyridine ratio depending on the nanopattern spacing required, was dissolved in p-xylene (99.0%, VWR, Radnor, P.S., U.S.A.)) and stirred for at least 12 hours. Gold (III) chloride trihydrate (Sigma Aldrich, St Louis, M.O., U.S.A.) was then added at 0.1 – 0.5 molar ratio to the total amount of 2-vinyl pyridine units and left to stir for another 24 hours to generate micelles with gold-loaded cores. Glass substrates were cleaned by immersion in a 1:3 v/v mixture of hydrogen peroxide 30% solution (VWR) and concentrated sulfuric acid (95%, VWR) for at least 2 hours, before rinsing in ultrapure water (18.2 MΩ). Substrates were coated with a monolayer of gold-loaded micelles by dip-coating using a home-built setup with a retraction speed of 0.36 mm/s. Gold nanosphere arrays were generated from these micelle-coated substrates by exposure to a hydrogen/argon plasma (10% hydrogen, 0.4 mbar, 350 W) in a plasma etcher model name (PVA TePla, Kirchheim, Germany). Sample nanoarrays from each batch were characterised by SEM (Leo Gemini at an EHT 5-10kV), after sputter-coating with a thin layer of carbon. Mean and standard deviation spacings were calculated by measuring a representative number of nearest neighbours.

7.3.2 F(ab')$_2$ fragmentation

TCEP (Sigma Aldrich) was used at a variety of concentrations (0.1-10mM) in PBS and incubated with F(ab')$_2$ for 20-40 minutes at room temperature before being transferred to ice. Fractioned samples were then purified using a centrifugal filter with the appropriate molecular weight cut off (Millipore, Billerica, M.A., U.S.A.) and fractions examined by gel electrophoresis. Gels were stained with silver (Biorad) and compared to an internal protein ladder standard.

7.3.3 Functionalisation of nanopatterned array

Nanopatterns were cleaned immediately before use by exposure to UV-ozone (10 mins, Procleaner Plus, Bioforce Nanoscience, Ames, I.A., U.S.A.), and an 8-well flexible chamber insert (PDMS, Sarstedt, Nuembrecht, Germany) was immediately affixed. To passivate the glass background against non-specific protein adsorption, wells were incubated with either poly(L-lysine) – graft – poly(ethylene glycol) (PLL-g-PEG) (PLL(Mw = 20kDa) grafted with an average of 3.5 chains of PEG(Mw = 2 kDa) chains, SuSOS, Zurich, Switzerland) or PLL-g-PEG-biotin (same with 51% of PEG chains biotinylated at free end, SuSOS, Zurich, Switzerland) at 1 mg/ml in PBS for 1.5 hours. UCHT-1 F(ab')$_2$ was fluorescently labeled using an AlexaFluor 488 kit (Invitrogen). Surfaces were rinsed with PBS and incubated with relevant biological ligands, with further PBS-rinsing after each step. UCHT-1 F(ab')$_2$ fragment (BioLegend, San Diego, CA) was incubated directly with PLL-g-PEG-biotin passivated gold nanoarrays (overnight, 0.1 mg/ml). Recombinant human ICAM-1 (Life Technologies, Carlsbad, C.A., U.S.A.) was biotinylated using EZ-link NHS-PEG(4)Biotin (Thermo Scientific, Waltham, M.A., U.S.A.) kit, and purified using a centrifugal filter with 50 kDa cutoff (Millipore, Billerica, M.A., U.S.A.). To incorporate ICAM-1 into the PLL-g-PEG-biotin background, UCHT-1 functionalized nanoarrays were first incubated with streptavidin (0.1 mg/ml, PBS, 1-2 hours) and then with biotinylated ICAM-1 (5 µg/ml, PBS, 1-2 hours). Control surfaces were glass coverslips cleaned with ethanol and UV-ozone and incubated with UCHT-1 F(ab')$_2$ fragments or ICAM-1 under the same conditions as the nanoarrays.

7.3.4 Protein Structures

Protein crystal structures were obtained from the European Protein Data Bank and projected using PyMOL. Structure 1igy_IgG1 was used to represent IgG, F(ab')$_2$ and F(ab') fragments.

7.3.5 Cellular experiments

Human CD4 T cells, cells were purified from fresh peripheral blood samples (New York blood center, NY) using Rosette separation kit (Stemcell Technologies, Vancouver, BC, Canada) according to manufacturer's protocol, then were rested at 37 °C for 1 – 5 days in complete RPMI. Prior to experiment the cells were suspended in HBS/HAS buffer (20 mM HEPES, pH 7.2; 137 mM NaCl; 5 mM KCl; 0.7 mM Na_2HPO_4; 6 mM D-glucose; 2 mM $MgCl_2$; 1 mM $CaCl_2$; 1% (v/v) human serum albumin (HSA; add from 25% human serum albumin (Williams Medical Company, Rhymney, U.K.)) and incubated at 37°C. Biofunctionalised nanoarrays with 8-well inserts were also equilibrated at 37 °C with HBS/HSA buffer. Cells were seeded at 1 million cells per ml (100 µl per well) and incubated for 5 minutes at 37 °C and 0% CO2. Cells were fixed (warm 2% paraformaldehyde in PHEMO buffer (10mM EGTA, 2mM $MgCI_2$, 60mM Pipes, 25mM HEPES, pH 7.2) for 10 mins) and permeabilized (0.1% Triton in PBS, 3 mins). Post-fixation, wells were blocked overnight at 4 C with 5% casein in PBS and stained with Alexa 568-labelled phalloidin (Life Technologies), the phosphotyrosine-binding monoclonal antibody 488-PY20 (Biolegend, San Diego, U.S.A.) and the CD45-binding mAb CD45RA (APC – e-Bioscience, San Diego, C.A., U.S.A.) for between 1-3 hours. Total Internal Reflection Fluorescence imaging was carried out using a Nikon Eclipse Ti with 100X 1.49 NA objective and an AndorDU897 back illuminated EMCCD camera. Images were processed using the FIJI software package, where average phosphotyrosine intensity was measured using a standard cell-sized region of interest (ROI), with subtraction of a corresponding background ROI. Average phosphotyrosine intensity was measured for each ROI. The number of adhered cells was counted in a standard area of 100 frames = 661456.9 μm^2, to distinguish cells adhered to the surface from cells floating above the surface in solution, fluorescent actin staining in the surface plane and Interference Reflection Microscopy (IRM) were used to determine if cells were attached. Cells possessing both actin in the surface plane, and an IRM contrast image (indicating contact with the nanoarray surface), were considered attached. The overall difference between spacing settings was tested using the nonparametric Kruskal-Wallis rank sum test, and the trend was test was conducted using the Spearman's rank correlation test. The pair-wise comparisons between two spacing settings were conducted using the Wilcoxon rank sum test. All tests assumed cells are independent units, and statistical analysis was conducted using R 3.0.1.

7.4 Results and Discussion

7.4.1 Functionalisation of nanoparticle arrays

Gold nanoparticle arrays with nano-scale inter-particle spacing were prepared by BCML. Scanning Electron Microscopy (SEM) was used to ascertain nanoarray spacing (Figure 7.4.1) and substrates were fabricated across the 25-104nm inter-particle length scale.

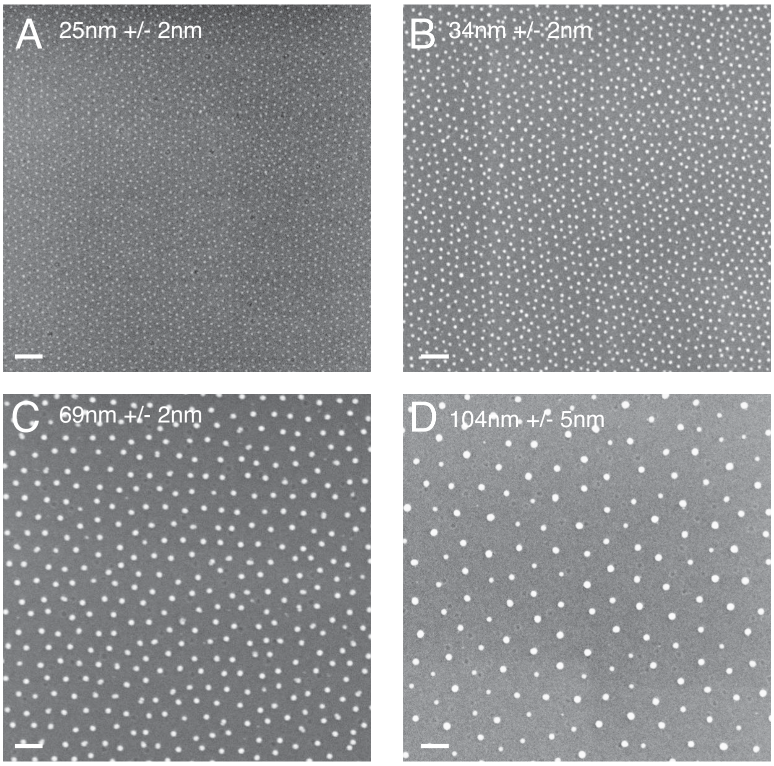

Figure 7.4.1: SEM micrographs of gold nanopattern arrays. BCML was used to fabricate gold nanopattern arrays. SEM images and inter-particle spacing analysis is shown, with mean values and standard deviation. Panels (A,C,D) were shown in Figure 6.4.1 for NK cell studies.

Previous work in this thesis (Chapter 6) described a nanoparticle functionalisation mechanism based on covalent antibody attachment through the streptavidin-biotin system. Here, we use the direct attachment of antibody fragments to the gold nanoparticle through the intrinsic disulfide as an alternative approach.[490, 491] The direct binding of the antibody fragments in this way enables further proteins to be bound into the background passivation layer using streptavidin-biotin chemistries using modified passivation agents.[504]

A standard IgG1 antibody consists of a pair of bound heavy and light chains, shown schematically in Figure 7.4.2(A), with a variety of disulfide environments. Of interest here is the disulfide bridge connecting each heavy chain to its light counterpart (Figure 7.4.2(A), labeled a) and further disulfides which interconnect the two heavy chains (Figure 7.4.2(A), labeled b). Cleavage of the antibody below the heavy chain connection yields a F(ab')$_2$ fragment (Figure 7.4.2(B)) which can further be cleaved to produce a F(ab') fragment by breaking the heavy-heavy disulfide link. Antibody fragments are then capable of binding directly to gold substrates, and this type of surface has been used extensively for immunosensing applications.[490, 491, 489, 403]

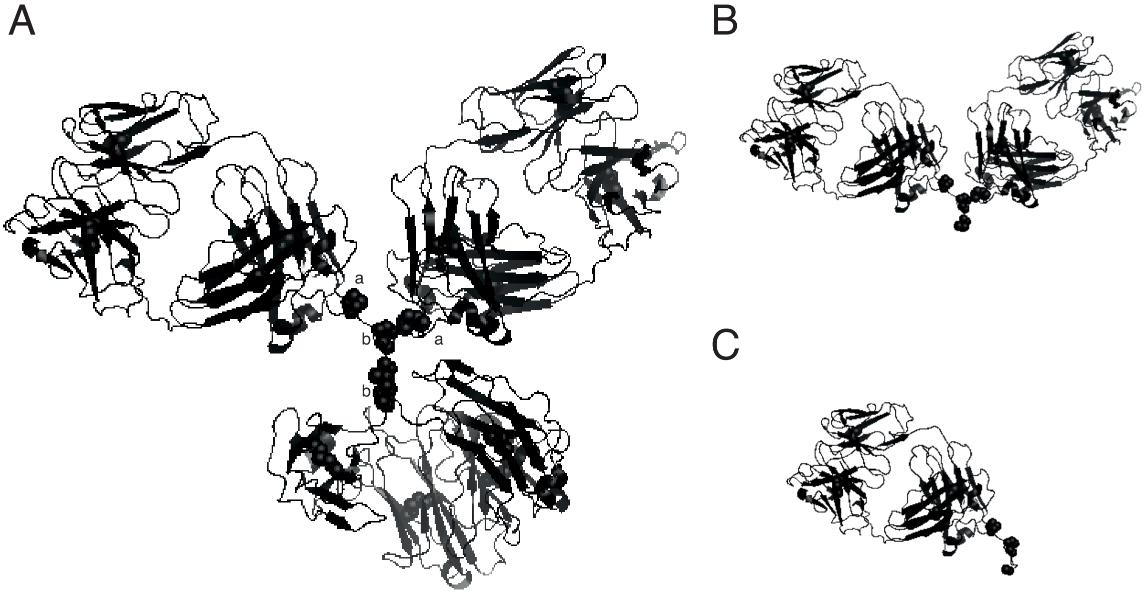

Figure 7.4.2: Antibody and fragments crystal structure. A) A standard IgG_1protein, B) $F(ab')_2$ antibody fragment and C) F(ab') fragment.

Gold nanopatterns were bound with fluorescently labeled $F(ab')_2$ (Figure 7.4.3) in order to demonstrate selective functionalization.

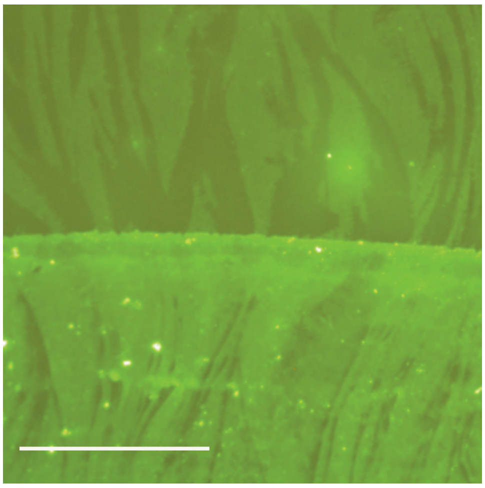

Figure 7.4.3: Gold nanopattern functionalisation. Surfaces were passivated with PLL-g-PEG and incubated with fluorescently labeled $F(ab')_2$. Scale bar 200µm.

Figure 7.4.3 demonstrates the successful functionalization of gold nanopatterns with $F(ab')_2$ fragments. A fluorescent gold nanopattern region (bottom), bright dipping line and reduced fluorescent background area (top) are seen, which are indicative of a protein resistant layer being successfully applied to the glass between nanopatterns and selective functionalization of the gold. The PLL-g-PEG used to create a protein resistant background layer can be functionalised with small biotin molecules, the inclusion of selected co-stimulatory proteins is now possible using additional chemistry, such as streptavidin and biotinylated proteins as shown schematically in Figure 7.4.4.

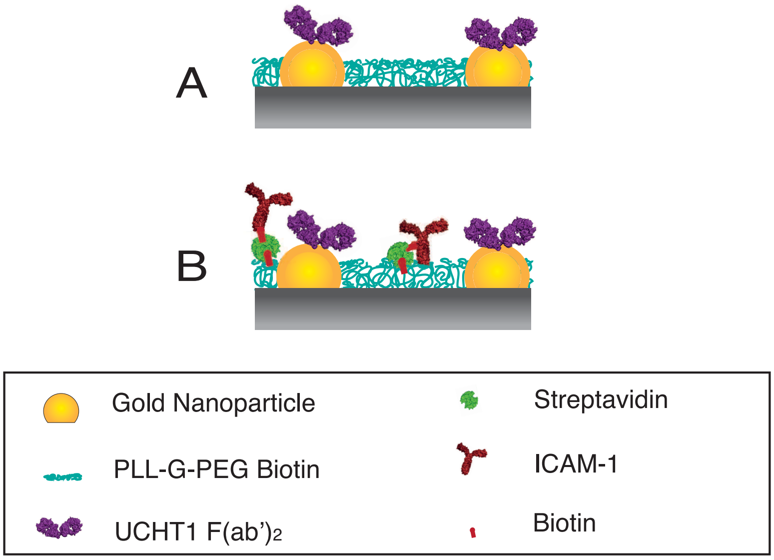

Figure 7.4.4: Schematic of protein binding. Gold nanopattern surfaces can be prepared to present F(ab')$_2$ protein fragments on gold nanoparticles. Additional proteins, such as adhesive and co-stimulatory molecules, can be bound into the background passivation layer (B) using biotin-streptavidin linkers.

Each F(ab')$_2$ molecule presents a bivalent ligand to the cellular receptor, images of to-scale protein models projected onto nanopattern SEMs indicate that it is highly likely each nanoparticle is functionalised with only one F(ab')$_2$ fragment (Figure 7.4.5) with limited position flexibility.[402] The figure suggests that each F(ab')$_2$ fragment binds in an orientated fashion through the thiol hinge region, presenting two accessible variable regions for binding. Despite the thermodynamically favourable thiol-gold interaction, it is possible that the protein could bind to the nanoparticle non-specifically, for example using lysine side chains, and so the orientation may not be upright. In this case, if the protein binds non-specifically and so in an alternative orientation, the availability of two CD3 engaging sites in close proximity may allow the protein to interact with the CD3 receptor through one of its variable regions. The figure also shows an individual F(ab')$_2$ fragment bound per nanoparticle, the small size of the nanoparticle and steric hindrance between proteins should prevent multiple antibody fragments being bound per nanoparticle. Additionally, with the passivation layer swollen to around 10nm[379] other systems have also been able to bind single proteins.[211] Although the F(ab')$_2$ presented on these surfaces is bivalent, each TCR complex presents two CD3ε receptors which orient adjacently,[505, 81] and so if multivalent interaction is possible, it is likely that each F(ab')$_2$ would bind to a single receptor complex rather than crosslinking them due to steric repulsion, ensuring that each functionalised particle can act as a binding site for a single surface receptor nanocluster of approximately 35-70nm.[375, 374, 328]

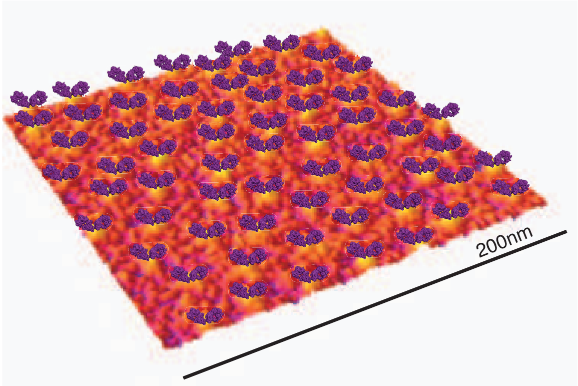

Figure 7.4.5: 3D nanoarray visualisation. A 25nm spaced nanoparticle array was examined by SEM, and is shown in 3D. Modeled F(ab')$_2$ fragments were layered. Image is to-scale in x-y plane.

In order to present a CD3ε engaging substrate, gold nanoparticles were functionalised with anti-CD3ε F(ab')$_2$ fragments derived from the UCHT-1 antibody. Additional evidence to suggest that the protein is immobilised in an orientated and accessible fashion is found in the cellular response to the nanoarrays, discussed in detail in the next section.

7.4.2 Cellular response to anti-CD3 nanopatterns

Successful engagement of the CD3 receptor within the TCR complex stimulates a cascade of intracellular pathways that, if other appropriate signals are also received, can lead to cellular activation.[17, 479] We used Total Internal Reflection Fluorescence (TIRF) microscopy to measure the degree of phosphorylation at the nanopattern-cell interface at early (5 minute) time points (Figures 7.4.6, 7.4.7, 7.4.8) as a measure of early activation signaling.[479] Phosphorylation of the ITAM motifs within the CD3 moiety is one of the earliest signaling events, as inhibition of this pathway restricts most of the other downstream signaling processes from occurring.[306] Additionally, although each TCR possesses up to 10 ITAMs [306], a minimum of two ITAMs must be phosphorylated for signaling to proceed[482, 300], and so measuring the phosphotryosine intensity indicates the comparative level of activation occurring inside the cell.

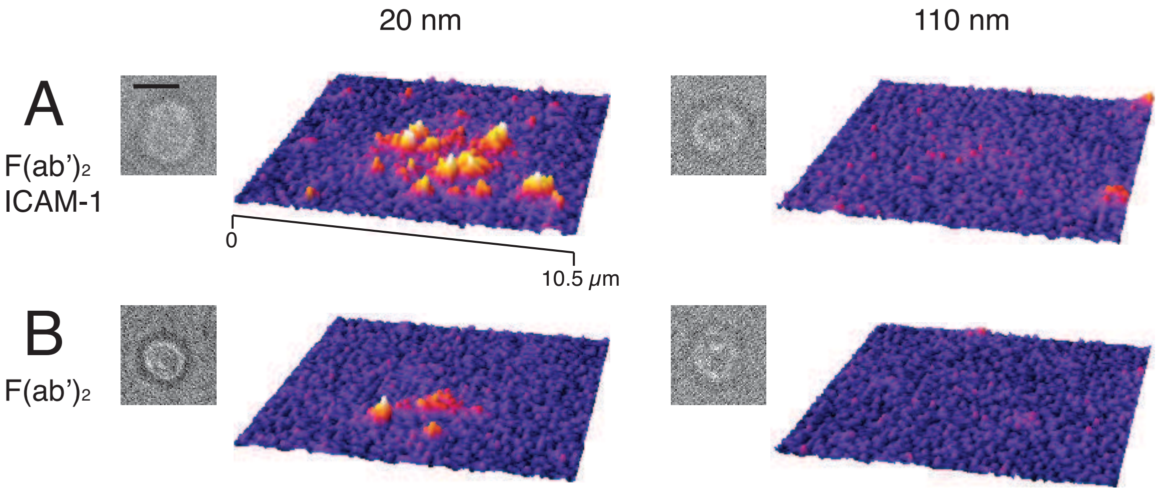

Figure 7.4.6: 3D phosphotyrosine signaling. Representative cells stimulated by nanoarrays presenting UCHT-1 F(ab')$_2$ fragments in the presence (A) or absence (B) of background ICAM-1, with inter-particle spacings 25 nm and 104 nm respectively: bright-field images (scale bar 5 μm) and TIRF-immunofluoresence of phosphotyrosine (3D representation).

Figure 7.4.6 shows a 3D representation of the in-plane phosphotryosine signaling, as measured by fluorescence intensity, for a typical cell in each condition. There is a clear difference in the phosphotryosine microcluster patterns between cells on closely spaced nanopatterns (25nm) and those at 104nm inter-ligand spacing. The difference between small and large spacing is conserved on surfaces with and without adhesive ICAM-1 in the background. A quantitative assessment of phosphotyrosine signaling across the full range of spacings (25, 34, 69 and 104nm) was performed for cells derived from a number of donors. Conditions with (Figure 7.4.7) or without (Figure 7.4.8) adhesive ICAM-1 backgrounds were analysed.

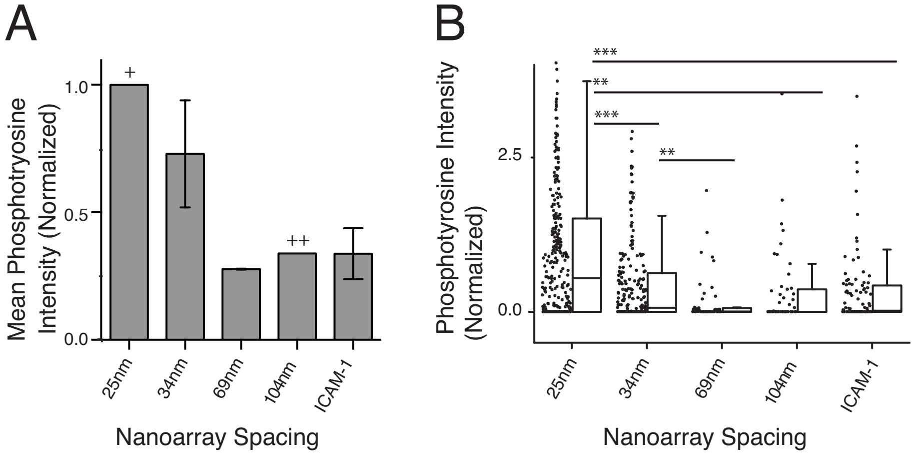

Figure 7.4.7: Cellular response to F(ab’)$_2$and ICAM-1 surfaces. Plots show intensity of TIRF-immunofluoresence of phosphotyrosine after 5 minutes stimulation, as a function of nanoarray spacing. (A) The mean of the phosphotyrosine intensity normalized to the 25 nm intensity for each donor and then averaged across 4 donors. (Only conditions with > 25 cells were included. + No error bar as normalized to 1 by definition, ++ No error bar as only one donor with > 25 cells.) (B) Individual cells shown as dots; cells from all donors were normalised to their own 25nm response, and combined. Central line shows the median, boxes the 25th to 75th percentile and whiskers the upper and lower inner fence values. *** = $p<0.001$, **= $p<0.01$ (Wilcoxon rank sum test).

Figure 7.4.7 shows analysis of the phosphotyrosine intensity in cells exposed to F(ab’)$_2$and ICAM-1 surfaces where the F(ab’)$_2$was anchored 25, 34, 69 or 104nm apart. The graphs show data where all donors have been normalized to their own 25nm surface; the average of each donors cellular responses per condition have been averaged to give a mean phosphotyrosine intensity value (the bar chart on the left). Separately, the data has been compared so that the cellular response from each donor is analysed to its own 25nm control, and then pooled (the box and whisker plot on the right). Here we are interested in investigating if changing the inter-ligand spacing results in a change in cellular activation, and so normalizing and comparing conditions against a fixed spacing standard (in this case 25nm) allows us to monitor if the spacing alteration leads to a signifcant difference in cellular activation.

Figure 7.4.7 shows phosphotyrosine signaling decreases as anti-CD3ε spacing increases. We see that the mean phosphotyrosine intensity decreases from 25nm through 34nm to 69nm. Between 69nm and 104nm, signaling intensity is comparable with that found on an ICAM-1 background. The box and whisker graph shows the phosphotyrosine intensity of all individual cells as dots, and the median of the cell population across all donors. There is a significant difference between signaling on 25nm surfaces as compared to ICAM-1 background, and a significant difference between 25nm signaling and signaling on all other spacings. The statistical analysis performed on the data (the individual condition by condition comparison using Wilcoxon rank sum tests, and the overall comparision across the spacing regime using the Spearman’s rank correlation $p<0.001$) both show statistical significance between the cellular activation levels at different spacings, indicating that cellular activation levels as measured by phosphotyrosine intensity are dependent on inter-ligand spacing at the nanoscale.

In additional analysis, the individual donor responses were normalised to their own ICAM-1 non-stimulatory control, and again a significant trend of decreasing activation with increasing CD3 engaging ligand spacing is seen. (Appendix D) Examination of surfaces functionalised with F(ab')$_2$ alone (Figure 7.4.8) similarly shows a significant decrease in signaling as spacing of ligands increases, and confirm that CD3ε engagement is sensitive to the nanoscale arrangement of ligands.

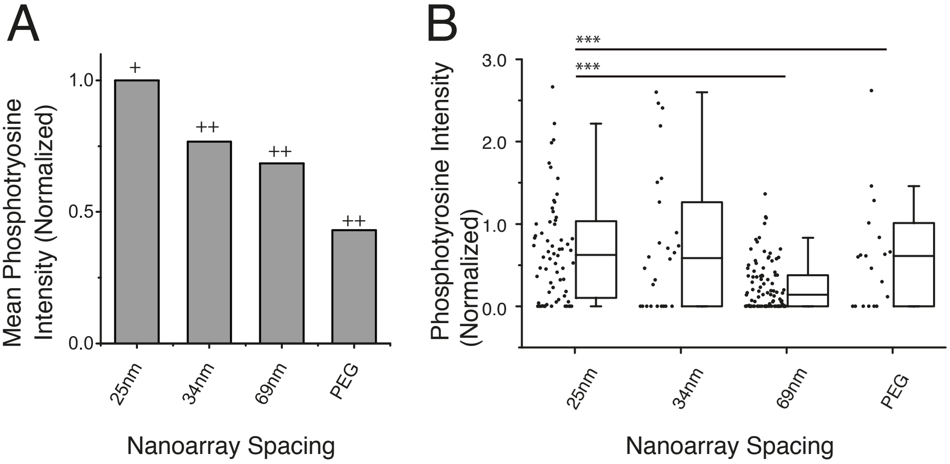

Figure 7.4.8: Cellular response to F(ab')$_2$ surfaces. Plots show intensity of TIRF-immunofluoresence of phosphotyrosine after 5 minutes stimulation, as a function of nanoarray spacing. (A) The mean of the phosphotyrosine intensity normalized to the 25 nm intensity for each donor and then averaged across 4 donors. (Only conditions with > 25 cells were included. + No error bar as normalized to 1 by definition, ++ No error bar as only one donor with > 25 cells.) (B) Individual cells shown as dots; cells from all donors were normalised to their own 25nm response, and combined. Central line shows the median, boxes the 25th to 75th percentile and whiskers the upper and lower inner fence values. *** = $p<0.001$, **= $p<0.01$ (Wilcoxon rank sum test).

Surfaces without additional ICAM-1 (Figure 7.4.8) show the same trend of decreasing activation with increasing nanopattern spacing. These surfaces have a low number of adherent cells per condition; so few cells adhere at 104nm anti-CD3ε spacing that analysis of this condition is no longer robust (it is not represented in the graph (Figure 7.4.8)). This is unsurprising, as *in vivo*, the immune synapse stability is normally augmented by several cell-surface receptors being engaged simultaneously, including ICAM-1 integrin binding. Here, with the passivated background being protein resistant, this implies that cellular adhesion to these surfaces is mediated in part by CD3 engagement in addition to ICAM-1 adhesion.[506]

Adhesion was quantified (Figure 7.4.9) as a function of substrate area on substrates with nanopatterned anti-CD3ε and adhesive ICAM-1 backgrounds. Here, the ICAM-1 background concentration is constant, but the spacing of anti-CD3ε is varied across the nanoscale.

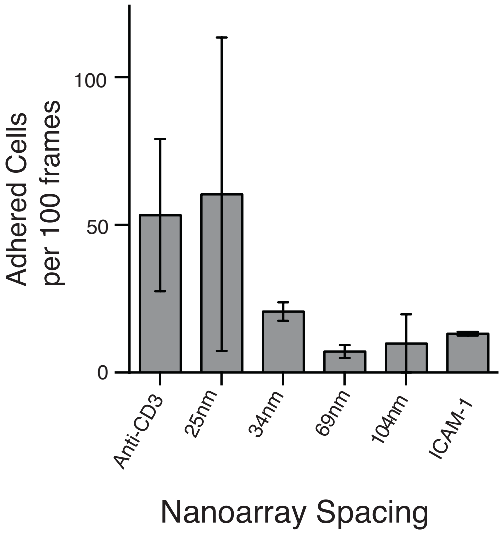

Figure 7.4.9: Adhesion as a function of anti-CD3ε spacing. Number of cells per unit area, 100 frames is equivalent to 661456.9 μm^2. Error bars shown are the standard error in the mean. The relatively large error bar in the 25nm sample is attributed to poor sample handling in one of three repeats.

As nanoarray spacing is increased, the number of cells adhered to each substrate decreases. This correlation further supports the phosphotyrosine evidence; as an additional indication that cell response to substrates is enhanced when the ligands are spaced closely together. The spatially dependent decrease in cellular adhesion could be due to inside-out activation of LFA-1, the cognate receptor for ICAM-1. This occurs when stimulation with the TCR induces signaling leading to stronger ICAM-1 mediated adhesion. Although the timescale for these experiments is relatively short, LFA-1 and ICAM-1 interaction has a bond lifetime of seconds, and LFA-1 engagement can increase the T cell antigen sensitivity up to 100-fold, so it is plausible that inside-out activation and receptor cross-talk can occur on the timescales used for these experiments.[507, 508, 334]

Previously, we showed that closely spaced nanoarrays of CD3 ligands did indeed induce greater activation in T cells. A possible hypothesis could therefore be that with closely spaced nanoarrays, T cells become more activated, leading to stronger ICAM-1 adhesion, and so average cell numbers per unit area are increased.

There are several possible theories to explain why T cells are more activated on closely spaced nanoarrays, including a minimal ligand engagement number being required per cell or per signaling focus, the required concatenation of TCR/CD3 nanodomains for sustained signaling, and mechanosensitive signaling through the TCR/CD3 bond. These hypotheses were described earlier in relation to the NK cell results (Chapter 6), and are discussed in detail in relation to T cells below.

The surfaces presented here showed that T cell activation has fallen to background levels when CD3 ligands were anchored 69nm apart. Substrates with 69nm and 104nm nanoarrays represent surfaces with a nanoparticle density of approximately 200-100/μm^2 respectively. T cell contact areas with activatory surfaces are usually much larger than 1μm^2, and so we can assume that each cell will be exposed to at least 100 particles on even the largest spaced nanoarrays. If we assume all nanoparticles are functionalised with at least one CD3 ligand, the number of TCR/CD3 engaging ligands presented here per T cell far exceeds the minimal number of ligands known to induce activation. There is a wealth of evidence to suggest that TCR signaling, downstream Zap-70 recruitment and CD45 exclusion can occur with only 1-4 agonist ligands per μm^2,[294, 481, 325] and so it is unlikely that the number of ligands per cell is the cause of the spatial response seen here.

A similar hypothesis suggests that there is a minimum number of ligands required per individual signaling focus rather than per cell.[335] TCR/CD3 has been shown to exist on T cells in protein domains of the nanoscale order, with data suggesting that these nanodomains are approximately 35-70nm across.[374, 375, 328] If each of these TCR/CD3 nanodomains requires a minimum number of engaged receptors per cluster in order to signal, this could explain our results. If we assume that each nanodomain can bind multiple receptors within its domain area, 25nm and 34nm particle arrays would allow multiple nanoparticle ligand-receptor anchoring points per cluster, whilst 69nm and 104nm spacing would allow ligation with only a single nanoparticle. This could explain the sharp threshold seen at 69nm, however is difficult to reconcile with the details of T cell signaling being stimulated through only a few receptor-ligand engagement interactions.[325, 481]

There is an alternative explanation, which suggests that for signaling to occur, several different protein nanodomains must concatenate together. The concatenation of CD3ζ and Lat nanodomains as a mechanism of activation in quiescent T cells has already been postulated,[328] however the requirement for pre-existing clusters of Lat for early stage T cell activation is questionable, [330] alternatively, it may be that several TCR/CD3 nanodomains are required to concatenate for activation to occur.

Assuming that each nanoparticle is capable of anchoring a TCR/CD3 nanodomain through CD3ε-ligand engagement, substrates with anti-CD3ε spacing of 104nm would only allow interaction with one nanoparticle, and one locality with ligand-receptor pair interaction, per TCR/CD3 nanodomain. This domain would be anchored by the ligand attached to the gold nanoparticle to the non-mobile surface, beyond the minimal distance to the next domain, preventing domain amalgamation. Spacing of 69nm presents an intermediate situation, where domain overlap could occur based on the exact domain size, with domains of approximately 70nm some concatenation/overlap could occur, for domains much smaller than this (~35nm across) the region of overlap between protein islands would be minimal. In all cases, nanoparticle arrays of 25 and 34nm shown here present anchoring points close enough to allow nanocluster concatenation. It may be that concatenation of nanodomains, either pre-formed TCR/CD3 domains coming together, or multiple TCR/CD3 nanodomains combining with clusters of other signaling proteins such as Lat on the cell surface, is required for cellular activation. The absolute measurement of TCR cluster size and the mechanism of TCR lateral diffusion around T cell membrane surfaces remain provocative questions, [509, 481, 325, 510, 329] however if we assume the minimum size of a TCR/CD3 protein island is 35-70nm [374, 375, 328] we can fit our data to a theory of protein island coalescence.

Finally, the differential response to nanoarrays may be due to the mechanical sensitivity of the TCR. TCR triggering can be induced by surface bound, but not soluble, agonist,[287] suggesting that the ability to resist a cytoskeletally applied force may be important to TCR function. Several groups have also identified that the TCR is a mechanosensitive receptor[281, 331, 294, 511, 287, 512] and that T cell activation is augmented by interaction with stimulatory ligands presented on “softer” substrates.[280] If we assume that cells interact with substrates through a number of TCR-ligand pairs across a domain area, substrates with smaller inter-particle spacing present more anchoring points per unit area. In turn, this means that the force generated on each ligand–receptor pair will be reduced for that substrate in comparison to surfaces with greater inter-ligand, and so ligand-receptor pair, spacing per nanodomain.[106] The potency of the CD3ε-ligand interaction could therefore be directly related to the mechanical force applied during the interaction in a similar way to other mechanosensitive receptors and signaling components, such as the catch bond[233, 285, 286], where a specific level of force initiates optimal signaling.

7.4.3 Phenotypic segregation on nanopatterns

There is evidence to suggest that T cell sensitivity, and therefore responsiveness, can be driven by prior exposure to antigen.[272, 513] Figure 7.4.10 demonstrates the phenotypic response to nanopatterned CD3ε engaging ligand arrays after five minutes incubation. We analysed all adherent cells per nanopattern spacing, and then calculated the percentage of those adherent cells expressing CD45RA, a marker for T cell naivety.

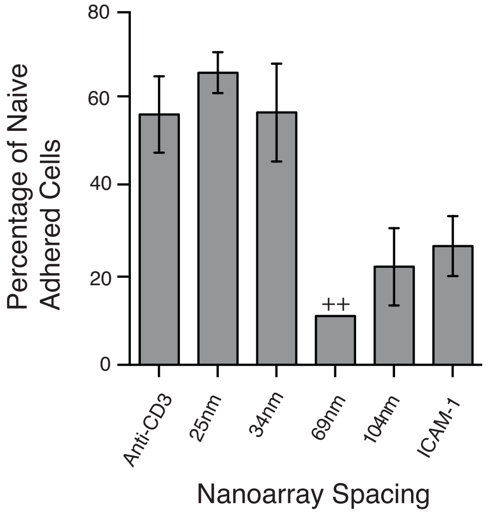

Figure 7.4.10: Phenotype as a function of anti-CD3 spacing. Percentage of CD45 positive adhered cells.

As the spacing of anti-CD3ε increased from 25 to 104nm the proportion of naïve cells (Figure 7.4.10) in the population decreases, separate from the general decrease in cellular adhesion described earlier (Figure 7.4.10). There are several possible explanations for this enrichment of memory cells at larger inter-ligand spacing based on both pre-existing levels of surface bound LFA-1, and different sensitivity to the nanopattern environment.

A plausible explanation lies in the LFA-1 ligand expression per cell type; naïve cells express less LFA-1 than memory cells.[506, 513, 272] As nanoscale spacing of CD3ε ligands increases, the level of inside-out CD3 engagement driven ICAM-1 mediated adhesion decreases, discussed earlier. With this decrease in ICAM-1 adhesion sensitivity, naïve cells do not have enough basal surface LFA-1 to remain engaged with the surface.

Separately, the differential response of the interaction at the TCR/CD3 could augment this phenotypic difference. Naive T cells require stronger stimulation in order to activate when compared to pre-stimulated cells.[272, 513, 514] The exact cause of the differential sensitivity to CD3 engagement by naive and memory cells remains to be elucidated, however may be due to the differences in surface based TCR distribution or

TCR oligomer size.[500] This may mean that a memory T cell is able to induce inside-out mediated ICAM-1 adhesion in response to antigen at greater CD3 ligand spacing, as it is requires less stimulation than a naive cell. In addition to the intrinsic differences in LFA-1 levels, this would make the memory cells more able to engage with nanopatterned substrates with lower stimulation potential than naive cells.

An alternative explanation can be found in the outside-in signaling mechanism. ICAM-1 engagement with LFA-1 mediates outside-in signaling by co-stimulating cytoskeletal processes that bring T cell signaling proteins to the immunological synapse.[60] In other cell types, this has been known to lower the threshold for activation and is key in programming CD8+ sensitivity.[515, 60] Both CD4+ T cell phenotypes will therefore respond to the ICAM-1 in the background by reorganising signaling receptors at the interface, which will augment responses to CD3 engagement on surfaces. Although these substrates present constant levels of ICAM-1 in the background, the memory and naive cells have different levels of surface LFA-1 expression, and so the memory cells are likely to be undergo more outside-in signaling, augmenting the differential adhesion.

It is likely the mechanisms described here are complementary and cyclical. Though the time scale for these experiments is too short, long term co-stimulation with ICAM-1 has also been shown to generate increased numbers of memory cells in the population.[514, 273] Whether naïve cells stimulated on these different CD3 engaging surfaces differentiate into different phenotypes based on the level of activation is an interesting question. Given the phenotypic variation with spacing, this offers the exciting possibility that these substrates could be used as a new method to isolate cell-subtypes. Furthermore, they could also be used as a tool to probe cellular education and naïve-memory differences in T cell development.

7.4.4 Functionalisation with F(ab') fragments

Earlier, we described the digestion of whole antibodies to produce F(ab')$_2$and F(ab)' antibody fragments; the F(ab')$_2$ fragments were then bound to gold nanoparticles through the disulfide hinge region. Here, we investigate the functionalisation of gold nanoparticles with monovalent F(ab') fragments in an alternative approach. F(ab') fragments are traditionally produced using enzymatic digestion with papain or pepsin.[516, 517, 489, 518] The generation of fragments using enzymatic digestion is not simple; the various IgG subclasses react differently to enzymatic digestion, and production of heterogeneous fragment mixes often occurs when reduction is not tightly controlled.[516] For these experiments, TCEP was chosen as a reductant due to its relatively short incubation times and sulfur free nature (as sulfur containing contaminants could interact directly with the gold). Generation of reactive F(ab)' fragments from F(ab')$_2$ antibody portions was optimized using TCEP to fragment UCHT-1 antibody, capable of binding the CD3ε component of the TCR complex, as described in the Materials and Methods section. Studies have shown that once fragmented, F(ab)' fragments are capable of binding with additional free thiols to reform disulfide bridges[31, 519] or can be bound directly to gold substrates for immunosensing applications.[490, 491, 489, 403] We used fluorescently labeled antibody fragments to bind passivated gold nanopatterns (Figure 7.4.11) in an analogous way to the F(ab')$_2$ system described earlier.

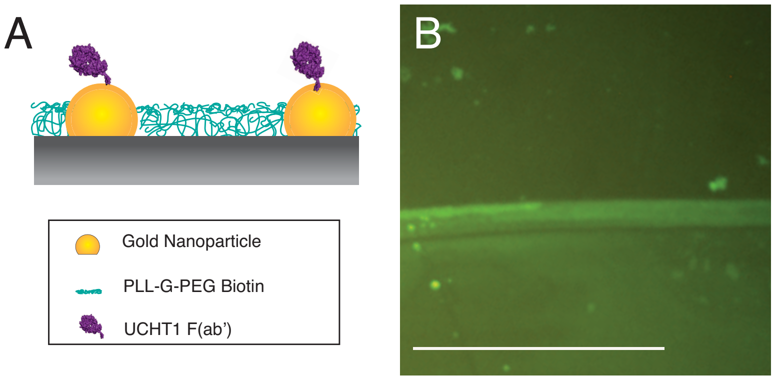

Figure 7.4.11: Gold nanopattern functionalisation. (A) Schematic of gold nanopattern surfaces functionalised with F(ab') fragments and (B) fluorescent micrographs of surfaces passivated with PLL-g-PEG and incubated with fluorescently labeled F(ab') fragments. Scale bar 200µm.

Figure 7.4.11 indicates the successful functionalization of gold nanopatterns with F(ab') fragments, producing surfaces with monovalent antibody fragments bound to gold nanoparticles. Although this technology offers increased versatility in immobilisation strategies, these surfaces do not yet offer a complementary system for cellular studies. Whilst it would be very interesting to compare the cellular response to nanomaterials functionalised with either bivalent or monovalent CD3 fragments over a variety of lengthscales, currently it is not possible to quantify the exact number of antibody fragments attached per individual gold nanoparticle. With advances in super-resolution microscopy it may soon be possible to confirm that a single F(ab') fragment is bound per nanoparticle, as depicted schematically. Functionalisation with specific secondary antibodies in conjunction with super-resolution techniques could also determine the percentage of these F(ab') fragments that are in an active conformation. Once these studies have been completed, and the exact number of F(ab') fragments bound per nanoparticle determined, we will be able to compare the cellular response to bivalent and monovalent nanopattern arrays. Without this data, it is difficult to draw robust conclusions from comparisons of cellular responses to the different functionalisation methods, and so the F(ab') cellular experiments have yet to be completed.

7.5 Conclusion

We have demonstrated the functionalization of nanopatterned arrays with anti- CD3ε fragments and have illustrated that the CD4+ immunogenic response to these materials is dependent on the inter-ligand spacing.

CD4+ cells show decreasing levels of phosphotyrosine signaling as the spacing of CD3 ligands increase, where signaling at 69nm and 104nm is not significantly greater than signaling on ICAM-1 backgrounds. Similarly, as the spacing of these ligands increases to 104nm, the cellular response measured by adhesion decreases to not significantly above background; the threshold for these effects seems to lie at 69nm.

There is also an interesting difference in the response of different phenotypes to these surfaces, where the cellular population is sensitive to the nanoscale inter-ligand spacing of CD3 ligands. A decreasing proportion of naïve cells in adherent cell populations is closely correlated to an increase in spacing between adjacent receptor engaging sites.

Whilst the exact physiological cause of this nanoscale sensitivity remains open to debate, our results are consistent with cell triggering being most responsive to surfaces where ligands are positioned to enable nanodomain concatenation, engage multiple sites within one nanodomain, or reduce CD3-ligand mechanical strain through multiple ligand-receptor pair engagement per signaling focus. It may be that there is a complex interplay between these parameters, however given the similarity of these results to the recently identified NK engagement threshold (between 69-104nm, Chapter 6) there is some indication that signaling in both innate and adaptive immune cells is sensitive to these ligand-engagement factors. These results demonstrate the first studies on early stage T cell responses and have interesting implications for the future direction of immunotherapies which can augment T cell activation.

7.6 Future Work

This work has focused primarily on monitoring early time point responses to CD3 engagement. Investigation into whether these nanopattern interfaces can also induce full activation, as determined by cytokine secretion, would be an obvious next step. Work completed simultaneously by collaborators on two slightly different systems (one using anti-MHC and one using anti-CD3 immobilised in an orientated fashion by NTA linkers) on gold nanoarrays confirm that inter-ligand spacing thresholds of the same order are key to inducing activatory responses in T cells, and suggest that the immobilised F(ab')$_2$ fragments used in our system are also bound in an accessible and orientated manner.[520, 521] The verification that both anti-CD3 and anti-MHC functionalized nanopatterns show a signaling dependence on inter-particle spacing in the 100nm lengthscale indicate that the nanospacing is important for both parts of the TCR/CD3 complex.

Immediate future work could include the direct comparison of the CD4+ cells with human cytotoxic T cells, and indeed other lymphocytes of the adaptive immune system. Additionally, the identification of differences in the sub-population response to these immunogenic materials offers the exciting possibility that substrates of this type could be used to investigate T cell education and sensitivity through sequential stimulation with nanopattern environments.

In order to determine whether it is cluster size, inter-ligand spacing, or the mechanical interaction with the substrate driving this sensitivity, each of these parameters will need to be tested individually. The advanced µCP substrates developed earlier (Chapter 4) could be used to test the effect of varying the local ligand spacing whilst maintaining the global ligand density, in order to see if it is in fact a nanocluster based integration threshold that drives the spacing response seen here.

Additionally, it would be interesting to test whether the formation of a stable artificial immune synapse capable of leading to cellular interaction is dependent on the mechanical transduction of force at multiple stable anchoring points as suggested. By disturbing the cells mechanosensing apparatus, or presenting the cell with substrates of varying rigidity, this could be investigated. The identification of some of the minimal stimulation requirements described here offers insight into immunological cell development.

Chapter 8

Microscale Mechanical T Cell Stimulation

Rigidity Controlled Spherical Particles for T Cell Activation

8.1 Introduction

Many cell types show sensitivity to the mechanical properties of their environments.[73, 70] The differential response of cells to substrates with varied rigidities has been used to direct growth and phenotypic differentiation in hematopoietic and mesenchymal stem cells, where activation and lineage are orchestrated by mechanical cues, discussed extensively in Chapter 2: Introduction.[62, 522, 523, 66, 524, 67, 63, 279, 69, 525, 526, 527, 71] Recently T cells,[280] B cells[282] and their precursor hematopoietic stem cells[62] have also been shown to respond selectively to stiffness controlled substrates; specifically, T cell activation and proliferation is augmented on substrates with “softer” matrices.

The differential response of T cells to TCR stimulation through substrates of different rigidities is likely due to the mechanosensitivity of the TCR. Several immune receptors have been identified as mechanosensitive, where engagement of receptors with their cognate ligands is sensitive to the force applied through each bond,[233] with the leukocyte catch bond in LFA-1-integrin binding being a well established example of cellular response to force applied through individual receptors.[286, 285] Interestingly, TCR-ligand affinity has recently been shown to play a major role in determining cellular activation levels, with low affinity ligand interactions resulting in different phenotypes[6] caused by currently undefined mechanisms. Together, this evidence suggests that T cell responses can be controlled by variations in the nature of the TCR-ligand engagement, and that stimulation may be augmented by softer substrates.

The ability to augment proliferation and activation in immune cells is of great interest for clinical immunotherapy applications.[528, 238, 529, 530, 234] New approaches to cancer therapies are focusing on the *ex vivo* expansion of selected immune cells for re-injection into patients. One approach involves the genetic modification of a patient’s T cell to express an activating surface receptor, termed a Chimeric Antigen Receptor (CAR), for specific leukocyte cancer markers.[531, 234, 532, 235, 533, 534] With this technique, a patient can undergo autologous transfer of their own modified T cells, and several clinical trials have indicated this a promising therapy in a range of leukocyte cancers. Given that this technique requires the *ex vivo* expansion and controlled activation of T cells, the development of advanced culture systems that can enhance activation and proliferation are paramount to delivering next generation therapies.

Some current clinical practice in adoptive immunotherapy involves the *ex vivo* expansion of T cells with stimulatory ligands before re-injection; stimulatory ligands can be presented in several forms, however a recent development is the use of magnetic polystyrene beads. These substrates allow stimulation in culture and easy separation of stimulants in applied magnetic fields, [535, 238] additionally, they mimic the natural conformation of APC-T cell engagement that occurs *in vivo.*[233, 280, 239] This chapter describes the design and fabrication of small, spherical hydrogel particles with controlled mechanical properties suitable for cell culture in suspension as an analogous tool for T cell activation. Additionally, T cell responses to CD3 engagement using these materials, termed “beads”, as culture substrates is investigated.

8.2 Contribution statement

The work reported in this chapter was supported by the following people;
Rheometry measurements were performed on bulk substrates made by, and measured by, Sajjad Jaffer.
Sizing measurements were performed by Derfogail Delcassian and Sajjad Jaffer on samples made by Derfogail Delcassian and Sajjad Jaffer.
PEGDA-700, PEGDA-6000 and bead formation methodology was developed by an MSc student, Octave Etard, and aspects of this work are reported in the MSc thesis “Hydrogel Micro-Spheres for Tissue Culture Applications, Octave Etard”. Fabrication of other PEGDA formulations was extended by Derfogail Delcassian and Sajjad Jaffer. Biofunctionalisation and cellular experiments were performed by Derfogail Delcassian.

8.3 Materials and Methods

8.3.1 Bead fabrication

Poly (ethylene glycol) diacrylate (PEGDA) of 700, 6000 or 35000 molecular weight (Sigma Aldrich) was dissolved in Phosphate Buffered Saline (PBS) at between 1:1 to 1:4 w/v%, and is termed the aqueous phase. UV initiator Darocur (Sigma Aldrich) added at 10% v/v. The oily phase was formed by adding between 0.1-50% w/v mannide monooleate (Sigma Aldrich) to mineral oil. 50µL of this aqueous phase was added to 500µL of the oily phase, and vortexed thoroughly for 1 minute. The solution was immediately exposed to UV radiation (365nm) approximately 20mm from source for 10 minutes. The particles formed were then resuspended in xylene, and washed and centrifuged 3 times with each of the following phases; xylene, ethanol and PBS at between 3000 and 7500rpm. Beads were then left to swell overnight in clean PBS solution, and concentration measured with a Haemocytometer. For biofunctionalisation, the aqueous phase was prepared with a mixture of PEGDA and streptavidin acrylamide at molar ratios of 1-4 times the number of free acrylate groups. Streptavidin acrylamide solutions of 100mg/10µL in PBS were used as stock solutions.

PEGDA Mw	Mass (µg)	Vol. PBS (µL)	Vol. Darocur (µL)	Vol. Strep. Acrylamide Stock (µL)
700	100	164	15.4	5.3
6000	100	192	10	8.1
35000	100	384	20	16.2

Table 8.3.1: Molecular weights of PEGDA and aqueous phase components.

PEGDA Mw	Ratio of aqueous: oil phase	Surfactant in oil phase	Bead Diameter (µm)
700	1:10	1%	11
6000	1:10	50%	15
35000	1:10	50%	45

Table 8.3.2: PEGDA bead formation; oily phase composition and typical bead size.

8.3.2 Bead functionalization

Streptavidin-functionalised beads were re-suspended at 1x10^6 in PBS containing biotinylated proteins in combinations of 5µg/ml anti-CD3, 5µg/ml anti-CD3 and 5µg/ml anti-CD28 or 5µg/ml anti-CD3, 5µg/ml anti-CD28 and 10µg/ml anti-ICAM-1 for 1 hour. For fluorescence visualisation 5µg/ml anti-CD16 labeled with Alexafluor 488 (Invitrogen) was used. Beads were then washed 3 times in PBS and re-suspended in cell media before incubation with cells. Alternatively, conjugated beads were resuspended in PBS in small centrifuge tubes. 100µL bead solution was extracted at time points of 0, 1, 2, 4, 6, 24 hours and spun at 5000rpm for 5 minutes. The supernatant was then added to a 96 well plate and fluorescence measured using a Perkin Elmer plate reader at excitation 488nm and emission 535nm. Fluorescent beads were imaged with an Olympus 1X51 microscope with DP70 camera.

8.3.3 Size analysis

Beads were sized using a Multisizer and analysed with Mastersizer 2000 software. 500µL of bead solution at concentration of 1x10^6/ml was used, with a minimum laser obscuration of 2%.

8.3.4 Bulk Mechanical Measurements

Bulk hydrogel disks were made in 8mm circular molds at 2mm depth, using the aqueous phases prepared earlier. Disks were cured as described, and left to swell overnight in water. Post-swelling, disks were measured for volume increase, and storage and loss modulus determined as a function of angular frequency using a parallel plate rheometer (TA instruments).

8.3.5 Cellular studies

Jurkat cells transfected with an NFAT-GFP reporter (cells transfected and a gift of Prof. Mike Milone, University of Pennsylvania, NFAT-GFP reporter a gift of Prof. Wendell Lim, UCSF) were routinely cultured in RPMI media supplemented with 10% Fetal Calf Serum (FCS) and 1% Antibiotics and Antimycotics. Cells were counted and re-suspended at 1x10^6 /ml in fresh supplemented RPMI media. Tissue culture plastic wells were incubated with 5µg/ml CD3 for 1 hour at 37°C, then rinsed with PBS. 100µL of cell suspension was added per well and incubated at 37°C for between 1-24 hours. Wells were fixed by adding equal volume of 4% Paraformaldehyde (Sigma Aldrich) for 10 minutes, then added to 1ml cold PBS until analysis. To determine the cellular response to beads, cells were incubated in positive control wells as described above, and unfunctionalised tissue culture plastic wells as negative controls. 50µL of cell suspension at $0.05\text{x}10^6$/ml concentration was added to 50 µL of $0.15\text{x}10^6$/ml bead solution such that the overall ratio of beads to cells was 3:1 per condition, and mixed in unfunctionalised wells. Wells were left to incubate for 8 hours before being fixed with PFA as described. Samples were analysed on a Fortessa Flow Cytometer using the FACSDiva software, where positive and negative gates were drawn for the controls of each experiment.

8.4 Results and Discussion

8.4.1 Bead Fabrication

The ideal hydrogel cell culture particle should be largely protein resistant, however functionalisable with specific stimulatory ligands so that chosen activatory receptors can be investigated. PEGDA was chosen as the material of the hydrogel particle due to its protein resistant nature and well documented use in hydrogel fabrication.[536, 132, 147, 537] Figure 8.4.1 shows the chemical crosslinking method used to form PEGDA hydrogels.

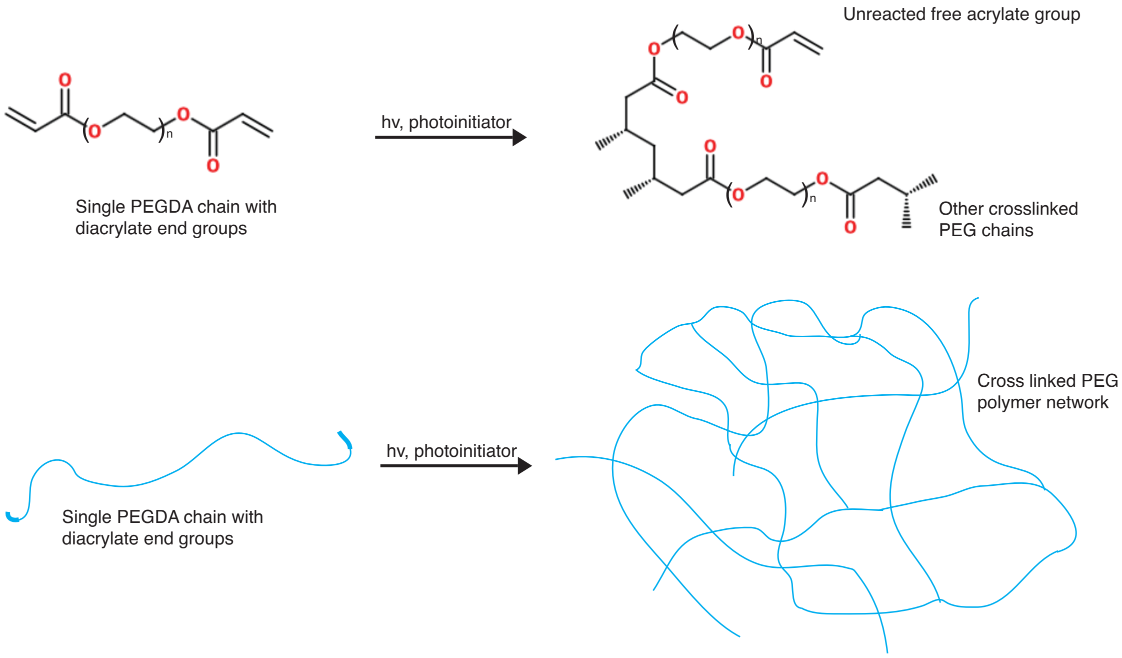

Figure 8.4.1: Schematic showing the PEGDA crosslinking mechanism and the chemical reaction undergone at the acrylate groups. Orientated bonds indicate additional crosslinking not shown.

An additional desirable feature is the ability to separate these particles easily from cell suspension, in an analogous method to that used with commercial polystyrene particles; the inclusion of magnetic material within the particle can therefore be envisaged and was carried out by Octave Etard (data not shown). In order to fabricate small spherical particles, encapsulation of the PEGDA polymer before UV curing is required. The microemulsion method was used to encapsulate the PEGDA material; this allows the particle size to be controlled by surfactant concentration. An increased proportion of surfactant in solution allows smaller volumes of PEGDA material to be encapsulated, as a larger surface area of PEGDA aqueous phase can be stabilised in the oily phase (Figure 8.4.2.) leading to the formation of smaller particles at the same overall aqueous volume. For these experiments, microparticles between 5 and 50μm in diameter are desired, typical particle size distribution is shown in Figure8.4.3, and Tables 8.3.1 and 8.3.2 in the Materials and Methods section details the exact surfactant concentrations used in these experiments.

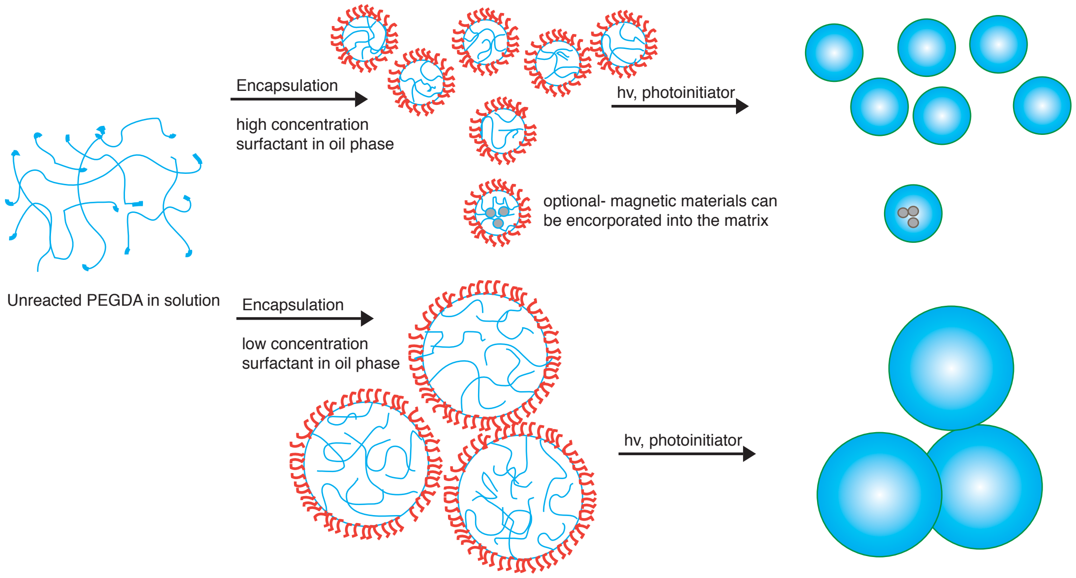

Figure 8.4.2: Schematic showing PEGDA microsphere formation through water-in-oil microemulsion method. When PEGDA aqueous phases are exposed to mineral oil with high concentrations of surfactant, many smaller stable particles can be formed. Conversely, lower surfactant concentrations result in larger particles being formed as the aqueous phase volume is packaged within surfactant stabilised microspheres before UV curing. Additionally, incorporation of magnetic material such as magnetite in the PEGDA phase allows magnetic particles to be encapsulated within the microsphere.

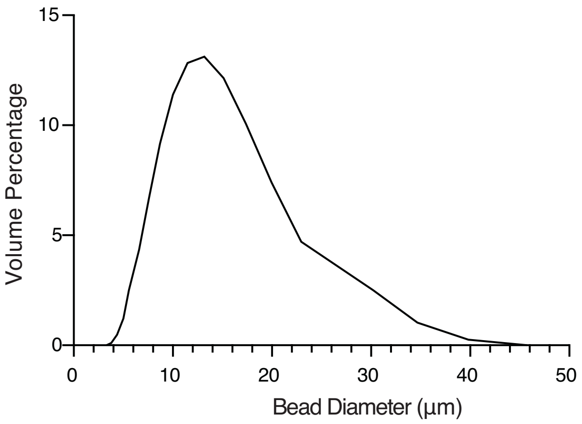

Figure 8.4.3: Particle size analysis of hydrogel bead populations using multisizer laser diffraction. Sample prepared by Derfogail Delcassian and Sajjad Jaffer. Size measurements performed by Sajjad Jaffer. Size analysis and plot by Derfogail Delcassian.

These particles show a narrow size distribution around the 12μm scale, indicating a range of particle sizes are formed. Importantly, all of the particles are above 3μm in diameter. This cut-off is key, as particles smaller than this can cause cytotoxic effects through endocytosis. Additionally, centrifugation can be used to remove very small particles if required. The surfactant method described here allows control of the bead size in a range of polymer molecular weights, average sizes of beads fabricated for these experiments are shown in Table 8.3.2 in the Materials and Methods section.

The ability to control the mechanical properties of these materials is essential to determine if the stiffness of microscale materials also has an effect on cellular activation. In this instance, mechanical properties were controlled by the length of PEGDA macromolecule units, where longer PEGDA chains resulted in lower bulk Young's Modulus values at maximal crosslinking. The rigidity values are based on properties of the bulk material (Appendix E) fabricated using identical aqueous phase and curing conditions, as the small particle size (between 5-50μm in diameter) renders traditional rheometry impractical. The material formed is highly elastic, where the storage modulus is much greater than the loss modulus at relevant angular frequencies, and beads with controlled rigidity between 3-5kPa and 2000kPa (shown in Table 8.4.1) have been formed.

PEGDA molecular weight	Young's Modulus (kPa)
700	2000
6000	200
35000	3-5

Table 8.4.1: Hydrogel rigidity as a function of PEGDA molecular weight. Young's Modulus measured on bulk samples prepared by and measured by Sajjad Jaffer.

The fabrication of spherical beads on the microscale with controlled geometry and mechanical properties provides a platform technology for investigation into the effects of mechanically controlled substrates on T cells. Due to the protein resistant nature of the PEGDA, additional chemistry needs to be employed in their fabrication in order to render them specifically functionalisable. The next section discussed the selective functionalisation of these bead materials.

8.4.2 Bead Functionalisation

A selective attachment mechanism that allows incorporation of the ligand into the bead surface is required to investigate mechanical sensitivity through specific receptors.[89, 43] Biotin-streptavidin binding is a powerful conjugation tool and one that has already been used in cellular studies in this thesis (Chapter 6: NK cells) Cross linking streptavidin into the PEGDA polymer matrix (Figure 8.4.4) enables biotinylated proteins to be bound to the accessible streptavidin on the bead surface.

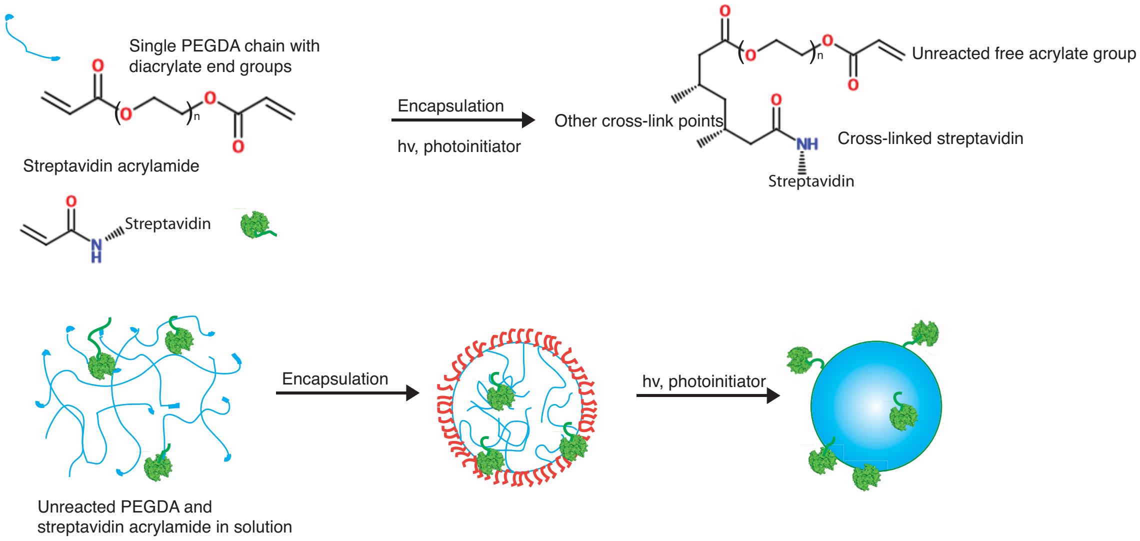

Figure 8.4.4: Schematic showing PEGDA and streptavidin acrylamide chemical crosslinking, and expected incorporation into the bead matrix.

In order to maintain equivalent streptavidin concentration across all rigidities and bead sizes, the swelling ratio of bulk material was calculated. Substrates with longer PEGDA molecular weight chains can swell more than their shorter chain equivalents, so increased concentration of streptavidin per aqueous phase is required to maintain equivalent numbers of streptavidin molecules per bead unit surface area. Details of the streptavidin concentrations are shown in Table 8.3.1 in the Materials and Methods section. The accessibility of the streptavidin on the bead surface was tested using fluorescently labeled small biotin molecules, and fluorescently labeled antibodies shown in Figure 8.4.5. The smallest beads in this figure are 4.1µm in diameter, and so above the minimal diameter threshold described earlier.

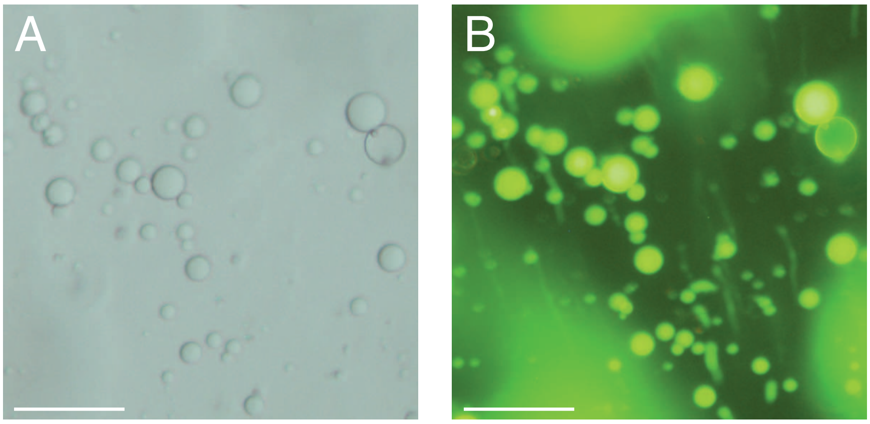

Figure 8.4.5: Bright-field (A) and fluorescent (B) images of hydrogel microsphere particles. Scale bar 50µm.

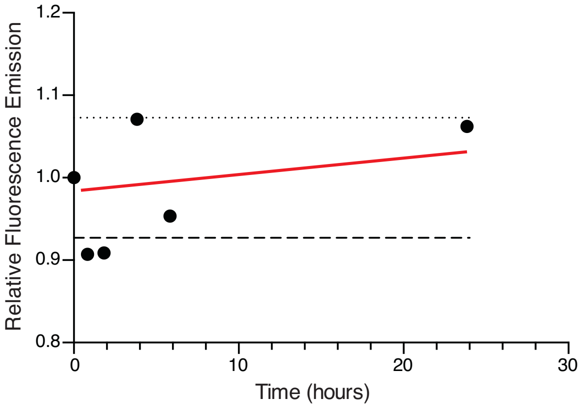

Figure 8.4.6: Fluorescence emission (and antibody release) from the bead over time. Dots are average emission values at relative time-points, red line is the line of best fit, excitation 488nm and emission 535nm. Dashed lines represent maximal and minimal variation from time zero. Maximal and minimal lines were calculated from the emission variations from average of nine blank wells.

Clear functionalization of the polymer matrix is seen in Figure 8.4.5, indicating the streptavidin moiety is available on the surface for binding. Due to the porous nature of the PEGDA material (a polymer matrix swollen with water) there is some possibility that the biotinylated antibody does not bind to the streptavidin but instead diffuses into the hydrated bead. This could mean that rather than acting as a rigidity controlled substrate, the bead acts as a drug delivery vehicle, releasing antibody over time. In order to test this hypothesis, beads functionalised with biotinylated fluorescent proteins were incubated at room temperature for 24 hours, and supernatant analysed by fluorescence emission at regular time points (Figure 8.4.6) Analysis of these results shows that the fluorescence intensity of the supernatant remained relatively constant, small fluctuations in emission were within those observed in blank control wells, and so antibody was not leached into the solution over time. The bead conjugation is therefore stable for up to 24 hours. Additionally, this data showed that the functionalisation and rinsing procedure were sufficient to remove excess unfunctionalised antibody during the conjugation step. Beads functionalised by this method were then used to investigate cellular response to mechanically controlled ligand presentation.

8.4.3 NFAT-GFP response to stimulatory surfaces (control experiments)

Cellular response to stimulatory materials was measured using Nuclear Factor of Activated T cell (NFAT) expression. NFAT is a transcription factor regulated by calcium signaling, and a result of stimulation of activatory pathways. For this project, a genetically modified T cell line was produced through transfection with NFAT-GFP, (NFAT-GFP cells produced by Prof. Mike Milone *et al*, University of Pennsylvania as described in the Materials and Methods section) which fluoresces green on expression of the NFAT protein. The level of fluorescence can therefore be monitored by expressed conjugated green fluorescence protein (GFP) levels as a measure of NFAT expression (and so activation) inside the cell. A time course of NFAT expression for these cells on tissue culture plastic functionalised with stimulatory antibodies (Figure 8.4.7) indicated that there is a fluctuation in NFAT expression across a range of time points. A relatively stable region of NFAT expression occurred between 7 and 9 hours, correlated with activation on planar surfaces using standard methods with anti-CD3 antibodies. The 8 hour time point (indicated by a red line in Figure

8.4.7) was therefore chosen as a comparative time point and the percentage of cells expressing NFAT-GFP at this point termed the marker for activation.

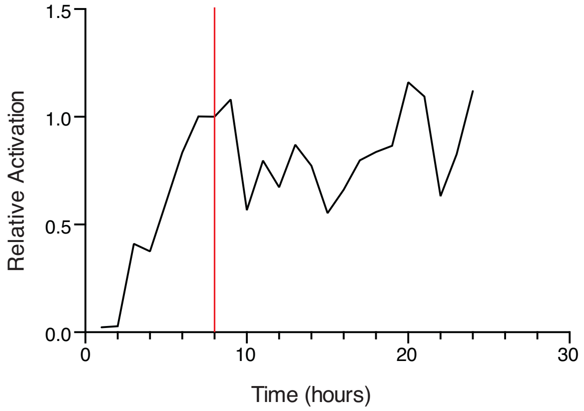

Figure 8.4.7: NFAT-GFP expression was monitored over time. Cells were incubated with planar OKT3 anti-CD3 antibody on tissue culture plastic and relative expression monitored. The red vertical line represents the 8 hour time-point chosen for cellular experiments.

8.4.4 Cellular response to beads

Cells were incubated with beads of differing rigidities functionalised with a range of stimulatory antibodies, and cellular response measured by NFAT-GFP expression though flow cytometry (Figure 8.4.8, Figure 8.4.9) where positive and negative gates were drawn based on cellular responses to standard tissue culture plastic controls.

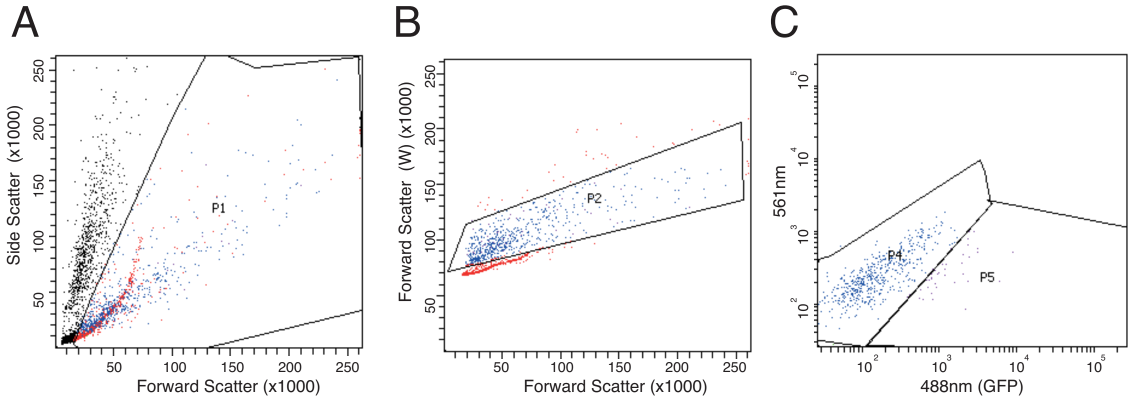

Figure 8.4.8: Flow cytometry gates used to analyse cellular activation. (A) Forward scatter vs side scatter, positive gate (B) Forward scatter vs forward scatter width, positive gate (C) 2-Dimensional 488nm scatter for GFP expression, negative (P4) and positive (P5) gate.

Figure 8.4.8 shows the flow cytometry gates used for these experiments. Figure 8.4.8(A) shows the forward scatter vs side scatter plot, where the dead cells, debris and aggregates are removed from the population. Figure 8.4.8 (B) shows the positive gate for selection of cell sized material, there is a tight band of red indicating the bead particles, which are picked up by the flow cytometer due to their comparative size. The tight clustering indicates that these particles have a narrow size distribution, and their position outside of the positive gate means they can be separated from the cellular population for analysis. Alternatively, the beads could be identified through fluorescent markers tethered to their surface, which would also allow elimination from analysis. Figure 8.4.8(C) shows the 2-Dimensional gate used to identify GFP positive and negative populations, based on responses to planar tissue culture plastic functionalised controls. Beads functionalised with a range of conjugated antibodies were then used to stimulate T cells in culture, and NFAT-GFP expression in response to culture with mechanically varied stimuli analysed, as seen in Figure 8.4.9.

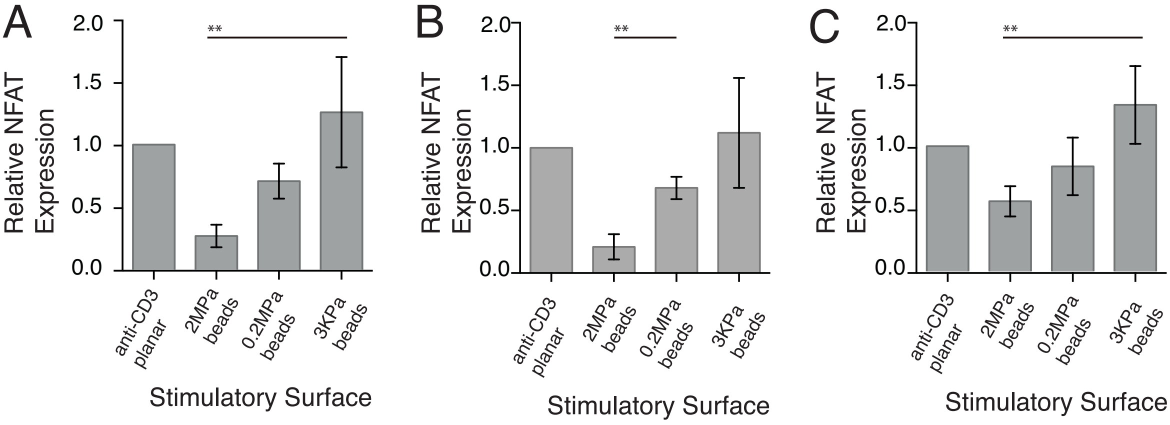

Figure 8.4.9: Cellular response to microscale rigidity controlled beads. Graphs show mean NFAT expression (normalised to planar anti-CD3 OKT3 controls) on beads functionalised with (A) anti-CD3, (B) anti-CD3 and anti-CD28 or (C) anti-CD3, anti-CD28 and ICAM-1 at 8 hours time-points. Error bars show the standard error in the mean across experiments. Statistical analysis *** p<0.001, ** p<0.01, * p<0.5

The response of the cells to stimulation on bead substrates (Figure 8.4.9) shows a clear trend of increasing activation, as measured by the relative number of cells expressing the NFAT-GFP construct, as the rigidity of the substrate decreases. On beads functionalised with anti-CD3, or anti-CD3, anti-CD28 and ICAM-1, the cellular activation on softer substrates is significantly greater than stiff substrates. Our results show maximal activation at around 3-5kPa, where only 2000kPa, 200kPa and 3-5kPa have been investigated. Additionally, soft substrates with Young's Modulus around 3-5kPa induce activation greater than the standard functionalised tissue culture plastic. It is important to note that the cells did not respond to unfunctionalised beads of varying stiffness values (data not shown) and so this substrate sensitivity must be mediated in part through the CD3 receptor.

In vivo T cell-APC cellular contact is maintained through a variety of cell surface receptors, including the co-stimulatory molecules which augment activation and adhesion molecules to hold cells in contact more firmly. The effect of beads functionalised with combinations of anti-CD3, co-stimulatory molecule anti-CD28 and LFA-1 integrin adhesion ligands ICAM-1 was compared (Figure 8.4.10) at each rigidity to determine if cellular response was enhanced on substrates with increased functionality.

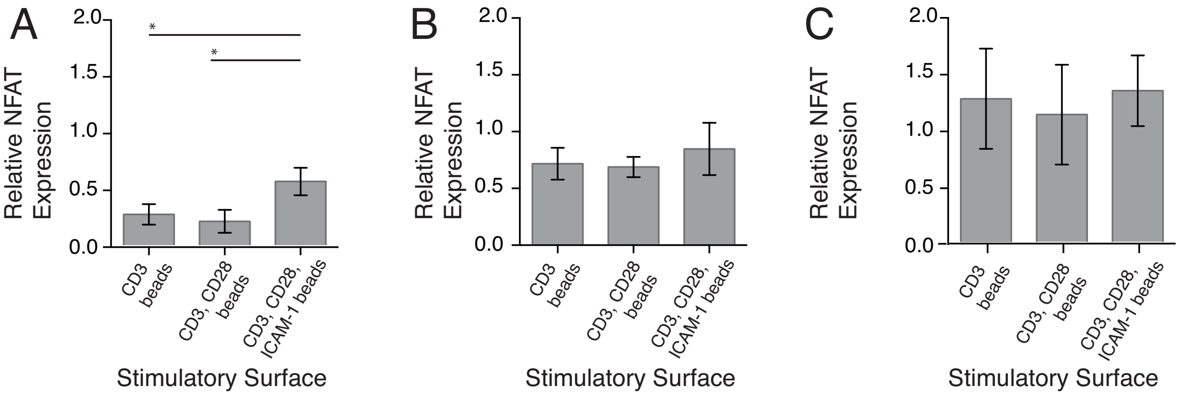

Figure 8.4.10: Cells were incubated for 8 hours with beads functionalised with anti-CD, anti-CD3 and anti-CD28 or anti-CD3, anti-CD38 and ICAM-1 on beads of different rigidities (A) 2000kPa, (B)200kPa or (C) 3-5kPa. Graphs represent average relative activation levels over multiple experiments, where activation levels have been normalised to planar OKT3 anti-CD3 controls. Error bars show the standard error in the mean across experiments. Statistical analysis *** p<0.001, ** p<0.01, * p<0.5

Interestingly, the inclusion of additional co-stimulatory and adhesive ligands (Figure 8.4.10) does not result in a significant increase in activation in most cases, however inclusion of both anti-CD28 and ICAM-1 results in a significant increase in activation compared to anti-CD3 alone, or anti-CD3 and anti-CD28 on stiff beads (2000kPa). An explanation for the similarity between conditions within each rigidity set lies in the nature of the cell line used; as the cells are not naïve, they are less sensitive to co-stimulation, and may require limited additional stimuli to signal. Whilst ICAM-1 is known to mediate adhesion in T cells, earlier we showed (Chapter 7) that adhesion and signaling on planar nanopatterned substrates is possible using only CD3 ligands.

Additionally, the similarities could be attributed to the relative amounts of each type of antibody on the surface, which have not been fully quantified in the mixed antibody systems. We could envisage a situation where the anti-CD3 beads have all surface available streptavidin bound to anti-CD3 biotinylated antibodies, however comparative surfaces with mixed antibodies may present a similar overall antibody level but relatively lower density of each antibody due to competition for binding sites, and so activation could be driven by different levels of CD3 engagement across the antibody functionalisation conditions. It would also be interesting to examine the effect of mechanical stimulation in each activatory receptor (using anti-CD3 and anti-CD28) by comparing cellular responses in bead systems where these antibodies are presented separately and combined, across rigidities. Further work to characterise the exact nature of the antibody binding, and ratios of mixed antibody of the surface, would be beneficial before these experiments are performed.

Observations from these results indicate that as cells are exposed to ligands presented on softer substrates, a significantly greater proportion of the cells become activated across a range of antibody conditions. This mechanosensitivity is mediated through CD3, and maximal activation is seen at around 3-5kPa, though only 2000kPa, 200kPa and 3-5kPa beads have been fabricated in this instance. It would be interesting to explore the range between 500-0.5kPa to determine which substrates drive maximal signaling.

The increased T cell activation on relatively softer substrates (in the 100kPa range compared to 2000kPa values) has been verified in planar PDMS systems. Cells showed enhanced proliferation and IL-2 stimulation on softer substrates, although the exact Young's Modulus value at which maximal activation occurs has yet to defined, and has been shown to be dependent on the type of hydrogel platform in other systems.[280, 43, 281]

That immune cells are sensitive to mechanical stimuli is unsurprising. Immune cell rigidity sensitivity has been proposed as a mechanism for B cells to receive information about infection status. The increased activation of B cells on stiffer substrates has been explained in terms of ligand presentation; mechanosensitivity in the B Cell Receptor complex (BCR) could allow the distinction between free antigen and antigen bound to viral particles for example,[282] allowing the B cell to induce differential responses dependent on the infection threat.

T cell stimulation is sensitive to cytoskeletal and structural changes in both APCs and within the T cell itself; alterations in the dendritic cytoskeleton network can influence T cell activation levels.[290, 275, 233, 482, 538, 333] It may be that alterations to the cytoskeletal network within other cells types act as a marker for infection. Many cell types undergo cytoskeletal rearrangement upon activation[254, 25, 463, 291, 539, 540] redistributing both tubulin and actin throughout the cell, and unhealthy cells are also known to have different mechanical properties.[541, 114, 511] It is not unlikely then, that cells may sense the "stiffness" of another cell and correlate this to an "expected" value for normal healthy cells. Cells whose surfaces have distinct rigidities would therefore be abnormal, and in conjunction with antigen presentation, may induce altered levels of T cell activation.

The exact mechanism underlying mechanosensitivity in T cells has yet to be described. One possibility describes an optimum applied force being required to induce conformational changes in internal signaling components. Mechanotransduction pathways of this type have been described in several cell types; a specific example is p130 CAS, an adaptor protein in focal adhesions, which possesses a conformationally sensitive phosphorylation region.[542, 89] Interestingly, the phosphorylation of these regions in p130 CAS is performed by SRC family kinases.

In T cells, SRC family kinases, such as Lyk and Fyn, play a crucial role in phosphorylating the ITAM domains and, further downstream, ZAP-70 which is required to induce cellular activation. Analogously, there may be SRC kinase substrates, or other crucial signaling molecules, tethered to or in close proximity to the CD3 moiety that require conformational changes before phosphorylation or other downstream signaling events can occur.

That conformational changes are required to induce signaling in T cells has already been shown. The distribution of Lck kinase on T cell surfaces is controlled by its conformational state, where in the open confirmation clustering of Lck is possible and leads to ITAM phosphorylation. Conversely, the closed confirmation results in its exclusion from receptor clusters and limited T cell activation.[271] The mechanism that induces natural conformational changes of this type has yet to be identified, but could be mechanical. There may also be other crucial signaling receptors with cryptic binding sites, or those that require mechanically driven conformational and proximity alterations in the T cell membrane with optimal force requirements.

Interestingly, the response of T cells to planar PDMS surfaces is non-linear, instead showing an optimal response at 100kPa,[281, 280] where values above and below this show decreased activation. At this stage, it is unclear if this is due to differences in the material preparation of the substrates, or a precise requirement for force as described in other leukocyte systems such as the catch bond. The catch bond is a receptor-ligand engagement system whose affinity is non-linearly related to the force applied through the bond. At very low forces, the receptor and ligand are in close proximity and bind with a certain affinity. Increasing the force through the bond increases the affinity by inducing a more favourable binding confirmation, however increasing the force too much deforms the binding conformation and reduces the affinity once more.[233, 285, 286] Our results have shown a inversely proportional relationship between rigidity and activation; it would be interesting to probe T cell sensitivity to rigidity values between 500-0.5kPa to investigate the relationship between signaling and force further.

A separate hypothesis relates to the rigidity of the T cell surface; when T cell surfaces are biochemically induced to have "stiffer" cell membranes, their ability to activate is compromised.[293] It is thought this may be due to an inability to move key receptor complexes laterally across the T cell surface membrane, possibly required for signaling. Similarly, a rigid substrate with firm CD3-receptor engagement may also reduce the fluidity of the T cell surface membrane, and so signaling receptors may be unable to migrate.

The intriguing results with ICAM-1 on stiff 2MPa beads could provide additional confirmation for the theory that optimal force is required for T cell activation, and that softer substrates with lower force per bond deliver this. Earlier, we showed that whilst inclusion of ICAM-1 on substrates of 200kPa and 3-5kPa did not statistically increase cellular activation compared to conditions with anti-CD3 alone, or anti-CD3 and anti-CD28, this was not true for 2MPa beads. Inclusion of ICAM-1 significantly increases the cellular activation compared to both anti-CD3 surfaces, and separately anti-CD3 and anti-CD28 combined (Figure 8.4.9) on 2MPa beads. This could indicate that on stiffer beads, the provision of ICAM-1 helps to "recover" the cellular activation to similar levels found on slightly softer substrates (note that there was no significant difference between 2MPa and 200kPa beads both functionalised with anti-CD3, anti-CD28 and ICAM-1, Figure 8.4.9). A plausible explanation for this can be found in the force mediated signaling mechanism postulated earlier. Without ICAM-1, the cells must adhere to the bead through CD3 or CD3 and CD28 mediated attachment. In the presence of ICAM-1, an additional adhesion ligand is provided for the cells, possibly reducing the "strain" felt through the CD3 receptor-ligand interaction and recovering some of the activation. Why this is not also the case in the 200kPa and 3-5kPa systems is unclear, it would be interesting to investigate the cellular response with naive cells, or cells expressing differential levels of ICAM-1 receptor LFA-1 on their surface, to verify this hypothesis.

Earlier, we investigated the effect of nanoscale CD3 ligand spacing on signaling in T cells, (Chapter 7) and found that inter-ligand spacing of 25nm induced much greater signaling than 104nm spacing. One explanation we suggested was that this difference was force mediated; a small spacing correlated with an increased number of surface ligands per individual signaling focus, and that would relate to lower force experienced in each CD3-ligand interaction.[106] This in turn would result in a "softer" engagement per receptor cluster when compared to systems with only one anchor per cluster. Although this is not an explanation for the mechanism through which T cells are mechanosensitive, it does correlate the cellular response to nanopattern engagement described earlier (Chapter 7) with the force dependent responses seen here.

There is also a biological relevance to this inter-ligand spacing mediated force sensitivity; an increased number of ligands presented on an APC, or anchoring points on an artificial surface, could be realistically analogous to an increase in infection or severity of infection *in vivo*. Surfaces with an increased number of anchoring points per receptor cluster would therefore induce a greater signaling response in the T cells, which could be "sensed" through the force applied through each bond. It is possible these sensing mechanisms are linked; imagining the inverse, then a "softer" substrate induces lower force per ligand-receptor interaction. The cell may interpret this as "increased infection" assuming multiple ligand receptor pairs are engaged due to the relatively low force, and so elicit an activatory response. Conversely, stiffer surfaces, or those with an increased force per interaction, would be correlated with reduced antigen presentation per cell surface.

8.5 Conclusions

Here we present a novel technology capable of stimulating T cells *ex vivo*. We demonstrate that T cell culture and stimulation can be performed on spherical particles, termed beads, in a cell culture environment. These beads have controllable mechanical properties, size and additional features such as magnetism can be incorporated into the particles. Particle sizes of between 5-50μm have been produced, and Young's Moduli of between 2MPa and 3kPa explored. These particles have been selectively functionalised with T cell stimulatory agents, and demonstrate firm attachment to the bead surface, rather than drug release properties.

Cellular response to these materials indicate that T cells have a mechanosensitive response to CD3 engaging ligands. Ligands presented on softer substrates, with rigidities between 3-5kPa show increased cellular activation, as measured by percentages of "on" NFAT-GFP expressing constructs at the 8 hour time point. The underlying mechanism to describe this effect has yet to be determined, however several hypotheses have been suggested. Firstly, that the force applied through the CD3-ligand bond induces conformational changes in key signaling components, and secondly, that the cell interprets the rigidity of a substrate and force applied through a bond as a measure of infection status. The second hypothesis correlates well with earlier results on nanopatterning, and may be mediated through the conformational mechanism described above.

This technology has the possibility to augment cellular activation in *ex vivo* stimulation, and could provide an alternative to current standard technologies based on rigid polystyrene matrices. Additionally, these substrates induce T cell activation that is greater than the standard tissue culture plastic functionalised with anti-CD3 antibodies, and so offer a potential new technology for *ex vivo* T cell expansion.

8.6 Future Work

Our results indicate that T cell activation can be controlled by mechanical variation in the presentation of CD3 ligands. An important direction for future work will be to determine the mechanism driving this sensitivity. An interesting experiment, but one beyond the scope of this thesis, would be to utilise Atomic Force Microscopy (AFM) or similar to pull on a single TCR/CD3 receptor with defined force, and compare changes in activation with applied force. Additionally, if the resulting changes in the confirmation of neighbouring proteins could be visualised this would be a very powerful technique to elucidate further details on the mechanosensitive signaling mechanism.

The rheological surface properties of a range of natural T cell engaging APC cells should be tested in order to give context to the optimal range of stimulation for T cells. Additionally, further exploration of cellular responses between 500-0.5kPa should be carried out in order to identify the maximal activatory surface properties.

Although the technology presented here allows the conjugation of several antibodies to one surface, where individual antibody concentration is controlled by ratio, the exact number of stimulating antibodies per bead has yet to be established. Additionally, the conjugation strategy described here still relies on the streptavidin/biotin binding mechanism. Further developments to this substrate could envisage the direct binding of protein molecules through activated beads, or indeed polymer matrices directly coupled with protein for added versatility.

Further studies should also investigate the long term effect of mechanical stimulation; stimulating cells through the receptors with ligands of differing affinity, or ligands substrate rigidity, has previously resulted in specific phenotypic differentiation.[279, 6, 543] It will be important to see if the proliferation and phenotypic differentiation of naïve cells is sensitive to substrate properties, as this could have interesting implications for vaccine therapy, where control of memory cell development is desired. Determining the mechanism that induces these changes could also have important implications in immunotherapeutic design.

Chapter 9

Conclusions and Future Work

9.1 Conclusions

This thesis has described the fabrication of biomimetic materials and their use in probing the sensitivity of immune cells to nanoscale ligand arrangement and substrate rigidity.

We have described the controlled fabrication of precisely controlled gold nanoparticle arrays on planar substrates through block copolymer micellar lithography. Using parameters described in the literature, nanoparticle arrays with controlled spacing on the order of 10-150nm have been produced. A range of nanoparticle sizes can be formed by varying the ionic loading in the micelles, and inter-particle spacing has been controlled by both dip-coating extraction rate and the molecular weight of the polymer templates used to produce the nanoparticles.

The micellar lithography technique was then employed to fabricate zinc sulfide particles as a complementary material for nanoparticle array formation and biofunctionalisation studies. The particles produced were verified as ZnS by their elemental composition and TEM lattice fringe spacings. Calculated optical properties of the particles confirm they are constrained on the nanoscale, with a band gap between 3.88-4.28eV. These nanoparticles are also the first to demonstrate a unique structure; small crystallite ZnS domains within an amorphous matrix as a single particle encapsulated inside polymer templates.

We have also used these zinc-based nanoparticles to produce a range of nanoparticle materials, including zinc sulfide, zinc and zinc oxide, in ordered arrays with nanoscale order. Advanced functionalisation methods have allowed the fabrication of more complex nanopatterns; micro-contact printing has been used to produce 600nm wide stripes of both gold and zinc-based micelles. Additionally, latticed arrays of gold nanoparticles have been produced using this technique, where stripes in orthogonal directions have been printed with different polymer templates to produce nanopatterns with different inter-particle spacing in perpendicular directions. Deposition of multiple gold micelle layers has led to the formation of binary nanoparticle arrays, and together these nanopattern functionalisation mechanisms represent an advance on the currently available nanopattern fabrication methodologies.

The highly ordered gold nanopatterned substrates were subsequently used for cell studies to elucidate minimal lateral signaling requirements in the immune system. Substrates have been treated with a protein resistant layer in between the particles, and selectively functionalised with immune cell surface receptor ligands. The NK cell CD16 stimulatory ligands anti-CD16 and Rituximab have been bound to gold nanoparticles using streptavidin linkage, and T cell TCR/CD3 complex surface receptor ligand anti-CD3 UCHT1 antibody fragments were bound to gold nanoparticles through the intrinsic exposed disulfide moieties.

These substrates were used to investigate early stage immune responses in both NK cells and T cells (as representative cells of the innate and adaptive immune system respectively) and found that both cell types were sensitive to the nanoscale ligand organisation on a 100nm lengthscale. NK cell responses were measured by cell spread area, and found a sharp threshold between 69nm and 104nm ligand spacing above which signaling was equivalent to background levels, independent of the ligand engagement mechanism. Early stage T cell responses were characterised by phosphotryosine signaling and adhesion at five minute time-points. Similarly, results indicated that at 104nm T cell response was not significantly greater than background, but in this case the threshold sensitivity seems to be below 69nm. An intriguing result highlighted that nanopatterns with larger inter-ligand spacing could enrich T cell populations for memory phenotypes. A decreasing proportion of naïve cells in adherent cell populations is closely correlated to an increase in spacing between adjacent receptor engaging sites.

The similar nature of the dependance of NK and T cell signaling on the nanoscale organisation of receptor ligands hints at a common requirement in the mechanism of activation. We have suggested several hypotheses to explain the nanosensitivity of the immune cells; protein nanodomain concatenation, a minimal number of receptor ligand interactions per signaling focus, and mechanosensitivity through the receptor engagement. Protein nanodomain concatenation describes the requirement for distinct receptor nanodomains to move into close proximity to induce signaling. This may be due to a requirement to integrate activatory signals above a basal or inhibitory threshold, or for the exclusion of key inhibitory receptors from the signaling focus. Separately, a minimal number of engaged receptors may be required per signaling focus or per cell, though this is unlikely given the known sensitivity of immune cells for low ligand densities. An alternative explanation links the nanoscale organisation of ligands to the mechanical strain felt by each receptor ligand pair, where closely spaced nanopatterns induce a lower strain through each ligand-receptor pair.

Given the enhanced proliferation and activation of T cells on softer substrates, and the clinical demand for advanced cell culture systems in adoptive immunotherapy, PEG microspheres with controlled mechanical properties were fabricated and investigated as T cell stimulatory substrates. Spherical PEG hydrogel particles of 5-50μm diameter were prepared with rigidity controlled between 3 to 2000kPa and selectively functionalised with CD3-engaging and co-stimulatory ligands. T cell responses were measured after eight hours, and indicated that T cells cultured on softer substrates of between 3-5kPa had significantly increased levels of activation compared to those on more rigid materials of Young's Modulus 2000kPa. Additionally, these particles were able to augment T cell responses to levels greater than conventional planar tissue culture plastic controls.

Although the mechanosensitivity of T cells and enhanced proliferation on softer planar substrates has been shown, here we developed a more clinically relevant culture substrate that recapitulates the geometry of the natural APC-T cell interaction. Our results demonstrate that biomimetic materials with nanoscale or mechanical control over stimulatory ligand presentation can determine activation levels in immune cells. The design of materials that can control or augment immune cell responses *ex vivo* has a huge range of applications ranging from fundamental signaling studies, such as those conducted here, to clinical therapies. The future of adoptive immunotherapy may lie in the design of therapeutics capable of increasing cellular activation through some of the mechanisms postulated here, such as driving nanocluster concatenation or developing substrates capable of enhanced and phenotype selective cell proliferation.

9.2 Future Work

This thesis describes studies in immune cell signaling requirements through fabricated biomimetic materials. The mechanism driving the sensitivity of immune cells to nanopatterns and rigidity controlled surfaces is currently not fully understood with several hypothesis being plausible. Current hypotheses explaining the results in this thesis focus on the following; differences in ligand density between nanoarray surfaces, the requirement for a certain number of stable anchoring points for force-mediated signal generation, and the postulated need for concatenation of signaling foci on the cell-material interface requiring ligand-receptor pairs with close proximity. Future work to test these hypotheses will focus on both the design of more complex biomaterials and further investigations into immune cell signaling requirements.

Advanced biomimetic materials can be envisioned using the bi-material micro-contact printing method described earlier. Development of printing techniques, using new masters fabricated through photo- or electron beam lithography, will allow a range of more complex geometries and nanoscale architectures to be produced. With orthogonal functionalisation mechanisms this technique allows presentation of multiple ligands with individual spatial control; the gold and zinc sulfide nanoparticle techniques developed in this thesis will provide such systems. Complex nanopatterned arrays could then be used to further investigate signaling requirements in immune cells, including the effect of inhibitory ligands, or small nanospaced ligand clusters.

The PEG beads fabricated in this thesis present a limited number of stiffness values over a wide range, further investigations should focus on advanced fabrication where beads have mechanical properties over a range of 500-0.5kPa in order to identify the maximal activatory surface properties. Additionally advanced fabrication methods could be employed that would allow the direct functionalisation of the beads with stimulatory ligands.

In order to determine whether it is cluster size, inter-ligand spacing, or the mechanical interaction with the substrate driving this sensitivity, each of these parameters will need to be tested individually. Aside from the synthesis of more advanced biomimetic materials, cellular modifications could be made to test these ideas. Specifically, investigation of whether the cells react similarly to these substrates when their force-sensing apparatus or ability to concatenate signaling foci is disturbed could be carried out.

A further development of this work includes investigation into the response of other immune cell types and cell phenotypes to these substrates, which could help to determine if there is a universal immune receptor signaling dependence on nanoscale receptor engagement, and whether these materials can be used for phenotypic differentiation. As different subsets of T cells appear to respond differently to nanopatterns based on their prior exposure to antigen, these nanopatterns also offer exciting new tools to probe T cell education using sequential nanopattern stimulation. Deriving the mechanism inducing these changes could also have important implications in immunotherapeutic design.

Bibliography

[1] World Health Organization. The top 10 causes of death, 2013.

[2] W. J. Pichler. Cellular immune-response in HIV-infection. *Schweizerische Medizinische Wochenschrift*, 116(44):1506–1513, 1986.

[3] Rebeca Geffin and Micheline McCarthy. Innate immune responses to HIV infection in the central nervous system. *Immunologic research*, 57(1-3):292–302, 2013.

[4] D. A. Dilernia, D. C. Monaco, M. Quipildor, A. Di Paolo, L. Yue, S. Kaur, C. Ibegbu, J. Altman, H. Salomon, and E. Hunter. Evidence of a less pathogenic HIV infection associated with high adaptation to HLA-I mediated immune response in a south american native community. *Aids Research and Human Retroviruses*, 29(11):A86–A86, 2013.

[5] Adel Benlahrech, Heather Donaghy, George Rozis, Martin Goodier, Linda Klavinskis, Frances Gotch, and Steven Patterson. Human NK cell up-regulation of CD69, HLA-DR, interferon gamma secretion and cytotoxic activity by plasmacytoid dendritic cells is regulated through overlapping but different pathways. *Sensors*, 9(1):386–403, 2009.

[6] G. P. Morris and P. M. Allen. How the TCR balances sensitivity and specificity for the recognition of self and pathogens. *Nature Immunology*, 13(2):121–128, 2012.

[7] N. J. Hill, A. Stotland, M. Solomon, P. Secrest, E. Getzoff, and N. Sarvetnick. Resistance of the target islet tissue to autoimmune destruction contributes to genetic susceptibility in Type I diabetes. *Biology Direct*, 2, 2007.

[8] N. Nagy, G. Kaber, D. J. Campbell, and T. N. Wight. Type 1 diabetes: Involvement of the extracellular matrix in immune-mediated pancreatic islet destruction. *Glycobiology*, 22(11):1568–1568, 2012.

[9] A. Naji, W. K. Silvers, D. Bellgrau, and C. F. Barker. Spontaneous diabetes in rats - destruction of islets is prevented by immunological-tolerance. *Science*, 213(4514):1390–1392, 1981.

[10] S. Tanaka, K. Aida, Y. Nishida, and T. Kobayashi. Pathophysiological mechanisms involving aggressive islet cell destruction in fulminant type 1 diabetes. *Endocrine Journal*, 60(7):837–845, 2013.

[11] S. Winer, H. Tsui, A. Lau, A. H. Song, X. M. Li, R. K. Cheung, A. Sampson, F. Afifiyan, A. Elford, G. Jackowski, D. J. Becker, P. Santamaria, P. Ohashi, and H. M. Dosch. Autoimmune islet destruction in spontaneous type 1 diabetes is not beta-cell exclusive. *Nature Medicine*, 9(2):198–205, 2003.

[12] J. T. Wong and R. B. Colvin. Selective reduction and proliferation of the CD4+ and CD8+ T-cell subsets with bispecific monoclonal-antibodies - evidence for inter-T-cell-mediated cytolysis. *Clinical Immunology and Immunopathology*, 58(2):236–250, 1991.

[13] Katherine Belov. The role of the major histocompatibility complex in the spread of contagious cancers. *Mammalian Genome*, 22(1-2):83–90, 2011.

[14] Robert L. Ferris, Michael T. Lotze, Stanley P. L. Leong, David S. B. Hoon, and Donald L. Morton. Lymphatics, lymph nodes and the immune system: barriers and gateways for cancer spread. *Clinical & Experimental Metastasis*, 29(7):729–736, 2012.

[15] Karl-Johan Malmberg, Yenan T. Bryceson, Mattias Carlsten, Sandra Andersson, Andreas Bjorklund, Niklas K. Bjorkstrom, Bettina C. Baumann, Cyril Fauriat, Evren Alici, M. Sirac Dilber, and Hans-Gustaf Ljunggren. NK cell-mediated targeting of human cancer and possibilities for new means of immunotherapy. *Cancer Immunology Immunotherapy*, 57(10):1541–1552, 2008.

[16] A. L. Shada, K. R. Molhoek, and C. L. Slingluff. Interface of signal transduction inhibition and immunotherapy in melanoma. *Cancer Journal*, 16(4):360–366, 2010.

[17] Josef M Penninger Shane J. F. Cronin. From T-cell activation signals to singanling control of anti-cancer immunity. *Immunological Reviews*, 220:151–168, 2007.

[18] Hannah V. Siddle, Jolanta Marzec, Yuanyuan Cheng, Menna Jones, and Katherine Belov. MHC gene copy number variation in Tasmanian devils: implications for the spread of a contagious cancer. *Proceedings of the Royal Society B-Biological Sciences*, 277(1690):2001–2006, 2010.

[19] Clare Y. Slaney, Jai Rautela, and Belinda S. Parker. The emerging role of immunosurveillance in dictating metastatic spread in breast cancer. *Cancer Research*, 73(19):5852–5857, 2013.

[20] T. J. Stewart and M. J. Smyth. Improving cancer immunotherapy by targeting tumor-induced immune suppression. *Cancer and Metastasis Reviews*, 30(1):125–140, 2011.

[21] K. Shen, V. K. Thomas, M. L. Dustin, and L. C. Kam. Micropatterning of costimulatory ligands enhances CD4+ T cell function. *Proc. Natl. Acad. Sci. U.S.A.*, 105(22):7791–6, 2008.

[22] A. Chauveau, A. Aucher, P. Eissmann, E. Vivier, and D. M. Davis. Membrane nanotubes facilitate long-distance interactions between natural killer cells and target cells. *Proceedings of the National Academy of Sciences of the United States of America*, 107(12):5545–5550, 2010.

[23] C. R. Almeida and D. M. Davis. Segregation of HLA-C from ICAM-1 at NK cell immune synapses is controlled by its cell surface density. *Journal of Immunology*, 177(10):6904–6910, 2006.

[24] P. Eissmann and D. M. Davis. Inhibitory and regulatory immune synapses. *Curr. Top. Microbiol. Immunol.*, 340:63–79, 2010.

[25] J. S. Orange. Formation and function of the lytic NK-cell immunological synapse. *Nature Reviews Immunology*, 8(9):713–725, 2008.

[26] Ferdinand Brandl, Florian Sommer, and Achim Goepferich. Rational design of hydrogels for tissue engineering: Impact of physical factors on cell behavior. *Biomaterials*, 28(2):134–146, 2007.

[27] M. D. Mager, V. LaPointe, and M. M. Stevens. Exploring and exploiting chemistry at the cell surface. *Nature Chemistry*, 3(8):582–589, 2011.

[28] L. E. Dickinson, S. Kusuma, and S. Gerecht. Reconstructing the differentiation niche of embryonic stem cells using biomaterials. *Macromolecular Bioscience*, 11(1):36–49, 2011.

[29] R. Vasita and D. S. Katti. Nanofibers and their applications in tissue engineering. *International Journal of Nanomedicine*, 1(1):15–30, 2006.

[30] M. Pfaff, M. A. McLane, L. Beviglia, S. Niewiarowski, and R. Timpl. Comparison of disintegrins with limited variation in the RGD loop in their binding to purified integrins alpha-IIB-beta-3, alpha-V-beta-3 and alpha-5-beta-1 and in cell-adhesion inhibition. *Cell Adhesion and Communication*, 2(6):491–501, 1994.

[31] G. Jung, U. Freimann, Z. Vonmarschall, R. A. Reisfeld, and W. Wilmanns. Target cell-induced T-cell activation with bispecific and trispecific antibody fragments. *European Journal of Immunology*, 21(10):2431–2435, 1991.

[32] Y. Tabata. Tissue regeneration based on growth factor release. *Tissue Engineering*, 9:S5–S15, 2003.

[33] R. Vasita and D. S. Katti. Growth factor-delivery systems for tissue engineering: a materials perspective. *Expert Review of Medical Devices*, 3(1):29–47, 2006.

[34] Shruti GuhaSarkar and R. Banerjee. Intravesical drug delivery: Challenges, current status, opportunities and novel strategies. *Journal of Controlled Release*, 148(2):147–159, 2010.

[35] Dominika Rudnicka, Anna Oszmiana, Donna K. Finch, Ian Strickland, Darren J. Schofield, David C. Lowe, Matthew A. Sleeman, and Daniel M. Davis. Rituximab causes a polarization of B cells that augments its therapeutic function in NK-cell-mediated antibody-dependent cellular cytotoxicity. *Blood*, 121(23):4694–4702, 2013.

[36] G. J. Weiner. Rituximab: Mechanism of action. *Seminars in Hematology*, 47(2):115–123, 2010.

[37] G. M. Keating. Rituximab: a review of its use in chronic lymphocytic leukaemia, low-grade or follicular lymphoma and diffuse large B-cell lymphoma. *Drugs*, 70(11):1445–76, 2010.

[38] S. Koristka, M. Cartellieri, A. Theil, A. Feldmann, C. Arndt, S. Stamova, I. Michalk, K. Topfer, A. Temme, K. Kretschmer, M. Bornhauser, G. Ehninger, M. Schmitz, and M. Bachmann. Retargeting of human regulatory T cells by single-chain bispecific antibodies. *Journal of Immunology*, 188(3):1551–1558, 2012.

[39] L. M. Portner, K. Schonberg, M. Hejazi, D. Brunnert, F. Neumann, L. Galonska, U. Reusch, M. Little, R. Haas, and M. Uhrberg. T and NK cells of B cell NHL patients exert cytotoxicity against lymphoma cells following binding of bispecific tetravalent antibody CD19 x CD3 or CD19 x CD16. *Cancer Immunology Immunotherapy*, 61(10):1869–1875, 2012.

[40] Dominique Bihan Samir Hamaia Christiane S. Smerling Nicholas Pugh Antonios Konitsiotis birgit Leitinger Philip G. de Groot Gavin E. Jarvis Nicolas Raynal Richard W. Farndale, Ton Lisman. Cell-collagen interactions: the use of peptide toolkits to investigate collagen-receptor interactions. *Biochemical Society Transactions*, 36(2):241–250, 2008.

[41] A. Shekaran and A. J. Garcia. Nanoscale engineering of extracellular matrix-mimetic bioadhesive surfaces and implants for tissue engineering. *Biochimica Et Biophysica Acta-General Subjects*, 1810(3):350–360, 2011.

[42] I. Wheeldon, A. Farhadi, A. G. Bick, E. Jabbari, and A. Khademhosseini. Nanoscale tissue engineering: spatial control over cell-materials interactions. *Nanotechnology*, 22(21), 2011.

[43] B. Trappmann, J. E. Gautrot, J. T. Connelly, D. G. T. Strange, Y. Li, M. L. Oyen, M. A. C. Stuart, H. Boehm, B. J. Li, V. Vogel, J. P. Spatz, F. M. Watt, and W. T. S. Huck. Extracellular-matrix tethering regulates stem-cell fate. *Nature Materials*, 11(7):642–649, 2012.

[44] A. S. G. Curtis, N. Gadegaard, M. J. Dalby, M. O. Riehle, C. D. W. Wilkinson, and G. Aitchison. Cells react to nanoscale order and symmetry in their surroundings. *Ieee Transactions on Nanobioscience*, 3(1):61–65, 2004.

[45] M. J. Dalby, M. O. Riehle, D. S. Sutherland, H. Agheli, and A. S. G. Curtis. Changes in fibroblast morphology in response to nano-columns produced by colloidal lithography. *Biomaterials*, 25(23):5415–5422, 2004.

[46] M. J. Dalby, C. C. Berry, M. O. Riehle, D. S. Sutherland, H. Agheli, and A. S. G. Curtis. Attempted endocytosis of nano-environment produced by colloidal lithography by human fibroblasts. *Experimental Cell Research*, 295(2):387–394, 2004.

[47] M. J. Dalby, N. Gadegaard, M. O. Riehle, C. D. W. Wilkinson, and A. S. G. Curtis. Investigating filopodia sensing using arrays of defined nano-pits down to 35 nm diameter in size. *International Journal of Biochemistry & Cell Biology*, 36(10):2005–2015, 2004.

[48] T. Sjostrom, M. J. Dalby, A. Hart, R. Tare, R. O. C. Oreffo, and B. Su. Fabrication of pillar-like titania nanostructures on titanium and their interactions with human skeletal stem cells. *Acta Biomaterialia*, 5(5):1433–1441, 2009.

[49] E. K. F. Yim, R. M. Reano, S. W. Pang, A. F. Yee, C. S. Chen, and K. W. Leong. Nanopattern-induced changes in morphology and motility of smooth muscle cells. *Biomaterials*, 26(26):5405–5413, 2005.

[50] H. L. Khor, Y. Kuan, H. Kukula, K. Tamada, W. Knoll, M. Moeller, and D. W. Hutmacher. Response of cells on surface-induced nanopatterns: Fibroblasts and mesenchymal progenitor cells. *Biomacromolecules*, 8(5):1530–1540, 2007.

[51] M. Arnold, M. Schwieder, J. Blummel, E. A. Cavalcanti-Adam, M. Lopez-Garcia, H. Kessler, B. Geiger, and J. P. Spatz. Cell interactions with hierarchically structured nano-patterned adhesive surfaces. *Soft Matter*, 5(1):72–77, 2009.

[52] K. S. Brammer, C. Choi, C. J. Frandsen, S. Oh, and S. Jin. Hydrophobic nanopillars initiate mesenchymal stem cell aggregation and osteo-differentiation. *Acta Biomaterialia*, 7(2):683–690, 2011.

[53] K. Anselme and M. Bigerelle. Role of materials surface topography on mammalian cell response. *International Materials Reviews*, 56(4):243–266, 2011.

[54] I. R. Asplin, S. M. Wu, S. Mathew, G. Bhattacharjee, and S. V. Pizzo. Differential regulation of the fibroblast growth factor (FGF) family by alpha(2)-macroglobulin: evidence for selective modulation of FGF-2-induced angiogenesis. *Blood*, 97(11):3450–3457, 2001.

[55] A. M. Pizzo, K. Kokini, L. C. Vaughn, B. Z. Waisner, and S. L. Voytik-Harbin. Extracellular matrix (ECM) microstructural composition regulates local cell-ECM biomechanics and fundamental fibroblast behavior: a multidimensional perspective. *Journal of Applied Physiology*, 98(5):1909–1921, 2005.

[56] C. C. Berry, M. J. Dalby, D. McCloy, and S. Affrossman. The fibroblast response to tubes exhibiting internal nanotopography. *Biomaterials*, 26(24):4985–4992, 2005.

[57] M. F. Berry, A. J. Engler, Y. J. Woo, T. J. Pirolli, L. T. Bish, V. Jayasankar, K. J. Morine, T. J. Gardner, D. E. Discher, and H. L. Sweeney. Mesenchymal stem cell injection after myocardial infarction improves myocardial compliance. *American Journal of Physiology-Heart and Circulatory Physiology*, 290(6):H2196–H2203, 2006.

[58] M. J. P. Biggs, R. G. Richards, N. Gadegaard, R. J. McMurray, S. Affrossman, C. D. W. Wilkinson, R. O. C. Oreffo, and M. J. Dalby. Interactions with nanoscale topography: Adhesion quantification and signal transduction in cells of osteogenic and multipotent lineage. *Journal of Biomedical Materials Research Part A*, 91A(1):195–208, 2009.

[59] M. J. Dalby, N. Gadegaard, R. Tare, A. Andar, M. O. Riehle, P. Herzyk, C. D. Wilkinson, and R. O. Oreffo. The control of human mesenchymal cell differentiation using nanoscale symmetry and disorder. *Nature Mater.*, 6(12):997–1003, 2007.

[60] M. C. Good, J. G. Zalatan, and W. A. Lim. Scaffold proteins: Hubs for controlling the flow of cellular information. *Science*, 332(6030):680–686, 2011.

[61] Jennifer L. Young, Jeremy Tuler, Rebecca Braden, Pamela Schuep-Magoffin, Jacquelyn Schaefer, Kyle Kretchmer, Karen L. Christman, and Adam J. Engler. In vivo response to dynamic hyaluronic acid hydrogels. *Acta Biomaterialia*, 9(7):7151–7157, 2013.

[62] Ji S. Choi and Brendan A. C. Harley. The combined influence of substrate elasticity and ligand density on the viability and biophysical properties of hematopoietic stem and progenitor cells. *Biomaterials*, 33(18):4460–4468, 2012.

[63] A. J. Engler, H. L. Sweeney, and D. E. Discher. Substrate elasticity alters human mesenchymal stem cell differentiation. *Biophysical Journal*, 88(1):500A–500A, 2005.

[64] A. Engler, C. Newman, A. Hategan, M. Sheehan, D. Discher, Ieee, Ieee, and Ieee. *Cells on gels: Smooth and skeletal muscle cell responses to substrate compliance*, pages 402–403. Proceedings of Annual International Conference of the Ieee Engineering in Medicine and Biology Society. 2002.

[65] D. E. Discher, A. Engler, C. Carag, and F. Rehfeldt. Matrix elasticity effects on cardiomyocytes and stem cells: Similarities, differences and therapeutic implications. *Biorheology*, 45(1-2):54–54, 2008.

[66] A. J. Engler, M. A. Griffin, S. Sen, C. G. Bonnetnann, H. L. Sweeney, and D. E. Discher. Myotubes differentiate optimally on substrates with tissue-like stiffness: pathological implications for soft or stiff microenvironments. *Journal of Cell Biology*, 166(6):877–887, 2004.

[67] A. J. Engler, L. Richert, J. Y. Wong, C. Picart, and D. E. Discher. Surface probe measurements of the elasticity of sectioned tissue, thin gels and polyelectrolyte multilayer films: Correlations between substrate stiffness and cell adhesion. *Surface Science*, 570(1-2):142–154, 2004.

[68] A. J. Engler, F. Rehfeldt, S. Sen, and D. E. Discher. *Microtissue elasticity: Measurements by atomic force microscopy and its influence on cell differentiation*, volume 83 of *Methods in Cell Biology*, pages 521–+. 2007.

[69] A. J. Engler, C. Carag-Krieger, C. P. Johnson, M. Raab, H. Y. Tang, D. W. Speicher, J. W. Sanger, J. M. Sanger, and D. E. Discher. Embryonic cardiomyocytes beat best on a matrix with heart-like elasticity: scar-like rigidity inhibits beating. *Journal of Cell Science*, 121(22):3794–3802, 2008.

[70] D. E. Discher, A. J. Engler, and Asme. *Mesenchymal stem cell injection after myocardial infarction improves myocardial compliance*. Proceeding of the Asme Summer Bioengineering Conference - 2007. 2007.

[71] D. E. Discher and A. J. Engler. Differentiation fate of human mesenchymal stem cell is influenced by substrate elasticity. *Abstracts of Papers of the American Chemical Society*, 229:U199–U199, 2005.

[72] Chandrasekhar R. Kothapalli and Roger D. Kamm. 3D matrix microenvironment for targeted differentiation of embryonic stem cells into neural and glial lineages. *Biomaterials*, 34(25):5995–6007, 2013.

[73] Michelle L. Previtera, Mason Hui, Devendra Verma, Abdelhamid J. Shahin, Rene Schloss, and Noshir A. Langrana. The effects of substrate elastic modulus on neural precursor cell behavior. *Annals of Biomedical Engineering*, 41(6):1193–1207, 2013.

[74] Michelle Nii, Janice H. Lai, Michael Keeney, Li-Hsin Han, Anthony Behn, Galym Imanbayev, and Fan Yang. The effects of interactive mechanical and biochemical niche signaling on osteogenic differentiation of adipose-derived stem cells using combinatorial hydrogels. *Acta Biomaterialia*, 9(3):5475–5483, 2013.

[75] I. V. Ogneva. Cell mechanosensitivity: Mechanical properties and interaction with gravitational field. *Biomed Research International*, 2013.

[76] I. B. Bischofs and U. S. Schwarz. Cell organization in soft media due to active mechanosensing. *Proceedings of the National Academy of Sciences of the United States of America*, 100(16):9274–9279, 2003.

[77] Rebecca A. Scott, Donald L. Elbert, and Rebecca Kuntz Willits. Modular poly(ethylene glycol) scaffolds provide the ability to decouple the effects of stiffness and protein concentration on PC12 cells. *Acta Biomaterialia*, 7(11):3841–3849, 2011.

[78] Jennifer D. Kiang, Jessica H. Wen, Juan C. del Alamo, and Adam J. Engler. Dynamic and reversible surface topography influences cell morphology. *Journal of Biomedical Materials Research Part A*, 101A(8):2313–2321, 2013.

[79] H. A. Levin, H. Levine, and Schlossm.Sf. Antigen recognition and antibody specificity - carrier specificity and genetic control of anti-dinitrophenyl-oligolysine antibody. *Journal of Experimental Medicine*, 133(6):1199–&, 1971.

[80] H. A. Levin, H. Levine, and Schlossm.Sf. Antigen recognition and antibody specificity. *Federation Proceedings*, 30(2):A469–&, 1971.

[81] K. L. Arnett, S. C. Harrison, and D. C. Wiley. Crystal structure of a human CD3-epsilon/delta dimer in complex with a UCHT1 single-chain antibody fragment. *Proc. Natl. Acad. Sci. U.S.A.*, 101(46):16268–73, 2004.

[82] J. Persson, M. Backstrom, H. Johansson, K. Jirstrom, G. C. Hansson, and M. Ohlin. Molecular evolution of specific human antibody against muc1 mucin results in improved recognition of the antigen on tumor cells. *Tumor Biology*, 30(4):221–231, 2009.

[83] L. Edelstein and R. Rosen. Enzyme-substrate recognition. *Journal of Theoretical Biology*, 73(1):181–204, 1978.

[84] M. R. Pincus and H. A. Scheraga. Theoretical calculations on enzyme-substrate complexes - the basis of molecular recognition and catalysis. *Accounts of Chemical Research*, 14(10):299–306, 1981.

[85] J. Revuelta, F. Corzana, A. Bastida, and J. L. Asensio. The unusual nucleotide recognition properties of the resistance enzyme ANT(4 '): Inorganic tri/polyphosphate as a substrate for aminoglycoside inactivation. *Chemistry-a European Journal*, 16(29):8635–8640, 2010.

[86] J. E. Blalock and K. L. Bost. Ligand receptor characteristics of peptides encoded by complementary nucleic-acids - implications for a molecular recognition code. *Recent Progress in Hormone Research*, 44:199–222, 1988.

[87] G. Plyashkevich Yu and V. P. Demushkin. Structural peculiarities of the cholinergic ligand recognition site of nicotinic acetylcholine receptor from squid optical ganglia. *Biokhimiya*, 50(7):1167–1174, 1985.

[88] D. J. Irvine, M. A. Purbhoo, M. Krogsgaard, and M. M. Davis. Direct observation of ligand recognition by t cells. *Nature*, 419(6909):845–9, 2002.

[89] V. Vogel and M. P. Sheetz. Cell fate regulation by coupling mechanical cycles to biochemical signaling pathways. *Current Opinion in Cell Biology*, 21(1):38–46, 2009.

[90] Y. G. Xiong, P. Rangamani, M. A. Fardin, A. Lipshtat, B. Dubin-Thaler, O. Rossier, M. P. Sheetz, and R. Iyengar. Mechanisms controlling cell size and shape during isotropic cell spreading. *Biophysical Journal*, 98(10):2136–2146, 2010.

[91] S. Sekula, J. Fuchs, S. Weg-Remers, P. Nagel, S. Schuppler, J. Fragala, N. Theilacker, M. Franzreb, C. Wingren, P. Ellmark, C. A. Borrebaeck, C. A. Mirkin, H. Fuchs, and S. Lenhert. Multiplexed lipid dip-pen nanolithography on subcellular scales for the templating of functional proteins and cell culture. *Small*, 4(10):1785–93, 2008.

[92] S. Lenhert, L. Zhang, J. Mueller, H. P. Wiesmann, G. Erker, H. Fuchs, and L. F. Chi. Self-organized complex patterning: Langmuir-blodgett lithography. *Advanced Materials*, 16(7):619–+, 2004.

[93] J. H. Huang, S. V. Grater, F. Corbellinl, S. Rinck, E. Bock, R. Kemkemer, H. Kessler, J. D. Ding, and J. P. Spatz. Impact of order and disorder in rgd nanopatterns on cell adhesion. *Nano Letters*, 9(3):1111–1116, 2009.

[94] Stefan V. Graeter, Jinghuan Huang, Nadine Perschmann, Monica Lopez-Garcia, Horst Kessler, Jiandong Ding, and Joachim P. Spatz. Mimicking cellular environments by nanostructured soft interfaces. *Nano Letters*, 7(5):1413–1418, 2007.

[95] J. P. Xiong, T. Stehle, B. Diefenbach, R. G. Zhang, R. Dunker, D. L. Scott, A. Joachimiak, S. L. Goodman, and M. A. Arnaout. Crystal structure of the extracellular segment of integrin alpha V beta 3. *Science*, 294(5541):339–345, 2001.

[96] Y. M. Xiong and L. Zhang. Structural analysis of the beta I-2-domain of integrin alpha(M)beta(2) by mutagenesis. *Molecular Biology of the Cell*, 12:1764, 2001.

[97] G. Maheshwari, G. Brown, D. A. Lauffenburger, A. Wells, and L. G. Griffith. Cell adhesion and motility depend on nanoscale rgd clustering. *Journal of Cell Science*, 113(10):1677–1686, 2000.

[98] W. A. Comisar, S. X. Hsiong, H. J. Kong, D. J. Mooney, and J. J. Linderman. Multi-scale modeling to predict ligand presentation within rgd nanopatterned hydrogels. *Biomaterials*, 27(10):2322–2329, 2006.

[99] W. A. Comisar, N. H. Kazmers, D. J. Mooney, and J. J. Linderman. Adhesion ligand nanopatterning influences differentiation of preosteoblast cells: A combined experimental and computational approach. *Developmental Biology*, 295:DOI 10.1016/j.ydbio.2006.04.426|395, 2006.

[100] W. A. Comisar, N. H. Kazmers, D. J. Mooney, and J. J. Linderman. Engineering rgd nanopatterned hydrogels to control preosteoblast behavior: A combined computational and experimental approach. *Biomaterials*, 28:4409–4417, 2007.

[101] W. A. Comisar, D. J. Mooney, and J. J. Linderman. Integrin organization: Linking adhesion ligand nanopatterns with altered cell responses. *Journal of Theoretical Biology*, 274(1):120–130, 2011.

[102] E. A. Cavalcanti-Adam, M. Bezler, P. Tomakidi, and J. P. Spatz. Integrin ligands arranged in nanopatterns modulate focal adhesion assembly and signaling in osteoblasts. *J. Bone Mineral Res.*, 19:S64–S64, 2004.

[103] E. A. Cavalcanti-Adam, A. Micoulet, J. Blummel, J. Auernheimer, H. Kessler, and J. P. Spatz. Lateral spacing of integrin ligands influences cell spreading and focal adhesion assembly. *European Journal of Cell Biology*, 85(3-4):219–224, 2006.

[104] E. A. Cavalcanti-Adam and J. Satz. Regulation of adhesion dynamics, motility and survival by spacing of extracellular matrix peptides. *Journal of Bone and Mineral Research*, 21:S134–S134, 2006.

[105] E. A. Cavalcanti-Adam, T. Volberg, A. Micoulet, H. Kessler, B. Geiger, and J. P. Spatz. Cell spreading and focal adhesion dynamics are regulated by spacing of integrin ligands. *Biophysical Journal*, 92(8):2964–2974, 2007.

[106] A. G. F. de Beer, E. A. Cavalcanti-Adam, G. Majer, M. Lopez-Garcia, H. Kessler, and J. P. Spatz. Force-induced destabilization of focal adhesions at defined integrin spacings on nanostructured surfaces. *Physical Review E*, 81(5), 2010.

[107] J. A. Deeg, I. Louban, D. Aydin, C. Selhuber-Unkel, H. Kessler, and J. P. Spatz. Impact of local versus global ligand density on cellular adhesion. *Nano Letters*, 11(4):1469–1476, 2011.

[108] V. C. Hirschfeld-Warneken, M. Arnold, A. Cavalcanti-Adam, M. Lopez-Garcia, H. Kessler, and J. P. Spatz. Cell adhesion and polarisation on molecularly defined spacing gradient surfaces of cyclic rgdfk peptide patches. *European Journal of Cell Biology*, 87(8-9):743–750, 2008.

[109] Roman Glass Jaques Blummel Wolfgang Eck Martin Kantlehnew Horst Kessler Joachim P. Spatz Marco Arnold, Elisabetta Ada Cavalcanti-Adam. Activation of integrin function by nanopatterned adhesive surfaces. *ChemPhysChem*, 5:383–388, 2004.

[110] H. Kogelberg, B. Tolner, G. J. Thomas, D. Di Cara, S. Minogue, B. Ramesh, S. Sodha, D. Marsh, M. W. Lowdell, T. Meyer, R. H. J. Begent, I. Hart, J. F. Marshall, and K. Chester. Engineering a single-chain Fv antibody to alpha v beta 6 integrin using the specificity-determining loop of a foot-and-mouth disease virus. *Journal of Molecular Biology*, 382(2):385–401, 2008.

[111] J. Ranzinger, A. Krippner-Heidenreich, T. Haraszti, E. Bock, J. Tepperink, J. P. Spatz, and P. Scheurich. Nanoscale arrangement of apoptotic ligands reveals a demand for a minimal lateral distance for efficient death receptor activation. *Nano Lett.*, 9(12):4240–4245, 2009.

[112] F. J. Hou, S. M. Lang, S. J. Hoshaw, D. A. Reimann, and D. P. Fyhrie. Human vertebral body apparent and hard tissue stiffness. *Journal of Biomechanics*, 31(11):1009–1015, 1998.

[113] S. Phipps. Prostate tissue stiffness as measured with a resonance sensor system: a study on silicone and human prostate tissue in vitro - editorial comment. *Medical & Biological Engineering & Computing*, 44(11):941–943, 2006.

[114] E. M. Timanin. On the possibility of measuring rheological properties of soft human-tissues based on registration of their transverse stiffness. *Biofizika*, 34(3):512–516, 1989.

[115] Christine T. Schwall and Ipsita A. Banerjee. Micro- and nanoscale hydrogel systems for drug delivery and tissue engineering. *Materials*, 2(2):577–612, 2009.

[116] Y. H. Deng, C. C. Wang, X. Z. Shen, W. L. Yang, L. An, H. Gao, and S. K. Fu. Preparation, characterization, and application of multistimuli-responsive microspheres with fluorescence-labeled magnetic cores and thermoresponsive shells. *Chemistry-a European Journal*, 11(20):6006–6013, 2005.

[117] D. H. Kang, S. M. Kim, B. Lee, H. Yoon, and K. Y. Suh. Stimuli-responsive hydrogel patterns for smart microfluidics and microarrays. *Analyst*, 138(21):6230–6242, 2013.

[118] Nguyen Minh Khanh and Doo Sung Lee. Injectable biodegradable hydrogels. *Macromolecular Bioscience*, 10(6):563–579, 2010.

[119] M. Motornov, H. Royter, R. Lupitskyy, Y. Roiter, and S. Minko. Stimuli-responsive hydrogel hollow capsules by material efficient and robust cross-linking-precipitation synthesis revisited. *Langmuir*, 27(24):15305–15311, 2011.

[120] Prinda Wanakule, Gary W. Liu, Asha T. Fleury, and Krishnendu Roy. Nano-inside-micro: Disease-responsive microgels with encapsulated nanoparticles for intracellular drug delivery to the deep lung. *Journal of Controlled Release*, 162(2):429–437, 2012.

[121] E. M. White, J. Yatvin, J. B. Grubbs, J. A. Bilbrey, and J. Locklin. Advances in smart materials: Stimuli-responsive hydrogel thin films. *Journal of Polymer Science Part B-Polymer Physics*, 51(14):1084–1099, 2013.

[122] X. G. Ying, L. L. Qi, X. Li, W. Y. Zhang, and G. X. Cheng. Stimuli-responsive recognition of bsa-imprinted poly vinyl acetate grafted calcium alginate core-shell hydrogel microspheres. *Journal of Applied Polymer Science*, 127(5):3898–3909, 2013.

[123] Cunman Zhang, Zhen Geng, and Jianxin Ma. Self-assembly synthesis of ordered mesoporous carbon thin film by a dip-coating technique. *Microporous and Mesoporous Materials*, 170:287–292, 2013.

[124] M. Kurisawa, J. E. Chung, Y. Y. Yang, S. J. Gao, and H. Uyama. Injectable biodegradable hydrogels composed of hyaluronic acid-tyramine conjugates for drug delivery and tissue engineering. *Chemical Communications*, (34):4312–4314, 2005.

[125] S. S. Abolmaali, A. M. Tamaddon, and R. Dinarvand. Nano-hydrogels of methoxy polyethylene glycol-grafted branched polyethyleneimine via biodegradable cross-linking of Zn2+-ionomer micelle template. *Journal of Nanoparticle Research*, 15(12), 2013.

[126] C. Gong, T. Qi, X. Wei, Y. Qu, Q. Wu, F. Luo, and Z. Qian. Thermosensitive polymeric hydrogels as drug delivery systems. *Current Medicinal Chemistry*, 20(1):79–94, 2013.

[127] D. W. Hong, P. L. Lai, K. L. Ku, Z. T. Lai, and I. M. Chu. Biodegradable in situ gel-forming controlled vancomycin delivery system based on a thermosensitive mpeg-plcppa hydrogel. *Polymer Degradation and Stability*, 98(9):1578–1585, 2013.

[128] Prathamesh M. Kharkar, Kristi L. Kiick, and April M. Kloxin. Designing degradable hydrogels for orthogonal control of cell microenvironments. *Chemical Society Reviews*, 42(17):7335–7372, 2013.

[129] L. H. Weng, N. Rostambeigi, N. D. Zantek, P. Rostamzadeh, M. Bravo, J. Carey, and J. Golzarian. An in situ forming biodegradable hydrogel-based embolic agent for interventional therapies. *Acta Biomaterialia*, 9(9):8182–8191, 2013.

[130] D. Zhu, X. X. Jiang, C. Zhao, X. L. Sun, J. R. Zhang, and J. J. Zhu. Green synthesis and potential application of low-toxic Mn : ZnSe/ZnS core/shell luminescent nanocrystals. *Chemical Communications*, 46(29):5226–5228, 2010.

[131] Katherine J. R. Lewis and Kristi S. Anseth. Hydrogel scaffolds to study cell biology in four dimensions. *Mrs Bulletin*, 38(3):260–268, 2013.

[132] Ross DeVolder and Hyun-Joon Kong. Hydrogels for in vivo-like three-dimensional cellular studies. *Wiley Interdisciplinary Reviews-Systems Biology and Medicine*, 4(4):351–365, 2012.

[133] U. S. Gunay, B. Ozsoy, H. Durmaz, G. Hizal, and U. Tunca. V-shaped graft copolymers via triple click reactions: Diels-alder, copper-catalyzed azide-alkyne cycloaddition, and nitroxide radical coupling. *Journal of Polymer Science Part a-Polymer Chemistry*, 51(21):4667–4674, 2013.

[134] J. P. Fisher, D. Dean, P. S. Engel, and A. G. Mikos. Photoinitiated polymerization of biomaterials. *Annual Review of Materials Research*, 31:171–181, 2001.

[135] B. V. Slaughter, S. S. Khurshid, O. Z. Fisher, A. Khademhosseini, and N. A. Peppas. Hydrogels in regenerative medicine. *Advanced Materials*, 21(32-33):3307–3329, 2009.

[136] Cole A. DeForest and Kristi S. Anseth. *Advances in Bioactive Hydrogels to Probe and Direct Cell Fate*, volume 3 of *Annual Review of Chemical and Biomolecular Engineering*, pages 421–444. 2012.

[137] M. Y. He and C. C. Chu. Dual stimuli responsive glycidyl methacrylate chitosan-quaternary ammonium hybrid hydrogel and its bovine serum albumin release. *Journal of Applied Polymer Science*, 130(5):3736–3745, 2013.

[138] Ibrahim M. E-Sherbiny and Hugh D. C. Smyth. Controlled release pulmonary administration of curcumin using swellable biocompatible microparticles. *Molecular Pharmaceutics*, 9(2):269–280, 2012.

[139] Guoxin Tan, Jingwen Liao, Chengyun Ning, and Lin Zhang. Preparation, characterization, and drug-release properties of PEG-DA-based copolymer hydrogel microspheres. *Journal of Applied Polymer Science*, 125(5):3509–3516, 2012.

[140] Esmaiel Jabbari. Bioconjugation of hydrogels for tissue engineering. *Current Opinion in Biotechnology*, 22(5):655–660, 2011.

[141] S. Moeinzadeh, S. N. Khorasani, J. Y. Ma, X. Z. He, and E. Jabbari. Synthesis and gelation characteristics of photo-crosslinkable star poly (ethylene oxide-co-lactide-glycolide acrylate) macromonomers. *Polymer*, 52(18):3887–3896, 2011.

[142] G. T. Franzesi, B. Ni, Y. B. Ling, and A. Khademhosseini. A controlled-release strategy for the generation of cross-linked hydrogel microstructures. *Journal of the American Chemical Society*, 128(47):15064–15065, 2006.

[143] S. Y. Yang, J. A. Yang, E. S. Kim, G. Jeon, E. J. Oh, K. Y. Choi, S. K. Hahn, and J. K. Kim. Single-file diffusion of protein drugs through cylindrical nanochannels. *Acs Nano*, 4(7):3817–3822, 2010.

[144] H. Yan, M. Nishino, Y. Tsuboi, N. Kitamura, and K. Tsujii. Template-guided synthesis and individual characterization of poly(n-isopropylacrylamide)-based microgels. *Langmuir*, 21(16):7076–7079, 2005.

[145] T. G. Van Thienen, J. Demeester, and S. C. De Smedt. Screening poly(ethyleneglycol) micro- and nanogels for drug delivery purposes. *International Journal of Pharmaceutics*, 351(1-2):174–185, 2008.

[146] E. A. Scott, M. D. Nichols, L. H. Cordova, B. J. George, Y. S. Jun, and D. L. Elbert. Protein adsorption and cell adhesion on nanoscale bioactive coatings formed from poly(ethylene glycol) and albumin microgels. *Biomaterials*, 29(34):4481–4493, 2008.

[147] Mar Diez, Vera A. Schulte, Filippo Stefanoni, Carlo F. Natale, Francesco Mollica, Claudia M. Cesa, Jingyu Chen, Martin Moeller, Paolo A. Netti, Maurizio Ventre, and Marga C. Lensen. Molding micropatterns of elasticity on PEG-based hydrogels to control cell adhesion and migration. *Advanced Engineering Materials*, 13(10):B395–B404, 2011.

[148] Sharon K. Hamilton, Hang Lu, and Johnna S. Temenoff. *Micropatterned Hydrogels for Stem Cell Culture*, volume 2 of *Studies in Mechanobiology Tissue Engineering and Biomaterials*, pages 119–152. 2010.

[149] P. Krsko, K. Vartanian, H. Geller, A. Libera, and Ieee. *Micropatterned hydrogel surfaces for controlled cell adhesion*, pages 4–6. Annual IEEE Northeast Bioengineering Conference. 2005.

[150] K. Yoshimoto, R. Kojima, E. Takahashi, M. Ichino, H. Miyoshi, and Y. Nagasaki. 3D cell co-culture system on hydrogel micro-patterned surface fabricated by photolithography. *Journal of Photopolymer Science and Technology*, 25(1):47–52, 2012.

[151] Ibrahim M. El-Sherbiny and Hugh D. C. Smyth. Smart magnetically responsive hydrogel nanoparticles prepared by a novel aerosol-assisted method for biomedical and drug delivery applications. *Journal of Nanomaterials*, 2011.

[152] Evan A. Scott, Michael D. Nichols, Lee H. Cordova, Brandon J. George, Young-Shin Jun, and Donald L. Elbert. Protein adsorption and cell adhesion on nanoscale bioactive coatings formed from poly(ethylene glycol) and albumin microgels. *Biomaterials*, 29(34):4481–4493, 2008.

[153] G. Karoubi, M. L. Ormiston, D. J. Stewart, and D. W. Courtman. Single-cell hydrogel encapsulation for enhanced survival of human marrow stromal cells. *Biomaterials*, 30(29):5445–5455, 2009.

[154] T. P. Kraehenbuehl, L. S. Ferreira, P. Zammaretti, J. A. Hubbell, and R. Langer. Cell-responsive hydrogel for encapsulation of vascular cells. *Biomaterials*, 30(26):4318–4324, 2009.

[155] A. Kumachev, J. Greener, E. Tumarkin, E. Eiser, P. W. Zandstra, and E. Kumacheva. High-throughput generation of hydrogel microbeads with varying elasticity for cell encapsulation. *Biomaterials*, 32(6):1477–1483, 2011.

[156] J. J. Liu, D. Gao, S. F. Mao, and J. M. Lin. A microfluidic photolithography for controlled encapsulation of single cells inside hydrogel microstructures. *Science China-Chemistry*, 55(4):494–501, 2012.

[157] Rebecca M. Rounds, Bennett L. Ibey, Hope T. Beier, Michael V. Pishko, and Gerard L. Cote. Microporated PEG spheres for fluorescent analyte detection. *Journal of Fluorescence*, 17(1):57–63, 2007.

[158] Ilia Platzman, Jan-Willi Janiesch, and Joachim Pius Spatz. Synthesis of nanostructured and biofunctionalized water-in-oil droplets as tools for homing T cells. *Journal of the American Chemical Society*, 135(9):3339–3342, 2013.

[159] Y. Q. Yu, L. B. Luo, Z. F. Zhu, B. Nie, Y. G. Zhang, L. H. Zeng, Y. Zhang, C. Y. Wu, L. Wang, and Y. Jiang. High-speed ultraviolet-visible-near infrared photodiodes based on p-ZnS nanoribbon-n-silicon heterojunction. *Crystengcomm*, 15(8):1635–1642, 2013.

[160] Hui Xu, Jun Wu, Chih-Chang Chu, and Michael L. Shuler. Development of disposable PDMS micro cell culture analog devices with photopolymerizable hydrogel encapsulating living cells. *Biomedical Microdevices*, 14(2):409–418, 2012.

[161] S. Sugaya, M. Yamada, A. Hori, and M. Seki. Microfluidic production of single micrometer-sized hydrogel beads utilizing droplet dissolution in a polar solvent. *Biomicrofluidics*, 7(5), 2013.

[162] Megan M. Flake, Peter K. Nguyen, Rebecca A. Scott, Leah R. Vandiver, Rebecca Kuntz Willits, and Donald L. Elbert. Poly(ethylene glycol) microparticles produced by precipitation polymerization in aqueous solution. *Biomacromolecules*, 12(3):844–850, 2011.

[163] J. Yan, J. M. Li, M. B. Runge, M. Dadsetan, Q. S. Chen, L. C. Lu, and M. J. Yaszemski. Cross-linking characteristics and mechanical properties of an injectable biomaterial composed of polypropylene fumarate and polycaprolactone co-polymer. *Journal of Biomaterials Science-Polymer Edition*, 22(4-6):489–504, 2011.

[164] M. F. Leong, J. K. C. Toh, C. Du, K. Narayanan, H. F. Lu, T. C. Lim, A. C. A. Wan, and J. Y. Ying. Patterned prevascularised tissue constructs by assembly of polyelectrolyte hydrogel fibres. *Nature Communications*, 4, 2013.

[165] G.A. Abrams S.L. Goodman P.F. Nealey R.G. Flemming, C.J. Murphy. Effects of synthetic micro- and nano-structured surfaces on cell behavior. *Biomaterials*, 20:573–588, 1999.

[166] R. C. Schmidt and K. E. Healy. Controlling biological interfaces on the nanometer length scale. *Journal of Biomedical Materials Research Part A*, 90A(4):1252–1261, 2009.

[167] B. Radjenovic and M. Radmilovic-Radjenovic. Top down nano technologies in surface modification of materials. *Central European Journal of Physics*, 9(2):265–275, 2011.

[168] E. G. Seebauer and K. W. Noh. Trends in semiconductor defect engineering at the nanoscale. *Materials Science & Engineering R-Reports*, 70(3-6):151–168, 2010.

[169] K. L. Christman, V. D. Enriquez-Rios, and H. D. Maynard. Nanopatterning proteins and peptides. *Soft Matter*, 2(11):928–939, 2006.

[170] N. A. Amro G. Y. Liu K. Wadu-Mesthrige, S. Xu. *Langmuir*, 15:8580–8583, 1999.

[171] V. W. Jones M. D. Porter J. R. Kenseth, J. A. Harnisch. Investigation of approaches for the fabrication of protein patterns by scnning probe lithography. *Langmuir*, 17:4105–4112, 2001.

[172] M. O. Stone G. Agarwal, R. R. Naik. Immobilization of histidine tagged proteins on nickel by electrochemical dip pen nanolithography. *J. Am. Chem. Soc*, 125:7408–7412, 2003.

[173] C. A. Mirkin J. C. Smith M. Mrksich K. B. Lee, S. J. Park. Direct patterning of modified oligonucleotides on metals and insulators by dip pen nanolithography. *Science*, 295:1702–1705, 2002.

[174] C. A. Mirkin K. B. Lee, J. H. Lim. Protein nanostructure formed via direct write dip pen nanolithography. *J. Am. Chem. Soc*, 125:5588–5589, 2003.

[175] W. K. Lee A. Chilkoti S. Zauscher J. Hyun, S. J. Ahn. Molecular recognition-mediated fabrication of protein nanostructures by dip pen lithography. *Nano Letters*, 2:1203–1207, 2002.

[176] G. Klenkar G. Trinkunas B. Lindberg R. Valiokas, S. Vaitekonis. Selective recruitment of membrane protein complexes onto gold substrates patterned by dip-pen nanolithography. *Langmuir*, 22:3456–3460, 2006.

[177] T.A. Taton Z. Li C.A. Mirkin L. M. Demers, S.J. Park. Orthogonal assembly of nanoparticle building blocks on dip pen nanolithographically generated templates of dna. *Angew. Chem.*, 40:3071–3073, 2001.

[178] F. Xu S. Hong C.A. Mirkin R.D. Piner, J. Zhu. "Dip-pen" Nanolithography. *Science*, 283:661–663, 1999.

[179] H. K. Yang K. H. Park S.Y. Choe C.S. Kang S.I. Chang M.H. Han I.C. Kang M. Lee, D. K. Kang. Protein nanoarray on Prolinker TM surface construct by atomic force microscopy dip-pen nanolithography for analysis of protein interaction. *Proteomics*, 6:1094–1103, 2006.

[180] Gheber L.A. Rousso I. Newman J. Sukenik C. Lewis A. Taha H., Marks R.S. Protein printing with an atomic force sensing nanofountainpen. *Applied Physics Letters*, 83:1041–1043, 2003.

[181] Ying L.M. Korchev Y.E. Abell C. Klenerman D. Bruckbauer A., Zhou D.J. Mulitcomponent submicron features of biomolecules created by voltage controlled desposition from a nanopipet. *J. Am. Chem. Soc*, 125(9834-9839), 2003.

[182] S. Hong M. Cronin-Golomb C.A. Mirkin D.L.Kaplan D.L. Wilson, R. Martin. *Proceedings of the National Academy of Sciences of the United States of America*, 98:13660–13664, 2001.

[183] H. Lorenz J.P. Kotthaus-M. Holland M. Wendel, S. Kuhn. Nanolithography with an atomic force microscope for integrated fabrication of quantum electronic devices. *Applied Physics Letters*, 65:1775–1777, 1994.

[184] H. Matsui Z. Zhao, I.A. Banerjee. Simultaneous targeted immobilisation of anti-human IgG coated nanotubes and anti-mouse IgG coated nanotubes on the complementary antigen-patterned surfaces via biological molecular recognition. *J. Am. Chem. Soc*, 126:8930–8931, 2005.

[185] P.E. Laibinis G.Y. Liu S. Xu, S. Miller. Fabrication of nanometer scale patterns within self-assembled monlayers by nanografting. *Langmuir*, 15:7244–7251, 1999.

[186] C.S. Chow G.Y. Liu M.Z. Liu, N.A. Amro. Fabrication and imaging of nanometer-sized protein patterns. *Nano Letters*, 2:863–867, 2002.

[187] G. Fichet W.T.S Huck H.W. Li, B.V.O Muir. Nanocontact printing: a route to sub-50-nm-scale chemical and biological patterning. *Langmuir*, 19:1963–1965, 2003.

[188] B. D. Gates, Q. B. Xu, M. Stewart, D. Ryan, C. G. Willson, and G. M. Whitesides. New approaches to nanofabrication: Molding, printing, and other techniques. *Chemical Reviews*, 105(4):1171–1196, 2005.

[189] P. M. Mendes, C. L. Yeung, and J. A. Preece. Bio-nanopatterning of surfaces. *Nanoscale Research Letters*, 2(8):373–384, 2007.

[190] G. M. Whitesides and D. J. Lipomi. Soft nanotechnology: "structure" vs. "function". *Faraday Discussions*, 143:373–384, 2009.

[191] E. Meyhofer L.J. Guo A.J. Hunt J.D Hoff, L.J.Cheng. Nanoscale protein patterning by imprint lithography. *Nano Letters*, 4:853–857, 2004.

[192] Wolfe DB Paul KE Whitesides GM Odom TW, Love JC. Improved pattern transfer in soft lithography using composite stamps. *Langmuir*, 18:5314–5320, 2002.

[193] K. Feldman F. Robin N.D. Spencer G. Csucs, T. Kunzler. Microcontact printing of macromolecules with submicrometer resolution by means of polyolefin stamps. *Langmuir*, 19:6104–6109, 2003.

[194] A. Bietsch B. Michel H.R. Bosshard E. Delamarche M. Krieter B. Hecht U.P. Wild J.P. Renault, A.Bernard. Fabricating arrays of single protein molecules on glass using microcontact printing. *J. Phys. Chem*, 107:703–711, 2003.

[195] Grigoropoulos CP Healy KE Schmidt RC, Hwang DJ. Femtosecond laser ablation to create nanometer-scaled cell adhesion ligand patterns. In *54th International Symposium of the American Vacuum Society*.

[196] H.D. Maynard K.L. Christman. Protein micropatterns using a pH responsive polymer and light. *Langmuir*, 21:8389–8393, 2005.

[197] V.D. Enriquez-Rios S.C.Ward K.A. Bradley K.L. Turner H.D. Maynard K.L. Christman, M.V. Requa. Submicron streptavidin patterns for protein assembly. *Langmuir*, 22:7444–7450, 2006.

[198] K. Yamada-I. Fukiwara N. Matsukawa I. Yamashita S. Kumagai, S. Yoshii. Nanopatterning of vapor-deposited aminaminos film using EB lithography for ferritin protein adsorption. *J. Photopoly. Sci. Technol*, 18:495–500, 2005.

[199] M. Libera Y. Hong, P. Krsko. Protein surface patterning using nanoscale PEG hydrogels. *Langmuir*, 20:11123–11126, 2004.

[200] A. A. Bergman, J. Buijs, J. Herbig, D. T. Mathes, J. J. Demarest, C. D. Wilson, C. T. Reimann, R. A. Baragiola, R. Hu, and S. O. Oscarsson. Nanometer-scale arrangement of human serum albumin by adsorption on defect arrays created with a finely focused ion beam. *Langmuir*, 14(24):6785–6788, 1998.

[201] B.M. Ocko Y. Cai. Large-scale fabrication of protein nanoarrays based on nanosphere lithography. *Langmuir*, 21:9274–9279, 2005.

[202] P.D. Laible-M.A. Firestone D. Batra, S. Vogt. Self assembled, mesoporous polymeric networks for patterned protein arrays. *Langmuir*, 21:10301–10306, 2005.

[203] Roman Glass, Martin Moller, and Joachim. P. Spatz. Block copolymer micelle nanolithography. *Nanotechnology*, 14:1153–1160, 2003.

[204] Martin Moller Joachim P. Spatz, Sergei Sheiko. Ion-stabilized block copolymer micelles: Film formation and intermicellar interaction. *Macromolecules*, 29:3220–3226, 1996.

[205] Stefan Mossmer, Joachim P. Spatz, and Martin Moller. Solution behaviour of poly(styrene)-block-poly(2-vinylpyridine) micelles containing gold nanoparticles. *Macromolecules*, 33:4791–4798, 2000.

[206] G. Finkelstein J.H. Reif T.H. LaBean H. Yan, S.H. Park. DNA template self assembly of protein arrays and highly conductive nanowires. *Science*, 301:1882–1884, 2005.

[207] Y. Liu J.H. Reif T.H. LaBean H. Yan S.H. Park, P.Yin. Programmable DNA self-assemblies for nanoscale organisation of ligands and proteins. *Nano Letters*, 5:729–733, 2005.

[208] P. Dalhaimer, A. J. Engler, R. Parthasarathy, and D. E. Discher. Targeted worm micelles. *Biomacromolecules*, 5(5):1714–1719, 2004.

[209] Alexy V Eliseev F. M Menger. Cross-linked micelles. *Langmuir*, 11:1855–1857, 1995.

[210] T. Wolfram, J. P. Spatz, and R. W. Burgess. Cell adhesion to agrin presented as a nanopatterned substrate is consistent with an interaction with the extracellular matrix and not transmembrane adhesion molecules. *Bmc Cell Biology*, 9, 2008.

[211] T. Wolfram, F. Belz, T. Schoen, and J. P. Spatz. Site-specific presentation of single recombinant proteins in defined nanoarrays. *Biointerphases*, 2(1):44–48, 2007.

[212] K. Thelen, T. Wolfram, B. Maier, S. Jahrling, A. Tinazli, J. Piehler, J. P. Spatz, and G. E. Pollerberg. Cell adhesion molecule dm-grasp presented as nanopatterns to neurons regulates attachment and neurite growth. *Soft Matter*, 3(12):1486–1491, 2007.

[213] R. Ganesan, K. Kratz, and A. Lendlein. Multicomponent protein patterning of material surfaces. *Journal of Materials Chemistry*, 20(35):7322–7331, 2010.

[214] E. A. Cavalcanti-Adam, D. Aydin, V. C. Hirschfeld-Warneken, and J. P. Spatz. Cell adhesion and response to synthetic nanopatterned environments by steering receptor clustering and spatial location. *Hfsp Journal*, 2(5):276–285, 2008.

[215] T. Lohmuller, D. Aydin, M. Schwieder, C. Morhard, I. Louban, C. Pacholski, and J. P. Spatz. Nanopatterning by block copolymer micelle nanolithography and bioinspired applications. *Biointerphases*, 6(1):MR1–MR12, 2011.

[216] E. Yoshida. Control of micellar size and critical micelle concentration for "nonamphiphilic" poly(vinyl phenol)-block-polystyrene diblock copolymers. *Polymer Journal*, 35(12):965–971, 2003.

[217] Y. Matsushita, A. Takano, N. Torikai, J. Watanabe, Y. Yoshida, H. Momose, and J. Suzuki. Preparation of graft copolymers of the AB(2) type and their equilibrium structures in bulk. *Kobunshi Ronbunshu*, 57(12):803–809, 2000.

[218] J. Noolandi. Theory of block copolymer compatibilizers in homopolymer blends above and below the critical micelle concentration (cmc). *Abstracts of Papers of the American Chemical Society*, 201:68–PMSE, 1991.

[219] K. Khougaz, Z. S. Gao, and A. Eisenberg. Determination of the critical micelle, concentration of block-copolymer micelles by static light-scattering. *Macromolecules*, 27(22):6341–6346, 1994.

[220] E. Pal, A. Oszko, P. Mela, M. Moller, and I. Dekany. Preparation of hexagonally aligned inorganic nanoparticles from diblock copolymer micellar systems. *Colloids and Surfaces A: Physicochemical and Engineering Aspects*, 331(3):213–219, 2008.

[221] J. Bansmann, S. Kielbassa, H. Hoster, F. Weigl, H. G. Boyen, U. Weidwald, P. Ziemann, and R. J. Behm. Controlling the interparticle spacing of Au-salt loaded micelles and Au nanoparticles on flat surfaces. *Langmuir*, 23:10150–10155, 2007.

[222] Jennifer Q. Lu and Sung Soo Yi. Uniformly sized gold nanoparticles derived from PS-b-P2VP block copolymer templates for the controllable synthesis of Si nanowires. *Langmuir*, 22(9), 2006.

[223] Hanying Zhao, Elliot P. Douglas, Benjamin S. Harrison, and Kirk S. Schanze. Preparation of CdS nanoparticles in salt-induced block copolymer micelles. *Langmuir*, 17:8428–8433, 2001.

[224] Yunlong Gu, Jean St-Pierre, and Harry J Ploehn. Pt/glassy carbon model catalysts prepared from PS-b-P2VP micellar templates. *Langmuir*, 24, 2008.

[225] Sung Young Park Yuhan Lee Tae Gwan Park Ki Hyun Bae, Seung Ho Choi. Thermosensitive pluronic micelles stabilized by shell cross-linking with gold nanoparticles. *Langmuir*, 22:6380–6384, 2006.

[226] J. Christopher Love, Lara A. Estroff, Jennah K. Kriebel, Ralph G. Nuzzo, and George M. Whitesides. Self-assembled monolayers of thiolates on metals as a form of nanotechnology. *Chem. Rev.*, 105:1103–1169, 2005.

[227] B. D. Liu, Y. Bando, X. Jiang, C. Li, X. S. Fang, H. B. Zeng, T. Terao, C. C. Tang, M. Mitome, and D. Golberg. Self-assembled ZnS nanowire arrays: synthesis, in situ Cu doping and field emission. *Nanotechnology*, 21(37), 2010.

[228] L. Liu, W. Wang, X. J. Ju, R. Xie, and L. Y. Chu. Smart thermo-triggered squirting capsules for nanoparticle delivery. *Soft Matter*, 6(16):3759–3763, 2010.

[229] D. Aydin, I. Louban, N. Perschmann, J. Blummel, T. Lohmuller, E. A. Cavalcanti-Adam, T. L. Haas, H. Walczak, H. Kessler, R. Fiammengo, and J. P. Spatz. Polymeric substrates with tunable elasticity and nanoscopically controlled biomolecule presentation. *Langmuir*, 26(19):15472–15480, 2010.

[230] Lewis L. Lanier. Shades of grey - the blurring view of innate and adaptive immunity foreword. *Nature Reviews Immunology*, 13(2):73–74, 2013.

[231] B. Pulendran and R. Ahmed. Translating innate immunity into immunological memory: implications for vaccine development. *Cell*, 124(4):849–63, 2006.

[232] E. Vivier. NK cells and innate immunity. *Human Gene Therapy*, 23(10):A14–A14, 2012.

[233] W. Chen and C. Zhu. Mechanical regulation of T-cell functions. *Immunological Reviews*, 256(1):160–176, 2013.

[234] Hawkins Robert E. Hombach Andreas A. Abken Hinrich Gilham David E. Bridgeman, John S. Building better chimeric antigen receptors for adoptive T cell therapy. *Current Gene Therapy*, 10(2):77–90, 2010.

[235] M. Cartellieri, M. Bachmann, A. Feldmann, C. Bippes, S. Stamova, R. Wehner, A. Temme, and M. Schmitz. Chimeric antigen receptor-engineered T cells for immunotherapy of cancer. *Journal of Biomedicine and Biotechnology*, 2010.

[236] Dotti Gianpietro Cooper Laurence J. N. Jena, Bipulendu. Redirecting T-cell specificity by introducing a tumor-specific chimeric antigen receptor. *Blood*, 116(7):1035–1044, 2010.

[237] J. N. Kochenderfer, M. E. Dudley, M. S. Stevenson, W. H. Wilson, J. E. Janik, D. A. N. Nathan, I. Maric, M. Raffeld, S. A. Feldman, R. A. Morgan, and S. A. Rosenberg. A phase I clinical trial of treatment of B cell malignancies with autologous anti CD19 CAR transduced T cells. *Blood*, 116(21):1179–1180, 2010.

[238] Carl H. June Michael C. Milone. Adoptive immunotherapy: New ways to skin the cat? *Clinical Immunology*, 117:101–103, 2005.

[239] Michael C. Milone and Lance C. Kam. Investigative and clinical applications of synthetic immune synapses. *Wiley Interdisciplinary Reviews-Nanomedicine and Nanobiotechnology*, 5(1):75–85, 2013.

[240] M. C. Ngo, C. M. Rooney, J. M. Howard, and H. E. Heslop. Ex vivo gene transfer for improved adoptive immunotherapy of cancer. *Human Molecular Genetics*, 20:R93–R99, 2011.

[241] Mio Kitano Mark E Dudley Carolyn M Laurencot Steven A Rosenberg Richard A Morgan, James C Yang. Case report of a serious adverse event following the administration of T cells transduced with a chimeric antogen receptor recognizing ERBB2. *Molecular Therapy*, 18(4):843–851, 2010.

[242] C. J. Turtle and S. R. Riddell. Genetically retargeting CD8(+) lymphocyte subsets for cancer immunotherapy. *Current Opinion in Immunology*, 23(2):299–305, 2011.

[243] C. J. Turtle and S. R. Riddell. Artificial antigen-presenting cells for use in adoptive immunotherapy. *Cancer Journal*, 16(4):374–381, 2010.

[244] E. Vivier, E. Tomasello, M. Baratin, T. Walzer, and S. Ugolini. Functions of natural killer cells. *Nature Immunology*, 9(5):503–510, 2008.

[245] E. Vivier, J. A. Nunes, and F. Vely. Natural killer cell signaling pathways. *Science*, 306(5701):1517–1519, 2004.

[246] M. J. Smyth, N. Zerafa, E. Cretney, M. W. L. Teng, J. Swann, and Y. Hayakawa. NK cell-mediated tumour immune surveillance. *Tissue Antigens*, 66(5):547–548, 2005.

[247] Y. T. Bryceson, M. E. March, D. F. Barber, H. G. Ljunggren, and E. O. Long. Cytolytic granule polarization and degranulation controlled by different receptors in resting NK cells. *Journal of Experimental Medicine*, 202(7):1001–1012, 2005.

[248] Jayajit Das. Activation or tolerance of natural killer cells is modulated by ligand quality in a nonmonotonic manner. *Biophysical Journal*, 99(7):2028–2037, 2010.

[249] D. A. Liu, M. Sasidharan, and K. Nakashima. Micelles of poly(styrene-b-2-vinylpyridine-b-ethylene oxide) with blended polystyrene core and their application to the synthesis of hollow silica nanospheres. *Journal of Colloid and Interface Science*, 358(2):354–359, 2011.

[250] G. D. Rak, E. M. Mace, P. P. Banerjee, T. Svitkina, and J. S. Orange. Natural killer cell lytic granule secretion occurs through a pervasive actin network at the immune synapse. *Plos Biology*, 9(9), 2011.

[251] J. L. Upshaw and P. J. Leibson. NKG2D-mediated activation of cytotoxic lymphocytes: Unique signaling pathways and distinct functional outcomes. *Seminars in Immunology*, 18(3):167–175, 2006.

[252] J. L. Upshaw, L. N. Arneson, R. A. Schoon, C. J. Dick, D. D. Billadeau, and P. J. Leibson. NKG2D-mediated signaling requires a DAP10-bound Grb2-Vav1 intermediate and phosphatidylinositol-3-kinase in human natural killer cells. *Nature Immunology*, 7(5):524–532, 2006.

[253] G. J. Weiner. CD16 and NK cell activation. *Immunology*, 135:20–20, 2011.

[254] J. S. Orange, K. E. Harris, M. M. Andzelm, M. M. Valter, R. S. Geha, and J. L. Strominger. The mature activating natural killer cell immunologic synapse is formed in distinct stages. *Proc. Natl. Acad. Sci. U.S.A.*, 100(24):14151–6, 2003.

[255] R. M. May, M. Okumura, C. J. Hsu, H. Bassiri, E. J. Yang, G. Rak, E. M. Mace, N. H. Philip, W. G. Zhang, T. Baumgart, J. S. Orange, K. E. Nichols, and T. Kambayashi. Murine natural killer immunoreceptors use distinct proximal signaling complexes to direct cell function. *Blood*, 121(16):3135–3146, 2013.

[256] E. O. Long. Regulation of immune responses through inhibitory receptors. *Annual Review of Immunology*, 17:875–904, 1999.

[257] E. O. Long, H. S. Kim, D. F. Liu, M. E. Peterson, and S. Rajagopalan. *Controlling Natural Killer Cell Responses: Integration of Signals for Activation and Inhibition*, volume 31 of *Annual Review of Immunology*, pages 227–258. 2013.

[258] C. R. Almeida and D. D. Davis. Patterning of MHC class I protein and its segregation from ICAM-1 at NK cell synapses reflects its cell surface density. *Journal of Immunology*, 176:S173–S173, 2006.

[259] S. Bessoles, G. S. Angelov, J. Back, G. Leclercq, E. Vivier, and W. Held. Education of murine NK cells requires both cis and trans recognition of MHC Class I molecules. *Journal of Immunology*, 191(10):5044–5051, 2013.

[260] M. S. Fassett, D. M. Davis, M. M. Valter, G. B. Cohen, and J. L. Strominger. Signaling at the inhibitory natural killer cell immune synapse regulates lipid raft polarization but not class I MHC clustering. *Proceedings of the National Academy of Sciences of the United States of America*, 98(25):14547–14552, 2001.

[261] Nathalie T. Joncker, Nataliya Shifrin, Frederic Delebecque, and David H. Raulet. Mature natural killer cells reset their responsiveness when exposed to an altered mhc environment. *Journal of Experimental Medicine*, 207(10):2065–2072, 2010.

[262] L. L. Lanier, T. J. Kipps, and J. H. Phillips. Functional properties of a unique subset of cytotoxic CD3+ T lymphocytes that express Fc receptors for IgG (CD16/Leu-11 antigen). *J. Exp. Med.*, 162(6):2089–106, 1985.

[263] Lewis L. Lanier. Up on the tightrope: natural killer cell activation and inhibition. *Nature Immunology*, 9(5):495–502, 2008.

[264] S. Y. Wang, E. Racila, R. P. Taylor, and G. J. Weiner. NK-cell activation and antibody-dependent cellular cytotoxicity induced by rituximab-coated target cells is inhibited by the C3b component of complement. *Blood*, 111(3):1456–1463, 2008.

[265] B. D. Liu, Y. S. Bando, M. S. Wang, C. Y. Zhi, X. S. Fang, C. C. Tang, M. Mitome, and D. Golberg. Electron-beam irradiation induced conductivity in ZnS nanowires as revealed by in situ transmission electron microscope. *Journal of Applied Physics*, 106(3), 2009.

[266] J. J. Oshea, A. M. Weissman, I. C. S. Kennedy, and J. R. Ortaldo. Engagement of the natural-killer-cell IgG Fc receptor results in tyrosine phosphorylation of the XI-chain. *Proceedings of the National Academy of Sciences of the United States of America*, 88(2):350–354, 1991.

[267] O. Letourneur, I. C. S. Kennedy, A. T. Brini, J. R. Ortaldo, J. J. Oshea, and J. P. Kinet. Characterization of the family of dimers associated with Fc-receptors (Fc-epsilon-RI and Fc-gamma-RIII). *Journal of Immunology*, 147(8):2652–2656, 1991.

[268] M. P. Scheid, M. K. Hoffmann, K. Komuro, Hammerli.U, J. Abbott, E. A. Boyse, G. H. Cohen, J. A. Hopper, R. S. Schulof, and Goldstei.Al. Differentiation of T-cells induced by preparations from thymus and by nonthymic agents - determined state of precursor cell. *Journal of Experimental Medicine*, 138(4):1027–1032, 1973.

[269] M. P. Scheid, Hammerli.U, J. Abbott, and E. A. Boyse. Thymic and nonthymic agents as inducers of T cell-differentiation. *Journal of General Physiology*, 62(5):652–652, 1973.

[270] J. Maher and E. T. Davies. Targeting cytotoxic T lymphocytes for cancer immunotherapy. *British journal of cancer*, 91(5):817–21, 2004.

[271] J. Rossy, D. M. Owen, D. J. Williamson, Z. M. Yang, and K. Gaus. Conformational states of the kinase Lck regulate clustering in early T cell signaling. *Nature Immunology*, 14(1):82–89, 2013.

[272] O. Acuto and F. Michel. CD28-mediated co-stimulation: A quantitative support for TCR signalling. *Nature Reviews Immunology*, 3(12):939–951, 2003.

[273] S. Goral. The three-signal hypothesis of lymphocyte activation/targets for immunosuppression. *Dialysis & Transplantation*, 40(1):14–16, 2011.

[274] M. C. Miceli, M. Moran, C. D. Chung, V. P. Patel, T. Low, and W. Zinnanti. Co-stimulation and counter-stimulation: lipid raft clustering controls TCR signaling and functional outcomes. *Seminars in Immunology*, 13(2):115–128, 2001.

[275] A. Babich and J. K. Burkhardt. Coordinate control of cytoskeletal remodeling and calcium mobilization during t-cell activation. *Immunological Reviews*, 256(1):80–94, 2013.

[276] D. Depoil, R. Zaru, M. Guiraud, A. Chauveau, J. Harriague, G. Bismuth, C. Utzny, S. Muller, and S. Valitutti. Immunological synapses are versatile structures enabling selective T cell polarization. *Immunity*, 22(2):185–94, 2005.

[277] M. L. Dustin and D. Depoil. New insights into the T cell synapse from single molecule techniques. *Nature Reviews Immunology*, 11(10):672–684, 2011.

[278] D. E. Discher and A. J. Engler. Material softness dictates differentiation of human mesenchymal stem cells. *Abstracts of Papers of the American Chemical Society*, 230:U1199–U1199, 2005.

[279] A. J. Engler, S. Sen, H. L. Sweeney, and D. E. Discher. Matrix elasticity directs stem cell lineage specification. *Cell*, 126(4):677–689, 2006.

[280] Roddy S. O'Connor, Xueli Hao, Keyue Shen, Keenan Bashour, Tatiana Akimova, Wayne W. Hancock, Lance C. Kam, and Michael C. Milone. Substrate rigidity regulates human T cell activation and proliferation. *Journal of Immunology*, 189(3):1330–1339, 2012.

[281] Edward Judokusumo, Erdem Tabdanov, Sudha Kumari, Michael L. Dustin, and Lance C. Kam. Mechanosensing in T lymphocyte activation. *Biophysical Journal*, 102(2):L5–L7, 2012.

[282] Zhengpeng Wan, Shaosen Zhang, Yilin Fan, Kai Liu, Feng Du, Angel M. Davey, Huiyuan Zhang, Weidong Han, Chunyang Xiong, and Wanli Liu. B cell activation is regulated by the stiffness properties of the substrate presenting the antigens. *Journal of Immunology*, 190(9):4661–4675, 2013.

[283] V. A. Barsegov. Two conformational state model for P-selectin catch-slip bond character. *Biophysical Journal*, 86(1):152A–152A, 2004.

[284] K. Konstantopoulos, W. D. Hanley, and D. Wirtz. Receptor-ligand binding: 'catch' bonds finally caught. *Current Biology*, 13(15):R611–R613, 2003.

[285] B. T. Marshall, M. Long, J. W. Piper, T. Yago, R. P. McEver, and C. Zhu. Direct observation of catch bonds involving cell-adhesion molecules. *Nature*, 423(6936):190–193, 2003.

[286] T. Yago, J. H. Wu, C. D. Wey, A. G. Klopocki, C. Zhu, and R. P. McEver. Catch bonds govern adhesion through L-selectin at threshold shear. *Journal of Cell Biology*, 166(6):913–923, 2004.

[287] Paul A. Janmey Terri H. finkel Zhengyu Ma, Kim A. Sharp. Surface- anchored monomeric agonist pMHC's alone trigger TCR with high sensitivity. *PLoS Biology*, 6(2):328–342, 2008.

[288] Rajat Varma Michael L. Dustin Ronald D. Vale Yoshihisa Kaizuka, Adam D. Douglass. Mechanisms for segregating T cell receptor and adhesion molecules during immunological synapse formation in Jurkat T cells. *PNAS*, 104(51):20296–20301, 2007.

[289] R. Varma, G. Campi, T. Yokosuka, T. Saito, and M. L. Dustin. T cell receptor-proximal signals are sustained in peripheral microclusters and terminated in the central supramolecular activation cluster. *Immunity*, 25(1):117–27, 2006.

[290] G. Campi, R. Varma, and M. L. Dustin. Actin and agonist MHC-peptide complex-dependent T cell receptor microclusters as scaffolds for signaling. *J. Exp. Med.*, 202(8):1031–6, 2005.

[291] A. C. Brown, I. M. Dobbie, J. M. Alakoskela, I. Davis, and D. M. Davis. Super-resolution imaging of remodeled synaptic actin reveals different synergies between NK cell receptors and integrins. *Blood*, 120(18):3729–40, 2012.

[292] J. Dinic, P. Ashrafzadeh, and I. Parmryd. Actin filaments attachment at the plasma membrane in live cells cause the formation of ordered lipid domains. *Biochimica Et Biophysica Acta-Biomembranes*, 1828(3):1102–1111, 2013.

[293] Yi Sun, Radhika D. Dandekar, Yuntao S. Mao, Helen L. Yin, and Christoph Wuelfing. Phosphatidylinositol (4,5) bisphosphate controls T cell activation by regulating T cell rigidity and organization. *Plos One*, 6(11), 2011.

[294] J. R. James and R. D. Vale. Biophysical mechanism of T-cell receptor triggering in a reconstituted system. *Nature*, 487(7405):64–69, 2012.

[295] K. D. Mossman, G. Campi, J. T. Groves, and M. L. Dustin. Altered TCR signaling from geometrically repatterned immunological synapses. *Science*, 310(5751):1191–3, 2005.

[296] A. L. DeMond, K. D. Mossman, T. Starr, M. L. Dustin, and J. T. Groves. T cell receptor microcluster transport through molecular mazes reveals mechanism of translocation. *Biophys. J.*, 94(8):3286–92, 2008.

[297] D. M. Davis and M. L. Dustin. What is the importance of the immunological synapse? *Trends in Immunology*, 25(6):323–327, 2004.

[298] S. J. Davis and P. A. van der Merwe. The kinetic-segregation model: TCR triggering and beyond. *Nature Immunol.*, 7(8):803–9, 2006.

[299] J. Doh and D. J. Irvine. Immunological synapse arrays: Patterned protein surfaces that modulate immunological synapse structure formation in T cells. *Proc. Natl. Acad. Sci. U.S.A.*, 103(15):5700–5705, 2006.

[300] L. Boding, M. W. Nielsen, C. M. Bonefeld, M. R. von Essen, B. L. Nielsen, J. P. H. Lauritsen, A. K. Hansen, M. M. Nielsen, M. Kongsbak, M. Rubin, M. T. Vennegaard, N. Odum, and C. Geisler. Polymorphisms of the T cell receptor CD3 delta and CD3 epsilon chains affect anti-CD3 antibody binding and T cell activation. *Molecular Immunology*, 47(15):2450–2457, 2010.

[301] S. G. Nathenson, W. G. Zhang, A. C. M. Young, and J. C. Sacchettini. The use of crystal-structure analysis of recombinant class-I MHC-peptide complexes to analyze the molecular-basis of peptide/MHC/TCR interactions. *Journal of Cellular Biochemistry*, pages 91–91, 1993.

[302] M. S. Cragg, S. M. Morgan, H. T. C. Chan, B. P. Morgan, A. V. Filatov, P. W. M. Johnson, R. R. French, and M. J. Glennie. Complement-mediated lysis by anti-CD20 mAb correlates with segregation into lipid rafts. *Blood*, 101(3):1045–1052, 2003.

[303] H. T. C. Chan, D. Hughes, R. R. French, A. L. Tutt, C. A. Walshe, J. L. Teeling, M. J. Glennie, and M. S. Cragg. CD20-induced lymphoma cell death is independent of both caspases and its redistribution into Triton X-100 insoluble membrane rafts. *Cancer Research*, 63(17):5480–5489, 2003.

[304] H. T. C. Chan, D. Hughes, R. R. French, A. L. Tutt, C. Walshe, M. J. Glennie, and M. S. Cragg. CD20 induced apoptosis is an antibody dependent phenomenon which does not require redistribution into TX-100 insoluble membrane rafts. *British Journal of Cancer*, 88:S36–S36, 2003.

[305] Gerhard J. Niederfellner, Alfred Lammens, Manfred Schwaiger, Guy Georges, Kornelius Wiechmann, Andreas Franke, Wolfgang Schaefer, Stefan Jenewein, Jerry Slootstra, Ekkehard Moessner, Pablo Umana, Karl-Peter Hopfner, and Christian Klein. Crystal structure analysis reveals that the novel Type II anti-CD20 antibody GA101 interacts with a similar epitope as rituximab and ocrelizumab but in a fundamentally different way. *Blood*, 114(22):1435–1435, 2009.

[306] R. L. Wange and L. E. Samelson. Complex complexes: Signaling at the TCR. *Immunity*, 5(3):197–205, 1996.

[307] D. Depoil, S. Fleire, B. L. Treanor, M. Weber, N. E. Harwood, K. L. Marchbank, V. L. J. Tybulewicz, and F. D. Batista. CD19 is essential for B cell activation by promoting B cell receptor-antigen microcluster formation in response to membrane-bound ligand. *Nature Immunology*, 9(1):63–72, 2008.

[308] N. Anikeeva, D. Gakamsky, J. Scholler, and Y. Sykulev. Evidence that the density of self peptide-MHC ligands regulates T-cell receptor signaling. *Plos One*, 7(8), 2012.

[309] K. Somersalo, N. Anikeeva, T. N. Sims, V. K. Thomas, R. K. Strong, T. Spies, T. Lebedeva, Y. Sykulev, and M. L. Dustin. Cytotoxic t lymphocytes form an antigen-independent ring junction. *Journal of Clinical Investigation*, 113(1):49–57, 2004.

[310] Y. Sykulev, N. Anikeeva, and D. Gakamsky. The role of peptide-MHC ligand density in stimulating T-cell receptor signaling. *Journal of Immunology*, 188, 2012.

[311] D. M. Davis, I. Chiu, M. Fassett, G. B. Cohen, O. Mandelboim, and J. L. Strominger. The human natural killer cell immune synapse. *Proceedings of the National Academy of Sciences of the United States of America*, 96(26):15062–15067, 1999.

[312] Bebhinn Treanor, Peter M. P. Lanigan, Sunil Kumar, Chris Dunsby, Ian Munro, Egidijus Auksorius, Fiona J. Culley, Marco A. Purbhoo, David Phillips, Mark A. A. Neil, Deborah N. Burshtyn, Paul M. W. French, and Daniel M. Davis. Microclusters of inhibitory killer immunoglobulin like receptor signaling at natural killer cell immunological synapses. *Journal of Cell Biology*, 174(1):153–161, 2006.

[313] S. Aguera-Gonzales, C. C. Gross, L. Fernandez-Messina, O. Ashiru, G. Esteso, H. C. Hang, H. T. Reyburn, E. O. Long, and M. Vales-Gomez. Palmitoylation of MICA, a ligand for NKG2D, mediates its recruitment to membrane microdomains and promotes its shedding. *European Journal of Immunology*, 41(12):3667–3676, 2011.

[314] K. Eleme, S. B. Taner, B. Onfelt, L. M. Collinson, F. E. McCann, N. J. Chalupny, D. Cosman, C. Hopkins, A. I. Magee, and D. M. Davis. Cell surface organization of stress-inducible proteins ULBP and MICA that stimulate human NK cells and T cells via NKG2D. *Journal of Experimental Medicine*, 199(7):1005–1010, 2004.

[315] S. V. Pageon, S. P. Cordoba, D. M. Owen, S. M. Rothery, A. Oszmiana, and D. M. Davis. Superresolution microscopy reveals nanometer-scale reorganization of inhibitory natural killer cell receptors upon activation of NKG2D. *Sci. Signal*, 6(285):ra62, 2013.

[316] Sophie Guia, Baptiste N. Jaeger, Stefan Piatek, Sebastien Mailfert, Tomasz Trombik, Aurore Fenis, Nicolas Chevrier, Thierry Walzer, Yann M. Kerdiles, Didier Marguet, Eric Vivier, and Sophie Ugolini. Confinement of activating receptors at the plasma membrane controls natural killer cell tolerance. *Science Signaling*, 4(167), 2011.

[317] T. B. Sanni, M. Masilamani, J. Kabat, J. E. Coligan, and F. Borrego. Exclusion of lipid rafts and decreased mobility of CD94/NKG2A receptors at the inhibitory NK cell synapse. *Molecular Biology of the Cell*, 15(7):3210–3223, 2004.

[318] M. Masilamani, T. B. Sanni, J. Kabat, F. Borrego, and J. E. Coligan. CD94/NKG2A inhibitory natural killer cell synapse, membrane dynamics and intracellular trafficking. *Molecular Biology of the Cell*, 15:428A–429A, 2004.

[319] Y. M. Vyas, H. Maniar, C. E. Lyddane, M. Sadelain, and B. Dupont. Spatial and temporal redistribution of inhibitory kir molecules in the natural killer cell immune synapse. *Faseb Journal*, 15(5):A1029–A1029, 2001.

[320] Y. M. Vyas, K. M. Mehta, M. Morgan, H. Maniar, L. Butros, S. Jung, J. K. Burkhardt, and B. Dupont. Spatial organization of signal transduction molecules in the NK cell immune synapses during MHC class I-regulated noncytolytic and cytolytic interactions. *Journal of Immunology*, 167(8):4358–4367, 2001.

[321] Y. M. Vyas, H. Maniar, and B. Dupont. Quantitation of distinct and sequential events that regulate the natural killer cell immune synapse. *Faseb Journal*, 16(5):A1055–A1055, 2002.

[322] Y. M. Vyas, H. Maniar, and B. Dupont. Visualization of signaling pathways and cortical cytoskeleton in cytolytic and noncytolytic natural killer cell immune synapses. *Immunological Reviews*, 189:161–178, 2002.

[323] T. Yokosuka, K. Sakata-Sogawa, W. Kobayashi, M. Hiroshima, A. Hashimoto-Tane, M. Tokunaga, M. L. Dustin, and T. Saito. Newly generated T cell receptor microclusters initiate and sustain T cell activation by recruitment of Zap70 and SLP-76. *Nature Immunology*, 6(12):1253–1262, 2005.

[324] A. M. Beal, N. Anikeeva, R. Varma, T. O. Cameron, G. Vasiliver-Shamis, P. J. Norris, M. L. Dustin, and Y. Sykulev. Kinetics of early T cell receptor signaling regulate the pathway of lytic granule delivery to the secretory domain. *Immunity*, 31(4):632–642, 2009.

[325] B. Alarcon, D. Gil, P. Delgado, and W. W. A. Schamel. Initiation of TCR signaling: regulation within CD3 dimers. *Immunological Reviews*, 191(1):38–46, 2003.

[326] Y. Chen, J. Qin, J. Y. Cai, and Z. W. Chen. Cold induces micro- and nano-scale reorganization of lipid raft markers at mounds of T-cell membrane fluctuations. *PLoS ONE*, 4(4), 2009.

[327] H. T. He and D. Marguet. T-cell antigen receptor triggering and lipid rafts: a matter of space and time scales - Talking Point on the involvement of lipid rafts in T-cell activation. *Embo Reports*, 9(6):525–530, 2008.

[328] B. F. Lillemeier, M. A. Mortelmaier, M. B. Forstner, J. B. Huppa, J. T. Groves, and M. M. Davis. TCR and Lat are expressed on separate protein islands on T cell membranes and concatenate during activation. *Nature Immunol.*, 11(1):90–6, 2010.

[329] P. Sharma, R. Varma, R. C. Sarasij, Ira, K. Gousset, G. Krishnamoorthy, M. Rao, and S. Mayor. Nanoscale organization of multiple GPI-anchored proteins in living cell membranes. *Cell*, 116(4):577–89, 2004.

[330] D. J. Williamson, D. M. Owen, J. Rossy, A. Magenau, M. Wehrmann, J. J. Gooding, and K. Gaus. Pre-existing clusters of the adaptor Lat do not participate in early T cell signaling events. *Nature Immunol.*, 12(7):655–62, 2011.

[331] Travis J. Crites, Lirong Chen, and Rajat Varma. A TIRF microscopy technique for real-time, simultaneous imaging of the TCR and its associated signaling proteins. *Journal of visualized experiments : JoVE*, (61), 2012.

[332] C. Yu, A. F. P. Sonnen, R. George, B. H. Dessailly, L. J. Stagg, E. J. Evans, C. A. Orengo, D. I. Stuart, J. E. Ladbury, S. Ikemizu, R. J. C. Gilbert, and S. J. Davis. Rigid-body ligand recognition drives cytotoxic T-lymphocyte antigen 4 (CTLA-4) receptor triggering. *Journal of Biological Chemistry*, 286(8):6685–6696, 2011.

[333] Y. Yu, A. A. Smoligovets, and J. T. Groves. Modulation of T cell signaling by the actin cytoskeleton. *Journal of Cell Science*, 126(5):1049–1058, 2013.

[334] A. Grakoui, S. K. Bromley, C. Sumen, M. M. Davis, A. S. Shaw, P. M. Allen, and M. L. Dustin. The immunological synapse: a molecular machine controlling T cell activation. *Science*, 285(5425):221–7, 1999.

[335] T. Lohmuller, S. Triffo, G. P. O'Donoghue, Q. Xu, M. P. Coyle, and J. T. Groves. Supported membranes embedded with fixed arrays of gold nanoparticles. *Nano Letters*, 11(11):4912–4918, 2011.

[336] H. Saiki. Scanning electron-microscopy in structural researches on wood and wood-based materials. *Mokuzai Gakkaishi*, 36(11):900–908, 1990.

[337] D. F. Blake. Scanning electron-microscopy - principles, practice, and application to the determination of surface-morphology, elemental composition and structure of minerals. *Abstracts of Papers of the American Chemical Society*, 196:116–GEOC, 1988.

[338] W. C. Nixon. General principles of scanning electron microscopy. *Philosophical Transactions of the Royal Society of London Series B-Biological Sciences*, 261(837):45–&, 1971.

[339] A. Senin. Scanning electron-microscopy - some general principles. *Journal of Submicroscopic Cytology and Pathology*, 10(1):148–148, 1978.

[340] E. Vicario and M. Pitaval. Diffraction contrast in scanning electron-microscopy - principles and applications. *Journal of Microscopy-Oxford*, 13(3):296–&, 1972.

[341] F. Li, Y. Jiang, L. Hu, L. Y. Liu, Z. Li, and X. T. Huang. Structural and luminescent properties of ZnO nanorods and ZnO/ZnS nanocomposites. *Journal of Alloys and Compounds*, 474(1-2):531–535, 2009.

[342] D. Liu, Y. T. Bryceson, T. Meckel, G. Vasiliver-Shamis, M. L. Dustin, and E. O. Long. Integrin-dependent organization and bidirectional vesicular traffic at cytotoxic immune synapses. *Immunity*, 31(1):99–109, 2009.

[343] M. Isaacson. Basic principles of scanning-transmission electron-microscopy as an analytical tool. *Abstracts of Papers of the American Chemical Society*, 181(MAR):11–MACR, 1981.

[344] D. Segets, J. M. Lucas, R. N. K. Taylor, M. Scheele, H. M. Zheng, A. P. Alivisatos, and W. Peukert. Determination of the quantum dot band gap dependence on particle size from optical absorbance and transmission electron microscopy measurements. *Acs Nano*, 6(10):9021–9032, 2012.

[345] T. Kuzuya, Y. Tai, S. Yamamuro, T. Hihara, D. L. Peng, and K. Sumiyama. Synthesis of zinc sulfide nanocrystals and fabrication of nanocrystal superlattice. *Materials Transactions*, 45(8):2650–2652, 2004.

[346] G. J. Brakenhoff, P. Blom, P. J. Barends, and C. Bakker. High-resolution confocal scanning light-microscopy. *Ultramicroscopy*, 4(1):115–115, 1979.

[347] G. J. Brakenhoff. Imaging modes in confocal scanning light-microscopy (CSLM). *Journal of Microscopy-Oxford*, 117(NOV):233–242, 1979.

[348] D. Axelrod. Total internal reflection fluorescence microscopy in cell biology. *Biophotonics, Pt B*, 361:1–33, 2003.

[349] Nima Aghaeepour, Greg Finak, Holger Hoos, Tim R. Mosmann, Ryan Brinkman, Raphael Gottardo, Richard H. Scheuermann, C. A. P. Consortium Flow, and Dream Consortium. Critical assessment of automated flow cytometry data analysis techniques (vol 10, pg 228, 2013). *Nature Methods*, 10(5):445–445, 2013.

[350] Yuki Morono, Takeshi Terada, Jens Kallmeyer, and Fumio Inagaki. An improved cell separation technique for marine subsurface sediments: applications for high-throughput analysis using flow cytometry and cell sorting. *Environmental Microbiology*, 15(10):2841–2849, 2013.

[351] J. P. Spatz, S. Mossmer, C. Hartmann, M. Moller, T. Herzog, M. Krieger, H. G. Boyen, P. Ziemann, and B. Kabius. Ordered deposition of inorganic clusters from micellar block copolymer films. *Langmuir*, 16(2):407–415, 2000.

[352] Cornelus F. van Nostrum. Covalently cross-linked amphiphilic block copolymer micelles. *Soft Matter*, 2010.

[353] Xiang-Sheng Liu Gong-Yan Liu Xuan Yang Jian Ji Li-Ping Lv, Jian-Ping xu. Disulfide-crosslinked biomimetic micelles: Formation, thiol reactivity and cytotoxicity behaviour. *Macromolecular Chemistry and Physics*, 211:2292–2300, 2010.

[354] Martina H. Stenzel Hien T. T. Duong, T. L. Uyen Nguyen. Micelles with surface conjugated rgd peptide and crosslinked polyurea core via raft polymerization. *Polym. Chem*, 1:171–182, 2010.

[355] D. F. Liu, J. A. Martina, X. S. Wu, J. A. Hammer, and E. O. Long. Two modes of lytic granule fusion during degranulation by natural killer cells. *Immunology and Cell Biology*, 89(6):728–738, 2011.

[356] R. Glass, M. Arnold, J. Blummel, A. Kuller, M. Moller, and J. P. Spatz. Micro-nanostructured interfaces fabricated by the use of inorganic block copolymer micellar monolayers as negative resist for electron-beam lithography. *Advanced Functional Materials*, 13(7):569–575, 2003.

[357] P. Mueller-Buschbaum, R. Gebhardt, E. Maurer, E. Bauer, R. Gehrke, and W. Doster. Thin casein films as prepared by spin-coating: Influence of film thickness and of pH. *Biomacromolecules*, 7(6):1773–1780, 2006.

[358] T. Lohmuller, M. Helgert, M. Sundermann, R. Brunner, and J. P. Spatz. Biomimetic interfaces for high-performance optics in the deep-uv light range. *Nano Letters*, 8(5):1429–1433, 2008.

[359] Jungseok Hahn and S. E. Webber. Deposition of cationic polymer micelles on planar SiO2 surfaces. *Langmuir*, 20:4211–4219, 2004.

[360] Levich B. Landau, L. Dragging of a liquid by a moving plate. *Acta Physicochimica U.R.S.S.*, 17(1-2):42–54, 1942.

[361] A. A. Darhuber, S. M. Troian, J. M. Davis, S. M. Miller, and S. Wagner. Selective dip-coating of chemically micropatterned surfaces. *Journal of Applied Physics*, 88(9):5119–5126, 2000.

[362] Joachim P. Spatz, Stefan Mossmer, Christoph Hartmann, and Martin Moller. Ordered deposition of inorganic clusters from micellar block copolymer films. *Langmuir*, 16:407–415, 2000.

[363] P. Yimsiri and M. R. Mackley. Spin and dip coating of light-emitting polymer solutions: Matching experiment with modelling. *Chemical Engineering Science*, 61(11):3496–3505, 2006.

[364] G. Lengl, A. Plettl, P. Ziemann, J. P. Spatz, and M. Moeller. Excimer laser ablation of gold-loaded inverse polystyrene-block-poly (2-vinylpyridine) micelles. *Applied Physics A Materials Science & Processing*, 72(6):679–685, 2001.

[365] K. Eljabaly and A. Reisman. Growth-kinetics and annealing studies of the cathodic plasma oxidation of silicon. *Journal of the Electrochemical Society*, 138(4):1064–1070, 1991.

[366] P. E. Dyer. Excimer laser polymer ablation: twenty years on. *Applied Physics A Materials Science & Processing*, 77:167–173, 2003.

[367] C. Gutierrez-Wing, J. A. Ascencio, M. Perez-Alvarez, M. Marin-Almazo, and M. Jose-Yacaman. On the structure and formation of self-assembled lattices of gold nanoparticles. *Journal of Cluster Science*, 9(4), 1998.

[368] T. Herzog. *Untersuchung zum Verhalten selbstorganisierter metallischer Nanoteilchen*. Herbert Utz Verlag Wissenschaft, Ulm, 1999.

[369] Olga Lopez-Acevedo Pablo D. Jadzinsky Guillermo Calero Christopher J Ackerson Robert L. Whetten Henrik Gronbeck Hannu Hakkinen Michael Walter, JaakkoAkola. A unified view of ligand protected gold clusters as superatom complexes. *PNAS*, 105(27):9157–9162, 2009.

[370] Tamas Haraszti Eva Bock Jessica Tepperink Joachim P. Spatz Peter Scheurich Julia Ranzinger, Anja Krippner-Heidenreich. Nanoscale arrangement of apoptotic ligands reveals a demand fora minimal lateral distance for efficient death receptor activation. *Nano Letters*, 9(12):4240–4245, 2009.

[371] B. Gorzolnik, P. Mela, and M. Moeller. Nano-structured micropatterns by combination of block copolymer self-assembly and UV photolithography. *Nanotechnology*, 17(19):5027–5032, 2006.

[372] P. Mela, B. Gorzolnik, M. Buckins, A. Mourran, J. Mayer, and M. Moller. Low-ion-dose FIB modification of monomicellar layers for the creation of highly ordered metal nanodot arrays. *Small*, 3(8):1368–1373, 2007.

[373] S. Jaehrling, K. Thelen, T. Wolfram, and G. E. Pollerberg. Nanopatterns biofunctionalized with cell adhesion molecule DM-GRASP offered as cell substrate: Spacing determines attachment and differentiation of neurons. *Nano Letters*, 9(12):4115–4121, 2009.

[374] J. R. Cochran, J. D. Stone, and L. J. Stern. Receptor spacing, but not intramolecular orientation, is critical for CD4(+) T cell triggering. *Faseb Journal*, 15(5):A1155–A1155, 2001.

[375] J. R. Cochran, T. O. Cameron, J. D. Stone, J. B. Lubetsky, and L. J. Stern. Receptor proximity, not intermolecular orientation, is critical for triggering T-cell activation. *J. Biol. Chem.*, 276(30):28068–28074, 2001.

[376] S. Y. Park and W. H. Sul. The effects of the selectivity of the toluene/ethanol mixture on the micellar and the ordered structures of an asymmetric poly(styrene-b-4-vinylpyridine). *Polymer*, 49(15):3327–3334, 2008.

[377] S. W. Yeh, K. H. Wei, Y. S. Sun, U. S. Jeng, and K. S. Liang. CdS nanoparticles induce a morphological transformation of poly(styrene-b-4-vinylpyridine) from hexagonally packed cylinders to a lamellar structure. *Macromolecules*, 38(15):6559–6565, 2005.

[378] M. F. Schulz, A. K. Khandpur, F. S. Bates, K. Almdal, K. Mortensen, D. A. Hajduk, and S. M. Gruner. Phase behavior of polystyrene-poly(2-vinylpyridine) diblock copolymers. *Macromolecules*, 29(8):2857–2867, 1996.

[379] S. Lee and N. D. Spencer. Adsorption properties of poly(L-lysine)-graft-poly(ethylene glycol) (PLL-g-PEG) at a hydrophobic interface: Influence of tribological stress, pH, salt concentration, and polymer molecular weight. *Langmuir*, 24(17):9479–9488, 2008.

[380] J. W. Lussi, D. Falconnet, J. A. Hubbell, M. Textor, and G. Csucs. Pattern stability under cell culture conditions - A comparative study of patterning methods based on PLL-g-PEG background passivation. *Biomaterials*, 27(12):2534–2541, 2006.

[381] R. Marie, J. P. Beech, J. Voros, J. O. Tegenfeldt, and F. Hook. Use of PLL-g-PEG in micro-fluidic devices for localizing selective and specific protein binding. *Langmuir*, 22(24):10103–10108, 2006.

[382] V. Saravia, S. Kupcu, M. Nolte, C. Huber, D. Pum, A. Fery, U. B. Sleytr, and J. L. Toca-Herrera. Bacterial protein patterning by micro-contact printing of PLL-g-PEG. *Journal of Biotechnology*, 130(3):247–252, 2007.

[383] M. Heuberger, T. Drobek, and N. D. Spencer. Interaction forces and morphology of a protein-resistant poly(ethylene glycol) layer. *Biophys. J.*, 88(1):495–504, 2005.

[384] C. E. D. Chidsey, M. D. Porter, and D. L. Allara. Electrochemical characterization of n-alkyl thiol, sulfide, and disulfide monolayers on gold. *Journal of the Electrochemical Society*, 133(3):C130–C130, 1986.

[385] A. J. Dahlstedt, A. Katz, and H. Westerblad. Injection of creatine kinase (CK) normalizes the contractile function of CK deficient muscle cells. *Acta Physiologica Scandinavica*, 170(4):A84–A85, 2000.

[386] L. M. Memmo and P. McKeown-Longo. The alpha v beta 5 integrin functions as an endocytic receptor for vitronectin. *Journal of Cell Science*, 111:425–433, 1998.

[387] P. Xu, X. Ji, V. Abetz, and S. M. Jiang. Micropatterning of Ag and Au nanoparticles by microcontact printing and block copolymer micelles. *Journal of Nanoscience and Nanotechnology*, 11(2):1135–1140, 2011.

[388] R. D. Bennett, A. J. Hart, A. C. Miller, P. T. Hammond, D. J. Irvine, and R. E. Cohen. Creating patterned carbon nanotube catalysts through the microcontact printing of block copolymer micellar thin films. *Langmuir*, 22(20):8273–8276, 2006.

[389] V. Meenakshi, Y. Babayan, and T. W. Odom. Benchtop nanoscale patterning using soft lithography. *Journal of Chemical Education*, 84(11):1795–U19, 2007.

[390] D. Qin, Y. N. Xia, and G. M. Whitesides. Soft lithography for micro- and nanoscale patterning. *Nature Protocols*, 5(3):491–502, 2010.

[391] T. Hashimoto, Y. Fukunishi, B. Zheng, Y. Uraoka, T. Hosoi, T. Shimura, and H. Watanabe. Electrical detection of surface plasmon resonance phenomena by a photoelectronic device integrated with gold nanoparticle plasmon antenna. *Applied Physics Letters*, 102(8), 2013.

[392] J. Y. Ouyang. Materials effects on the electrode-sensitive bipolar resistive switches of polymer: gold nanoparticle memory devices. *Organic Electronics*, 14(6):1458–1466, 2013.

[393] D. Qu, F. Liu, J. F. Yu, W. L. Xie, Q. Xu, X. D. Li, and Y. D. Huang. Plasmonic core-shell gold nanoparticle enhanced optical absorption in photovoltaic devices. *Applied Physics Letters*, 98(11), 2011.

[394] Y. Q. Wen, F. B. Y. Li, X. C. Dong, J. Zhang, Q. H. Xiong, and P. Chen. The electrical detection of lead ions using gold-nanoparticle- and DNAzyme-functionalized graphene device. *Advanced Healthcare Materials*, 2(2):271–274, 2013.

[395] G. J. Bakeine, L. Benedetti, D. Galli, G. Grenci, A. Pozzato, M. Prasciolu, M. Tormen, and G. Cusella. Effects of substrate nanopatterning on human osteosarcoma cells (SaOs-2) behavior. *Microelectronic Engineering*, 87(5-8):830–833, 2010.

[396] C. X. Li, D. Y. Jiang, L. L. Zhang, J. F. Xia, and Q. Li. Controlled synthesis of ZnS quantum dots and ZnS quantum flakes with graphene as a template. *Langmuir*, 28(25):9729–9734, 2012.

[397] P. Liu, J. G. Sun, J. H. Huang, R. Peng, J. Tang, and J. D. Ding. Fabrication of micropatterns of nanoarrays on a polymeric gel surface. *Nanoscale*, 2(1):122–127, 2010.

[398] Rodrigo Yelin and Shimon Schuldiner. Purification of vesicular monoamine transporters: From classical techniques to histidine tags. *Neurotransmitter Transporters*, 296:64–72, 1998.

[399] D. L. Peterson. Immunoassay technique using histidine tags, metals, and chelating agents, October 1997.

[400] Daniel J. O'Shannessy, Kevin C. O'Donnell, John Martin, and Michael Brigham-Burke. Detection and quantitation of hexa-histidine-tagged recombinant proteins on western blots and by a surface plasmon resonance biosensor technique. *Analytical Biochemistry*, 229(1):119–124, 1995.

[401] Michal Wasowicz, Subramanian Viswanathan, Anzhela Dvornyk, Krystyna Grzelak, Barbara Kludkiewicz, and Hanna Radecka. Comparison of electrochemical immunosensors based on gold nano materials and immunoblot techniques for detection of histidine-tagged proteins in culture medium. *Biosensors & Bioelectronics*, 24(2):284–289, 2008.

[402] R. Vallina-Garcia, M. D. Garcia-Suarez, M. T. Fernandez-Abedul, F. J. Mendez, and A. Costa-Garcia. Oriented immobilisation of anti-pneumolysin Fab through a histidine tag for electrochemical immunosensors. *Biosensors & Bioelectronics*, 23(2):210–217, 2007.

[403] M. Wasowicz, M. Milner, D. Radecka, K. Grzelak, and H. Radecka. Immunosensor incorporating anti-his (C-term) IgG F(ab') fragments attached to gold nanorods for detection of his-tagged proteins in culture medium. *Sensors*, 10(6):5409–5424, 2010.

[404] Tobias Schoen Joachim P. Spatz Tobias Wolfram, Ferdinand Belz. Site-specific presentation of single recombinant proteins in defined nanoarrays. *Biointerphases*, 2(1):44–48, 2007.

[405] X. Ai, Q. Xu, M. Jones, Q. Song, S. Y. Ding, R. J. Ellingson, M. Himmel, and G. Rumbles. Photophysics of (CdSe) ZnS colloidal quantum dots in an aqueous environment stabilized with amino acids and genetically-modified proteins. *Photochemical & Photobiological Sciences*, 6(9):1027–1033, 2007.

[406] N. Anikeeva, T. Lebedeva, A. R. Clapp, E. R. Goldman, M. L. Dustin, H. Mattoussi, and Y. Sykulev. Quantum dot/peptide-MHC biosensors reveal strong CD8-dependent cooperation between self and viral antigens that augment the T cell response. *Proceedings of the National Academy of Sciences of the United States of America*, 103(45):16846–16851, 2006.

[407] J. R. Li, L. Shi, Z. Deng, S. H. Lo, and G. Y. Liu. Nanostructures of designed geometry and functionality enable regulation of cellular signaling processes. *Biochemistry*, 51(30):5876–93, 2012.

[408] G. P. Li, J. F. Zhai, D. Li, X. N. Fang, H. Jiang, Q. Z. Dong, and E. K. Wang. One-pot synthesis of monodispersed ZnS nanospheres with high antibacterial activity. *Journal of Materials Chemistry*, 20(41):9215–9219, 2010.

[409] S. Li, J. S. Lian, and Q. Jiang. Modeling size and surface effects on ZnS phase selection. *Chemical Physics Letters*, 455(4-6):202–206, 2008.

[410] Y. Li, C. H. Ye, X. S. Fang, L. Yang, Y. H. Xiao, and L. D. Zhang. Fabrication and photoluminescence of SiO2-sheathed semiconducting nanowires: the case of ZnS/SiO2. *Nanotechnology*, 16(4):501–505, 2005.

[411] B. J. Li, J. B. Liang, X. Y. Jiang, M. Zhou, W. Li, Y. L. Na, and T. S. Li. Solar energy storage using a ZnS thin film. *Energy Sources*, 22(10):865–868, 2000.

[412] X. S. Fang, T. Y. Zhai, U. K. Gautam, L. Li, L. M. Wu, B. Yoshio, and D. Golberg. ZnS nanostructures: From synthesis to applications. *Progress in Materials Science*, 56(2):175–287, 2011.

[413] X. S. Fang, Y. Bando, M. Y. Liao, T. Y. Zhai, U. K. Gautam, L. Li, Y. Koide, and D. Golberg. An efficient way to assemble ZnS nanobelts as ultraviolet-light sensors with enhanced photocurrent and stability. *Advanced Functional Materials*, 20(3):500–508, 2010.

[414] X. S. Fang, O. Bando, and D. Golberg. Synthesis and property of nanostructured ZnS. *Microscopy and Microanalysis*, 15:1158–1159, 2009.

[415] X. S. Fang, Y. Bando, U. K. Gautam, T. Y. Zhai, H. B. Zeng, X. J. Xu, M. Y. Liao, and D. Golberg. ZnO and ZnS nanostructures: Ultraviolet-light emitters, lasers, and sensors. *Critical Reviews in Solid State and Materials Sciences*, 34(3-4):190–223, 2009.

[416] X. S. Fang, Y. Bando, M. Y. Liao, U. K. Gautam, C. Y. Zhi, B. Dierre, B. D. Liu, T. Y. Zhai, T. Sekiguchi, Y. Koide, and D. Golberg. Single-crystalline ZnS nanobelts as ultraviolet-light sensors. *Advanced Materials*, 21(20):2034–2039, 2009.

[417] X. S. Fang, U. K. Gautam, Y. Bando, B. Dierre, T. Sekiguchi, and D. Golberg. Multiangular branched zns nanostructures with needle-shaped tips: Potential luminescent and field-emitter nanomaterial. *Journal of Physical Chemistry C*, 112(12):4735–4742, 2008.

[418] X. S. Fang, Y. Bando, and D. Golberg. Recent progress in one-dimensional ZnS nanostructures: Syntheses and novel properties. *Journal of Materials Science & Technology*, 24(4):512–519, 2008.

[419] M. H. Fang, Y. G. Liu, Z. H. Huang, J. T. Huang, and D. S. Quan. Synthesis of YxGd3-xAl5O12 for thermal barrier coating by solid-state reaction method. *Rare Metal Materials and Engineering*, 36:263–265, 2007.

[420] X. S. Fang, C. H. Ye, L. D. Zhang, Y. H. Wang, and Y. C. Wu. Temperature-controlled catalytic growth of ZnS nanostructures by the evaporation of ZnS nanopowders. *Advanced Functional Materials*, 15(1):63–68, 2005.

[421] S. Y. Ding, G. Rumbles, M. Jones, M. P. Tucker, J. Nedeljkovic, M. N. Simon, J. S. Wall, and M. E. Himmel. Bioconjugation of (CdSe)ZnS quantum dots using a genetically engineered multiple polyhistidine tagged cohesin/dockerin protein polymer. *Macromolecular Materials and Engineering*, 289(7):622–628, 2004.

[422] X. Ai, Q. Xu, M. Jones, Q. Song, S. Y. Ding, R. J. Ellingson, M. Himmel, and G. Rumbles. Photophysics of (CdSe) ZnS colloidal quantum dots in an aqueous environment stabilized with amino acids and genetically-modified proteins. *Photochemical & Photobiological Sciences*, 6(9):1027–1033, 2007.

[423] D. P. Kern, K. Y. Lee, S. A. Rishton, and S. J. Wind. Nanofabrication for quantum devices. *Japanese Journal of Applied Physics Part 1-Regular Papers Short Notes & Review Papers*, 31(12B):4496–4500, 1992.

[424] C. T. Liang, M. Y. Simmons, C. G. Smith, G. H. Kim, D. A. Ritchie, and M. Pepper. Experimental evidence for coulomb charging effects in an open quantum dot at zero magnetic field. *Physical Review Letters*, 81(16):3507–3510, 1998.

[425] C. T. Liang, M. Y. Simmons, C. G. Smith, G. H. Kim, D. A. Ritchie, and M. Pepper. Multilayered gated lateral quantum dot devices. *Applied Physics Letters*, 76(9):1134–1136, 2000.

[426] S. J. Chorley, J. Frake, C. G. Smith, G. A. C. Jones, and M. R. Buitelaar. Quantized charge pumping through a carbon nanotube double quantum dot. *Applied Physics Letters*, 100(14), 2012.

[427] A. S. Dzurak, C. G. Smith, C. H. W. Barnes, M. Pepper, L. MartinMoreno, C. T. Liang, D. A. Ritchie, and G. A. C. Jones. Thermoelectric signature of the excitation spectrum of a quantum dot. *Physical Review B*, 55(16):10197–10200, 1997.

[428] Z. X. Zou, D. Du, J. Wang, J. N. Smith, C. Timchalk, Y. Q. Li, and Y. H. Lin. Quantum dot-based immunochromatographic fluorescent biosensor for biomonitoring trichloropyridinol, a biomarker of exposure to chlorpyrifos. *Analytical Chemistry*, 82(12):5125–5133, 2010.

[429] A. J. Zilkie, J. Meier, M. Mojahedi, P. J. Poole, P. Barrios, D. Poitras, T. J. Rotter, C. Yang, A. Stintz, K. J. Malloy, P. W. E. Smith, and J. S. Aitchison. Carrier dynamics of quantum-dot, quantum-dash, and, quantum-well semiconductor optical amplifiers operating at 1.55 mu m. *Ieee Journal of Quantum Electronics*, 43(11-12):982–991, 2007.

[430] J. Zhang, Y. D. Yang, F. H. Jiang, J. P. Li, B. L. Xu, X. C. Wang, and S. M. Wang. Fabrication, structural characterization and photoluminescence of Q-1D semiconductor ZnS hierarchical nanostructures. *Nanotechnology*, 17(10):2695–2700, 2006.

[431] E. B. Voura, J. K. Jaiswal, H. Mattoussi, and S. M. Simon. Tracking metastatic tumor cell extravasation with quantum dot nanocrystals and fluorescence emission-scanning microscopy. *Nature Medicine*, 10(9):993–998, 2004.

[432] N. S. Nirmala Jothi, Amish G. Joshi, R. Jerald Vijay, A. Muthuvinayagam, and P. Sagayaraj. Investigation on one-pot hydrothermal synthesis, structural and optical properties of ZnS quantum dots. *Materials Chemistry and Physics*, 138(1):186–191, 2013.

[433] G. J. Liu, X. H. Yan, Z. H. Lu, S. A. Curda, and J. Lal. One-pot synthesis of block copolymer coated cobalt nanocrystals. *Chemistry of Materials*, 17(20):4985–4991, 2005.

[434] D. Wahl, A. Ladenburger, M. Feneberg, W. Schoch, K. Thonke, and R. Sauer. Semiconductor quantum dots through conversion of micelle-generated metal clusters. *Applied Physics Letters*, 95(9), 2009.

[435] H. Yusuf, W. G. Kim, D. H. Lee, M. Aloshyna, A. G. Brolo, and M. G. Moffitt. A hierarchical self-assembly route to three-dimensional polymer-quantum dot photonic arrays. *Langmuir*, 23(10):5251–5254, 2007.

[436] N. Goswami and P. Sen. UV-Visible spectroscopic study of ZnS nanostructures synthesized by a novel micellar method. *Journal of Materials Science*, 47(6):2903–2909, 2012.

[437] Xionghui Fu, Xianfeng Yang, Zhiren Qiu, Fenghua Zhao, Jianle Zhuang, Aihua He, Liqiao Chen, Chunlei Wu, Xianjian Duan, Chaolun Liang, and Mingmei Wu. Outward conversion of core-shell nanostructured ZnS microspheres to mesoporous ZnO ones. *Crystengcomm*, 15(17):3334–3340, 2013.

[438] Yanpeng Fu, Rodrigo Saez-Araoz, Tristan Koehler, Martin Krueger, Daniel Abou-Ras, Alexander Steigert, Iver Lauermann, Ulrike Bloeck, Martha Ch Lux-Steiner, and Christian-H. Fischer. Self-assembled, stabilizer-free ZnS nanodot films using spray-based approaches. *Journal of Physical Chemistry C*, 117(46):24632–24639, 2013.

[439] Yinghuan Fu, Ke Teng, Xiaoli Dong, Chunling Yu, Chun Ma, and Hongchao Ma. *Hydrothermal preparation, characterization and photocatalytic properties of C, N co-doped ZnO/ZnS composites*, volume 610-613 of *Advanced Materials Research*, pages 1841–1844. 2013.

[440] Robert K. Prud'homme. Ostwald ripening of nanoparticle systems. *Abstracts of Papers of the American Chemical Society*, 245, 2013.

[441] Peter J. Skrdla. Use of dispersive kinetic models for nucleation and denucleation to predict steady-state nanoparticle size distributions and the role of ostwald ripening (vol 116, pg 214, 2012). *Journal of Physical Chemistry C*, 117(25):13337–13338, 2013.

[442] Y. C. Wang and S. Gunasekaran. Spectroscopic and microscopic investigation of gold nanoparticle nucleation and growth mechanisms using gelatin as a stabilizer. *Journal of Nanoparticle Research*, 14(10), 2012.

[443] Puspanjali Sahu and B. L. V. Prasad. Fine control of nanoparticle sizes and size distributions: temperature and ligand effects on the digestive ripening process. *Nanoscale*, 5(5):1768–1771, 2013.

[444] S. Wageh, S. M. Liu, and X. R. Xu. Effect of aging on CdSe nanocrystals. *Physica E-Low-Dimensional Systems & Nanostructures*, 16(2):269–273, 2003.

[445] W. Vogel, J. Urban, M. Kundu, and S. K. Kulkarni. Sphalerite-wurtzite intermediates in nanocrystalline CdS. *Langmuir*, 13(4):827–832, 1997.

[446] S. Wageh, Z. S. Ling, and X. Xu-Rong. Growth and optical properties of colloidal ZnS nanoparticles. *Journal of Crystal Growth*, 255(3-4):332–337, 2003.

[447] S. Wageh, S. M. Liu, T. Y. Fang, and X. R. Xu. Optical properties of strongly luminescing mercaptoacetic-acid-capped ZnS nanoparticles. *Journal of Luminescence*, 102:768–773, 2003.

[448] P. K. Ghosh, U. N. Maiti, S. Jana, and K. K. Chattopadhyay. Field emission from zns nanorods synthesized by radio frequency magnetron sputtering technique. *Applied Surface Science*, 253(3):1544–1550, 2006.

[449] J. Nanda, S. Sapra, D. D. Sarma, N. Chandrasekharan, and G. Hodes. Size-selected zinc sulfide nanocrystallites: Synthesis, structure, and optical studies. *Chemistry of Materials*, 12(4):1018–1024, 2000.

[450] C. H. Ye, X. S. Fang, G. H. Li, and L. D. Zhang. Origin of the green photoluminescence from zinc sulfide nanobelts. *Applied Physics Letters*, 85(15):3035–3037, 2004.

[451] X. Y. Ye, W. D. Zhuang, Y. Fang, Y. S. Hu, K. Zhao, and X. W. Huang. A facile two-phase approach to nearly monodisperse ZnS nanocrystals. *Materials Chemistry and Physics*, 112(3):730–733, 2008.

[452] D. D. Ye, C. Y. Xiao, R. R. Qi, and P. K. Jiang. Preparation and characterization of PLA/ZnS nanocomposites via an in situ solvothermal process. *Journal of Applied Polymer Science*, 125:E117–E124, 2012.

[453] C. H. Ye, X. S. Fang, M. Wang, and L. D. Zhang. Temperature-dependent photoluminescence from elemental sulfur species on ZnS nanobelts. *Journal of Applied Physics*, 99(6), 2006.

[454] Y. Q. Chang, M. W. Wang, X. H. Chen, S. L. Ni, and W. J. Qiang. Field emission and photoluminescence characteristics of ZnS nanowires via vapor phase growth. *Solid State Communications*, 142(5):295–298, 2007.

[455] X. Fan, Y. Kong, I. Shafiq, S. Lee, F. Q. Li, X. M. Meng, and L. Jiang. ZnO and ZnS composited tri-crystal nanoribbons. *Materials Letters*, 65(11):1621–1624, 2011.

[456] X. S. Fang, C. H. Ye, X. S. Peng, Y. H. Wang, Y. C. Wu, and L. D. Zhang. Large-scale synthesis of ZnS nanosheets by the evaporation of ZnS nanopowders. *Journal of Crystal Growth*, 263(1-4):263–268, 2004.

[457] Emilie Narni-Mancinelli, Sophie Ugolini, and Eric Vivier. Tuning the threshold of natural killer cell responses. *Current opinion in immunology*, 25(1):53–8, 2013.

[458] Jeff J. Subleski, Robert H. Wiltrout, and Jonathan M. Weiss. Application of tissue-specific NK and NKT cell activity for tumor immunotherapy. *Journal of Autoimmunity*, 33(3-4):275–281, 2009.

[459] C. A. Biron. Natural killer cell regulation during viral infection. *Biochemical Society Transactions*, 25(2):687–690, 1997.

[460] P. D. Sun. Structure and function of natural-killer-cell receptors. *Immunol. Res.*, 27(2-3):539–48, 2003.

[461] Adel Benlahrech, Julian Harris, Andrea Meiser, Timos Papagatsias, Julia Hornig, Peter Hayes, Andre Lieber, Takis Athanasopoulos, Veronique Bachy, Eszter Csomor, Rod Daniels, Kerry Fisher, Frances Gotch, Len Seymour, Karen Logan, Romina Barbagallo, Linda Klavinskis, George Dickson, and Steven Patterson. Adenovirus vector vaccination induces expansion of memory CD4 T cells with a mucosal homing phenotype that are readily susceptible to HIV-1. *Proceedings of the National Academy of Sciences of the United States of America*, 106(47):19940–19945, 2009.

[462] Jordan S. Orange. Human natural killer cell deficiencies. *Current Opinion in Allergy and Clinical Immunology*, 6(6):399–409, 2006.

[463] J. S. Orange, S. Roy-Ghanta, E. M. Mace, S. Maru, G. D. Rak, K. B. Sanborn, A. Fasth, R. Saltzman, A. Paisley, L. Monaco-Shawver, P. P. Banerjee, and R. Pandey. IL-2 induces a WAVE2-dependent pathway for actin reorganization that enables WASp-independent human NK cell function. *Journal of Clinical Investigation*, 121(4):1535–1548, 2011.

[464] G. Cartron, L. Dacheux, G. Salles, P. Solal-Celigny, P. Bardos, P. Colombat, and H. Watier. Therapeutic activity of humanized anti-CD20 monoclonal antibody and polymorphism in IgG Fc receptor FcgammaRIIIa gene. *Blood*, 99(3):754–8, 2002.

[465] W. Alduaij and T. M. Illidge. The future of anti-CD20 monoclonal antibodies: are we making progress? *Blood*, 117(11):2993–3001, 2011.

[466] Yenan T. Bryceson and Hans-Gustaf Ljunggren. Tumor cell recognition by the NK cell activating receptor NKG2D. *European Journal of Immunology*, 38(11):2957–2961, 2008.

[467] E. J. Allenspach, P. Cullinan, J. K. Tong, Q. Z. Tang, A. G. Tesciuba, J. L. Cannon, S. M. Takahashi, R. Morgan, J. K. Burkhardt, and A. I. Sperling. ERM-dependent movement of CD43 defines a novel protein complex distal to the immunological synapse. *Immunity*, 15(5):739–750, 2001.

[468] P. M. Cullinan, E. J. Allenspach, Q. Z. Tang, J. K. Tong, A. L. Sperling, and J. K. Burkhardt. The assembly of an ERM-dependent protein complex at the distal T cell pole. *Molecular Biology of the Cell*, 12:300A–300A, 2001.

[469] J. Delon, K. Kaibuchi, and R. N. Germain. Exclusion of CD43 from the immunological synapse is mediated by phosphorylation-regulated relocation of the cytoskeletal adaptor moesin. *Immunity*, 15(5):691–701, 2001.

[470] B. Treanor, D. Depoil, A. Bruckbauer, and F. D. Batista. Dynamic cortical actin remodeling by ERM proteins controls BCR microcluster organization and integrity. *Journal of Experimental Medicine*, 208(5):1055–1068, 2011.

[471] S. B. Taner, B. Onfelt, N. J. Pirinen, F. E. McCann, A. I. Magee, and D. M. Davis. Control of immune responses by trafficking cell surface proteins, vesicles and lipid rafts to and from the immunological synapse. *Traffic*, 5(9):651–661, 2004.

[472] D. Liu, M. E. Peterson, and E. O. Long. The adaptor protein Crk controls activation and inhibition of natural killer cells. *Immunity*, 36(4):600–11, 2012.

[473] Tadashi Yokosuka Michael L. Dustin Rajat Varma, Gabriele Campi. T cell receptor-proximal signals are sustained in peripheral microclusters and terminated in the central supramolecular activation cluster. *Immunity*, 25:117–127, 2006.

[474] F. J. Culley, M. Johnson, J. H. Evans, S. Kumar, R. Crilly, J. Casasbuenas, T. Schnyder, M. Mehrabi, M. P. Deonarain, D. S. Ushakov, V. Braud, G. Roth, R. Brock, K. Kohler, and D. M. Davis. Natural killer cell signal integration balances synapse symmetry and migration. *PLoS Biol.*, 7(7):e1000159, 2009.

[475] O. Mandelboim, L. Pazmany, D. M. Davis, M. Vales-Gomez, H. T. Reyburn, B. Rybalov, and J. L. Strominger. Multiple receptors for HLA-G on human natural killer cells. *Proceedings of the National Academy of Sciences of the United States of America*, 94(26):14666–14670, 1997.

[476] D. Mazia, G. Schatten, and W. Sale. Adhesion of cells to surfaces coated with polylysine - applications to electron-microscopy. *Journal of Cell Biology*, 66(1):198–200, 1975.

[477] O. Carpen, I. Virtanen, V. P. Lehto, and E. Saksela. Polarization of NK cell cytoskeleton upon conjugation with sensitive target-cells. *Journal of Immunology*, 131(6):2695–2698, 1983.

[478] E. Sherman, V. Barr, S. Manley, G. Patterson, L. Balagopalan, I. Akpan, C. K. Regan, R. K. Merrill, C. L. Sommers, J. Lippincott-Schwartz, and L. E. Samelson. Functional nanoscale organization of signaling molecules downstream of the T cell antigen receptor. *Immunity*, 35(5):705–20, 2011.

[479] J. S. Bezbradica and R. Medzhitov. Role of ITAM signaling module in signal integration. *Curr. Opin. Immunol.*, 24(1):58–66, 2012.

[480] Johanne M. Kaplan, Michele E. Youd, and Tracey A. Lodie. Immunomodulatory activity of mesenchymal stem cells. *Current Stem Cell Research & Therapy*, 6(4):297–316, 2011.

[481] W. W. Schamel, I. Arechaga, R. M. Risueno, H. M. van Santen, P. Cabezas, C. Risco, J. M. Valpuesta, and B. Alarcon. Coexistence of multivalent and monovalent TCRs explains high sensitivity and wide range of response. *J. Exp. Med.*, 202(4):493–503, 2005.

[482] L. P. Kane, J. Lin, and A. Weiss. Signal transduction by the TCR for antigen. *Current Opinion in Immunology*, 12(3):242–249, 2000.

[483] M. Li, L. Q. Liu, N. Xi, Y. C. Wang, Z. L. Dong, O. Tabata, X. B. Xiao, and W. J. Zhang. Imaging and measuring the rituximab-induced changes of mechanical properties in B-lymphoma cells using atomic force microscopy. *Biochemical and Biophysical Research Communications*, 404(2):689–694, 2011.

[484] Claire E. Chivers, Apurba L. Koner, Edward D. Lowe, and Mark Howarth. How the biotin-streptavidin interaction was made even stronger: investigation via crystallography and a chimaeric tetramer. *Biochemical Journal*, 435:55–63, 2011.

[485] Claire E. Chivers, Estelle Crozat, Calvin Chu, Vincent T. Moy, David J. Sherratt, and Mark Howarth. A streptavidin variant with slower biotin dissociation and increased mechanostability. *Nature Methods*, 7(5):391–U76, 2010.

[486] Mark Howarth, Wenhao Liu, Sujiet Puthenveetil, Yi Zheng, Lisa F. Marshall, Michael M. Schmidt, K. Dane Wittrup, Moungi G. Bawendi, and Alice Y. Ting. Monovalent, reduced-size quantum dots for imaging receptors on living cells. *Nature Methods*, 5(5):397–399, 2008.

[487] K. Bonroy, F. Frederix, G. Reekmans, E. Dewolf, R. De Palma, G. Borghs, P. Declerck, and B. Goddeeris. Comparison of random and oriented immobilisation of antibody fragments on mixed self-assembled monolayers. *Journal of Immunological Methods*, 312(1-2):167–181, 2006.

[488] S. J. Guo and S. J. Dong. Biomolecule-nanoparticle hybrids for electrochemical biosensors. *Trac-Trends in Analytical Chemistry*, 28(1):96–109, 2009.

[489] W. Lee, B. K. Oh, W. H. Lee, and J. W. Choi. Immobilization of antibody fragment for immunosensor application based on surface plasmon resonance. *Colloids and Surfaces B-Biointerfaces*, 40(3-4):143–148, 2005.

[490] I. Vikholm-Lundin and W. M. Albers. Site-directed immobilisation of antibody fragments for detection of C-reactive protein. *Biosensors & Bioelectronics*, 21(7):1141–1148, 2006.

[491] I. Vikholm. Self-assembly of antibody fragments and polymers onto gold for immunosensing. *Sensors and Actuators B-Chemical*, 106(1):311–316, 2005.

[492] H. Wang, J. Wu, J. S. Li, Y. J. Ding, G. L. Shen, and R. Q. Yu. Nanogold particle-enhanced oriented adsorption of antibody fragments for immunosensing platforms. *Biosensors & Bioelectronics*, 20(11):2210–2217, 2005.

[493] Steven A. Rosenberg Nicholas P. Restifo Luca Gattinoni, Daniel J Powell Jr. Adoptive imunotherapy for cancer: building on sucess. *Nature Reviews*, 6:383–393, 2006.

[494] H. R. Koene, M. Kleijer, J. Algra, D. Roos, Aegk vondemBorne, and M. deHaas. Fc gamma RIIIa-158V/F polymorphism influences the binding of IgG by natural killer cell Fc gamma RIIIa, independently of the Fc gamma IIIa-48L/R/H phenotype. *Blood*, 90(3):1109–1114, 1997.

[495] W. K. Weng and R. Levy. Two immunoglobulin G fragment C receptor polymorphisms independently predict response to rituximab in patients with follicular lymphoma. *Journal of Clinical Oncology*, 21(21):3940–3947, 2003.

[496] A. Sulica, C. Galatiuc, M. Manciulea, A. C. Bancu, A. Deleo, T. L. Whiteside, and R. B. Herberman. Regulation of human natural cytotoxicity by IGG .4. association between binding of monomeric IGG to the Fc-receptors on large granular lymphocytes and inhibition of natural-killer (NK) cell-activity. *Cellular Immunology*, 147(2):397–410, 1993.

[497] M. Manciulea, A. Sulica, H. Rabinovich, W. Lin, T. Whiteside, A. Deleo, R. Herberman, and S. Corey. Phosphotyrosine proteins, PI 3-kinase and calcium changes distinguish activating and inhibitory pathways via Fc-gamma-RIIIA in human NK cells. *Blood*, 82(10):A247–A247, 1993.

[498] S. Valitutti, D. Coombs, and L. Dupre. The space and time frames of T cell activation at the immunological synapse. *Febs Letters*, 584(24):4851–4857, 2010.

[499] Lawrence J. Stern Jennifer D. Stone. CD8 T cells, like CD4 T cells, are triggered by multivalent engagement of TCRs by MHC-Peptide ligands but not by monovalent engagement. *Journal of Immunology*, 176:1498–1505, 2006.

[500] C. Brossard, V. Feuillet, A. Schmitt, C. Randriamampita, M. Romao, G. Raposo, and A. Trautmann. Multifocal structure of the t cell - dendritic cell synapse. *European Journal of Immunology*, 35(6):1741–1753, 2005.

[501] W. Senaratne, P. Sengupta, V. Jakubek, D. Holowka, C. K. Ober, and B. Baird. Functionalized surface arrays for spatial targeting of immune cell signaling. *Journal of the American Chemical Society*, 128(17):5594–5595, 2006.

[502] R. Fishler, A. Artzy-Schnirman, E. Peer, R. Wolchinsky, R. Brener, T. Waks, Z. Eshhar, Y. Reiter, and U. Sivan. Mixed alkanethiol monolayers on submicrometric gold patterns: a controlled platform for studying cell-ligand interactions. *Nano Lett.*, 12(9):4992–6, 2012.

[503] K. C. Garcia, M. Degano, R. L. Stanfield, A. Brunmark, M. R. Jackson, P. A. Peterson, L. Teyton, and I. A. Wilson. An alpha beta T cell receptor structure at 2.5 angstrom and its orientation in the TCR-MHC complex. *Science*, 274(5285):209–219, 1996.

[504] N. P. Huang, J. Voros, S. M. De Paul, M. Textor, and N. D. Spencer. Biotin-derivatized poly(l-lysine)-g-poly(ethylene glycol): A novel polymeric interface for bioaffinity sensing. *Langmuir*, 18(1):220–230, 2002.

[505] P. M. Rudd, M. R. Wormald, R. L. Stanfield, M. D. Huang, N. Mattsson, J. A. Speir, J. A. DiGennaro, J. S. Fetrow, R. A. Dwek, and I. A. Wilson. Roles for glycosylation of cell surface receptors involved in cellular immune recognition. *Journal of Molecular Biology*, 293(2):351–366, 1999.

[506] T. Nakamura, K. Takahashi, T. Fukazawa, M. Koyanagi, A. Yokoyama, H. Kato, H. Yagita, and K. Okumura. Relative contribution of CD2 and LFA-1 to murine-T and natural-killer-cell functions. *Journal of Immunology*, 145(11):3628–3634, 1990.

[507] K. Tkach and G. Altan-Bonnet. T cell responses to antigen: hasty proposals resolved through long engagements. *Current Opinion in Immunology*, 25(1):120–125, 2013.

[508] T. A. Springer and M. L. Dustin. Integrin inside-out signaling and the immunological synapse. *Current Opinion in Cell Biology*, 24(1):107–115, 2012.

[509] T. M. Fahmy, J. G. Bieler, M. Edidin, and J. P. Schneck. Increased TCR avidity after T cell activation: a mechanism for sensing low-density antigen. *Immunity*, 14(2):135–43, 2001.

[510] T. Tian, S. J. Plowman, R. G. Parton, Y. Kloog, and J. F. Hancock. Mathematical modeling of K-Ras nanocluster formation on the plasma membrane. *Biophys. J.*, 99(2):534–43, 2010.

[511] Yun-Ta Yang, Jiunn-Der Liao, Chou-Ching K. Lin, Cheng-Tao Chang, Shyh-Hau Wang, and Ming-Shaung Ju. Characterization of cholesterol-depleted or -restored cell membranes by depth-sensing nano-indentation. *Soft Matter*, 8(3):682–687, 2012.

[512] A. J. Zilkie, J. Meier, M. Mojahedi, A. S. Helmy, P. J. Poole, P. Barrios, D. Poitras, T. J. Rotter, C. Yang, A. Stintz, K. J. Malloy, P. W. E. Smith, and J. S. Aitchison. Time-resolved linewidth enhancement factors in quantum dot and higher-dimensional semiconductor amplifiers operating at 1.55 mu m. *Journal of Lightwave Technology*, 26(9-12):1498–1509, 2008.

[513] D. Leitenberg and K. Bottomly. Regulation of naive T cell differentiation by varying the potency of TCR signal transduction. *Seminars in Immunology*, 11(4):283–292, 1999.

[514] F. Sallusto, D. Lenig, R. Forster, M. Lipp, and A. Lanzavecchia. Two subsets of memory T lymphocytes with distinct homing potentials and effector functions. *Nature*, 401(6754):708–12, 1999.

[515] F. D. Batista, E. Arana, P. Barral, Y. R. Carrasco, D. Depoil, J. Eckl-Dorna, S. Fleire, K. Howe, A. Vehlow, M. Weber, and B. Treanor. The role of integrins and coreceptors in refining thresholds for B-cell responses. *Immunological Reviews*, 218:197–213, 2007.

[516] M. Adamczyk, J. C. Gebler, and J. Wu. Papain digestion of different mouse IgG subclasses as studied by electrospray mass spectrometry. *Journal of Immunological Methods*, 237(1-2):95–104, 2000.

[517] L. Coleman and S. M. Mahler. Purification of fab fragments from a monoclonal antibody papain digest by gradiflow electrophoresis. *Protein Expression and Purification*, 32(2):246–251, 2003.

[518] M. Mariani, M. Camagna, L. Tarditi, and E. Seccamani. A new enzymatic method to obtain high-yield F(ab')2 suitable for clinical use from mouse IGG1. *Molecular Immunology*, 28(1-2):69–77, 1991.

[519] T. Nitta, H. Yagita, T. Azuma, K. Sato, and K. Okumura. Bispecific F(ab')2 monomer prepared with anti-CD3 and anti-tumor monoclonal-antibodies is most potent in induction of cytolysis of human T-cells. *European Journal of Immunology*, 19(8):1437–1441, 1989.

[520] J. Deeg, M. Axmann, J. Matic, A. Liapis, D. Depoil, J. Afrose, S. Curado, M. L. Dustin, and J. P. Spatz. T cell activation is determined by the number of presented antigens. *Nano Letters*, 13(11):5619–5626, 2013.

[521] J. Matic, J. Deeg, A. Scheffold, I. Goldstein, and J. P. Spatz. Fine tuning and efficient T cell activation with stimulatory aCD3 nanoarrays. *Nano Letters*, 13(11):5090–5097, 2013.

[522] A. Engler, L. Bacakova, C. Newman, M. Sheehan, and D. Discher. *Mechanical role of cytoskeletal components in vascular smooth muscle cell adhesion in vitro*. Proceedings of the Ieee 28th Annual Northeast Bioengineering Conference. 2002.

[523] A. Engler, L. Bacakova, C. Newman, A. Hategan, M. Griffin, and D. Discher. Substrate compliance versus ligand density in cell on gel responses. *Biophysical Journal*, 86(1):388A–388A, 2004.

[524] A. J. Engler, M. Berry, H. L. Sweeney, and D. E. Discher. Substrate compliance alters human mesenchymal stem cell morphology. *Molecular Biology of the Cell*, 15:298A–298A, 2004.

[525] F. Rehfeldt, A. J. Engler, and D. E. Discher. BIOT 7-differentiation of adult human stem cells guided by mechano-sensing of matrix elasticity. *Abstracts of Papers of the American Chemical Society*, 234, 2007.

[526] F. Rehfeldt, A. J. Engler, A. Eckhardt, F. Ahmed, and D. E. Discher. Cell responses to the mechanochemical microenvironment - implications for regenerative medicine and drug delivery. *Advanced Drug Delivery Reviews*, 59(13):1329–1339, 2007.

[527] S. Sen, A. J. Engler, and D. E. Discher. Matrix strains induced by cells: Computing how far cells can feel. *Cellular and Molecular Bioengineering*, 2(1):39–48, 2009.

[528] Carmine Carpenito richard G. Carroll Gwendolyn K. Binder David Teachey Minu Samanta Mehdi Lakhal Brian Gloass Gwenn Danet-Desnoyers Dario Campana James L Riley Stephan A. Grupp Carl H. June Michael C Milone, Jonathan D. Fish. Chimeric receptors containing CD137 signal transdcution domains mediate enhanced survival of T cells and increased antiluekemic efficacy in vivo. *Molecular Therapy*, pages 1–12, 2009.

[529] Renier J Brentjens Alena A Chekmasova. Adoptive T cell immunotherapy strategies for the treatment of patients with ovarian cancer. *Discovery Medicine*, 9(44):62–70, 2010.

[530] J. C. Becker. Active immunotherapy: Vaccination and adoptive cell transfer. *Onkologie*, 36:220–220, 2013.

[531] Gmpg Attianese, V. Hoyos, B. Savoldo, V. Marin, M. Brandi, A. Biondi, G. Dotti, and E. Biagi. Generation of a new chimeric antigen receptor (CAR) to target CD23 expressed on chronic lymphocytic leukemia (B-CLL) cells. *Molecular Therapy*, 17:230, 2009.

[532] Thomas Brocker. Chimeric Fv-Zeta or FV- Eta receptors are not sufficient to induce activation or cytokine production in peripheral T cells. *Blood*, 96(5):1999–2001, 2000.

[533] Macolm Brenner Gianpietro Dotti, Barbara Savolodo. fifteen years of gene therapy based on chimeric antigen receptors: "are we nearly there yet?". *Human Gene Therapy*, 20:1229–1239, 2009.

[534] Julie Foster David M Davies Sylvain Julien Lucienne Cooper Sefina Arif Stephen J Mather Joyce Taylor Papdimitriou Joy M Burchell-John Maher Scott Wilkie, Gianfranco Picco. Retargeting of human T cells to tumour-associated MUC1: The evolution of a chimeric antigen receptor. *Journal of Immunology*, 180L:4901–4909, 2008.

[535] M. C. Milone, L. C. Kam, K. Shen, X. Hao, R. Oconnor, G. Hickey, and R. O'Connor. Culture system useful for stimulating T cells in culture comprises biocompatible substrate with tunable rigidity, where substrate displays on its surface agent that stimulates T cell receptor/complementarily determining 3 complex.

[536] Hailin Cong, Alexander Revzin, and Tingrui Pan. Non-adhesive PEG hydrogel nanostructures for self-assembly of highly ordered colloids. *Nanotechnology*, 20(7), 2009.

[537] K. M. Gattas-Asfura, Y. J. Zheng, M. Micic, M. J. Snedaker, X. J. Ji, G. D. Sui, J. Orbulescu, F. M. Andreopoulos, S. M. Pham, C. M. Wang, and R. M. Leblanc. Immobilization of quantum dots in the photo-cross-linked poly(ethylene glycol)-based hydrogel. *Journal of Physical Chemistry B*, 107(38):10464–10469, 2003.

[538] A. S. Sechi and J. Wehland. Interplay between TCR signalling and actin cytoskeleton dynamics. *Trends in Immunology*, 25(5):257–265, 2004.

[539] V. I. Chubinskiy-Nadezhdin, T. N. Efremova, S. Y. Khaitlina, and E. A. Morachevskaya. Functional impact of cholesterol sequestration on actin cytoskeleton in normal and transformed fibroblasts. *Cell Biology International*, 37(6):617–623, 2013.

[540] V. I. Chubinskiy-Nadezhdin, A. V. Sudarikova, N. N. Nikolsky, and E. A. Morachevskaya. Role of submembranous actin cytoskeleton in regulation of non-voltage-gated sodium channels. *Doklady Biochemistry and Biophysics*, 450(1):126–129, 2013.

[541] Zin Z. Khaing, Brian D. Milman, Jennifer E. Vanscoy, Stephanie K. Seidlits, Raymond J. Grill, and Christine E. Schmidt. High molecular weight hyaluronic acid limits astrocyte activation and scar formation after spinal cord injury. *Journal of Neural Engineering*, 8(4), 2011.

[542] Y. Sawada, M. Tamada, B. J. Dubin-Thaler, O. Cherniavskaya, R. Sakai, S. Tanaka, and M. P. Sheetz. Force sensing by mechanical extension of the Src family kinase substrate p130Cas. *Cell*, 127(5):1015–1026, 2006.

[543] Chunming Wang, Rohan R. Varshney, and Dong-An Wang. Therapeutic cell delivery and fate control in hydrogels and hydrogel hybrids. *Advanced Drug Delivery Reviews*, 62(7-8):699–710, 2010.

[544] D. T. Nguyen, D. J. Kim, M. G. So, and K. S. Kim. Experimental measurements of gold nanoparticle nucleation and growth by citrate reduction of HAuCl4. *Advanced Powder Technology*, 21(2):111–118, 2010.

[545] S. P. Shields, V. N. Richards, and W. E. Buhro. Nucleation control of size and dispersity in aggregative nanoparticle growth. a study of the coarsening kinetics of thiolate-capped gold nanocrystals. *Chemistry of Materials*, 22(10):3212–3225, 2010.

[546] H. Yan, S. Cingarapu, K. J. Klabunde, A. Chakrabarti, and C. M. Sorensen. Nucleation of gold nanoparticle superclusters from solution. *Physical Review Letters*, 102(9), 2009.

Appendix A

Fabrication of encapsulated gold nanoparticles using hydrazine

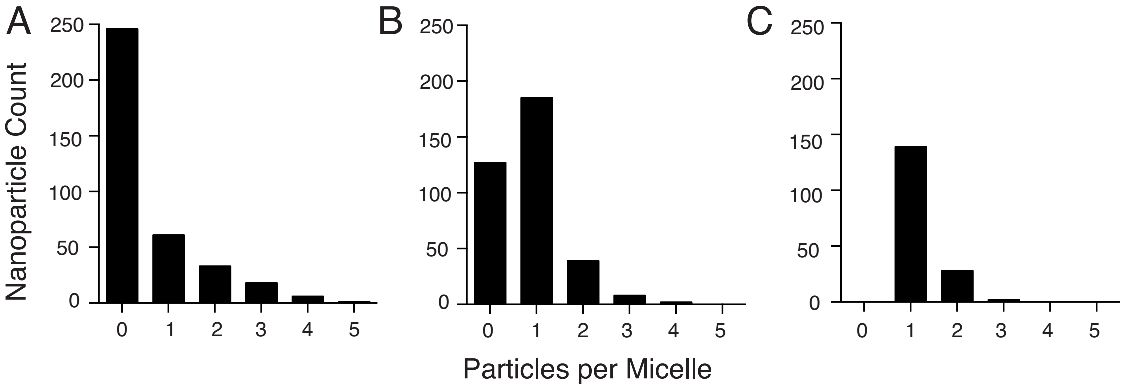

Figure A.0.1: Hydrazine reduction; histogram of distribution of nanoparticles formed per micelle. $PS_{(110000)}$-b-$P2VP_{(52000)}$ was exposed to hydrazine at (A) 1× concentration (B) 10× concentration or (C) 30× concentration. Samples were dip-coated and examined by SEM. The number of particles visible per micelle was calculated, over 150 micelles were analysed in each case.

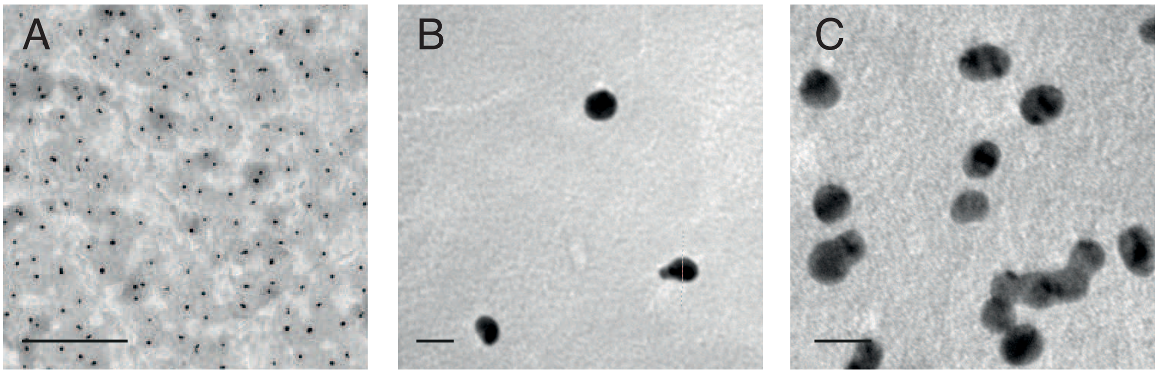

Figure A.0.2: TEM analysis of reductant concentration and nanoparticle nucleation. Solutions of gold-loaded micelles were treated with various concentrations of hydrazine reducing agent, and drop coated onto TEM grids before analysis in an FX 2000 TEM. Samples were prepared by Derfogail Delcassian and imaged by Karla-Luise Herpolt. (A, B) 30× hydrazine (C) 10× hydrazine. Scale bar (A) 0.5µm (B,C) 20nm. Increased reductant concentration results in a smaller particle, the harder reduction may induce a single nucleation site. [544, 545, 442, 546]

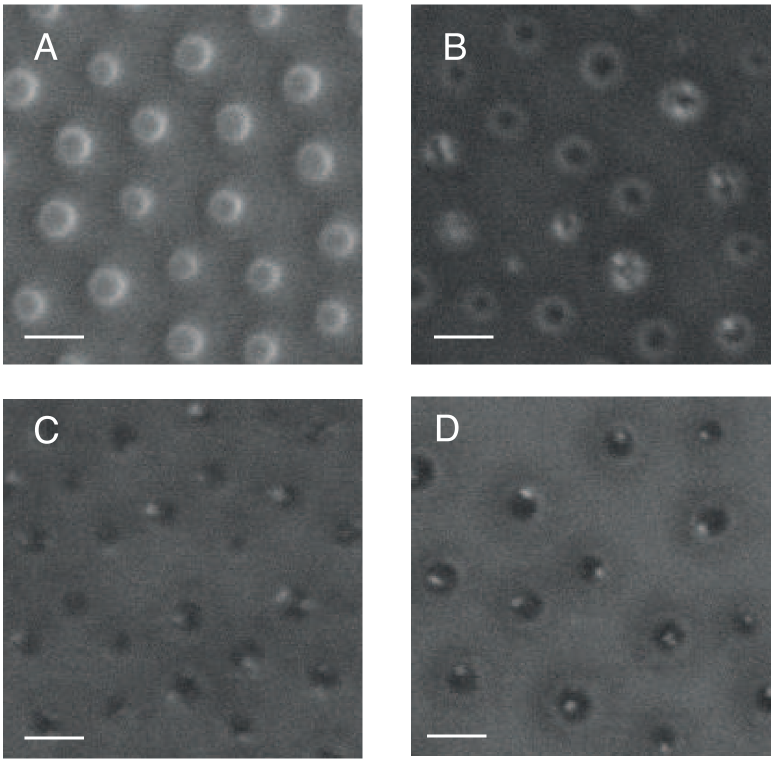

Figure A.0.3: SEM analysis of gold nanoparticle formation post reduction. $PS_{(110000)}$-b-$P2VP_{(52000)}$ gold loaded micelles were exposed to hydrazine at (A) 1× concentration (B) 10× concentration or (C) 30× concentration. Samples were dip-coated and examined by FEG-SEM. Scale bar 100nm. Samples exposed to lower reductant concentrations have induced polynucleation, or remain un-nucleated, possibly due to poor diffusion.

Appendix B

Fabrication of advanced nanopatterned arrays; density based arrays

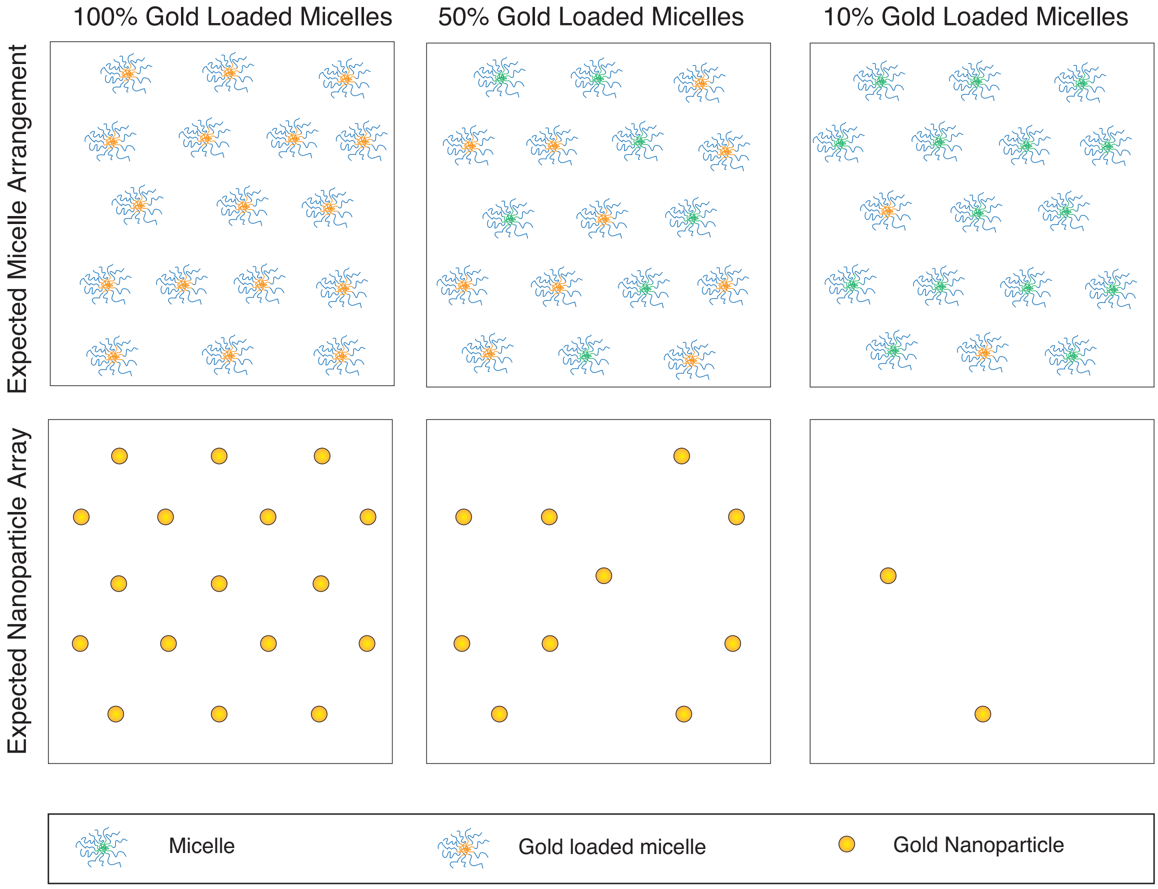

Figure B.0.1: Schematic of density gradient for micelle recombination Micellar solutions of loaded and unloaded micelles should allow the fabrication of nanoparticle arrays where the minimal spacing between two nanoparticles is controlled by the polymer template, but the overall density per µm^2 can be altered based on the ratio of empty to full micelles.

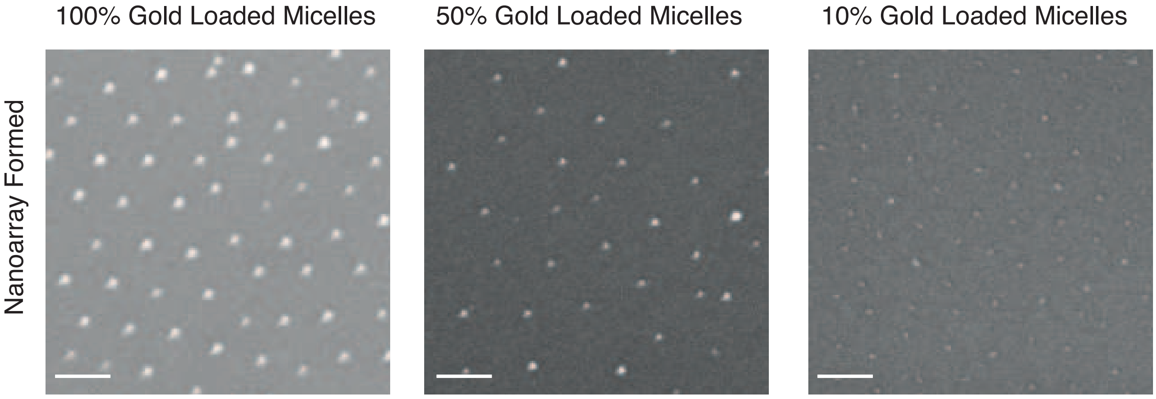

Figure B.0.2: Particle Density Arrays $PS_{(110000)}$-b-$P2VP_{(52000)}$ unloaded and gold-loaded micelles were mixed at various rations. Substrates were dip-coated within 5 minutes, exposed to plasma and examined by SEM. Scale bar 100nm. Rather than producing surfaces coated with a percentage of standard nanoparticles, gold ions are redistributed to produce uniform nanoparticle arrays.

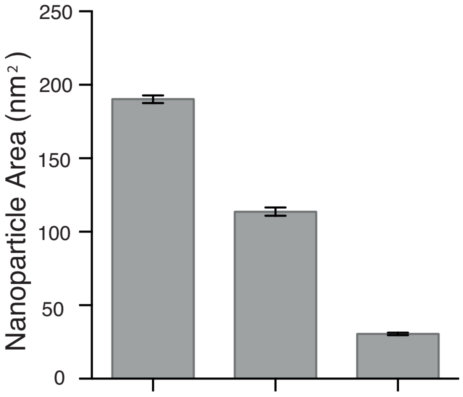

Figure B.0.3: Particle size, ionic redistribution. Nanoparticle area of particles formed from mixed ratio solutions were analysed. Bars represent mean of over 120 particles per condition and error bar is the standard error in the mean.

Appendix C

SAXS and SANS analysis of nanoparticles

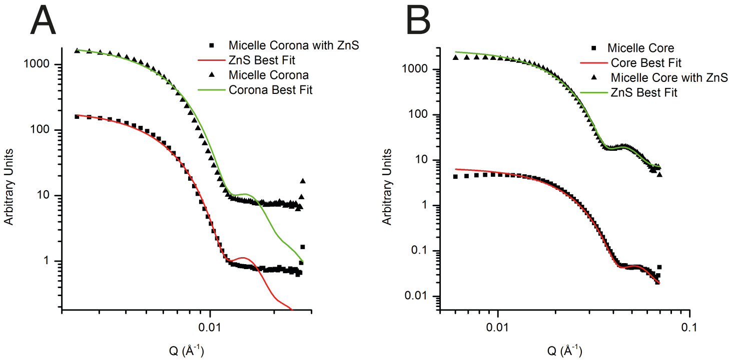

Figure C.0.1: SANS analysis performed on micelles pre and post zinc sulfide formation. Examination of the core and corona size change post ZnS fabrication is included. SANS analysis performed by Dr. Iain Dunlop, and fitted by Lucia Pordhoska, on samples made by Derfogail Delcassian.

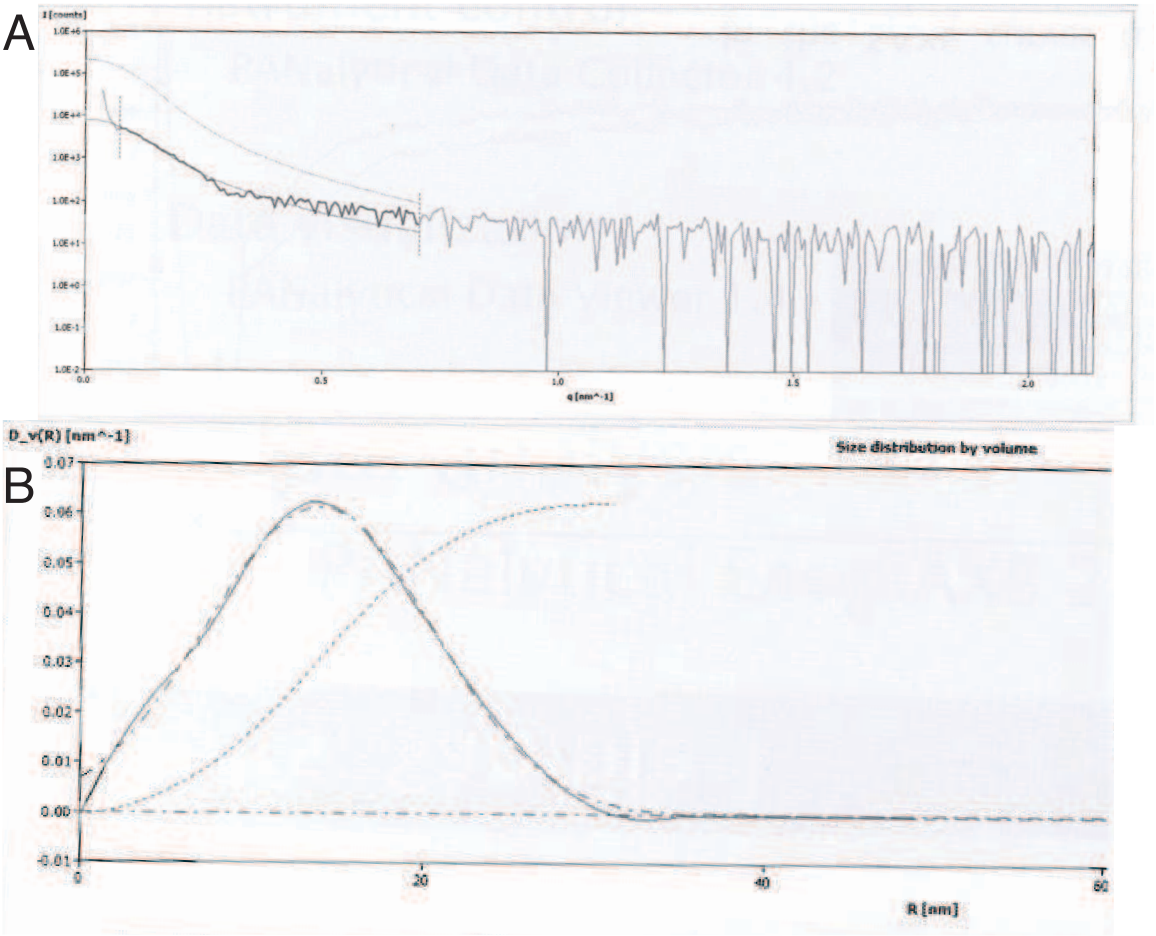

Figure C.0.2: SAXS analysis performed on micelles with encapsulated ZnS particles, using a scan type 2Theta. (A) Q vs I and (B) fitted data to a spherical assumption of size distribution by volume. Analysis performed by PANylitical on samples made by Derfogail Delcassian.

Appendix D

Phosphotyrosine intensity in T cells: further analysis

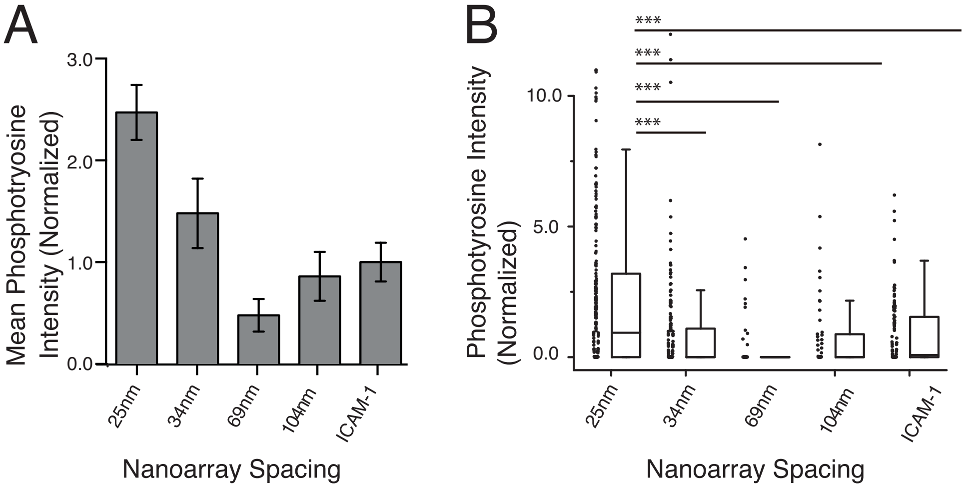

Figure D.0.1: Cellular response to F(ab’)$_2$and ICAM-1 surfaces. Plots show intensity of TIRF-immunofluoresence of phosphotyrosine after 5 minutes stimulation, as a function of nanoarray spacing. (A) The mean of the phosphotyrosine intensity normalized to the ICAM-1 background intensity for each donor and then averaged across donors. Error bars respresent the standard error in the mean. (B) Individual cells shown as dots; cells from donors were normalised to their own ICAM-1 response, and combined. Central line shows the median, boxes the 25th to 75th percentile and whiskers the upper and lower inner fence values. *** = $p<0.001$, (Mann-Whitney non-parametric analysis)

Appendix E

Mechanical properties of bulk PEGDA materials

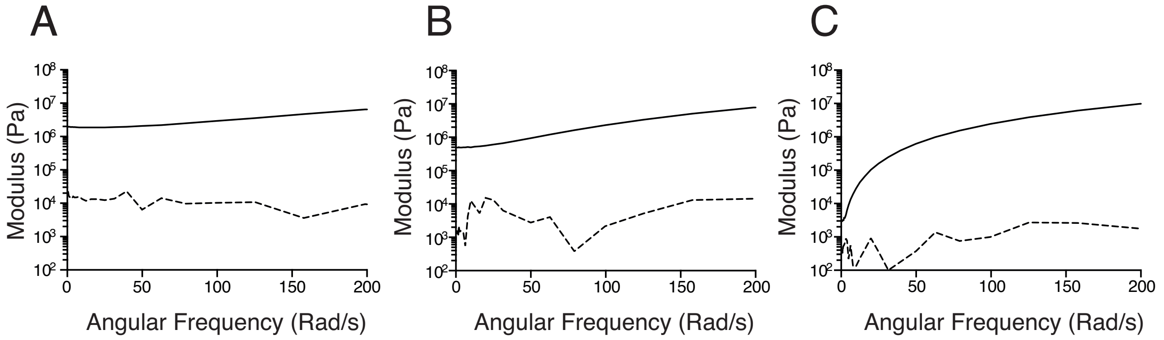

Figure E.0.1: Rheometry of bulk PEGDA hydrogels was performed. Graphs represent storage (solid line) and loss (dotted line) values against angular frequency. A) PEGDA Molecular weight 700, B) PEGDA Molecular weight 6000 C) PEGDA molecular weight 35000.